UNIVERSITÀ DEGLI STUDI DI NAPOLI
FEDERICO II

Dottorato di Ricerca in
Ingegneria Elettronica e delle Telecomunicazioni
XVIII Ciclo

# PHOTONIC WIDEBAND PHASED ARRAY: AN OPTICAL TIME STEERED ANTENNA BASED ON A NEW TRUE TIME DELAY UNIT


Relatore
Ch.mo Prof. Giuseppe D'Elia

Candidato
Claudio Curcio

Coordinatore
Ch.mo Prof. Giovanni Poggi

*to my parents*

# INDEX

# INTRODUCTION

The modern and the future communication systems employed in the military and civilian applications, such as radars, remote sensing, satellite and spaceborn applications, air traffic control, wireless LAN, radio telescope and automotive systems require innovative and flexible antenna systems. The primary requirements regard the attainable beam control features, the antenna apparatus physical properties, the system cost and reliability. In particular the features of interest are:

- Advanced beam control features
  - high spatial scan coverage
  - high scanning resolution and low beam scanning time
  - fine sidelobe control
  - wide or ultrawide bandwidth
  - beam squint free steering
  - multiple contemporaneous beams
  - independent control of the different beams
  - sum and difference beam patterns

- Physical and environmental requirements
  - Reduced size and weight
  - interference immunity
  - transportability
  - antenna conformable to an assigned geometry
  - wide operating temperature range
  - mechanical reliability

- High maintainability and reliability, and low system cost

To satisfy these high performance requirements, array antennas are often employed. The discrete nature of the array, in fact, gives to the designer many degrees of freedom to attain some of the needed beam control features: fine beam shaping and beam steering, multiple contemporaneous beams. However, the need for high beam control flexibility could require an array control apparatus, the beamforming network (BFN), not satisfying the requirements regarding compactness, reliability, low complexity and cost. Moreover, to achieve the desired wideband (WB) radiative behavior, the BFN has to be properly designed, taking into account for the bandwidth limitation typical of the arrays.

Accordingly, to efficiently meet the mentioned high performance requirements, the designer has to exploit proper control techniques and choose the best suited technology. In fact, a trade-off among the BFN compactness and complexity and a flexible beam control can be found by using the phase-only control techniques: the

BFN structure does not control the amplitude of the excitation coefficients of the elements. This strategy allows a good beam control performances and reduces the BFN hardware complexity, size and weight.

Regarding the WB beam control, it is possible to reduce efficiently the antenna pattern variations with the frequency only if we refer to some peculiar applications and features. In particular, in the beam steering applications, the beam pointing direction can became constant with the frequency if the True Time Delay (TTD) principle is applied by substituting the phase control units with time shifters.

However, when realizing the time control units by using the conventional microwave (MW) technology, complex, heavy and bulky BFNs are obtained. In fact, the antenna systems based on the classical MW technology have, usually, high size and weight. Moreover, such devices suffer from losses and bandwidth problems.

Improvements have been obtained by using the MW monolithic integrated circuits (MMIC). However, the MMIC technology can not efficiently satisfy the above mentioned requirements dictated by the WB beam squint free systems. Accordingly, better solutions are mandatory.

Since the early '90s, the research activity have been attempted to overcome the limitations of the standard technologies. A promising alternative, among the other, is the optical technology. In fact, the optical systems represent the easiest and efficient way to realize the TTD principle, and allow to realize BFNs having low size and weight, high interference immunity and an ultra wide operative bandwidth.

The thesis has been devoted to the design of an high performance phased array antenna prototype able of the WB beam steering control and based on an innovative optical TTD control unit.

To design efficiently the optical time steering antenna (OTSA) prototype, taking into account also for the unavoidable troubles affecting the nominal characteristics of the antenna system, the following issues have been faced:

- Analysis of the photonic BFN architectures attainable in the open specialized literature
- Analysis of the performances achievable with a new photonic integrated TTD module
- Optimization of the working configurations of the new TTD module
- Modeling of the OTSA devices: detailed simulation of the antenna behavior
- Study of the electromagnetic mutual coupling effects on the BFN working
- Study of the effects on the distribution of the excitation coefficients of the array due to the realization defects and the quantization errors
- Reduction of the effects due to the errors introduced by the BFN devices: implementation of an evolutionary algorithm to optimize the compensation unit configuration
- Introduction of a new, full optical, architecture realizing sum and difference beam squint free patterns

In the 1$^{st}$ Chapter the peculiar features of the WB phased array antennas are introduced: the attention is mainly focused on the BFN. In the first part of the chapter, by referring to the literature, the main WB BFN architectures and the most important design issues, such as the electromagnetic mutual coupling, the random and quantization errors, are enlighten. In the second part of the chapter, the optical

technology for phased array is introduced, by discussing the optical beamforming principles.

To efficiently design the optical control unit of the antenna prototype, a wide analysis of the optical BFN principles, rationales and architectures has been carried out. The review has two ends: to enlighten the key aspects of the main optical BFN architectures and to thoroughly go into the issues related to the implementation of such structures.

The analyzed architectures have been classified, by distinguishing them according to the optical systems realizing the phase or the time delay control. The first approach is discussed in the 2nd Chapter, while the second is studied in the 3rd Chapter.

Accordingly, the 2nd Chapter shows the main schemes and the most interesting realizations of the optical *phase control* architectures. The most part of these architectures are based on the coherent detection scheme and allows to realize BFN, mainly based on bulk optics or integrated optics devices, performing an agile beam shaping and steering control of 2D phased array antennas, for multiple beams applications. Non coherent optical phase control systems have also been proposed, even if a minor interest has been devoted to them. However, this topic is covered at the end of the Chapter.

However, the *phase control* techniques are not suited for WB beam squint free applications. The systems able to perform the optical *time control* are needed. Accordingly, in the 3rd Chapter the two main optical TTD architectures are described: the switched delay lines and the variable propagation velocity lines. In particular, for each category, the main approaches have been enlightened and the performance factors of the most relevant realizations have been reported. A summary frame has also been presented to make easier the comparison among different approaches. Finally, the optical TTD hardware compressive architectures, suited for large phased array and save hardware complexity have been considered.

The scheme of an OTSA has been identified, thanks also the reasoned analysis of the literature.

The core of the OTSA is the time delay control unit. A new optical integrated TTD unit (TTDU) has been proposed to implement a switched delay lines matrix. The chip is based on a cross-connect switch innovative for the antenna applications and adopts the low cost inkjet technology.

The 4th Chapter presents the feasibility study that has been carried out to evaluate the performances attainable with the TTDU. In particular the time control capabilities are considered, the TTDU working configurations are studied to achieve good time delay quantization levels, to reduce the losses due to the BFN, to vary the time delay distribution needed to drive different aperture antennas and provide a flexible beam control, to drive as many radiating elements as possible by using only one TTDU and save the required hardware.

Once the TTDU features have been optimized, the achievable beam capabilities and the radiating systems properties have been evaluated. Regarding the radiating system implementation, printed array antennas have been considered since they allows to get a compact radiating system, having good bandwidth properties, low fabrication costs and can be easily integrated with the BFN to obtain a compact OTSA prototype. The design and realization of the antenna prototypes is discussed in the Appendix C.

The first section of the 5th Chapter shows, for each TTDU working configurations, the achievable beam features and the radiating system properties. In

particular, a design chart has been introduced, which allows to evaluate the maximum beam steering angle and the antenna aperture size, avoiding grating lobes. The choice of the prototype beam, related to the amplitude of the excitations distribution, has been discussed. Moreover, the prototype tolerances have been evaluated. To this end, a statistical and numerical analysis have been carried out to evaluate the maximum acceptable errors on the antenna excitation coefficients, once the maximum acceptable pattern degradation is known.

In the second part of the chapter, the model of the OTSA, as similar as possible to the real-world one, has been derived. The OTSA model allows to accurately study the antenna behaviour. It is based on a proper modelling of each optical and MW components employed in the OTSA. In order to obtain an effective description, the real characteristics of the commercial devices and the unavoidable realization defects have been taken into account and the effects of the related errors on the antenna excitation distribution have been evaluated.

On the other hand other error sources have to be taken into account. In fact, the signals driven by TTDU experience some losses that can deteriorate the antenna amplitude distribution and vary the beam features. The compensation of these errors can be carried out by employing trim units. However, the compensation is not trivial, since the errors vary with the beam pointing direction. Accordingly, to efficiently use such trim units, an evolutionary algorithm has been implemented: it optimizes the trim units configurations, their number, and the trim amount in order to reduce the effects of the TTDU losses errors and achieve an amplitude distribution as close as possible to the desired one. Some results obtained by using the proposed approach are reported in the $5^{th}$ Chapter.

At the end of the Chapter the all optical architecture proposed to realize sum and difference beam squint patterns has been described.

Three appendices have also been reported.

In the Appendix A, the well-known array antenna results are presented, in order to fix the notation exploited during the whole thesis.

In the Appendix B, the optical links employed in antenna applications, are reported. Moreover, the link figures of merit are also discussed.

The Appendix C shows the design, realization and characterization procedures of printed array antennas prototype set up thanks to the equipments of the Antenna Lab and the Anechoic Chamber of the EM Lab of the Department of Electronic and Telecommunication Engineering of the University of Naples Federico II.

In particular, the radiating element design is discussed, and the results related to three different antenna prototypes, properly designed to verify the accuracy of the process, are presented.

## *Acknowledgments*

*To conclude these three years I would like to thank all the people who allowed me to have this important experience.*

*In particular, I would like to thank my advisor Prof. G.D'Elia, for giving me the chance to carry out this interesting research activity.*

*Moreover, I would like to thank Prof. A. Capozzoli for the unfailing help and valued support he gave me during these three years.*

*Thank you very much.*

*Claudio Curcio*

# LIST OF ACRONYMS

| ACRONIM | DESCRIPTION |
|---|---|
| AOD | Acousto optic device |
| AU | Amplitude uniformity |
| AWG | Arrayed waveguide grating |
| BFN | Beamforming network |
| BIFODEL | Binary fiber optic delay lines |
| BW | Beamwidth |
| C/N | Carrier to noise ratio |
| CDR | Compression dynamic range |
| CFBG | Chirped fiber bragg grating |
| DFB | Distributed Feedback |
| DC | Direct current |
| DM | Direct modulation |
| DR | Dynamic range |
| DSB+C | Double side band plus carrier |
| DSF | Dispersion shifted fiber |
| EA | Electro-absorption |
| EM | External modulation |
| EMI | Electromagnetic interference immunity |
| FBG | Fiber bragg grating |
| FLC | Ferroelectric liquid crystal |
| FOB | Fourier optic beamformer |
| FOP | Fiber optic prism |
| FT | Fourier transform |
| G | Gain |
| HDF | High dispersion fiber |
| IL | Insertion loss |
| $IL_T$ | Insertion loss related to the time control unit |
| IMD | Intermodulation third-order |
| IMFDR | Intermodulation free dynamic range |
| IO | Integrated optics |
| I-Q | In-phase quadrature |
| ISC | Integrated star coupler |
| LC | Liquid crystal |
| MMIC | Monolithic microwave integrated circuits |
| MW | Microwave |
| MWA | Microwave amplifier |
| MZM | Mach-Zender modulator |

| | |
|---|---|
| NF | Noise figure |
| NLC | Nematic liquid crystal |
| OA | Optical amplifier |
| OBFN | Optical beamforming network |
| OCP | Optical control processor |
| OCPS | Optically controlled phase shifter |
| OFS | Optical frequency shifter |
| OPH | Optical phaser |
| OPS | Optical phase shifter |
| OTSA | Optical time steered antenna |
| PAA | Phased array antenna |
| PADEL | Parallel optical delay line |
| PC | Phase control |
| PDM | Programmable dispersion matrix |
| PS | Phase Shifter |
| PSH | Pseudo self-heterodyne |
| RIN | Relative Intensity Noise |
| RMS | Root mean square |
| SC | Star coupler |
| SDL | Switched delay lines |
| SEP | Scan element pattern |
| SI | Scan impedance |
| SLL | Sidelobe level |
| SLM | Spatial light modulator |
| SNR | Signal to noise ratio |
| SRODEL | Square root optical delay line |
| SSB | Single side band |
| SSFIP | Strip-slot-foam-inverted patch |
| T/R | Transmit/Receive |
| TPH | Time phaser |
| TS | Time Shifter |
| TTD | True Time Delay |
| TTDU | True time delay unit |
| VCSEL | Vertical cavity surface emitters |
| VPVL | Variable propagation velocity lines |
| WB | Wideband |
| WDM | Wavelength Division Multiplexing |

# LIST OF SYMBOLS

| SYMBOL | UNIT | DESCRIPTION |
|---|---|---|
| $a_n$ | [1] | Amplitude of the excitation coefficient of the n-th array element |
| B | [1] | Number of bits of a digital phase shifter/time shifter |
| C, T, R | [dB] | Insertion loss factors related to the TTDU |
| CDR | [dB·Hz] | Compression dynamic range |
| $C_F$ | [1] | Complexity factor related to the number of fibers |
| $C_L$ | [1] | Complexity factor related to the number of lasers |
| $c_n$ | [1] | Complex excitation coefficient of the n-th array element |
| $C_S$ | [1] | Complexity factor related to the number of switches |
| D | [1] | Array directivity |
| d | [m] | Array element spacing |
| $D_{DHF}$ | [s/m$^2$] | Chromatic dispersion of an high dispersion fiber |
| $D_{DSF}$ | [s/m$^2$] | Chromatic dispersion of dispersion shifted fiber |
| $d_\lambda$ | [1] | Array element spacing normalized to the wavelength |
| f | [Hz] | Frequency of the microwave signal |
| F | [m] | Lens focal length |
| $f_A$ | [1] | Array factor |
| $f_{ac}$ | [Hz] | Frequency of the acoustic wave |
| $f_S$ | [1] | Subarray factor |
| G | [dB] | Gain |
| $G_d$ | [m] | Grating spacing |
| $i_{DSB}$ | [A] | Downconverted current related to a double sideband modulation |
| $i_L$ | [A] | Laser diode driving current |
| IL | [dB] | Insertion loss |
| $IL_{LINK}$ | [dB] | Link losses |
| IMFDR | [dB·Hz$^{2/3}$] | Intermodulation free dynamic range |
| $i_{PD}$ | [A] | Photodetector output current |
| $i_{PD,DC}$ | [A] | DC term of the photodetector output current |

*Note: [1] means that the quantity is dimensionless*

| | | |
|---|---|---|
| $i_{SSB}$ | [A] | Downconverted current related to a single sideband modulation |
| K | [1] | Number of radiated beams |
| L | [m] | Aperture of a linear array |
| $L_g$ | [m] | Bragg grating length |
| $L_M$ | [m] | Mask aperture |
| M | [1] | Magnification factor |
| $m_\theta$ | [1] | Angular magnification |
| N | [1] | Number of radiating elements |
| NF | [dB] | Noise figure |
| $N_{g\text{-}max}$ | [1] | Maximum number of gratings |
| $N_{in}$, $N_{out}$ | [dBm] | Noise power at input and output of a link |
| $N_{RIN}$ | [dBm] | Noise power due to the laser relative intensity noise |
| $N_{SHOT}$ | [dBm] | Noise power due to shot noise |
| $N_{TH}$ | [dBm] | Noise power due to thermal noise |
| p | [1] | Versor associated to the horizontal polarization |
| $P_{opt}$ | [dBm] | Power of the optical signal |
| $QL_{dB}$ | [dB] | Quantization lobe level |
| $R_{LAS}$ | [ohm] | Laser diode resistance |
| $R_{LOAD}$ | [ohm] | Load resistance |
| $R_{MOD}$ | [ohm] | Modulator resistance |
| $r_{PD}$ | [A/W] | Photodetector responsivity |
| s | [1] | Versor associated to the vertical polarization |
| $s_L$ | [W/A] | Laser slope efficiency |
| u, v | [1] | Direction cosines |
| V | [volt] | Voltage |
| $V_\pi$ | [volt] | Mach-Zender modulator switch voltage |
| $Z_{Ai}$ | [ohm] | Active impedance of the i-th element |
| $Z_{ii}$ | [ohm] | Autoimpedance of the i-th element |
| $Z_{ij}$ | [ohm] | Mutal impedance between the i-th and the j-th element |
| $\Delta_n$ | [1] | Amplitude error related to the n-th array element |
| $\delta_n$ | [rad] | Phase error related to the n-th array element |
| $\theta$ | [rad] | Beam pointing angle |
| $\theta_3$ | [rad] | Half power beamwidth |
| $\theta_{max}$ | [rad] | Maximum beam pointing angle |
| $\lambda$ | [m] | Wavelength of the microwave signal |
| $\Lambda$ | [m] | Wavelength of the optical signal |
| $\lambda_{ac}$ | [m] | Wavelength of the acoustic wave |
| $\nu_{ac}$ | [m/s] | Velocity of the acoustic wave |
| $\sigma^2_{SLL}$ | [1] | Average side lobe level |
| $\sigma^2_{Tavg}$ | [1] | Average side lobe level due to the time delay quantization |

*Note: [1] means that the quantity is dimensionless*

| | | |
|---|---|---|
| $\sigma_a^2$ | [1] | Variance of the amplitude errors |
| $\sigma_{BP}^2$ | [rad$^2$] | Variance of the beam pointing error |
| $\sigma_{IL}^2$ | [1] | Variance of the insertion loss |
| $\sigma_T^2$ | [rad$^2$] | Variance of the phase error due to the time delay quantization |
| $\sigma_\psi^2$ | [rad$^2$] | Variance of the phase errors |
| $\sigma_{CFBG}^2$ | [s$^2$] | Variance of the time delay response error of a Chirped fiber bragg grating |
| $\sigma_{LASER}^2$ | [s$^2$] | Variance of the time delay related to the laser wavelength stability in Chirped fiber bragg grating structure |
| $\tau$ | [s] | Time delay |
| $\tau_{max}$ | [s] | Maximum time delay achievable with a time shifter unit |
| $\tau_\Delta$ | [s] | Elementary delay related to the TTDU |
| $\varphi$ | [rad] | Phase shift |
| $\psi_n$ | [rad] | Phase of the excitation coefficient of the n-th array element |
| $\omega$ | [rad/s] | Pulsation of the microwave signal |
| $\Omega$ | [rad/s] | Pulsation of the optical signal |

# CHAPTER 1

# WIDEBAND PHASED ARRAY ANTENNAS

## 1. INTRODUCTION

The current and future communication systems will require innovative antenna systems, characterized by advanced features, physical and environmental requirements, low cost and high reliability:

- Advanced features
  - high spatial scan coverage
  - high scanning resolution and low beam scanning time
  - fine sidelobe control
  - wide or ultrawide bandwidth
  - beam squint free steering
  - multiple contemporaneous beams
  - independent control of the different beams
  - sum and difference beam patterns

- Physical and environmental requirements
  - reduced size and weight
  - interference immunity
  - transportability
  - antenna conformable to an assigned geometry
  - wide operating temperature range
  - mechanical reliability

- High maintainability and reliability, and low system cost

Furthermore, these high performance requirements are more and more required to implement advanced multifunction antenna systems employed in military and civilian

*Note: [1] means that the quantity is dimensionless*

applications, such as radars, air traffic control, remote sensing, satellite and spaceborn applications, smart antennas for mobile telephony, wireless LAN, radio telescope, automotive systems [*Fourikis; Hajimiri et al.*; *Kane et al.*; *Tokoro*]. In particular, multifunction apparatus are desirable since they allow to realize with a unique radiating systems several functions, requiring a wide band signal and/or signals at different frequencies, by using a time-sharing approach [*Fourikis*; *Hemmi et al.*; *Lacomme*]. As an example, the modern antenna systems proposed for air traffic control are made by means of a single wide band active array that, operate as an airport surveillance radar, a precision approach radar, a Doppler weather radar and an airport surface detector radar, i.e. it substitutes four different systems [*Fourikis*]. Moreover the system provides an accurate control of the radiated beam properties, thus improving the radar performances with respect to the four systems implementation.

Generally, to satisfy the requirements of the modern high performance systems is a hard task that requires a proper design methodology for both the radiating system and the control unit.

Array antennas represent an attractive solution since its discrete nature can be exploited to realize advanced beam control features such as fine beam shaping, rapid beam steering, multiple simultaneous beams and null positioning, by suitably adjusting the contributions of the radiating elements. However, the control system has to be carefully designed to reduce the complexity of the antenna apparatus. To this end, the phase-only control techniques have been studied [*Bucci and D'Elia*; *Bucci et al. 2004a*]: the beam features are changed by controlling only the phase or time delay distribution of the antenna excitation coefficients, while maintaining a constant amplitude distribution. This approach allows to save hardware and reduce the complexity of the antenna apparatus.

In particular here we are mainly interested in beam steering applications, eventually multi-frequency and multi-beam. To realize such applications, phased array antennas (PAA) are widely employed [*Brokner*; *Fourikis*; *Mailloux 2005*; *Parker and Zimmermann 2002b*]. The PAA are made of many radiating elements fed by means of a beamforming network (BFN). The BFN is made of proper control units, phase shifters (PS) and/or time shifters (TS), allowing to change the beam pointing direction with high agility and with a scanning time much lower than the mechanical scanning systems. Accordingly, the PAA performances are mainly dictated by the BFN architecture and technology.

To realize the control units the conventional microwave (MW) BFN technology can be adopted. In radar and communication systems, the most employed technologies are the vacuum-tube one, used in amplifier and oscillator, and the solid-state microwave integrated circuits (MMIC) [*Fourikis*].

The vacuum-tube technology is preferred to implement high power systems in the millimeter range. Regarding the MMIC technology, large investments have been done, since 1990s, to reduce the cost and improve the MMIC manufacturing technology. The reported improvements allowed the MMIC technology to replace the existing tube technology in different applications, thanks to important advantages such as reliability, reduced size and weight, bandwidth. In particular, MMICs are the preferred microwave technology for medium and high power applications below 20 GHz. The MMIC technology made possible the wide diffusion of active electronic

scanned PAA. For large production the nowadays price of a control module is about $1000, but this is still too high for many applications [*Mailloux 2005*].

However, the drawbacks of the MW technologies for the BFN are related to the size, weight, bandwidth, interference immunity and cost. These drawbacks prevented the application of these technologies in some fields, such as spatial communication apparatus or ultra wide band systems.

Accordingly, since early '90s, to face the challenge of the next generation communication systems, alternative technologies have been investigated. The most relevant beamforming alternatives are the optical technology, the microelectromechanical systems (MEMS) and the digital beamforming [*Mailloux 2005*].

The aim of this chapter is to discuss about the design guidelines and issues of WB PAA, independently from the BFN technology, in particular by referring to the True Time Delay (TTD) architecture that realize the WB beam steering control. Moreover, we show the advantages, the features and the beamforming principles of the optical technology control systems.

## 2. DESIGN OF A WIDEBAND PHASED ARRAY

Before discussing the details of the design of WB PAA, it is worth to introduce some key aspects of the modern arrays, although these are well known. To establish a notation reference, we will use the fundamentals of the array theory reported in the Appendix A.

The first aspect is related to the feeding architecture. The array feeding is obtained using the Transmit/Receive (T/R) modules. Such a module, generally, contains a power amplifier, used in the transmit mode to control the power of the generated signal, a low noise amplifier, employed in the receive mode to attain a proper signal to noise ratio at the receiver, and a switch or a circulator to select the operative modality. Accordingly, there are two main feeding schemes, which differ regarding the number of T/R modules employed: the passive and active one.

In Fig.1.1 the passive and active control architectures are reported. In the passive modality (Fig.1.1a), one T/R module drives the BFN that furnish the desired amplitude and phase distribution to the array elements [*Mailloux 2005*]. This scheme allows for simultaneous or switched sum and difference patterns. Severe losses can be reported due to T/R circulator, the control units and the power division, thus making this solution unpractical, especially for large antennas.

In Fig.1.1b the active mode scheme is depicted. In this case each radiating element is feed with a T/R module [*Mailloux 2005*; *Agrawal and Holzmann*]. The active arrays have been developed thanks to the rapid improvement of the MMIC technology. A MMIC T/R module contains one or more MMIC chips realizing all the desired features: T/R switching, low noise receive amplifier (LNA), high power transmit amplifier and gain control. In this way active arrays reduce the impact of the BFN losses. Separate BFN can be used for the transmit and the receive mode, since different sidelobe requirements are needed.

The second aspect is related to the control units. As told before, here we are interested in beam steering applications. Then, to realize the beam steering two

different control units can be employed: the phase and time control modules, i.e. PS and TS.

To show the main difference among the two modules, let us refer to the antenna feeding scheme depicted in Fig.1.2. A linear array of N elements, with uniform spacing d, is controlled by using PS/TS to furnish the phase/time delay distribution suited to make the antenna beam pointing toward the desired direction. The excitation coefficient of the n-th radiating element has magnitude $a_n$ and phase $\psi_n$, while $\theta$ is the angle formed between the normal to the array and the beam pointing direction.

Accordingly, to attain a certain beam pointing direction $\theta_0$, a linear phase distribution has to be realized, as indicated in the (A.7). In turn we have:

$$\psi_n = -(n-1)kd\sin\theta_0 \qquad \text{(I.1)}$$

where $k=2\pi/\omega$, $\omega$ being the signal frequency.

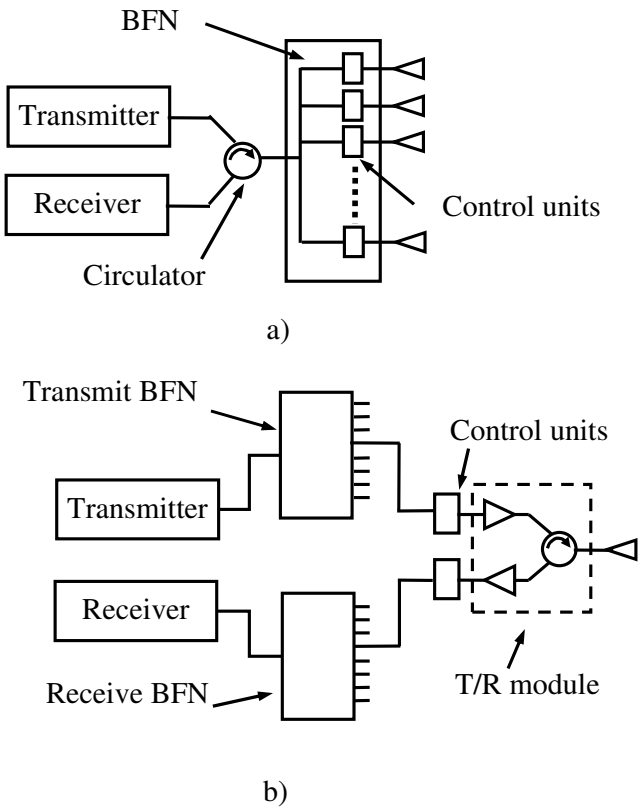


**Figure 1.1** *Array control architectures: a) passive components b) active components*

If the array is controlled by means of PS, realizing phase variations constant with the frequency, the (I.1) can be satisfied only at one frequency, equal to $\omega$. Then, when considering a frequency variation $\Delta\omega$, a beam pointing change $\Delta\theta_0$, often referred as beam squint, will occur and is given by:

$$\Delta\theta_0 = -\tan\theta_0\left(\frac{\Delta\omega}{\omega}\right) \qquad \text{(I.2)}$$

The array bandwidth, related to the beam squint phenomenon, is given by [*Mailloux 2005*]:

$$\frac{\Delta f}{f_0} \propto \left( \frac{\lambda}{Lu_0} \right) \qquad (I.3)$$

where L is the antenna aperture, $f=\omega/2\pi$, $\lambda=c/f$ is the signal wavelength, and $u_0=\sin\theta_0$ is the direction cosine related to the angle $\theta_0$.

When the array is driven using TSs, the beam squint phenomenon can be avoided. In fact, TSs realize phase terms proportional to the frequency ω. In particular to steer the beam toward the angle $\theta_0$, the n-th element has to be fed with a signal having delay $\tau_n$ given by:

$$\tau_n = \frac{nd \cos\theta_0}{c} \qquad (I.4)$$

where c is the light speed.

The time delay control is generally referred as TTD technique. In the conventional TS the different time delays, needed to realize the electronic beam steering, are, usually, obtained by switching among delay lines having different lengths. In particular, the maximum time delay $\tau_{max}$ to be realized depends on the antenna aperture L and the maximum scan angle, say, $\theta_{max}$ and is given by:

$$\tau_{max} = \frac{L}{c} \sin\theta_{max} \qquad (I.5)$$

The TS devices used in large arrays require bulky and expensive delay lines and a complex switching network, and their performance can be limited by the dispersion phenomenon [*Mailloux 2005*]. Moreover, as discussed later, the use of TS involves more issues than the PS case.

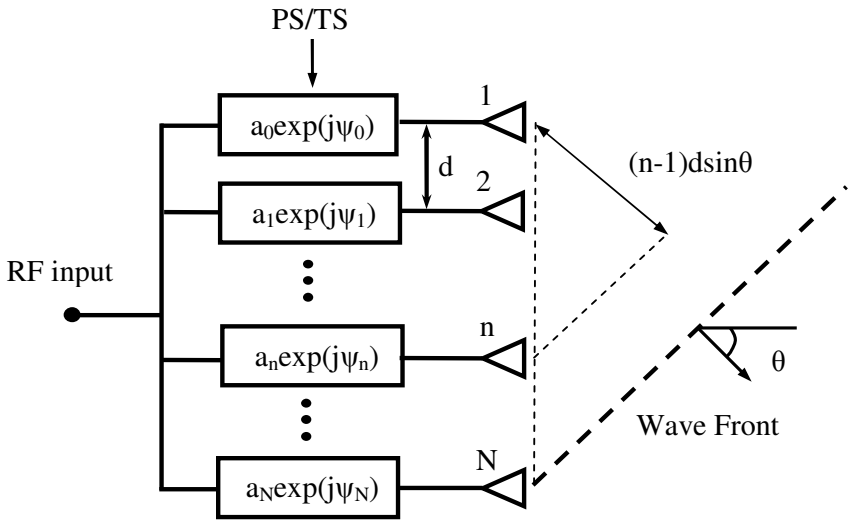


**Figure 1.2** *Beam steering control scheme for a linear PAA*

Once some useful aspects have been resumed, the design of WB PAA can be discussed. In particular, in the following we present the WB BFN architectures and the main design issues.

## 2.1 WIDEBAND BFN ARCHITECTURES

We recognize two types of WB PAA, according to the bandwidth requirements of the specific applications: the truly WB and the fractional WB PAA. In both schemes, the total system bandwidth $B_S$ is very large and extends over several octaves.

In the first category, the considered signal requires a bandwidth as large as the whole system bandwidth $B_S$. Then, to avoid the beam squint phenomenon, the BFN has to be realized by using TSs.

In the fractional WB systems, the signal has a bandwidth that is only a few percent of the total bandwidth $B_S$, and its centre frequency can be changed over $B_S$ according to the considered application. Then, the BFN can be realized by using not only TSs, but also PSs, arranged in a proper configuration.

Obviously, in both WB and fractional WB systems, the configuration complexity represents a fundamental issue.

The main control architecture schemes for the truly WB and fractional WB PAA are reported in Fig. 1.3 and Fig.1.4, respectively.

The scheme of Fig.1.3a realizes the WB beam squint free steering. Here one TS and one T/R module are used for each antenna element. This control scheme can be conveniently adopted only for small WB arrays. In fact, in the case of large PAA, the architecture becomes excessively bulky and complex also because is difficult to realize TS furnishing the wide delays needed. It is worth noting that an amplification stage is needed for each element because the TS can have high insertion losses usually increasing with the introduced delay.

A most useful approach (Fig.1.3b) can be obtained by grouping together the antenna elements in subarrays, using small TS for each element, and feeding each subarray with a single T/R module and a TS providing longer delays. Optical, analog or digital TS units can be used at this stage.

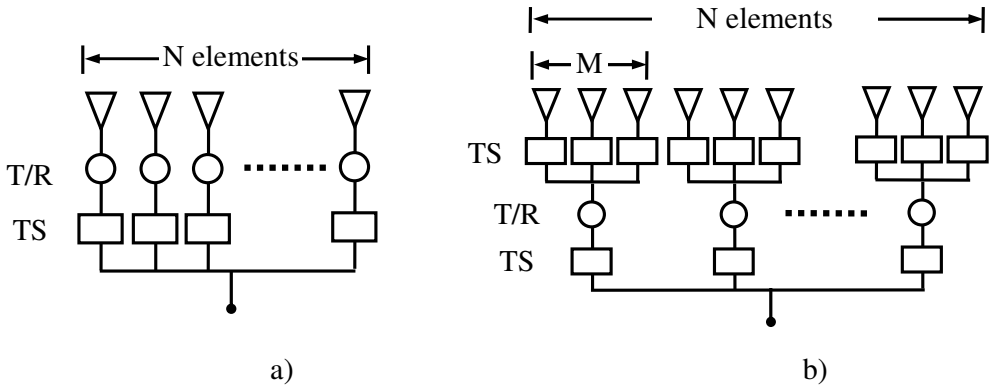


**Figure 1.3** *Wideband array control architectures: a) TS for each element b) cascaded TS scheme*

A simple control scheme for fractional WB PAA is reported in Fig.1.4. TSs and T/R modules are used at subarray level while PSs are used before each element. This architecture, obviously, does not provide a wide array bandwidth, but the achieved bandwidth is Q times the bandwidth of a full phase steered array, Q being the number of subarrays. In this way the desired fractional bandwidth is obtained. This architecture is simple and easy to build, but can produce significant quantization lobes, due to the use of digital PS/TS and amplitude control units. This important phenomenon is discussed later.

Another fractional WB architecture has been proposed for beam steering applications [*Mailloux 2005*]. The idea is to provide the needed time delays only for a small number K of fixed beam positions, while using PSs to realize the beam steering (Fig.1.5): the scanning range is divided in K sections so that the PS have to realize the beam scanning over an angular range reduced by a factor K. Accordingly, the system bandwidth results increased by the same factor K. On the other hand, TSs made of different sets of delay lines are needed for each element, thus increasing the system cost when dealing with large arrays with a high K.

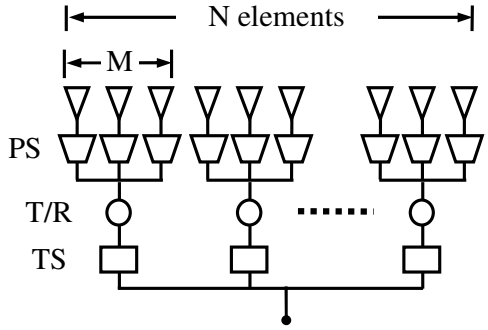


**Figure 1.4** *Fractional wideband array control architecture using contiguous time delayed subarrays*

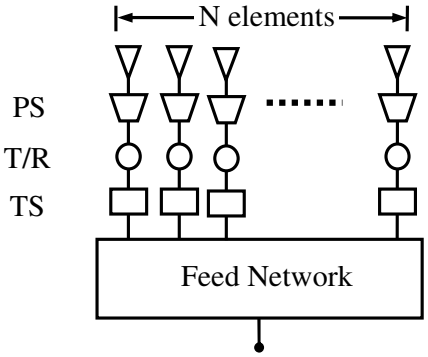


**Figure 1.5** *Control scheme for fractional WB scanning over fixed beam positions*

## 2.2 WIDEBAND SYSTEMS ISSUES

Apart from the BFN architecture, WB and fractional WB systems share common issues due to the whole apparatus bandwidth that is usually very large, or multi-band. The design of such systems is, then, a hard task because both theoretical and practical difficulties arise. Accordingly, all the PAA subsystems have to be carefully designed by facing the trade off emerging from the large bandwidth issues. In particular, the main issues are related to:

- the choice of the antenna components: T/R modules, radiating elements, etc.
- grating lobes phenomenon
- electromagnetic mutual coupling
- random and quantization errors

These aspects are widely discussed in the specialized literature [*Mailloux 2005*; *Fourikis*; *Hansen*; *Skolnik*]. A detailed treatment of these issues being beyond our scope, we will enlighten the main design aspects by discussing the electromagnetic coupling and the random and quantization errors issues, in the section 2.2.1 and 2.2.2, respectively.

As far as the choice of all the antenna components is concerned, it is necessary that all devices ensure good properties across the system bandwidth. Nowadays, wideband T/R modules are available for both power and low noise applications [*Fourikis*].

Regarding the radiating element, it is necessary to adopt radiators whose input impedance, or equivalently the Voltage Standing Wave Ratio (VSWR), and the radiation pattern are well behaved within the considered frequency range and scan angles. However, a large variety of WB antenna elements exist so that the designer can choose the one best suited to his needs. The most used are the printed wideband dipoles having a 40% fractional bandwidth, tapered slot lines, often named Vivaldi antennas, having a 1-3 octaves bandwidth [*Fourikis*], spiral mode microstrip antennas having a 6:1 bandwidth [*Wang and Tripp*], microstrip log periodic antennas having 4:1 bandwidth [*Hall*], planar broad band flared microstrip slot antennas having multioctaves bandwidth [*Fourikis*], or aperture stacked patch antennas having bandwidth up to 2 octaves [*Ghorbani and Waterhouse*].

Regarding the grating lobes, usually the element spacing is such that this undesired phenomenon, which can generate spatial ambiguities, is avoided. In some cases, grating lobes are tolerable in transmit or receive mode, but non tolerable on the pattern obtained from the multiplication of transmit and receive ones [*Fourikis*]. Equation (A.15) establishes the minimum uniform element spacing to be used for a maximum scan angle $\theta_0$, at a given signal frequency $\omega$. Usually an half wavelength spacing is used to avoid grating lobes and, in the case of a wide frequency range, to avoid lobes across the whole bandwidth, the required array elements spacing is essentially equal to $\lambda_U/2$, $\lambda_U$ being the wavelength corresponding to the highest frequency of the system bandwidth. This choice can lead to mutual coupling between the radiating elements, especially at the lower frequency, as described in the next Section.

### 2.2.1 MUTUAL COUPLING

A wide discussion about the electromagnetic coupling can be found in [*Mailloux 2005*; *Hansen*; *James and Hall*; *Skolnik; Oliner*; *Parker and Zimmermann 2002a*]. Here we present the main aspects of the mutual coupling phenomenon and we discuss the practical solutions adopted.

The electromagnetic coupling among radiating elements causes a deterioration of the input impedance and the radiation pattern of the element, since it alters the element current distribution. These effects vary with the frequency and with the scan angle, and, in principle, can not be explicitly taken into account.

The unwanted variation of the input impedance of the antenna can generate a mismatching of the feeding line that can modify the behaviour of the feed network. Usually, broad band matching circuits and/or isolators are exploited to reduce the mismatching effects.

As far as the deterioration of the radiating behaviour of the antenna is concerned, due to the coupling effects, the radiation pattern is not the same for all the array elements so that the array far-field pattern can not be described by using the array factor. However, when dealing with large arrays, with a number of elements much larger that the edge elements, it can be assumed that the radiation pattern is essentially the same for all the elements and the effect of mutual coupling can be approximately evaluated by considering an infinite array. Obviously, the resulting radiation pattern of each element differs from the one of the same isolated element, since it takes into account for the mutual coupling effects. As a consequence of these approximations, the radiating properties of the array can be described by means of the array factor.

To account for the mutual coupling effects, two useful approaches have been introduced: the scan impedance (SI) one, also known as active impedance, and the scan element pattern (SEP) one [*Hansen*]. The SI is defined as the element input impedance as function of the scan angle (the other elements are properly driven) and allows to evaluate the scan reflection coefficient $\Gamma_S(\theta)$. The SI based approach assumes that the current distribution on each array element is the same as in the case of the isolated element so that the coupling effect only influences the element input impedance. Accordingly, for large arrays, the array radiation power pattern can be easily evaluated as the product of the isolated element power pattern, the array power factor and the impedance mismatch factor $(1-|\Gamma_S(\theta)|^2)$ [*Hansen*].

The SEP is defined as the radiation pattern of an element when all the other elements are terminated on a matched load and is given by the product between the isolated element pattern and the mismatch factor. As the array beam is scanned, the peak of the array radiation pattern is given by the SEP in the same direction. As an example, for slot or dipoles the scan element power pattern $g_S$ can be given by [*Hansen*]:

$$g_S(\theta) \approx \frac{4\pi A_{elem}}{\lambda^2}\cos\theta\left(1-\left|\Gamma_S(\theta)\right|^2\right) \qquad \text{(I.6)}$$

where $A_{elem}$ is approximately equal to the area of the unit cell around the considered element, and the $\cos\theta$ term is due to the beam scanning.

In some cases, the mutual coupling effects can lead to the array blindness phenomenon: at certain scan angle the antenna beam is completely cancelled

[*Hansen*]. This resonance phenomenon corresponds to a scan reflection coefficient near the unity, or to a SEP near zero and happens when far field contributions due to higher current modes combine and cancel the contribution due to the dominant mode. The higher order modes can be generated by an external or internal structure. Some dielectric radomes are an example of external structure causing this problem [*Hansen*]. Internal structures allowing the blindness are dielectric loaded waveguide elements and brick waveguide arrays: the waveguide elements support the high order mode that causes the resonance at the blind angle.

On the other hand, the pattern null is associated to the presence of leaky waves. These waves usually have amplitude depending on the SI and on the size of the array face. In fact the leaky waves are more easily excitable in large arrays [*Hansen*].

The evaluation of the coupling effects of complex antenna structures can be performed by a number of different full analysis methods, based on integral and integrodifferential equation formulations, actually available on commercial simulators. These approaches allow estimating the impedance and pattern deteriorations due to the mutual coupling with a good degree of accuracy. Moreover, these simulators are often employed to verify how to reduce the coupling effects by varying the antenna parameters. This approach is very useful when dealing with wideband scanning arrays, where it is necessary to optimize the parameter of interest across a very large bandwidth.

To compensate the mutual coupling effects, some techniques, essentially based on the engineering practice, have been implemented [*Mailloux 2005*]. Among these, the most important ones involve the use of compensating feed network or baffles and pin between elements, the use of close element spacing, dielectric sheets for wide angular impedance matching, etc..

A further solution reducing mutual coupling effects, particularly useful when dealing with WB arrays, exploits thinned arrays [*Fourikis*], i.e., arrays with an aperiodic spatial element distribution. The approach is also useful to reduce the grating lobes phenomenon.

### 2.2.2 QUANTIZATION AND RANDOM ERRORS

When designing the antenna system, the designer has to take into account for different errors which affect the array excitation coefficients and deteriorate the radiated pattern properties. These errors can be random or spatially correlated. In general, the random errors are due to the tolerance limits, realization defects or faults of the feeding devices, while the spatial correlated ones are due to the BFN architecture, as is the case of quantization errors on both amplitude and phase/time distribution. Due to their periodic nature, the latter errors can cause pattern deteriorations more serious than the ones due to random errors.

Here, since we are mainly interested in WB PAA, the attention is focused on the PS and TS quantization errors encountered in the WB BFN architectures. In particular, we consider the truly WB system in Fig.1.3a and the fractional WB system in Fig.1.4.

The results of our analysis will be successively used as a guideline when facing the design of a WB PAA. In the case of the WB system of Fig. 1.3, we derive the quantization sidelobe level (SLL) by following the approach described by Mailloux [*2005*] for the PS and we will make a comparison between the PS and the TS quantization errors. In the case of the fractional WB system of Fig. 1.4, we report the

results available in the open literature. In both cases the error analysis can be done by assuming that the array is subdivided into subarrays due to the periodic errors..

The main available results concerning the random errors will be also reported.

It is worth noting that, once the maximum acceptable pattern deterioration has been defined, all the results on the quantization errors are very useful to establish the maximum allowable tolerances.

#### 2.2.2.1 QUANTIZATION ERRORS

***WB SYSTEMS:*** Let us refer to Fig.1.3a and assume that digital TS with B-bit are used. Each TS realizes $2^B$ delays: 0, $\tau_e$, $2\tau_e$,…, $(2^B-1)\tau_e$, where $\tau_e$ is the elemental delay and $\tau_{max}=(2^B-1)\tau_e$ is the maximum delay.

Then, the beam can be perfectly collimated only at angles requiring an incremental delay multiple of the $\tau_e$. In the other beam pointing directions a time delay distribution error occurs due to the time quantization [*Mailloux 1984*].

In this case, some array sections can have an incremental time delay $\Delta\tau_S=du_S/c$, that is some multiple of $\tau_e$, and make the beam pointing in the direction cosine $u_S$, instead that in the desired direction cosine $u_0$. This produces a time delay error $\Delta\tau-\Delta\tau_S$, where $\Delta\tau=du_0/c$ is the inter-element delay required to steer the beam towards $\theta_0$.

This error causes the most serious effects on the radiated pattern when it is entirely periodic. Then, the array can be assumed as divided in virtual subarrays, with M elements, having the same time delay distribution. The distance between the subarrays is such that the time delay error increment across the subarray is equal to the time delay of the least significant bit $\tau_e$:

$$M\left|\Delta\tau-\Delta\tau_S\right| = M\frac{d}{c}\left|u_0-u_S\right| = \frac{\tau_{max}}{(2^B-1)} \qquad \text{(I.7)}$$

The time delay quantization error leads to the formation of quantization lobes. In fact, since the array is made of subarray that can be several wavelengths apart, grating lobes will occur at the direction cosines:

$$u_q = u_0 + \frac{q\lambda}{Md} \qquad q=(\pm1,\pm2,...) \qquad \text{(I.8)}$$

where $\lambda$ is the signal wavelength.

The array pattern in correspondence of each lobe of the grating is equal to the value of the subarray pattern in the considered direction. Since the subarrays are equal in size and are feed with uniform amplitude coefficients, the subarray pattern $f_S(z)$ can be written as:

$$f_S(z) = \frac{\sin(Mz/2)}{M\sin(z/2)} \qquad \text{(I.9)}$$

where $z=2\pi d(u-u_S)/\lambda$.

Then the subarray pattern evaluated in the directions indicated by the (I.8) is:

$$f_S(z)=\frac{\sin\left[M\frac{\pi d}{\lambda}\left(u_0-u_S+\frac{q\lambda}{Md}\right)\right]}{M\sin\left[\frac{\pi d}{\lambda}\left(u_0-u_S+\frac{q\lambda}{Md}\right)\right]}=(-1)^q\frac{\sin\left[M\frac{\pi d}{\lambda}(u_0-u_S)\right]}{M\sin\left[\frac{\pi d}{\lambda}(u_0-u_S)+\frac{q\pi}{M}\right]} \qquad \text{(I.10)}$$

From the (I.7) we can write:

$$M\frac{d}{\lambda}|u_0-u_S|=\frac{f\tau_{max}}{(2^B-1)} \qquad \text{(I.11)}$$

where f is the signal frequency.

Using the (I.11) in the (I.10) and considering the quantization lobe power $P_{QL}$, we have:

$$P_{QL}=|f_S(z)|^2=\left[\frac{\sin\left(\frac{\pi f\tau_{max}}{(2^B-1)}\right)}{M\sin\left(\frac{\pi q'}{M}\right)}\right]^2 \qquad \text{(I.12)}$$

where $q'$ is given by:

$$q'=q+\frac{f\tau_{max}}{(2^B-1)} \qquad \text{(I.13)}$$

The (I.12) is analogous to the expression proposed by Mailloux for the PS, except for the phase error due to the phase quantization, equal to $2\pi/2^B$ for a B bit PS, that is now replaced by the phase error due to the time quantization, i.e., by $2\pi f\tau_{max}/(2^B-1)$ [*Jespersen and Herczfeld*]. As for the PS, the factor $[M\sin(\pi q'/M)]^{-2}$ is the envelope of the subarray pattern peak power sampled at the $q'$-th quantization lobe point. Accordingly, the quantization lobe level $QL_{dB}$, is given by:

$$\begin{aligned} QL_{dB} &= 10\log P_{QL} = \\ &= \text{envelope(dB)} + 20\log\pi + 20\log f\tau_{max} - 20\log\left(2^B-1\right) \end{aligned} \qquad \text{(I.14)}$$

where for $B\geq 6$ we have:

$$QL_{dB}=\text{envelope(dB)}+9.94+20\log f\tau_{max}-6.02B \qquad \text{(I.15)}$$

In Fig.1.6 the array pattern of a 64 elements array, with half wavelength spacing, at f=15GHz, for $\tau_{max}\approx 1.80$ns and B=7, is considered. In particular, the array factor at 15GHz and 10GHz is reported for a steering angle of 28.8º that produces a periodicity factor M=8. The horizontal lines show the approximate quantization lobe level calculated with the (I.15) for both frequencies. A good agreement has been obtained. The beam pointing angle does not change with the frequency, as expected, and, the quantization lobe level decreases while decreasing the frequency.

Here we are interested in the peak quantization lobe and his variation due to antenna main parameters.

Accordingly, since the upper bound of the envelope function is $1/M^2$, for $B\geq 6$ we have:

$$QL_{dB} < -20\log M + 9.94 + 20\log f\tau_{max} - 6.02B \qquad (I.16)$$

where the maximum is obtained for M=2.

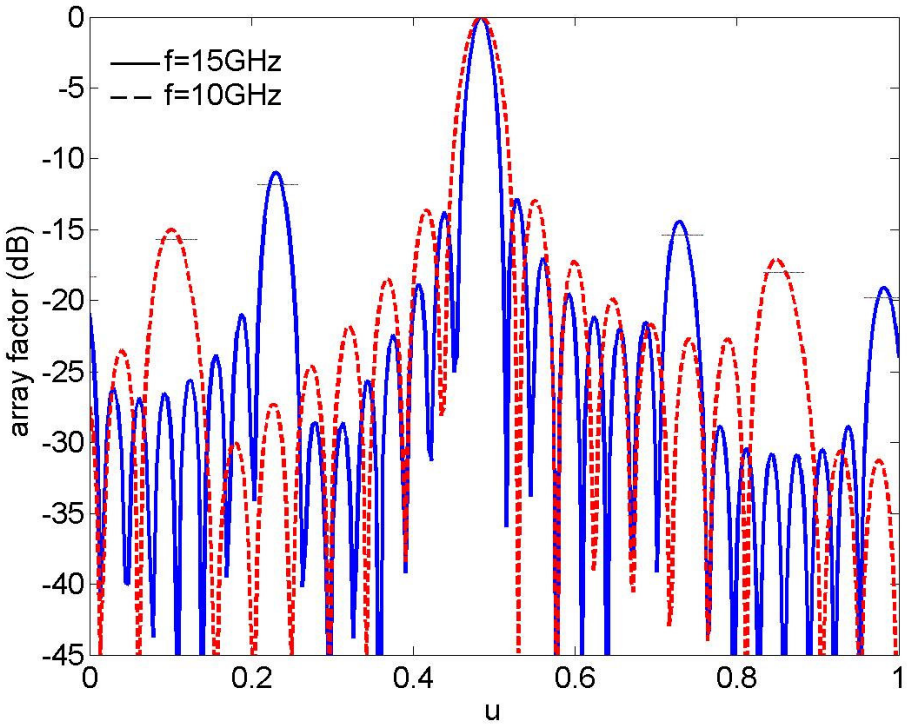


**Figure 1.6** *WB time steered array: quantization lobes*

Then, if we consider that the array spacing is equal to $\lambda_U/2$, where $\lambda_U$ corresponds to the upper system frequency $f_U$, and that the maximum allowable delay $\tau_{max}$ is set in order to guarantee a wide scanning range (about 60º), for $f=f_U$, the product $f\tau_{max}$ can be easily related to the number N of radiating elements:

$$f\tau_{max} = (N-1)d_\lambda u_{max} = \frac{\sqrt{3}}{4}(N-1) \qquad (I.17)$$

where $d_\lambda$ is the element spacing normalized to the wavelength.

Using the (I.17) in the (I.16) the quantization lobe peak power behavior with the number of bit and radiating elements can be easily obtained by:

$$QL_{dB} = 2.67 + 20\log(N-1) - 6.02(B+1) \qquad (I.18)$$

Figure 1.7 represents graphically the (I.18) for quantization lobe levels below 10dB and compare quantization peak lobe due to time and phase quantization. When the array is driven with PS, the peak quantization lobe $QL_{dB\_PS}$ is independent from the array size and decrease with B [*Mailloux 2005*]. In particular $QL_{dB\_PS}$, for M=2 and B≥3, is given by:

$$QL_{dB\_PS} = 9.94 - 6.02(B+1) \qquad (I.19)$$

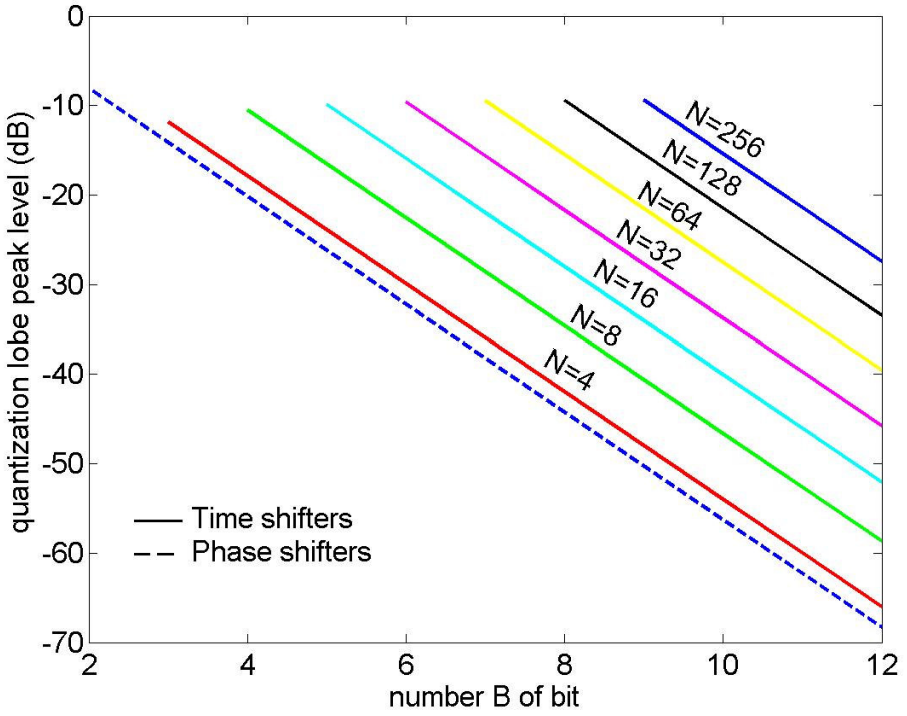


**Figure 1.7** *Peak sidelobe due to time and phase quantization*

When dealing with large time steered antennas, to obtain the same peak quantization lobe level as a phase steered array with B bit, TSs with an higher number of bits are needed. In particular Maillox [*2005*] suggested to employ TSs with B+(4÷6) bits. In fact, for antennas with a large number of elements the time delay quantization can produce serious alterations on the antenna pattern if the TSs do not provide a very fine quantization.

To reduce the peak quantization lobe level, one recommended way is to break up the quantization error periodicity [*Mailloux 2005*; *Smith and Guo*].

Regarding the average sidelobe level due to the quantization error, according to the previous considerations relating the $P_{QL}$ expression (I12) to the one in the PS case, we can proceed as for the PS case [*Mailloux 2005*], using the phase error due to the time quantization $2\pi f\tau_{max}/(2^B-1)$ in place of the phase error due to the time quantization $2\pi/2^B$. As a result, the mean square phase error due to time quantization, say $\sigma_T^2$, is given by:

$$\sigma_T^2 = \frac{1}{3}\frac{\left(\pi f\tau_{max}\right)^2}{\left(2^B-1\right)^2} \qquad \text{(I.20)}$$

while the average SLL $\sigma_{Tavg}^2$ is:

$$\sigma^2_{Tavg} = \frac{1}{3D}\frac{\left(\pi f \tau_{max}\right)^2}{\left(2^B - 1\right)^2} \tag{I.21}$$

D being the array directivity, given by the (A.9) for isotropic radiators placed at an integer number of half wavelengths. Usually, to take into account for scan and taper losses, the average SLL is raised by 2dB with respect to the (I.21) [*Mailloux 2005*].

***FRACTIONAL WB SYSTEMS:*** For fractional bandwidth WB systems TSs are used at subarray level while PSs are adopted at element level (Fig.1.4). Let us assume that the array is divided in Q subarrays with M elements each. The array pattern $f_{ANT}$ is, then, given by the product of a time steered array factor $f_A$ and a phase steered subarray pattern $f_S$. The array factor $f_A$ presents grating lobes due to the subarray spacing that extends about several wavelengths. Moreover, both $f_A$ and $f_S$ can have quantization lobes due, respectively, to the use of digital TSs and PSs, although the most deleterious effect on the $f_{ANT}$ is given by the grating lobes in the $f_A$ pattern.

At the design frequency, when the PS and the TS are set in order to steer the beam towards the direction $u_0$, the pattern $f_S$ have nulls located in correspondence of the $f_A$ grating lobes. Then the $f_{ANT}$ only presents undesired lobes due to the quantization of both the $f_A$ and the $f_S$ patterns. By using the previous analysis the quantization lobes for both $f_A$ and $f_S$ can be found. Then, the $f_{ANT}$ lobes can be easily found by summing the $f_A$ and $f_S$ patterns in correspondence of the founded quantization lobes.

On the other hand, away from the design frequency, the phase steered array factor $f_S$ squints and the $f_A$ grating lobes move due to the frequency variation. Accordingly, the nulls of the $f_S$ do not cancel the $f_A$ grating lobes, hence the $f_{ANT}$ presents additional quantization lobes, given easily by the $f_S$ calculated in correspondence of the $f_A$ grating lobes [*Mailloux 2005*].

In particular, the $f_S$ can be found from the (I.9), properly modified to take into account for phase steering [*Mailloux 1984*]:

$$f_S(u) = \frac{\sin\left[\pi M d\left(\frac{u}{\lambda} - \frac{u_0}{\lambda_0}\right)\right]}{M \sin\left[\pi d\left(\frac{u}{\lambda} - \frac{u_0}{\lambda_0}\right)\right]} \tag{I.22}$$

Here the quantization due to the phase shifter has been neglected, since we are interested in the deterioration due to frequency variations.

Then, by calculating the (I.22) in the direction set by the (I.8) we have:

$$f_S(u) = (-1)^q \frac{\sin\left[\pi M d \frac{u_0}{\lambda_0}\frac{\Delta f}{f_0}\right]}{M \sin\left[\pi d \frac{u_0}{\lambda_0}\frac{\Delta f}{f_0} + \frac{\pi q}{M}\right]} \tag{I.23}$$

By using the (I.23), the power of the q-th quantization lobe due to frequency variation can be written as:

$$P_{QL} \approx \frac{(\pi X)^2}{\sin^2\left[\pi X + \frac{\pi q}{M}\right]} \quad \text{with } X = \frac{du_0}{\lambda_0}\frac{\Delta f}{f_0} \tag{I.24}$$

In Fig.1.8 we report the quantization lobe power behavior with the variable X, for different level of the ratio q/M.

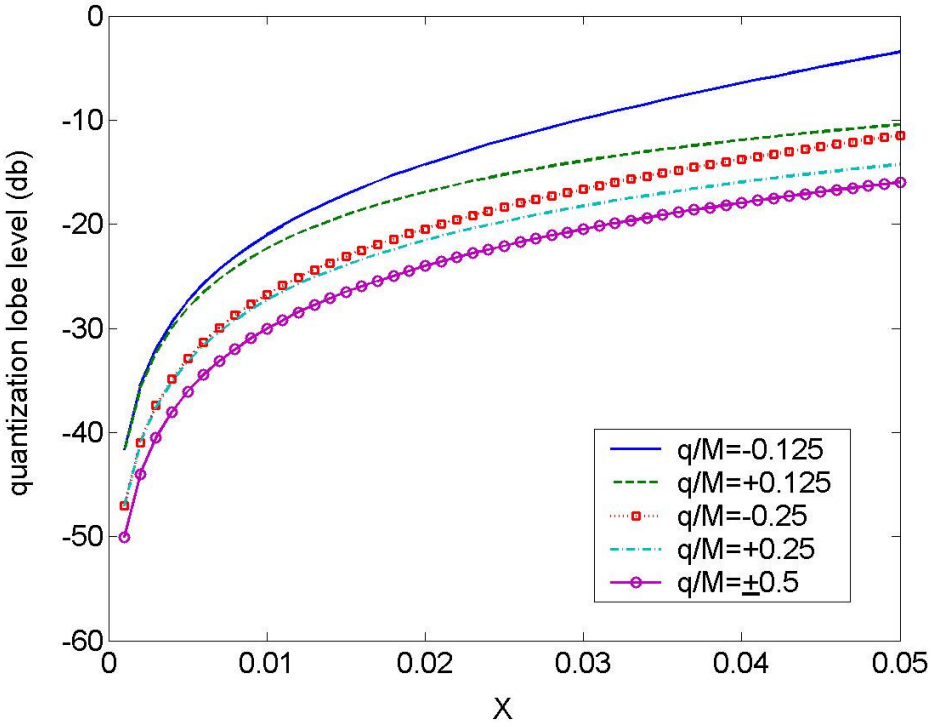


**Figure 1.8** *Quantization lobe level for time delay units at subarray ports*

Then, to overcome the quantization lobe problem in fractional wideband applications, the overlapped subarray scheme, reported in Fig.1.9, has been introduced. These special feeding network schemes allows a good pattern control but increase the system complexity [*Mailloux 2005*]. For example such architecture can provide flat-topped subarray patterns that are maximum towards the beampointing direction and zero outside in order to suppress the grating lobes [*Mailloux 1981*; *Mailloux 2005*].

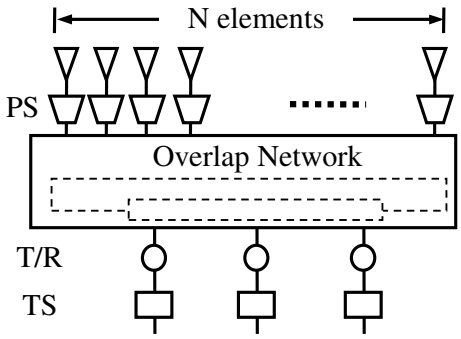


**Figure 1.9** *Fractional wideband array control architecture using contiguous time delayed subarrays*

#### 2.2.2.2 RANDOM ERRORS

The effects of random array errors on the main interest pattern parameters have been widely treated in literature [*Collin and Zucker*; *Fourikis*; *Lo and Lee; Mailloux 200; Rondinelli*]. Here we report the results related to the average SLL, the peak SLL and the beampointing error.

Let us consider an amplitude error $\Delta_n$ and a phase error $\delta_n$ at the n-th element, such that the related feeding signal has amplitude $a_n(1+\Delta_n)$ and phase $\psi_n+\delta_n$, $a_n$ and $\psi_n$ being the nominal amplitude and phase coefficients, respectively. Moreover, let us assume that the amplitude and the phase errors have the same statistic for each element and can be described by a Gaussian density function with zero mean and variance $\sigma_a^2$ and $\sigma_\psi^2$, respectively.

Under these conditions, the average power pattern, normalized to the beam peak, $f_{An}$ is given by [*Mailloux 2005*]:

$$\overline{\left|f_{An}(\theta,\varphi)\right|^2} = \left|f_{An0}(\theta,\varphi)\right|^2 + \left[\sigma_a^2 + \sigma_\psi^2\right]\frac{1}{D} \qquad \text{(I.25)}$$

where $f_{An0}$ is the normalized nominal pattern and D is the array directivity given by the (A.9) for isotropic radiators located at an integer number of half wavelengths apart each other.

As seen, the average power pattern is given by the nominal power pattern, plus a constant term with no angular dependence. The latter allows us to introduce the average SLL $\sigma_{SLL}^2$, often called the residual SLL, defined by:

$$\sigma_{SLL}^2 = \left[\sigma_a^2 + \sigma_\psi^2\right]/D \qquad \text{(I. 26)}$$

The residual SLL can be normalized to the element isotropic radiation level, by multiplying eq. (I.26) by the factor $d_eD$, where $d_e$ is the element pattern directivity. In Fig.1.10 the residual SLL, normalized to the isotropic radiation, assuming $d_e=\pi$, is reported in dB as function of the root mean square (RMS) amplitude and phase errors.

The random errors deteriorate the antenna pattern by raising the SLL. The nominal SLL is, in fact, raised by means of a random term having average power uniform in the angular space. Accordingly, to estimate the peak SLL it is necessary to take in to account for the statistic of the error term.

In particular, considering an ensemble of array having the same statistic, the probability, say $p(\hat{f}_A)$, that at any angle the field intensity will be between $\hat{f}_A$ and $\hat{f}_A + d\hat{f}_A$ can be described by means of a Ricean distribution [*Mailloux 2005*]:

$$p(\hat{f}_A) = \left(2\hat{f}_A / \sigma_{SLL}^2\right) I_0\left(2\hat{f}_A \hat{f}_{A0} / \sigma_{SLL}^2\right) \exp\left[-\left(\hat{f}_A^2 + \hat{f}_{A0}^2\right) / \sigma_{SLL}^2\right] \qquad \text{(I.27)}$$

where $\hat{f}_{A0}$ is the nominal pattern level at the considered angle and $I_0$ is the modified Bessel function of zero order. In Fig.1.11 a schematic radiation pattern is reported showing the designed pattern value $\hat{f}_{A0}$ and the residual term.

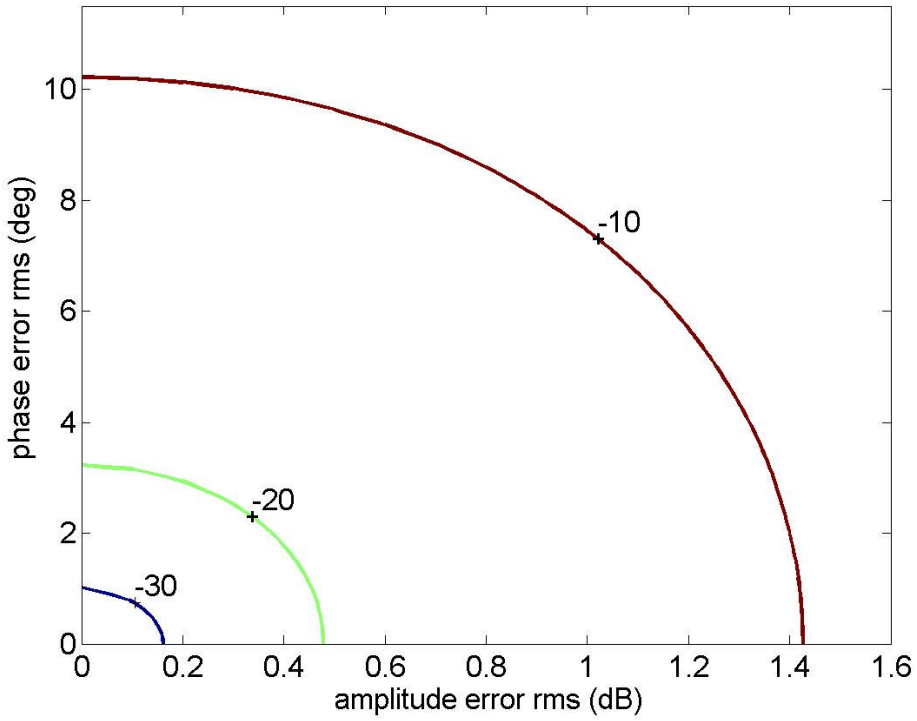


**Figure 1.10** *Residual sidelobe level (in dB) normalized to the isotropic radiation*

The Ricean distribution in (I.27) can be approximated with a Gaussian one, when dealing with errors much smaller than the designed pattern level, as for example in the first sidelobe region ($\hat{f}_{A0}^{\,2} >> \sigma_{SLL}^2$):

$$p(\hat{f}_A) = \left(2\hat{f}_A / \sigma_{SLL}^2\right) \exp\left(-\hat{f}_A^2 / \sigma_{SLL}^2\right) \qquad \text{(I.28)}$$

Then, by using the cumulative distribution function, related to the (I.27) or (I.28), according to the pattern zone of interest, the probability that the pattern exceeds a specified level can be estimated [*Rondinelli*].

For example, regarding the first sidelobe, the peak SLL $\hat{f}_{peak}$ can be easily estimated. In fact, the sidelobe level variation due to the random errors can be at most equal to $2\sigma_{SLL}$ with a confidence level >94%. In particular $\hat{f}_{peak}$ is given by [*Lo and Lee*]:

$$\hat{f}_{peak} = \left|\hat{f}_{A0}\right| + 2\left[\left(\sigma_a^2 + \sigma_\psi^2\right)/D\right]^{0.5} \tag{I.29}$$

Finally, let us consider the effect on the beampointing error. For symmetrical array excitation, the variance of the beampointing error $\sigma_{BP}^2$ is given by [*Mailloux 2005*]:

$$\sigma_{BP}^2 = \sigma_\psi^2 \frac{\sum_n a_n^2 x_n^2}{\left(\sum_n a_n x_n^2\right)^2} \tag{I.30}$$

where $x_n$ is the position of the n-th element divided by the element spacing d. For uniform amplitude we have:

$$\sigma_{BP}^2 = \frac{12}{N^3}\sigma_\psi^2 \tag{I.31}$$

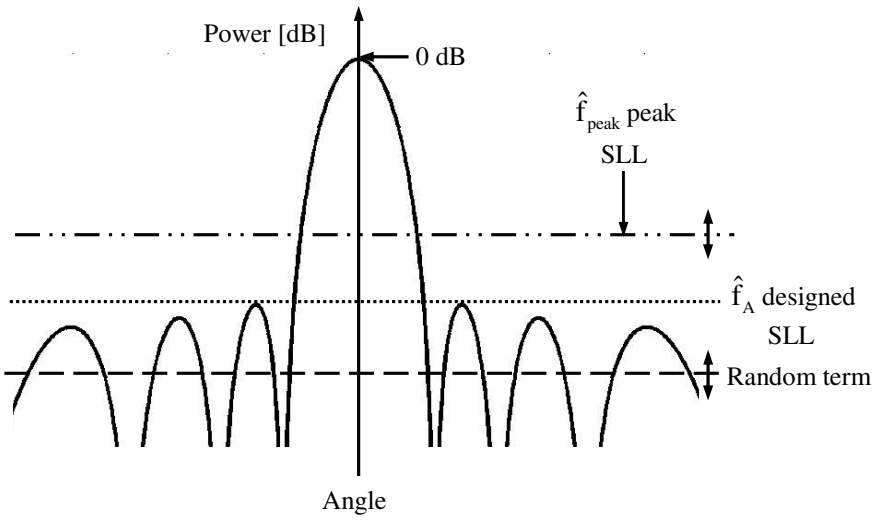


**Figure 1.11** *Array radiation patter with random, designed and peak level*

As shown in (I.31), for large PAA the effect of the random errors on the beampointing direction is not significant.

# 3 OPTICAL TECHNOLOGY FOR PHASED ARRAY

The interaction between optical and MW signals signed, several decades ago, the born of a new MW engineering branch: the microwave photonics (MWP) [*Bowers*; *Galwas; Izutsu*; *Matthews 2000*; *Nirmalathas et al.*; *Pan*; *Seeds 2002*; *Seeds 2004*; *Tang et al.*; *vanBlaricum*]. The interest in the photonic technology has been driven by the attractive features of optical transmission lines and devices:

- low transmission loss
- low weight
- low volume
- wide bandwidth
- high electromagnetic interference immunity (EMI).

At the beginning, the photonic technology has been introduced to implement long distance communication links. The main attraction was the low transmission loss attainable with the optical fibers. Figure 1.12 represents a comparison among silica-glass fiber and metallic waveguide regarding the MW attenuation. Optical fibers, operating at three different wavelength, .8μm, 1.3μm and 1.55μm, ensure a loss factor independent of frequency and well below the loss factor for the 9.5mm coaxial and the WG16 waveguide, working in the X band (8.2GHz-12.4GHz).

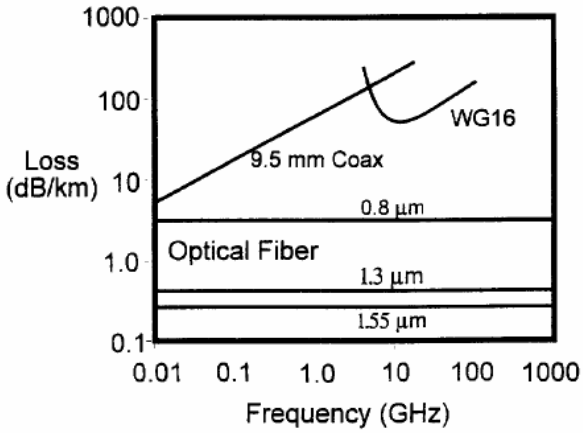


**Figure 1.12** *Attenuation in silica-glass fiber versus metallic waveguide [vanBlaricum]*

Moreover, the further mentioned interesting features contributed to deploy fiber optic communications.

But MWP does not only mean the metal replacement. In fact, thanks to the rapid development of the photonics and optoelectronics integrated circuits, optics has been employed in MW applications, not only to realize communications on long distance links, but also to implement more sophisticated tasks.

In particular, nowadays photonics is setting up in three different MW application fields [*Nirmathalas et al.*; *Seeds 2002; Seeds 2004*]: antenna remoting, optical signal processing and phased array antenna beam forming.

***ANTENNA REMOTING:*** In such applications, different antenna systems are remotely controlled by one centralized MW signal processing unit by means of a distribution network. The phenomenal growth of cellular phone systems improved the demand for remotely managed systems for antenna terminals.

Nodaway photonic links are widely employed to realize the remote control of antenna stations. The low cost together with the EMI and noise reduction has set the introduction of fiber optic links in such applications. The remote control is achieved by means of a fiber distribution network that deliver the radio signals, managed by a centralized MW signal processing unit, to the multiple antenna sites. Today, thanks to the development of efficient low noise optical amplifiers, optical links can guarantee acceptable link gain and noise figures. A cellular fiber fed base station, a fiber and a photonic driving module are reported in Fig.1.13 [*Ackerman and Cox*]

For a detailed description of the use of optical link employed in such applications, useful references are [*Ackerman and Cox*; *Zmuda and Toughlian 1994*; *Cox et al.*; *Bratchikov 1998; Daryoush et al.*].

***OPTICAL SIGNAL PROCESSING:*** Optical signal processing systems are used principally to realize analog to digital conversion and to synthesize high resolution microwave filters [*Seeds 2004*; *Nirmalathas et al.*]. The demand for faster signal processing circuits in a number of military and commercial applications has promoted the use of the optical technology. In fact, photonics allows broad band sampling and good potentiality for parallel processing. Furthermore, high resolution tunable filters, such as fiber Bragg gratings, dispersion fiber links and array waveguide grating, can now be realized thanks to the advancements in the optical systems technology [*Zmuda and Toughlian 1994*].

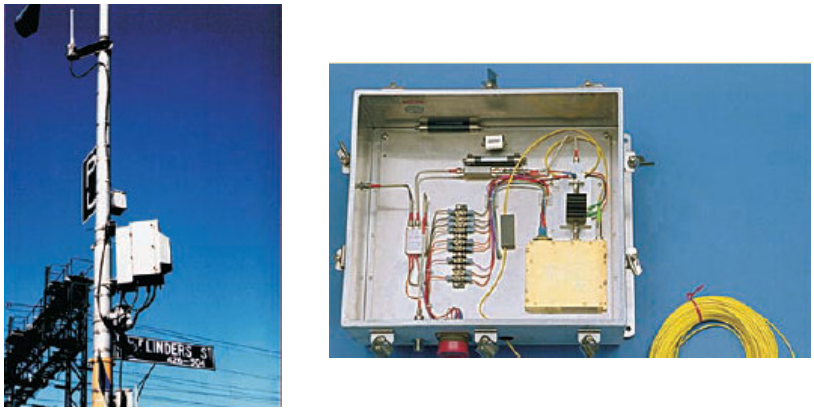


a) b)

**Figure 1.13** *a) A 900-MHz fiber fed microcellular base station. b) A similar module used for receive only phased array [Ackerman and Cox].*

***ANTENNA BEAMFORMING:*** MWP founds application in antenna beam forming and beam steering systems. This is the application field we are here essentially interested.

The basic idea is to take advantage of the attractive features of the optical waveguide and devices to implement light and compact BFNs able to realize the

desired amplitude and phase/time distribution and to perform advanced beamforming capabilities.

Photonics, in fact, can provide significant add-ons. A comparison among conventional and fiber-optic manifold for PAA shows that the photonic manifold can offer good advantages in term of weight and volume, with reasonable power consumption [*Goutzoulis and Gouse*]. The optical BFN (OBFN) can be up to 75% smaller and lighter than the electronic one [*Fourikis*]. On the other hand, optics allows high Electromagnetic immunity (EMI), ultra-wide band, flexible and agile beam control and the simultaneous beams formation. Moreover, photonics represents an easy and efficient way to implement the TTD principle, thus realizing wide band beam squint free antennas.

Initially the photonic technology has been employed in the PAA apparatus for military research activities, such as radar applications. Today, the technology advancements allow employing OBFNs in different sectors such as space, radio astronomy [*Bratchikov et al.*] and commercial applications. Silica based OBFNs have been proposed to realize smart antennas, working at 60 GHz, for mobile communication systems [*Kuhlow et al.*; *Grosskopf et al.*].

Photonics control systems for PAA have been introduced since ‘80s. A wide number of different approaches have been proposed. Two relevant books have been written about the subject. Riza [*1997*] describes the optical control techniques, studied until ’97, by means of a wide paper collection. Zmuda and Thouglian [*1994*] discuss about the photonic technology applied to radar systems, referring to photonic beam forming and signal processing. Moreover, a description of the beam forming and beam scanning methods can be found in [*Kumar*]. Other useful references are [*Jespersen and Herczfeld*; *Benjamin and Seeds*; *Bratchikov 2000*; *Dolfi et al. 2000; Paul*; *Paul et al.*; *Matthews 2000*; *Seeds 1997*;]

It is worth noting that the photonic technology can realize both phase and time control techniques, useful in the WB and fractional WB systems.

Then, in the following we present the optical beamforming principles and the related main issues. Moreover, we introduce the optical schemes employed to realize the transmit and receive mode. Later we discuss about the photonic technology limits.

In the next two chapters we analyze the beam forming and beam steering photonic control techniques for PAA. At this end we will classify the solution implemented in the specialized literature by enlightening not only the different working schemes but also the practical issues related to the antenna system realizations, since we are mainly interested in really employed photonic antennas. We separately analyze the phase and the time control architectures. Within each section, for each proposed implementation we will illustrate the different working principles, dwelling upon the optical devices and the conversion schemes exploited to realize the phase/time control, and discussing the main practical issues.

## 3.1 OPTICAL BEAMFORMING PRINCIPLES

There are two main optical beamforming techniques: the optical phase control (PC) technique, and the optical time control, or TTD, technique. A further optical beam control method is the one related to the implementation of time integral correlators, adopted for signal processing, time steering and jammer cancellation

[*Frankel et al. 1998*]. This last approach has received a considerable less effort than the two main methods, and therefore is not treated here.

It is worth noting that the phase control approach is usually referred as phase steering (PST). Nevertheless, here we will use the more generic term "phase control", since it indicates a wide gamma of applications referring to a generic phase aperture distribution rather than to a phase steered one. However it is important to stress that the PC technique realizes a narrow-band beam control, while the TTD, obviously, realizes a WB control.

A wide gamma of schemes have been proposed for both phase and time control techniques [*Riza 1997a*]. In particular, photonic architectures able to perform beam forming and/or beam steering have been proposed. A common layout for both PC and TTD architecture can de devised and is made of four sections, as reported in Fig.1.14.

The first section, referred as section a), is the generation and modulation one, whose task is to provide the proper light signals set needed to feed the optical BFN. The signals within the block a) can be obtained by using only one or more laser sources. The modulation adopted to impose the MW signal upon the optical carrier depends on the detection scheme exploited in the conversion stage. Generally speaking, both direct and heterodyne detection scheme can be employed in the PC and TTD approaches.

The light signals enter the block b), the OBFN. The latter provides the feeding signals related to each radiating element, with the phase/time and amplitude distributions according to the desired beam properties. The optical signals are then downconverted within the the block c) that represents the optical to MW conversion section. The latter furnishes the right MW signals needed to drive the radiating systems, labelled as section d).

Later on we will call the blocks a), b) and c) as Optical Phaser (OPH).

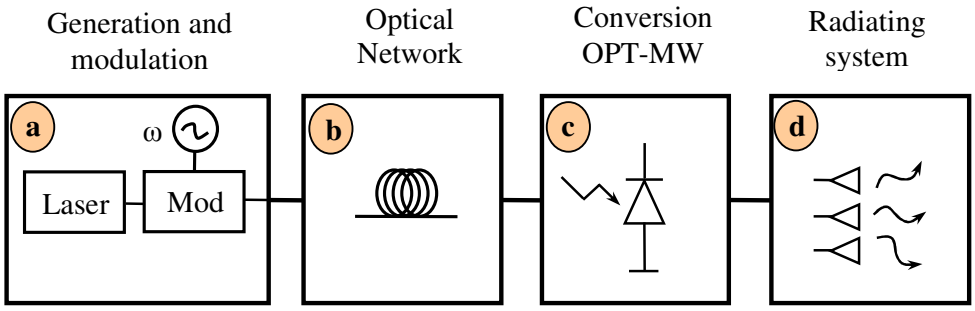


**Figure 1.14** *Layout of an optical controlled phased array*

### 3.1.1 DETECTION SCHEMES

Since the detection scheme represents a key element of the OPH, it is worth to enlighten some aspects about the conversion schemes. In this way we will also show the principles for both PC and TTD techniques.

In Fig.1.15 both direct and heterodyne detection schemes are represented.

In the direct detection scheme (1.15a), the MW signal x(t) modulates the optical carrier, having frequency Ω. Usually amplitude modulators are employed. The optical

modulated signal is transmitted along the optical systems, here schematically represented by a fiber. Then, the optical signal is downconverted in order to obtain the proper MW signal.

Accordingly, the modulated optical signal s(t) is given by:

$$s(t) = w(t)\cos(\Omega t) = A\left(1 + mx(t)\right)\cos(\Omega t) \tag{I.32}$$

where m is the modulation index and A is a proper amplitude factor.

In the following we always will use uppercase letters when referring to optical quantities, and lowercase letters for MW quantities.

In our simplified direct detection scheme (Fig.1.15a) we assume that the modulated signal propagates through a low dispersion fiber channel, with length l and refraction index n. If we consider, for simplicity x(t)=Bcos(ωt), where B and ω are the amplitude and frequency of the MW tone, respectively, the detected signal will be:

$$y(t) = H\cos(\omega t - \varphi) = \cos\left(\omega t - \frac{\omega n l}{c}\right) \tag{I.33}$$

where the DC terms have been neglected and H is a constant taking into account for the constant terms and the amplitude attenuation imposed by the optic link. Then, this is the easiest way to realize an optical time delay: the detected MW signal, is a delayed version of the modulating tone, and the delay amount depends on the fiber properties.

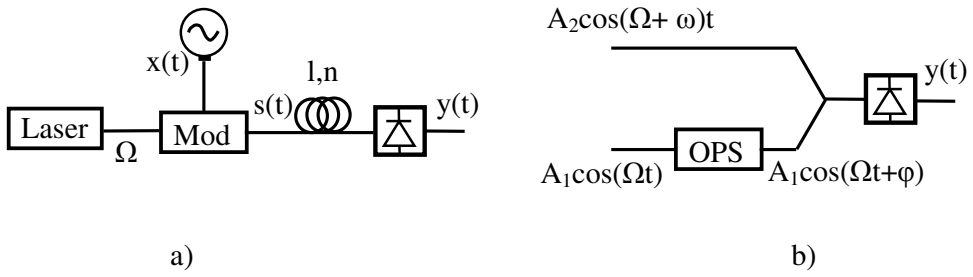


**Figure 1.15** *Detection schemes: a) direct b) heterodyne*

In the coherent scheme in Fig.1.15b, two optical beating signals are employed. The first beating signal, the one on the lower arm, having amplitude $A_1$ and frequency Ω, is controlled by an Optical Phase Shifter (OPS) that imposes a variable phase shift φ on it. The upper arm signal has amplitude $A_2$ and frequency equal to Ω+ω, where ω is the frequency of the desired MW signal that will arise after the coherent detection process.

Accordingly the intensity i(t) of the signal at the photodetector input is given by:

$$\begin{aligned} i(t) &= \left|A_1\cos(\Omega t + \varphi) + A_2\cos((\Omega+\omega)t)\right|^2 = \\ &= \left[A_1\cos(\Omega t + \varphi)\right]^2 + \left[A_2\cos((\Omega+\omega)t)\right]^2 + 2A_1A_2\cos((\Omega+\omega)t)\cos(\Omega t + \varphi) \end{aligned} \tag{I.34}$$

Then, the detector output current y(t) is given by:

$$y(t) = r\, i(t) * h_{PD}(t) \tag{I.35}$$

where r takes into account for the detector responsivity, the operator * represent the convultion and $h_{PD}$ is the photodetector impulse response. Since the photodetector bandwidth is usually much lower than the frequency of the exploited optical signals, the convultion operation with the $h_{PD}$ is equivalent to take only the signals having frequency up to the MW range.

Then the y(t) is given by:

$$y(t) = r\left( \frac{A_1^2}{2} + \frac{A_2^2}{2} + A_1 A_2 \cos\left(\omega t - \varphi\right) \right) \tag{I.36}$$

In this way the OPS controls the phase of the output MW signals. However, high phase coherence between the signals is required to obtain high quality MW signals, as discussed in the 2nd Chapter.

It can be easily noted that the direct detection scheme can be readily used to implement TTD architectures, while the heterodyne detection system can be used to implement the PC systems. Nevertheless, it is important to observe that both detection schemes can be arranged in order to realize both PC and TTD approaches, as will be shown in the following chapters.

Moreover, it is worth noting that the system performances are, obviously, affected by the optical link properties, although in our study we are interested in comparing the different optical control architectures independently from the optical link properties. The optical link properties and figures of merit are reported in Appendix B.

### 3.1.2 TRANSMIT AND RECEIVE SCHEMES

In the mentioned applications it is important to exploit an antenna system able to perform both transmit and receive operation. This feature can be achieved with the OBFN by adopting a suitable control scheme.

In particular, let us consider the receive mode with reference to the TTD antenna beam control in the receive mode and analyze two general control schemes reported in the literature. Similar considerations can be applied also for the PC schemes, without any variation.

In a first scheme the correct delay on the received signals is obtained by their propagation within the OBFN (Fig.1.16). Each received signal modulates the optical carrier and the modulated light signal is properly delayed while propagating through the optical network, represented by an ensemble of TS in Fig. 1.16. All the time delayed light signals are finally combined and downconverted. An example of such a scheme is reported in [*Lee et al. 1995a*].

A different scheme is reported in Fig.1.17 [*Koepf*; *Frankel et al. 1995*]. In this case the OBFN realizes properly phased local oscillator (LO) signals, for downconverting the received signals. The received signals are mixed with the OBFN signals and the resulting intermediate frequency signals are combined together. In this case the time delay distribution to be used is complementary to the one used in the transmit mode, since the intermediate frequency signals have phase term opposite to the related OBFN signals: for a given beam pointing angle, a time delay required in the transmit mode corresponds to a time advance in the receive mode.

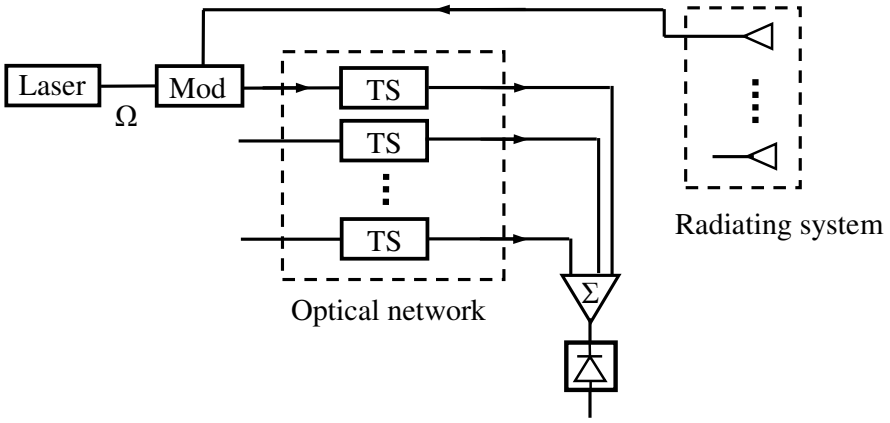


**Figure 1.16** *Optical architecture for the receive mode: the correct signal reception is achieved by propagating it within the OBFN*

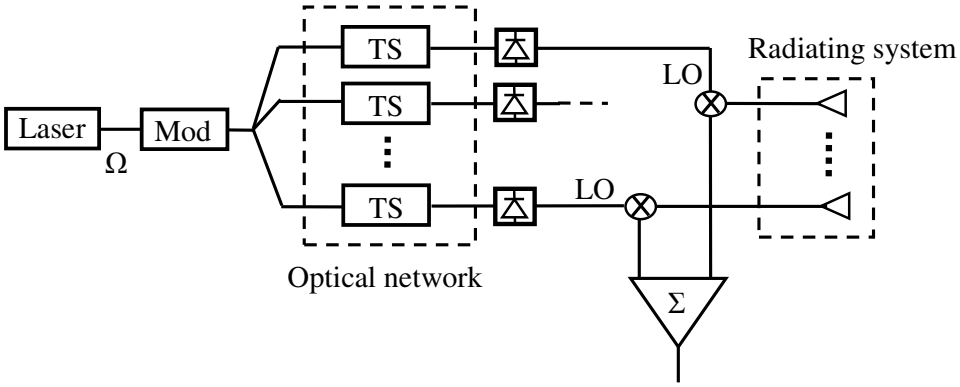


**Figure 1.17** *Optical architecture for the receive mode: the OBFN realizes the properly phased LO signals to perform the correct signal reception*

## 3.2 OPTICAL BEAMFORMING ISSUES AND LIMITS

***OPTICAL BEAMFORMING ISSUES:***

The main issues are the system performances, the BFN complexity and cost.

In particular, the most important system performances are related to the beamforming and beamsteering capabilities such as angular resolution, maximum scan angle, beam shaping features, number of possible contemporaneous beams, eventually reconfigurable, transmission and/or receive modes, beamforming/beamsteering speed. Moreover, the BFN characteristics such as the Insertion Loss (IL), dynamic range, signal to noise ratio are other important figure of merit for the control system.

In particular, regarding the IL of the optical system, it is worth to enlighten an important aspect that will be encountered in the 4$^{th}$ and the 5$^{th}$ Chapter, when

designing the OTSA prototype. In fact, according to the employed OBFN architecture, the optical system losses can vary while changing the phase/time delay to be realized.

This causes an unbalance of the amplitude of the excitation coefficients that can deteriorate the radiated pattern shape. Accordingly, these unbalances have to be properly compensated to reduce the pattern deformation. To analyze this aspect we will refer to the Amplitude Uniformity factor (AU), which set the ratio between the maximum and the minimum of the amplitude excitation coefficient set.

Regarding the OBFN complexity and cost, these aspects are related to the employed BFN architecture.

In some architectures, the OBFN is made of as many PS/TS as many radiating elements are considered, as shown in Fig.1.17 where TS are considered. In such schemes, the complexity and the cost of the OBFN depend on the complexity of the TS and on the number of radiating element. Accordingly, when dealing with PAA with a large number of elements, realizing a high number of multiple contemporaneous beams, it is necessary to adopt TS having as low complexity and cost as possible.

However, for very large structures the number of devices and interconnections needed can be so high to make the BFN implementation unaffordable not only because of the cost but also because of the complexity of practical realization, the size and weight of the BFN.

In such application it is necessary to adopt BFN architecture able to reduce the hardware as much as possible in order to make it possible to realize large PAA.

The hardware compressive architectures have been proposed for both PC and TTD approaches. Regarding the PST, hardware compressive BFN can be found within the bulk optics BFN schemes, as discussed in the following chapters. Concerning the optical TTD schemes, a proper hardware compressive approach has been studied, the Wavelength Division Multiplexing (WDM) one. We will discuss it within the chapter voted to the optical TTD techniques.

Moreover, for each structure other practical issues have to be evaluated. These are stressed in [*Matthews 1999*]:

- the OBFN size, weight, robustness, cost and reliability
- the efficient use of the optical power
- random amplitude and phase errors due to OBFN asymmetries and drift
- periodic amplitude and phase errors due to quantized amplitude and phase control and/or to the subarray architecture
- environmental issues

***OPTICAL BEAMFORMING LIMITS:***

The drawbacks and limits of the photonic beam control techniques are an important argument under discussion since the late ‘80s, when the optically controlled antennas have been introduced. The key aspect is the photonic technology impact in the PA design.

Curtis and Mailloux, in the ’93, appreciated the photonics potentialities such as control signal distribution and TTD implementation, but they were also critical with respect to the conversion loss, costs and the dynamic range [*Curtis and Mailloux*]. Matthews [*1999*] identifies the natural resistance by MW engineer to new technology and the advancements of the solid-state devices technology as key aspects which

contributed to reduce the interest in photonics solutions. Herczfeld [*2004*], in a recent article, discusses the photonics drawbacks and the future opportunities. On his opinion, costs, high speed digital MW apparatus enhancements, high power consumption and relatively low reliability of the photonic components limit the optically controlled PA impact. At the same time, the author discusses the possibility and potentiality of the optically controlled terahertz antennas, as the future of the MW photonics in PAA applications.

Nevertheless, in certain applications the photonic advantages can overcome its drawbacks when compared to the classical MW technology. Photonic are very attractive for airborne and satellite born applications, in realizing BFN for multiple staring beams [*Fourikis*; *Cardone*; *Alameh et al.*], or for large PAA operating over a wide band.

On our opinion, the photonics main actual limits are, on one side, the conversion losses and the MW systems enhancements on the other side. Accordingly, the photonic control for PAA guarantees significant add-ons for high performance medium-large antenna systems, where compact and low weight apparatus, able to perform an agile control of the radiated beams are of interest.

In the future, optics can surely drive the terahertz antennas development. Moreover, the promising photonic technology enhancements could allow optic control systems to overcome the actual limits and enlarge the optically controlled PA application fields. This will, obviously, depends also on the MW technology improvements, on the natural resistance by MW engineer to the new technologies and on the performances required in the future commercial applications.

# CHAPTER 2

# OPTICAL PHASE CONTROL TECHNIQUES

## 3. INTRODUCTION

As discussed in the 1st Chapter (Section 3), the optical technology can be used to implement both MW phase shifter and time shifters. This chapter is voted to the analysis of the optical techniques proposed to realize MW phase shifters, not only for the sake of completeness but also because, as discussed in the 5th Chapter, we proposed to employ optical WB phase shifters to realize an optical architecture realizing sum and difference patterns.

Different approaches can be exploited to optically control the phase of the down-converted MW signals. These are mainly distinguished according to the optical devices employed to achieve the desired phase. Most control schemes are based on the heterodyne detection architecture, as discussed in the Section 3.1.1 of the 1st Chapter [*Riza 1997a*]. Accordingly, we will widely discuss about these techniques. However, we will also spend some words about the phase control approaches based on a non coherent detection scheme [*Riza 1997a*].

In Fig.2.1 the scheme of the optical phase control techniques, here described, is depicted.

Regarding the coherent optic systems, as shown in Fig.1.15b, these are based on an interferometer scheme having an optical phase shifter on one arm. Then, the different approaches are divided according to the optical devices adopted to realize the phase shifting of the optical signal.

Generally speaking, two main classes of systems have been considered: bulk optics systems and integrated optics (IO) systems. For both approaches a simplified scheme is depicted in Fig.2.1, by referring to a linear array of N radiating element.

In the bulk optic systems (Fig.2.1) the two optical wavefronts, usually propagating in the free space, are processed by means of an optical control processor (OCP), that, for graphical convenience, is depicted only in the lower arm. It provides the phase, and eventually the amplitude control of the optical wavefront. The two wavefronts are combined upon a plane, referred as the sampling plane, where the resulting field is properly sampled and then downconverted. Usually, optic fibers are

used to sample the field at the sampling plane and feed the photodetector to realize the downconversion, as shown in Fig.2.1.

The OCP is realized by means of optical devices such as lens, beam splitter, polarizers, beam expanders, and spatial light modulators (SLM). In particular, the latter are important devices able to modify the optical beam properties and are, then, widely used in bulk optics BFN to achieve the desired control.

There are two main bulk optic OBFN categories [*Riza 1997a*]. The first employs SLMs to obtain the radiated beam control. In particular we will discuss about beamformers based on acousto-optic and liquid crystal SLMs. These are the widely employed in those applications we are here mainly interested in [*Riza 1997a*].

The second category, called the Fourier Optic Beamformer (FOB), exploits the Fourier Transform properties of a lens to obtain the distribution of the excitation coefficients needed to obtain the desired properties on the antenna pattern [*Koepf*; *Hong and McMichael*]. The key element of these structures is the transforming lens, although also SLMs are employed to control the properties of the optical beams. This approach provides agile beam shaping and beam steering. Moreover it can be easily employed to realize multiple beams applications.

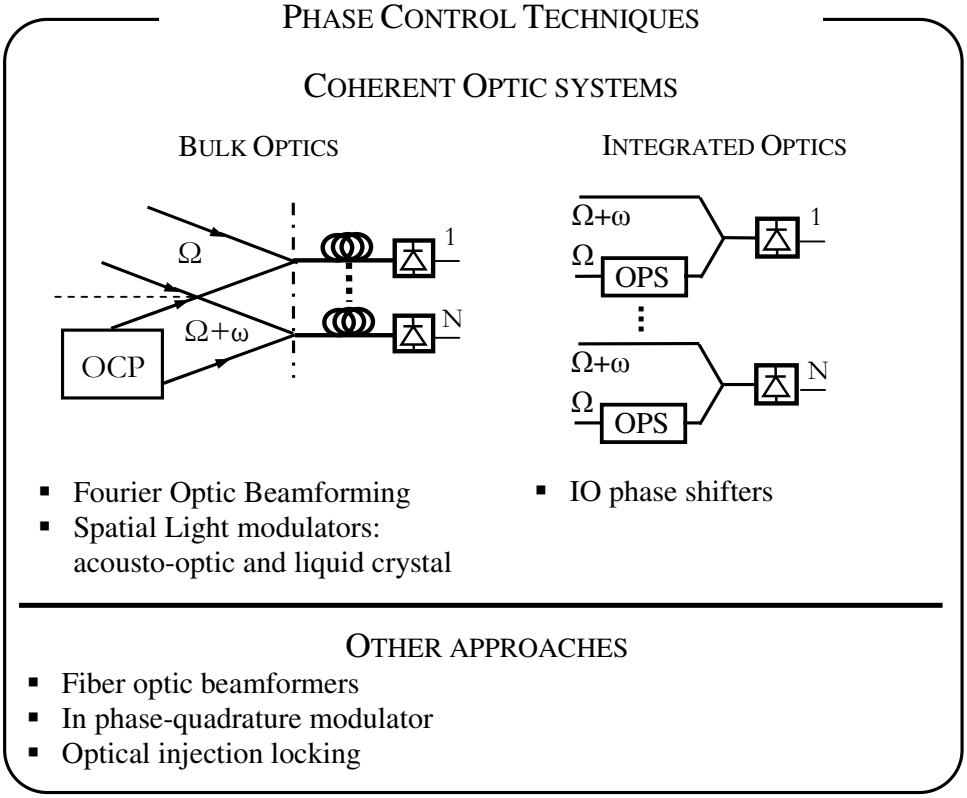


**Figure 2.1** *Phase control techniques*

Generally speaking, the bulk optics schemes are best suited for large antennas systems. In fact, a single OCP can easily provide amplitude and phase control of the excitation coefficient of large two dimension (2-D) arrays. This is due to the availability of a single compact optical processor providing a parallel signal control,

instead of more control units related to each radiating element. The drawback of the bulk optic systems is due to high mechanical tolerances, related to the optical wavelength, and to distortions in the interferometer paths that could be caused by air currents or thermal instabilities [*Surette et al.*].

Regarding the integrated optics systems, IO waveguides are used to realize the interferometer structure shown in Fig.2.1. The phase control is obtained by means of IO PS that can be based essentially on the electro-optic or thermo-optic effect. Moreover, to provide the beam shaping, amplitude modulators can be inserted in the scheme.

With respect to bulk optics system, IO BFNs offer an higher stability, reliability and precision but are not suited for very large structure, since, as shown in Fig.2.1, are component intensive [*Surette et al.*].

# 4. COHERENT PHASE STEERING TECHNIQUES

Before starting the extensive discussion about the main optical coherent phase control techniques, we will clarify some aspects related to the heterodyne detection scheme.

The heterodyne scheme, reported in Fig.1.15b, provides a MW signal having a proper frequency and phase. The phase control is obtained by means of an optical phase shifter (OPS), while the signal frequency is set according to the difference between the frequencies of the two interfering beams.

The first issue is related to the necessity to have at disposal two optical signals having a certain frequency and phase difference. Generally speaking, the generation of the two interfering beams can be carried out by using a single laser and an optical frequency shifter (OFS) (Fig.2.2a), or by using two locked lasers (Fig.2.2b).

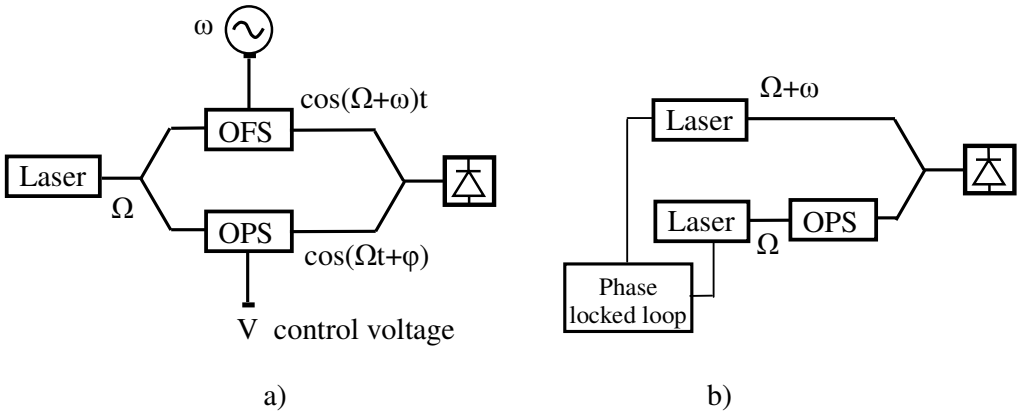


**Figure 2.2** *Optically controlled MW PS: a) single laser scheme b) two lasers scheme*

However, when adopting two beat lasers, the phase noise of each laser contributes to the phase noise of the beat MW signal, thus widening the detected signal linewidth [*Goldberg et al.*]. Accordingly, to generate high quality MW signals it is necessary to establish a phase coherence between the two lasers. This is usually accomplished by

using optical frequency modulation (FM) sideband injection locking techniques, or by frequency offset electronic phase locking.

The FM sideband injection locking is achieved by employing a master laser and one or two slave lasers to be injection locked [*Goldberg et al.*]. The master laser is modulated by means of a MW signal thus creating sidebands in the master laser spectrum. Two of these sidebands can be selectively amplified by one or two slave lasers that are injection locked by the master laser. In fact, the operative frequency of the slave laser is adjusted by varying it heat-sink temperature and bias so that it coincides with the desired master laser sideband. In this way phase coherence among the two generated signals, separated by a multiple of the master laser modulation frequency, is established.

Optical phase locked loop is achieved comparing the two laser beat signal with a MW reference signal [*Blanchflowers and Seeds*]. The comparator output, that is proportional to the phase difference between the laser beat signal and the MW one, is used as an error signal to adjust the phase and frequency of the laser. In fact, by using for example piezoelectric devices, the laser cavity length can be tuned and the operative frequency varied. The error signal then provides the feedback needed to obtain the phase lock. The error signal is filtered by means of a proper filter in order to guarantee a fine locking. In fact, the features of the locking circuits are fundamental to obtain an high quality MW signal.

A detailed treatment of the laser phase locking techniques can be found in [*Goldberg et al.*]. Generally speaking we can say that the two laser technique can provide for high quality signal generation at high frequency, not easily achievable with the single laser approach. Moreover, the two laser scheme can potentially offer a better insertion loss than the single laser one, since the external modulator loss can be avoided. However, until satisfying technology developments for the two laser scheme have not been reached, it was preferred to employ the single laser schemes.

The second aspect we would like to enlighten is related to the interferometer structure. In Fig.2.1 we depicted a classical Mach-Zender two arms interferometer. This is not the only structure adopted. Moreover, such a structure is sensitive to asymmetries in the interferometer arms, due to the slight differences in the paths or to mechanical or environmental stresses. To overcome this problem some authors adopted an on-line interferometer wherein the beating signals propagate along the same path, thus experiencing the same unwanted variations.

Once the main heterodyne scheme aspects related to the optical phase control have been clarified, we can discuss about the different approaches.

## 2.1 BULK OPTICS FOR BFN

In this section we describe bulk optical processors for the PAA control. As told before, we distinguish two main bulk optics processors for beam control: the coherent OCP structure realized by means of SLMs, and the Fourier Optic Beamformers (FOB).

The SLMs are devices able to modify the polarization, phase and/or amplitude of an optical wavefront as function of the time and the position across the wavefront, according to electrical or optical drive signal. Amplitude and phase SLMs, working in transmission or reflection mode, are widely employed in coherent BFNs. Obviously, amplitude SLMs are used to control the amplitude distribution of the MW excitation

coefficients upon the antenna aperture, while phase SLMs are employed usually to provide the phase control.

The SLMs can spatially, and temporally, modulate a 2-D optical wavefront, thus giving a high degree of parallelism not achievable with electronics systems. This allows an hardware reduction and a compact feeding structure for large or very large array antennas.

The basic coherent phase control scheme implemented in bulk optics is depicted in Fig.2.3. Here, the OCP is made of an amplitude and a phase SLM, that, as before, are represented both in the lower arm for graphical convenience. Moreover, on the sampling plane, we represent schematically the current term, generated after the downconversion, due to the interference between the two optical wavefronts.

Accordingly, by using a phase SLM, the spatial phase distribution of the interfering beam, and in turn of the MW signals, can be controlled.

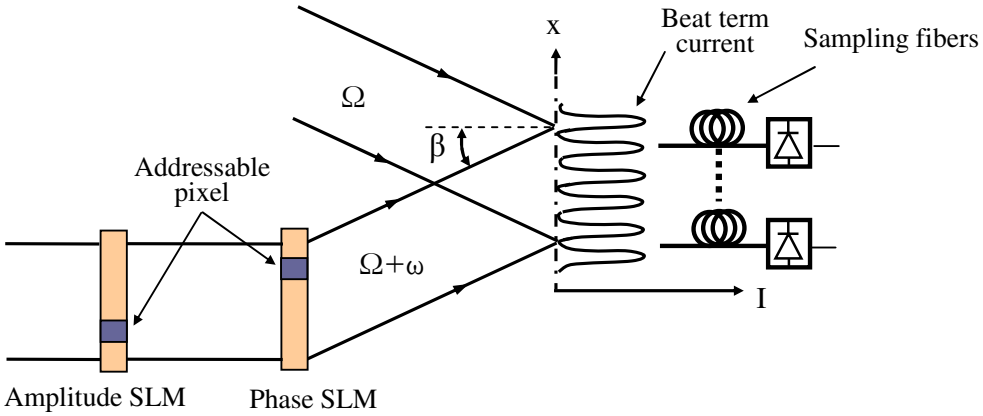


**Figure 2.3** *Bulk Optics phase steering principle*

In particular, a simple way to steer the antenna beam is to tilt the optical interfering beam, as shown in Fig.2.3. In fact, by changing the wavefront tilt angle, the periodicity of the interference pattern, on the plane where the interfering beams are combined, can be varied. In this way the phase slope of the MW excitation coefficients can be controlled [*Tamburrini et al.*].

In the following we will indicate with $\Omega$ and $\Lambda$ respectively the optical frequency and wavelength and with $\omega$ and $\lambda$ respectively the MW frequency and wavelength.

Let us call $\beta$ the angle between the lower beam and the normal to the interfering plane and let us assume that also the upper beam forms the same angle with the normal to the interfering plane. In correspondence of the interfering plane a fiber array, with uniform spacing $\Delta$, is used to sample the field and lead the light signals to the photodetectors. Apart from the dc and high order terms, the photodetection provides the beat term that furnishes the right MW signals. This current term has the form:

$$i \propto \cos(\omega t - 2\frac{\Omega}{c} x \sin\beta) \qquad \text{(II.1)}$$

where x is the variable on the interfering plane.

Accordingly, the resulting phase of the n-th antenna excitation coefficient is:

$$\varphi_n = -\frac{2\pi}{\Lambda} n\Delta \sin\beta \qquad \text{(II.2)}$$

where the multiplicative term has been removed since the phase is usually controlled by changing the angle of only one beam.

Then, by comparing the (II.2) with the phase term needed at the antenna aperture to steer the beam toward $\theta_0$, reported in the (A-7), we have:

$$\sin\theta_0 = -\frac{\Delta/\Lambda}{d/\lambda}\sin\psi = m_\theta \sin\beta \qquad \text{(II.3)}$$

where $m_\theta=\Delta\lambda/d\Lambda$ is called the angular magnification. It represents the magnification coefficient between the antenna beam pointing angle and the deflection angle of the optical beam in the optical processor.

Therefore, by using beam deflectors the antenna beam pointing angle can be varied. Such a scheme does not provide for an independent control of the phase of the excitation coefficients across the array, but it can adopted only for beam steering applications. Obviously, an independent phase control would be preferable.

Different SLMs have been proposed, such as acousto-optic, liquid crystal, ferroelectric, magneto-optic, etc. A wide description of the SLM for optically controlled PAA signal processing can be found in [*Zmuda and Toughlian 1994*; *Neff et al.*]. These references discuss the main SLM parameters such as spatial resolution, framing speed, etc.

Here we discuss about optical coherent processors based on acousto-optic and liquid crystal SLMs. Later, the FOB approach is treated.

### 2.1.1 ACOUSTO-OPTIC AND LIQUID CRYSTAL BEAMFORMING

In this section two different SLMs proposed to realize optical control of PAA are considered: acousto-optic SLM and the liquid crystal (LC) SLM.

***ACOUSTO-OPTIC SLM*:** The acousto-optic devices (AOD) are SLMs able to modulate a light beam according to an RF signal [*Zmuda and Toughlian 1994*; *Chang*]. It can be used to realize some of the basic operations needed in an OCP: beam deflection and light modulation.

A bulk AOD is made of an acoustic cell with sufficiently wide aperture, made of isotropic or anisotropic materials, where acoustic waves are generated by an RF signal applied upon a piezoelectric transducer (Fig.2.4). The traveling acoustic wave causes, by means of the photoelastic effect, the sinusoidal variation of the refraction index of the material. Accordingly, the light beam incident on the AOD is diffracted. When the acoustic interaction length L is relatively large, with respect to the optical wavelength, and incident angle of the optical beam is equal to the Bragg angle $\theta_B$, the maximum light diffraction in a single diffraction order occurs. An AOD having a large L is said to be operating in the Bragg regime. On the other hand, when using a short L, all diffraction order are diffracted. In this case the AOD is said to be operating in the Raman-Nath regime. In the optical signal processing applications, AOD operating in the Bragg regime are, usually, considered [*Zmuda and Toughlian* 1994].

When the light beam is incident on the AOD at the angle $\theta_B$, a portion of the light signal is diffracted at angle that is twice the Bragg angle from the undiffracted light, as reported in Fig.2.4, where $\theta_B$ is given by:

$$\sin\theta_B = -\frac{\Lambda}{2n\lambda_{ac}} = \frac{\Lambda}{2n\nu_{ac}} f_{ac} \qquad \text{(II.4)}$$

where $\Lambda$ is the optical frequency in the free space, n is the medium refraction index, $\lambda_{ac}$, $\nu_{ac}$, and $f_{ac}$ are the wavelength, the velocity and frequency of the acoustic wave, respectively.

The angle of deflection of the diffracted signal varies linearly with the acoustic frequency, and the intensity of the diffracted light increases linearly with the power of the AOD driving signal, until saturation is reached [*Bass et al.*].

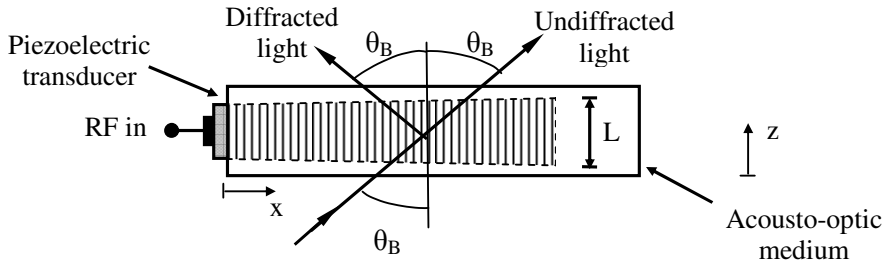


**Figure 2.4** *Bulk acousto-optic Bragg device*

The frequency of the diffracted light beam $\Omega_d$ can be upshifted or downshifted by the frequency of the acoustic wave $\omega_{ac}$: the diffracted signal is up-shifted when the Bragg angle is positive and is down-shifted when is negative:

$$\Omega_d = \Omega_i \pm \omega_{ac} \qquad \text{(II.5)}$$

where $\Omega_i$ is the frequency of the light incident signal.

Accordingly, the beam deflection can be varied by changing the AOD driving frequency within the allowed bandwidth with center $f_0$ and amplitude $\Delta f$. The maximum deflection angle $\Delta\alpha$ is given by:

$$\Delta\alpha = \frac{\Lambda\Delta f}{\nu_{ac}} \qquad \text{(II.6)}$$

The number of resolvable angles $N_s$ is given by the ratio of the $\Delta\alpha$ and the angular spread of the nominally collimated light. Then, if the light beam has width d, we have:

$$N_s = \frac{\Delta\alpha}{\Lambda/d} = \frac{d}{\nu_{ac}}\Delta f = T\Delta f \qquad \text{(II.7)}$$

where $T=d/\nu_a$ is the transit time of the acoustic wave through the optical beam. In fact, $N_S$ deflected beams can be generated by changing the RF frequency increment f across the AOD bandwidth, in accord to:

$$f = kdf = \frac{k}{T} \qquad k = -N_S/2,...0,...,N_S/2 \qquad \text{(II.8)}$$

where df is the frequency variation.

When changing the driving frequency the diffracted beam is frequency shifted too. Accordingly, to obtain a pure beam deflector or a pure frequency shifter, two AOD, properly driven, have to be used [*Chang and Tarng*]: the second AOD can driven in order to cancel the frequency shift imposed by the first AOD thus achieving a pure deflector, or to cancel the deflection, thus realizing a pure frequency shifter.

Moreover, let us consider the optical signal processing properties of an AOD. The AOD driving signal is made of an information signal s(t), with amplitude b, that is added to a dc bias $S_0$, needed to control the linear operation of the AOD, and mixed with a radiofrequency carrier with frequency $\omega_{ac}$. The strain field perturbation inside the AOD is given by:

$$S(x,t) = \left[S_0 + bs(t - x/v_{ac})\right]\cos\left[\omega_{ac}\left(t - x/v_{ac}\right)\right] \qquad \text{(II.9)}$$

where the acoustic attenuation term has been ignored. The strain field is modulated by the information signal s(t) delayed by the time delay $x/v_{ac}$ the acoustic wave takes to propagate within the cell. Accordingly, the amplitude of the diffracted optical beam is:

$$\begin{aligned} A_{d\pm}(x,t) &= jA_0\left[S_0 + bs(t - x/v_{ac})\right]\exp\left(\pm\omega_{ac}(t - x/v_{ac})\right) \\ A_0 &= C\exp\left(j\Omega_i t\right)\exp\left(-j\frac{2\pi}{\Lambda}Ln\right) \end{aligned} \qquad \text{(II.10)}$$

where C is a proper constant [*Zmuda and Toughlian 1994*].

***AOD BEAMFORMING ARCHITECTURES:*** The BFN based on AODs have been widely discussed by Riza [*1991a*; *Riza and Psaltis*]. He initially proposed a single laser structure where two AODs are arranged in an in-line interferometer architecture used to obtain the needed frequency shift and provide the phase control. The proposed solution is obtained by changing the AOD drive frequency and thus the delay term due to AOD.

In Fig.2.5 the acousto-optic processor proposed by Riza is depicted. As shown in the figure, the two AODs allow the formation of the two interfering beams, with properly controlled frequency and phase. Let us indicate with $s_1(t)$ and $s_2(t)$ the driving signals of the AOD1 and AOD2 respectively. In particular, we have:

$$s_1(t) = b\cos(\omega_C t) \qquad s_2(t) = b\cos[(\omega_C + \omega_0)t] \qquad \text{(II.11)}$$

where $f_C=\omega_C/2\pi$ is the center frequency of both the AODs, $f_0=\omega_0/2\pi$ is the control frequency to steer the array beam.

The laser light is collimated along the x direction and focused along the y direction. Then it passes through the AOD1. From the AOD1 two beams emerge: the undiffracted beam, the DC beam in the following, and the +1-order diffracted light signal. The frequency of the +1-order beam is upshifted according to driving signal $s_1$. Both beams are imaged 1:1 into the AOD2. The +1-order beam passes unaffected through AOD2. The DC beam is Bragg matched to the AOD2, thus generating a -1-order diffracted beam. The related signal is downshifted in accord to frequency of the signal $s_2(t)$ and the beam deflection makes the -1-order beam almost collinear to the +1-order one. Accordingly, both +1 and -1-order beams, are imaged upon the detector array with a magnification M, while the undeflected DC beam is properly blocked as shown in the scheme (Fig.2.5). The intensity of the field at the detector plane is:

$$I(x,t) = \left|E(x,t)\right|^2 = \left(\frac{b^2}{2} + G_0 \cos\left[(2\omega_C + \omega_0)t - \frac{\omega_0}{M\nu_{ac}}x\right]\right) \text{rect}\left(\frac{x - 0.5MX}{MX}\right) \quad \text{(II.12)}$$

where X represents the AOD's length, $G_0=b^2/2$ and the rect(·) represents the rectangular window function.

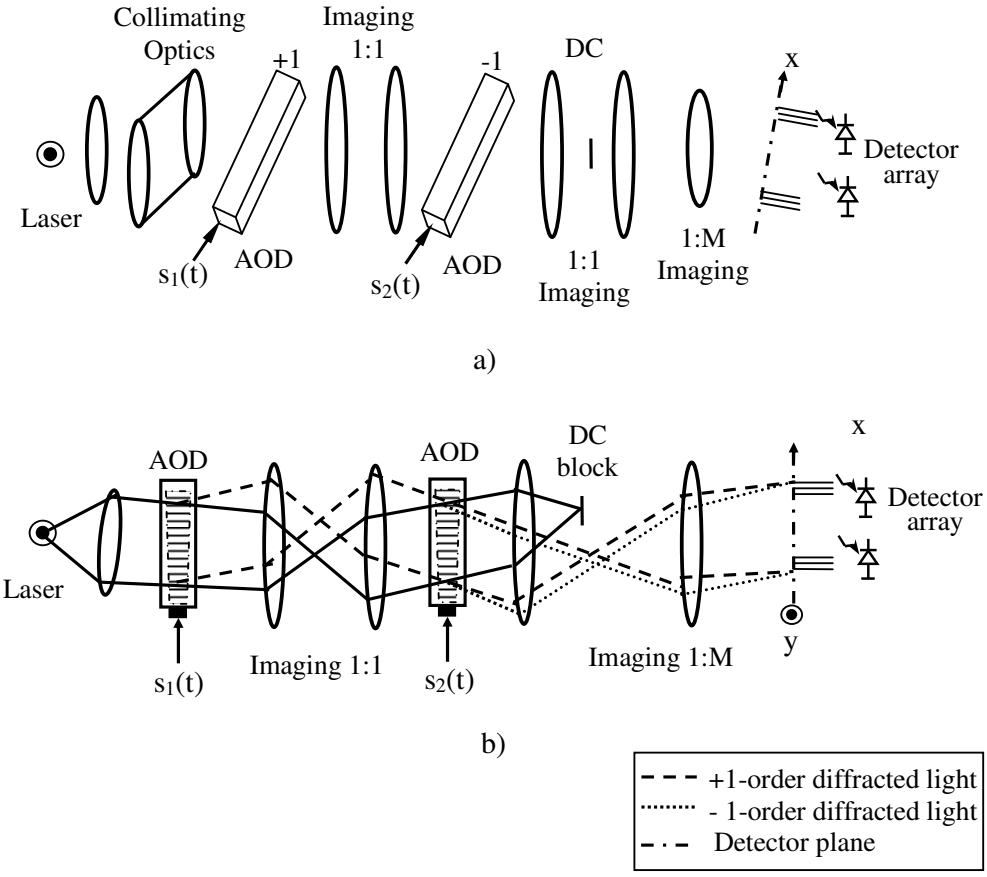


**Figure 2.5** *Acousto-optic beam steerer processor: a), side view b).*

The intensity pattern across the detectors plane is sampled by uniformly spaced detectors, with spacing Δ. Accordingly, if we assume that the size of the detector in the sampling direction, namely $\alpha_x$, is much lower than the spatial period of the intensity pattern, that is $f_0/M\nu_a$, the sampling can be assumed ideal, and the current of the n-th detector can be written as:

$$i_n(t) = 0.5G_0\alpha_x\alpha_y \cos\left[\omega t - \frac{n\omega_0\Delta}{M\nu_{ac}}\right] \quad \text{(II.13)}$$

where $\alpha_y$ is the detector size along the y direction, while $\omega = 2\omega_C + \omega_0$ is the antenna driving frequency. Thus, the phase difference between the radiating elements is equal to $\omega_0\Delta/M\nu_{ac}$. At the same time, the frequency ω of the MW signal also depends on $\omega_0$. Accordingly, by comparing the phase difference needed to steer the antenna beam at

the angle $\theta_0$ with the phase difference achieved with the acousto-optic processor, we have:

$$\frac{2\pi d}{\lambda}\sin\theta_0 = \frac{\omega_0 \Delta}{M v_{ac}} - 2m\pi \qquad \text{(II.14)}$$

where m=0,±1, ±2, … Therefore, the beam pointing angle $\theta_0$, is controlled by the varying the frequency $f_0$, according to:

$$\theta_0 = \arcsin\left[\frac{\lambda}{d}\left(\frac{f_0 \Delta}{M v_{ac}} - m\right)\right] = \arcsin\left[\frac{\lambda}{d}\left(\frac{kdf\Delta}{M v_{ac}} - m\right)\right] \qquad \text{(II.15)}$$

This BFN thus allows to achieve a flexible control of the beam pointing angle. Moreover, simultaneous beams can be achieved by using more driving signals having different frequency [*Riza 1992a*]: in particular for m=hλ/d, where h=1, 2, .., the same angle $\theta_0$ can be obtained in correspondence of two values of the control frequency, as graphically shown in Fig.2.6

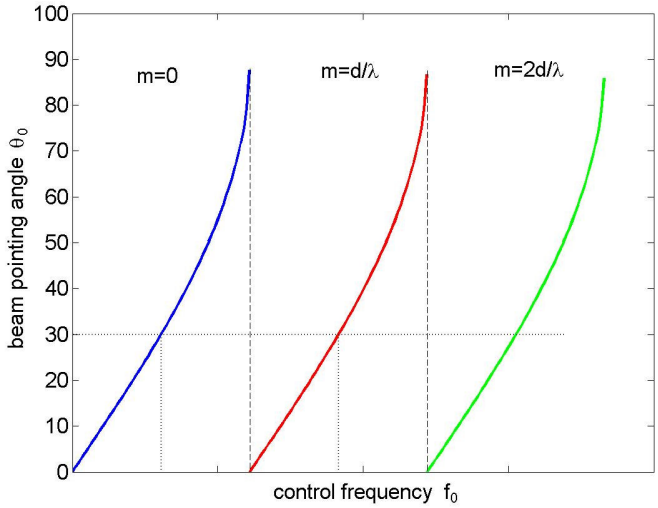


**Figure 2.6** *Control of the beampointing angle*

In their paper, Riza and Psaltis [*1991*] also discussed the related performances issues. Firstly, the processor described provides an antenna driving frequency ω that changes with the steering control frequency $\omega_0$. This undesired behavior could be avoided by using [*Riza 1992b*]:

$$s_1(t) = b\cos((\omega_C + \omega_0)t) \qquad s_2(t) = b\cos[(\omega_C - \omega_0)t] \qquad \text{(II.16)}$$

In this way, the antenna signal frequency became $\omega=2\omega_C$, independent from $\omega_0$.

The relationship (II.15) is an important design formula. In fact, once the element spacing d, the AODs and the minimum scan angle have been chosen, by using k=1 and m=0 in (II.15) the value M/Δ can be found. In this way, fixed a phase-sampling error due to detector aperture, $\eta = (\alpha_x/\Delta)\times 100$, the detectors spacing Δ and the optical magnification M are obtained.

Important parameters are the number of allowable beam positions and the beam-switching speed. The former is $W_{beam}=k_{max}+1$, where $k_{max}$ is obtained from (II.15)

with m=0. It is easy to verify that $W_{beam}$ is inversely proportional to the detector spacing $\Delta$. The beam switching time is related to the cell transit time T, in particular is equal to 1/2T.

Riza also proposed a 2D architecture in two different configurations: an in-line interferometer scheme using 4 AODs and a Mach-Zender architecture with 2 AODs [*Riza 1991a*; *Riza 1993*]. The scheme is suited to drive up to 1000 elements.

The major limits of the BFN based on the AODs are the low optical efficiency, e.g. 20% with RF AOD working around 50-100 MHz, and the maximum frequency, e.g. 8GHz with the wideband AOD reported by Riza [*Riza 1994*]. Moreover, the BFN does not provide an independent control of the phase of the excitation coefficients, since the inter-element phase variation is fixed.

***LIQUID CRYSTAL SLM:*** The second SLMs here considered are the LC. LCs are considered to be among to most promising SLMs for low-voltage, high speed and high resolution. Different types of LCs have been studied. Nematic (NLC) and ferroelectric (FLC) are widely used. In particular they have been employed to perform both the phase and amplitude analog control for PAA.

Riza proposed different configurations of optical processors for PAA control employing both NLCs and AODs [*Riza 1992c*; *Riza 1994*].

LCs have properties similar to liquids as well as crystals. The LC molecules have some degree of freedom of motion. Thus, by applying a voltage across the LC cell, the orientation of LC molecules can be changed, thus varying the effective refractive index of the cell [*Hecht*].

The NLC molecules are prolate ellipsoids exhibiting birefringence. For a linear polarized field directed along the major axis the refractive index is $n_e$, while for polarization parallel to the minor axis the refraction index is $n_0$. The index $n_e$ can be changed by applying an external electric field. A NLC modulator is, in fact, obtained by sandwiching the NLC cell between two parallel glass plates where transparent electrodes to supply the external field are applied (Fig.2.7)

A NLC can be arranged in order to realize a phase modulator (Fig.2.7). Let us consider an electric field incident normal to a NLC cell, whose width is w, and polarized vertically (s-polarization). When no voltage is applied to the NLC, the refraction index associated to the s-polarized field is $n_s=n_e$ (Fig.2.7a). As a non zero voltage is applied across the NLC the LC molecules begin to lie perpendicular to the glass plates. This changes the refraction index associate the the s-polatization, in accord to the applied voltage: $n_s=n(V)$ (Fig.2.7b). When the molecules lie perpendicular to the glass plates, we have $n_s=n_0$ (Fig.2.7c). Note that the refractive index for the horizontal polarization (p-polarization) remains always equal to $n_0$. In this way a phase shift equal to $\varphi=(2\pi/\Lambda)(n_e-n_0)w$ can be imposed on the s-polarized field passing through the NLC cell, where $\Lambda$ is the optical wavelength.

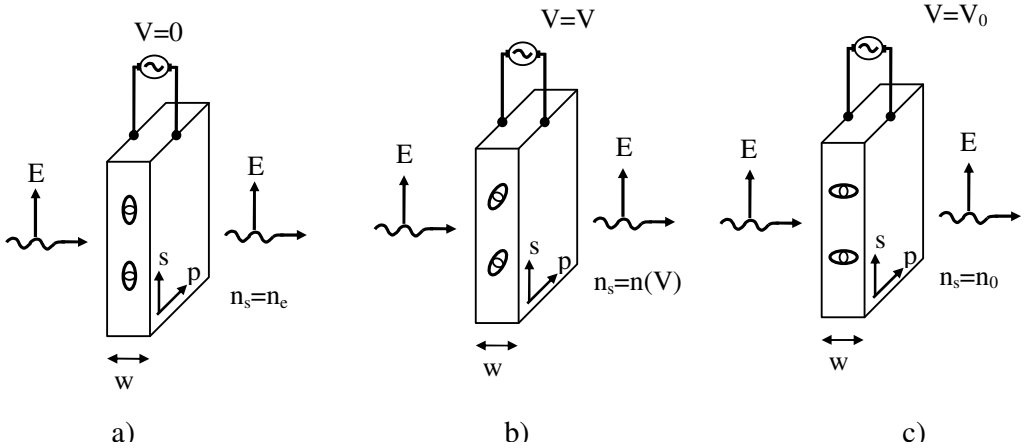


**Figure 2.7** *NLC Phase modulator. a) no voltage applied b) voltage applied: the LC molecules start to move c) voltage applied: the LC molecules lie perpendicular to the glass plates*

Exploiting the same principle, an analog amplitude modulator can be obtained. Let us refer to Fig.2.8. A lightwave is incident normal to the NLC cell and is polarized along the y-axis. The NLC is tilted around the z-axis by an angle β, e.g. 45º. An analyzer has been placed after the NLC allowing to pass only the linear polarization component placed along the x-axis. This analyzer produces an output field given by:

$$\begin{aligned} E &\propto \operatorname{sen}\beta\cos\beta\left(\cos(\Omega t+\varphi_p)-\cos(\Omega t+\varphi_s)\right)= \\ &= 2\operatorname{sen}\beta\cos\beta\sin\left(\frac{\varphi_p-\varphi_s}{2}\right)\sin\left(\Omega t+\frac{\varphi_p+\varphi_s}{2}\right) \end{aligned} \qquad \text{(II.17)}$$

where Ω represent the frequency of the light beam, $\varphi_p=(2\pi/\Lambda)n_0w$ is the phase variation associated to the refraction index $n_0$, and $\varphi_s=(2\pi/\Lambda)n(V)w$ is the phase variation controlled in accord to the applied voltage V. Thus, the intensity of the output beam can be controlled by changing the voltage V. The phase of the optical beam is changed too.

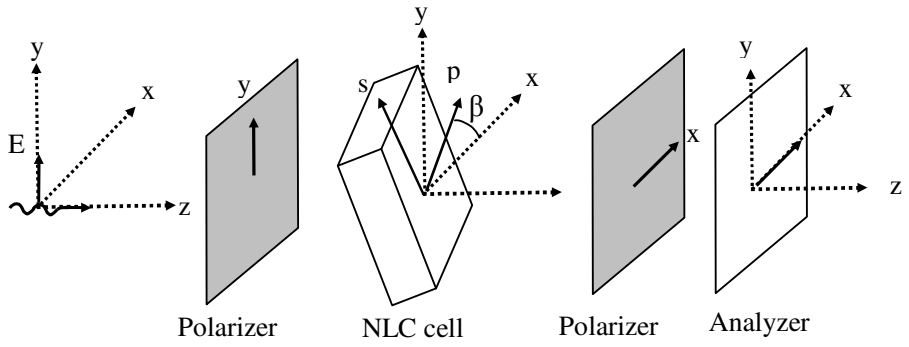


**Figure 2.8** *NLC Intensity modulator scheme*

***LC BEAMFORMING ARCHITECTURES:*** Riza proposed a beamformer based on AOD and NLC SLMs [*Riza 1992c*; *Riza 1994*]. In this structure, the AOD in-line interferometer scheme, similar the one proposed in [*Riza and Psaltis*], is adopted only to generate the two beating signals needed in the OCP scheme. The two generated beams are linearly polarized along orthogonal directions, labeled as s and p. The light beams, before being detected, illuminate two NLC 2-D array needed to get the phase and the amplitude control (Fig.2.9). The NLC directors are placed along the direction associated to the s-polarization. Two polarizers are employed to get the amplitude control. The first polarizer, at 45º, acts as an optical adder, while the exit polarizer let pass only the desired polarization. This scheme allows for a 6/8-bit phase control and about 50dB RF analog controlled attenuation.

In place of the single laser scheme, realized by means of the AOD in-line interferometer, a proper two lasers system can be employed, to overcome the low efficiency and the limited frequency range drawbacks of the AOD scheme [*Riza 1994*]. At this end the author considered a scheme based on two highly stable color-shifted lasers, provided with the suited phase locking. This method has been implemented in [*Kobayashi and Ogawa 1995*], where a NLC based BFN using fiber and integrated optics has been realized and tested up to 20GHz. This solution offers high phase stability and compactness since the interferometer is formed on a single signal path. The carrier to noise ratio C/N of the NLC BFN has been also studied, demonstrating that the NLC does not degrade the C/N [*Kobayashi and Ogawa 1996*].

Regarding the beam switching rate, a time multiplexed scanning BFN has been proposed by Riza for radar applications, in order to overcome the switching time reported with the NLC (about 1-0.1ms) not suited for radars. The BFN compactness allows to employ a couple of NLC array working alternatively: while one channel is active, the other is resetting for the next beam.

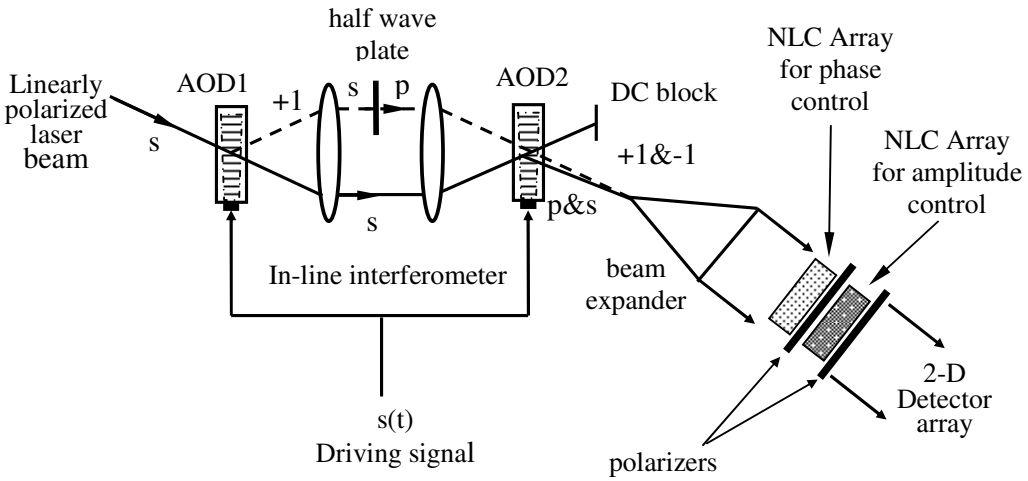


**Figure 2.9** *NLC based optical BFN*

More recently, Riza and coworkers, [*Riza and Kahn*; *Riza et al.*] proposed a BFN, based on LC SLM, that can be easily employed to feed antennas having a different number of element. In fact, the number of the pixel of the pixelated LC SLM, usually adopted in the described BFN, dictates the number of the PAA radiating elements.

Accordingly, when the antenna system has to be upgraded, a new optical apparatus is needed. To solve this problem, a proper LC system has been proposed. It is made by two LC SLM, a non pixelated reflective LC and a pixelated transmissive LC. The pixelated LC is used to transfer the phase information upon the non pixelated LC. The latter, imposes the correct phase information upon the BFN signals.

### 2.1.2 FOURIER OPTIC BEAMFORMING

The Fourier-optic beamforming (FOB) approach represents an elegant solution to perform narrow band beam shaping and steering.

It is based on the fact that the antenna aperture illumination can be described as the Fourier transform (FT) of the far field pattern and that a simple lens performs the FT on the optical wave passing through it. Accordingly, by using a mask representing a scaled-down replica of the desired far field pattern and a lens to realize the FT of this pattern, the needed excitation distribution is obtained on the lens focal plane. By down-converting the optical beam the right excitation coefficients are obtained.

In the following we describe the FOB working principle, the design guidelines and the main issues [*Hong and McMichael*; *Koepf*; *Konishi et al.*; *Nickerson et al.*].

***FOB ARCHITECTURE DESCRIPTION:*** Let us consider the FOB scheme depicted in Fig.2.10. The light generated by the laser source is splitted among the two interferometer arms. In the lower arm an optical frequency shifter imposes a frequency shift equal to MW frequency $\omega$ on the light wave. In the upper arm the plane wave illuminates the mask reproducing the desired antenna pattern and passes through a FT lens. The beams coming from the two arms are combined on the lens back focal plane where the light distribution is sampled by a fiber array. Thus, the second arm provides a phase reference and the right frequency shift needed to furnish the proper MW signal to the antenna elements. The sampled signals are down-converted to feed the corresponding radiating elements, furnishing the desired excitation distribution.

To describe the FOB design principle, we refer to a linear array structure, although the analysis can be easily extended to the 2-D case. In particular, we are interested to the relationship between the antenna far field pattern $f_A(\theta)$ and the optical amplitude g(x') on the mask.

The lens realizes a FT relationship between the optical amplitude g(x') at the front focal plane, where the mask lies, and the amplitude G(x) in the back focal plane, in correspondence of the sampling fiber array. In particular, G(x) and g(x') are related by:

$$G(x) = \int_{-\infty}^{\infty} g(x') \exp\left(-j\frac{2\pi}{\Lambda F} x\, x'\right) \qquad \text{(II.18)}$$

where $\Lambda$ is the optical wavelength and F is the focal length.

The optical beam in the upper arm, having frequency $\Omega$ and amplitude G(x), is combined on the back focal plane with the wave coming from the lower interferometer arm, having frequency $\Omega+\omega$. The resultant distribution on the focal plane is sampled by means of the fiber array lineary spaced at a distance $\Delta$. Each signal is, then, down converted by means of a photodetector.

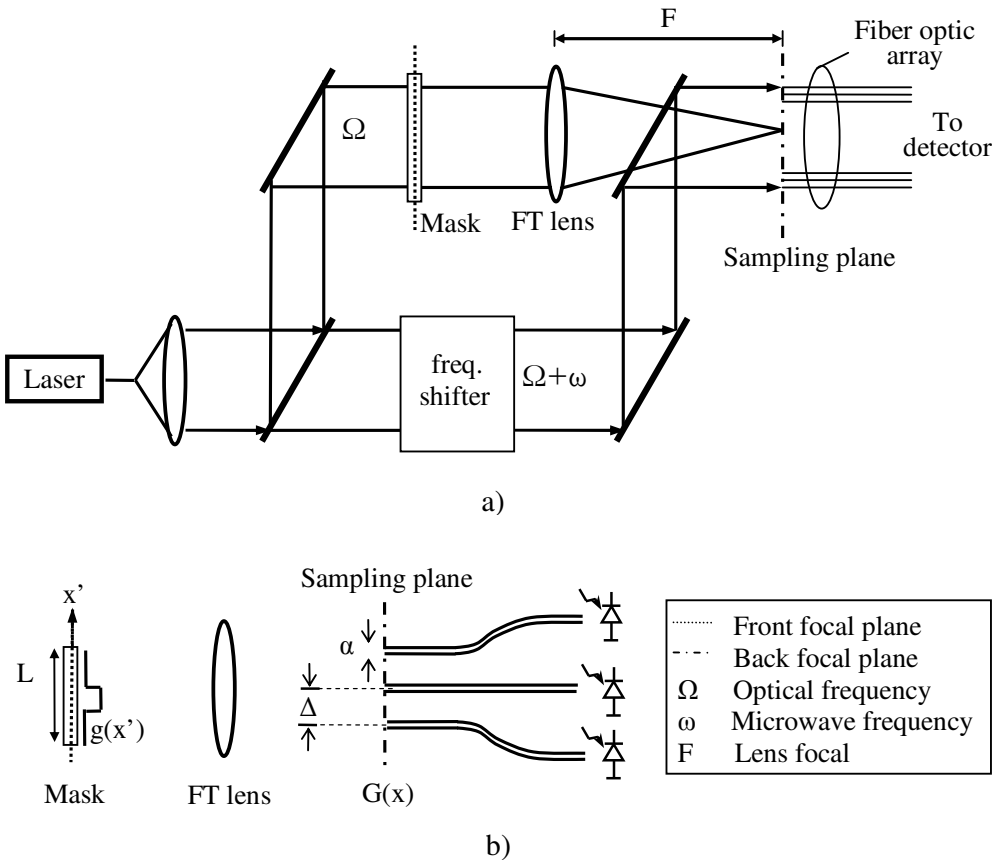


**Figure 2.10** *FOB scheme: a) interferometer system setup b) detailed view of the upper arm of the FT setup*

The coherent detection allows to obtain a signals set having frequency ω and with a proper amplitude and phase. Accordingly, the coefficients $a_n$ can be written as the convolution among the G(x) and the sampling response of the fibers. As consequence, if we assume that the sampling realized by the fiber can be described by means of a rectangular widow function depending on the fiber aperture α, the $a_n$ are given by:

$$a_n = A_0 \int_{-\infty}^{\infty} G(x)\,\mathrm{rect}\left(\frac{x_\Delta + x}{\alpha}\right)dx \qquad \text{with } x_\Delta = n\Delta \tag{II.19}$$

where $A_0$ is a proper amplitude factor. Thus we have:

$$a_n = A_0 \int_{-\infty}^{\infty} dx \int_{-\infty}^{\infty} g(x')\exp\left(-j\frac{2\pi}{\Lambda F}x'x\right)\mathrm{rect}\left(\frac{x + x_\Delta}{\alpha}\right)dx' \tag{II.20}$$

By assuming $\xi = \dfrac{x + x_\Delta}{\alpha}$ we have:

$$a_n = A_0\alpha \int_{-\infty}^{\infty} dx'\,g(x')\exp\left(-j\frac{2\pi}{\Lambda F}x_\Delta x'\right)\int_{-\infty}^{\infty}\mathrm{rect}(\xi)\exp\left(-j\frac{2\pi}{\Lambda F}\xi\alpha x'\right)d\xi \tag{II.21}$$

where the inner integral is the FT of the rect function calculated in x'α/ΛF. The coefficients $a_n$ are given by:

$$a_n = A_0 \int_{-\infty}^{\infty} dx'\, g(x') \exp(+j\frac{2\pi}{\Lambda F} x_\Delta x')\, \mathrm{sinc}(\frac{x'\alpha}{\Lambda F}) \qquad \text{(II.22)}$$

Accordingly, by using eq. (II.22) into the array factor in (A-5), limiting the integral to the mask aperture $L_M$ and using $x_\Delta = n\Delta$, the far field pattern expression is:

$$f_A(\theta) = A_0 \int_{-L_M/2}^{L_M/2} dx'\, g(x') \mathrm{sinc}(\frac{x'\alpha}{\Lambda F}) \sum_{n=-(N-1)/2}^{(N-1)/2} \exp[-j2\pi n(\frac{d}{\lambda}\sin\theta - \frac{x'\Delta}{\Lambda F})\ ] =$$

$$= A_0 \int_{-L_M/2}^{L_M/2} dx'\, g(x') \mathrm{sinc}(\frac{x'\alpha}{\Lambda F}) \frac{\sin\left\{\pi N\left[\frac{d}{\lambda}\sin\theta - \frac{x'\Delta}{\Lambda F}\right]\right\}}{\sin\left\{\pi\left[\frac{d}{\lambda}\sin\theta - \frac{x'\Delta}{\Lambda F}\right]\right\}} \qquad \text{(II.23)}$$

Therefore, in order to have a far field pattern $f_A(\theta)$ as similar as possible to the optical amplitude g(x) obtained on the mask, the two terms in (II.23) have to be properly treated. The sinc function represents the fiber aperture response. To keep this term nearly constant in the integration region, the fiber aperture α, has to fulfill the following relationship:

$$\alpha \le \frac{2\Lambda F}{L_M} \qquad \text{(II.24)}$$

On the other hand, the last term of the integral represents the array pattern function. To ensure that only the array function main lobe fall within the integration region, we should have:

$$\left|\frac{d}{\lambda}\sin\theta_{max} - \frac{x'\Delta}{\Lambda F}\right| < 1 \qquad \text{(II.25a)}$$

$$|x'| < \frac{L_M}{2} \qquad \text{(II.25b)}$$

where $\theta_{max}$ is the maximum scan angle.

Under these approximations, the far field pattern is:

$$f_A(\theta) \propto g\left(\frac{\Lambda}{\Delta}\frac{d}{\lambda} F \sin\theta\right) \qquad \text{(II.26)}$$

The points on the mask are related to the far field scanning angle by:

$$x = \frac{\Lambda}{\Delta}\frac{d}{\lambda} F \sin\theta \qquad \text{(II.27)}$$

Accordingly, useful conditions for an efficient sampling can be derived. In particular for $d/\lambda = 0.5$ and $\theta_{max} = 90^\circ$, the (II.25a) and (II.25b) lead to:

$$\Delta \leq \frac{\Lambda}{L_M} F \tag{II.28}$$

The relationships (II.24) and (II.28) are useful to ensure an efficient sampling of the field distribution across the focal plane in order to achieve a far field pattern with shape as similar as possible to (II.26). Obviously, the analysis we presented here does not take into account for other important practical design issues affecting the real far field pattern, we will consider later.

***DESIGN GUIDELINES:*** Koepf in his paper [*1984*] discusses some practical design guidelines. He suggests a useful rule: to improve the efficiency, only the central fringe of the pattern G(x) on the lens focal plane has to be sampled by the fiber array. As consequence, if the optical mask reproduces a window with aperture $L_M$, the related optical beam diameter on the focal plane has to cover the fiber array aperture $N\Delta$, N being the radiating elements number. Therefore, the beamwidth of the optical beam is $\Theta_B=N\Delta/F$. In particular it results:

$$\Theta_B = \frac{N\Delta}{F} = C\frac{\Lambda}{L_M} \tag{II.29}$$

where C is a proper constant.

On the other hand, the beamwidth $\theta_B$ of the radiated beam is given by:

$$\theta_B = C\frac{\lambda}{Nd} \tag{II.30}$$

Accordingly, once the desired beamwidth $\theta_B$ is known, the number of antenna radiating elements is set from (II.30). Moreover, fixed the radiating frequency f, the ratio $d/\lambda$ is set, for example in such a way to avoid grating lobes, and $\Delta$ is set to achieve an angular magnification, defined in the (II.3) usually around 100 or more. Therefore, the (II.29) can be used to set the mask window aperture $L_M$ and the lens focal length. Finally, to avoid distortion due to the fiber aperture and spacing sampling, the fiber aperture $\alpha$ has to respect (II.24), while the spacing $\Delta$ used to achieve the desired magnification has to fulfil the (II.28).

The beam steering can be easily obtained by using a lateral displacement of the mask or an angular displacement of the reference light beam coming from the lower interferometer arm [*Koepf*].

The FOB scheme features are very interesting: it allows a very flexible beam control without requiring a large amount of hardware. In fact, phase shifters and amplitude control devices for each antenna elements are not required, but the whole antenna distribution is controlled within the OCP. In particular this structure allows electronically reconfigurable shaped beams when optical devices realizing the electronic control of the mask profile are adopted [*Anderson et al.*]. At this end, usually SLM devices are employed.

Moreover, FOB can realize continuous beamsteering control and multiple contemporaneous beams operation for large antennas, an interesting feature for satellite communications [*Akiyama et al. 1999; Akiyama et al. 2001*]. The latter feature is easily achieved by employing multiple laser sources [*Ji et al.*]. In particular, let us refer to Fig.2.11 where a K beams FOB BFN is depicted. The K beams are obtained by introducing K laser sources and a reference laser which are phased-lock

each other. The n-th laser, with frequency $\Omega_n$, provides a spot amplitude distribution on the front focal plane, and its position sets the beam pointing direction of the radiated beam. This beam is radiated at a frequency $\omega_n$ that is, in principle, given by $\omega_n=\Omega_n-\Omega_R$, $\Omega_R$ being the reference laser frequency.

Analogously, the FOB approach allows continuous beamsteering by moving the source in order to translate the light beam on the front focal plane.

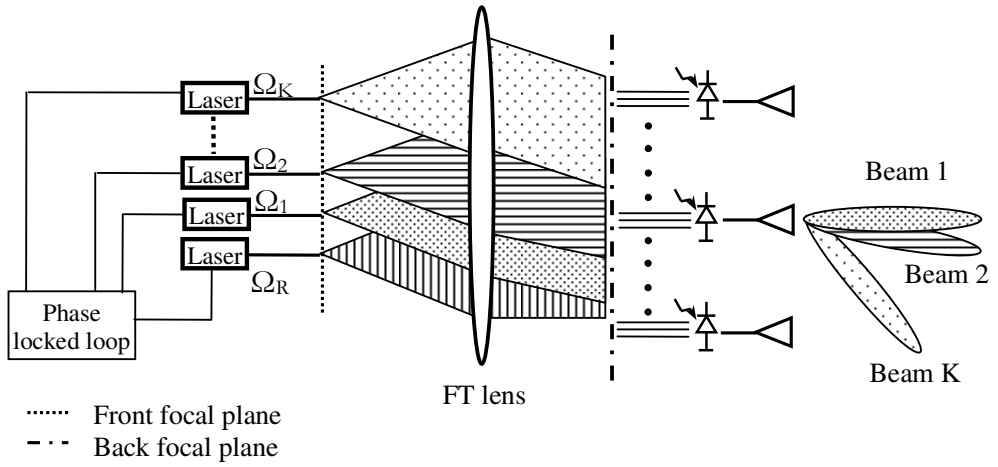


**Figure 2.11** *FOB multibeam architecture*

***DESIGN ISSUES:*** Generally speaking, the performance of the devices employed to realize the desired optical amplitude distribution g(x') on the front focal plane represent a crucial aspect in the FOB structure design, especially when the BFN is intended for beam shaping applications.

FOB beamsteering processors use circularly shaped profile sources, with controlled size, such as a mechanical pinhole used by Koepf [*1984*] to realize the field distribution on the front focal plane, or employ acousto-optic deflector [*Tamburrini et al.; Chang and Tarng*] to change the desired phase distribution.

On the other hand beam shaping BFNs adopt a more sophisticated control system: Anderson et al. [*1987*] used a LC light valve SLM to realize the simultaneous control of the beam shape and direction. Moreover magneto-optic SLM [*Nickerson et al.*], ferroelectric liquid crystal SLM [*Pan et al.*], and deformable mirror devices [*Toughlian et al.*] have been also proposed. A tapered amplitude distribution for the optical reference beam has been proposed to control the sidelobe level [*Konishi et al.*]

Different kinds of SLM have been proposed to realize the desired mask profile. Nickerson et al.[*1991*] employed a 48x49 pixel magneto-optic binary amplitude SLM with 1KHz framing speed, characterized by small size, no quiescent power requirements, low cost, but with a low efficiency (2% at 632nm). Pan et al. [*1992*] proposed an optical shutter switch matrix based on a FLC SLM, that perform a binary amplitude control, with a 24.2dB extinction ratio, a 120μs switching time. Moreover deformable mirror devices SLMs have been proposed to realize continuous beamsteering [*Zmuda and Toughlian* 1994]. However, technology improvements are

demanded in this area to increment the framing speed generally limited to few KHz, the efficiency and the spatial resolution.

Finally, some other important design issues have to be taken into account when considering the performance of a real FOB antenna. The shape of the radiated beam is affected not only by the sampling due to the fiber optic array, but it is also influenced by other factors. Firstly, the finite antenna size sets an upper bound on the spatial bandwidth of the achieved pattern: the radiated beam could not be able to follow too sharp variations on the amplitude distribution g(x') [*Nickerson et al.*].

Moreover, according to the aperture of the employed detectors, a deterioration of the far field pattern can be observed. In fact, to maximize the efficiency one would like to use large aperture detectors. However, the optical sampled signals are convoluted with the detector aperture response, determining a phase gradient distortion. The alteration becomes more serious for large phase slopes, associated to wide beam pointing angles. This convolution involves a multiplicative term, the detector aperture function, on the far field pattern expression [*Nickerson et al.*].

Regarding the feeding scheme, Konishi et al. [*1992*] compared the single-laser scheme, and a two-lasers architecture. They proved that the latter scheme allows the required laser output to be 10dB less than the single-laser structure, while achieving the same C/N. In [*Konishi et al.*] the effects of aperture amplitude and phase errors on the C/N and sidelobe level are also reported.

The errors due to realization defects or BFN feature drifts have to be controlled and adequately compensated. These are due to aberrations in the lens, imperfections in the mirror, beam splitter or frequency shifter, distortion in the interferometer paths due to air current, degradation of the SLM performances due to thermal instability. Such errors lead to an optical beam distortion causing the far field pattern degradation. Hong and McMichael [*1991*] proposed an optical phase conjugator to achieve the correction of aberration and alignment problems. Improved mechanical stability and optical alignment feature have been recently demonstrated by employing an integrated polymeric multilayer optical waveguide 2D array [*Akiyama et al. 2001*].

## 2.2 INTEGRATED OPTICS FOR BFN

Compared to bulk optics assemblies, IO circuits guarantee compactness, stability and improved reliability.

The IO systems have been used to realize optically controlled MW phase shifters (OCPS), usually able to drive one radiating element, or integrated BFNs to feed an entire array.

***OPTICALLY CONTROLLED MW PHASE SHIFTERS:*** The basic principle needed to realize an OCPS has been described in the Section 3.1.1 of the 1st Chapter. The main design issues rely in the implementation of the OFS and the OPS. In particular more difficulties arise when realizing the OFS.

In the IO systems, in fact, an OPS can be easily realized by exploiting the electro-optic effect within an integrated waveguide structure. The $LiNbO_3$ is one of the most employed materials since it can show an excellent electro-optic effect and low loss $LiNbO_3$ waveguide can be easily fabricated [*Gupta et al.*].

Regarding the OFS implementation, both single laser and two laser schemes have been proposed. Application of the two laser scheme to the optical control of MW PS can be found in [*Surette et al.*]. Here, the main issues are related to the phase-locking system, and have been already discussed at the beginning of the section 2.

Accordingly, let us refer to the single laser scheme (Fig.2.12).

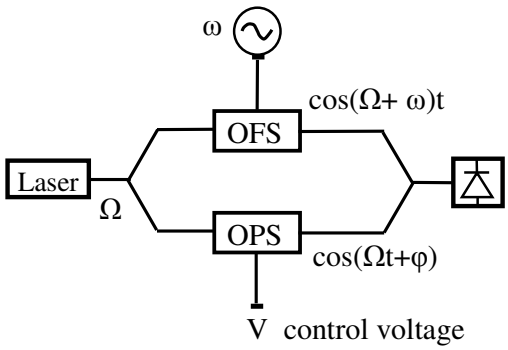


**Figure 2.12** *Optically controlled MW PS: single laser structure*

The first optical solution for an OCPS has been proposed by Soref [*1985*]. In his paper Soref describes both bulk optics and IO implementations. In the bulk optics scheme he propose a Pockels-type OPS and an acousto-optic OFS, while in the IO version he suggest a titanium-diffused $LiNbO_3$ electro-optic waveguide chip that realizes both the OPS and the OFS. In this way an OCPS, with low-voltage control, fast switching and great stability with respect to environmental factors is achieved. Moreover, IO devices can overcome the frequency limit of the AODs. The OFS cited by Soref is based on the single-side band (SSB) quadrature method adopted in electronic communications [*Carlson*].

In Fig.2.13 the scheme of the OFS SSB and the related frequency spectra diagram are reported [*Matsumoto et al.*], while in Fig.2.14 the IO layout of the whole PS is depicted. The SSB modulator is based on an interferometer structure [*Matsumoto et al.; Horikawa et al.*]. On both arms there are OPS driven by the same signal properly phase shifted 90º out of phase. Moreover a dc bias is applied to maintain a $\pi/2$ optical phase difference among the two interferometer arms This is schematically represented by using a box, with a label indicating the phase shift, in the lower arm in Fig.2.13a.

Accordingly, when using a MW signal, for example a tone at frequency ω, to drive the OPS, the modulated signal is:

$$V = A\sin\left(\Omega t + \alpha\pi\sin(\omega t)\right) \qquad \text{(II.31)}$$

where A is the wave amplitude, Ω is the laser frequency, $\alpha\pi$ is the modulation index, α being the modulation depth. This expression can be expanded showing that the phase modulated optical signal is made of a set of sidebands, whose amplitude is given by a Bessel function. In fact, we have:

$$V = A\sum_{n=-\infty}^{\infty} J_n(\alpha\pi)\sin\left(\Omega t + n\omega t\right) \qquad \text{(II.32)}$$

where $J_n$ is the Bessel function with order n.

Accordingly, by using eq. (II.32) the frequency spectra at the output of the upper and lower OPS, indicated in Fig.2.13b with the label C and D, respectively, can be evaluated. In this case, the $+1^{st}$ order sideband of the spectra C and D are in phase, while the $-1^{st}$ order sidebands cancel each other. As consequence, the desired SSB frequency shifter is realized, as shown in the spectra E in Fig.2.3b.

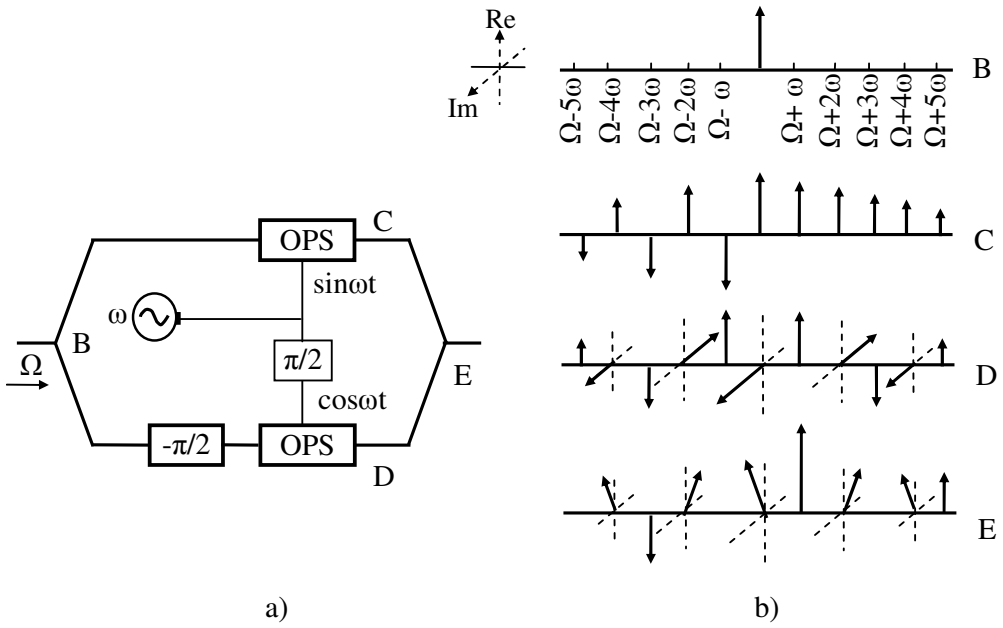


**Figure 2.13** *SSB optical frequency shifter: a) schematic layout of the structure b) frequency spectra*

Moreover, the amplitude of the frequency components at the OPS output can be controlled with certain degree of freedom by acting on the modulation index [*Horikawa et al.; Matsumoto et al.*]. In fact, the amplitude of the n-th frequency components depends on the term $J_n(\alpha\pi)$. In Fig.2.15 the amplitude of the $1^{st}$, $2^{nd}$ and $3^{rd}$ order components are shown as function of the modulation index. It can be seen that for a modulation index equal to 1.8rad, the $1^{st}$ order component is maximum with conversion efficiency equal to -4.7dB, and the harmonic distortion is 10dB down the incident optical carrier.

However, this OFS scheme is, extremely sensitive to the MW and optical amplitude and phase variations. In fact, small differences in the amplitude and phase levels do not allow the harmonic suppression to take place.

Afterwards, when realizing an optically controlled phase shifter, the frequency behaviour of the OFS has to be carefully controlled. In fact, the OFS output signal has to be mixed with the OPS light beam. Accordingly, if the harmonic levels are not exactly controlled, the mixing causes the deterioration of the detected MW signal. In particular, the MW phase does not vary linearly with the control voltage across all the whole $2\pi$ range, and the power of the MW signal shows serious fluctuations [*Jez et al*; *Han et al. 2003*].

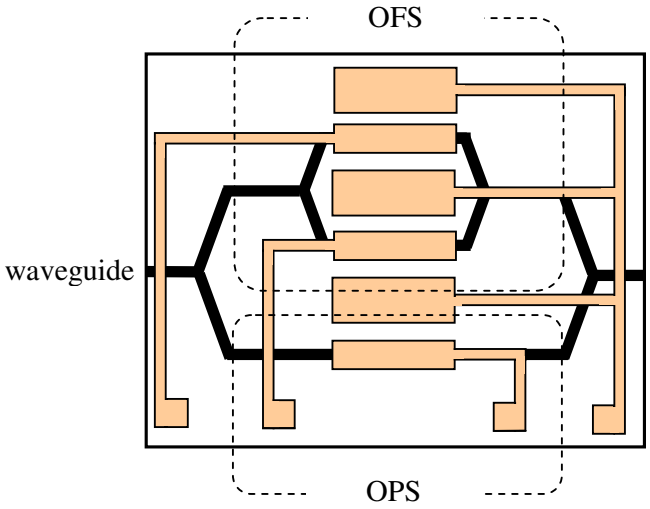


**Figure 2.14** *IO layout of the whole OCPS*

The most detrimental effect is caused by the presence of the optical carrier signal, not exactly suppressed due to slightly inevitable imbalances, at the output of the OFS. Accordingly, Horikawa et al. [*1995*], suggested to adopt a modulation index of about 2.5rad to suppress the optical carrier, thus making the PS more stable regarding small imbalances (see Fig.2.15). However, this solution requires a large amount of MW source power and causes the signal distortion to increase, as shown in Fig.2.15 [*Han et al. 2003*]. To solve this problem, when operating in small signal range, a balancing arm with power splitting ratio α and an additional OPS can be used: this scheme, reported in Fig.2.16, allows to remove the carrier signal at the output of the OFS, thus reducing the MW signal phase deviation and power fluctuations [*Han et al. 2002*; *Han et al. 2003*].

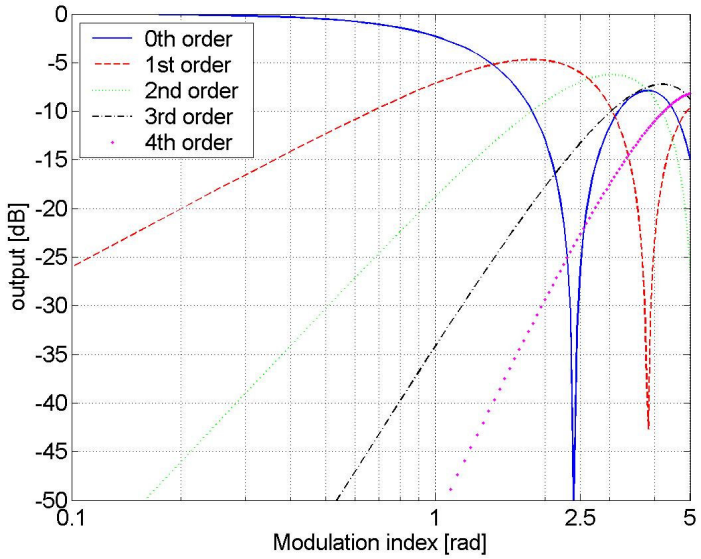


**Figure 2.15** *Amplitude of the frequency components as function of the modulation index*

Multiple outputs OCPS have been proposed. Hietala et al. [*1991*] proposed a photonic integrated circuit composed of one OFS and of a stage with N OPSs and combiners required to feed the N radiators. This solution avoids replicating N times the OFS, as shown in Fig.2.16. A similar scheme has been realized on a $LiNbO_3$ substrate allowing to feed an 8 elements array up to 18GHz, providing an electronically controlled beam steering with a sensitivity of 1.5º per volt from -15º to 15º [*Horikawa et al.*]. Multiple outputs PS structure have been also presented in [*Jez et al.*] and in [*Han et al. 2002*; *Han et al . 2003*; *Fetterman et al. 2002*] where electro-optic polymer materials have been employed. In such structures, especially when dealing with large number of elements, the antenna phase control can be obtained by using a common voltage for the OPSs while adequately setting the electrode length for each OPS.

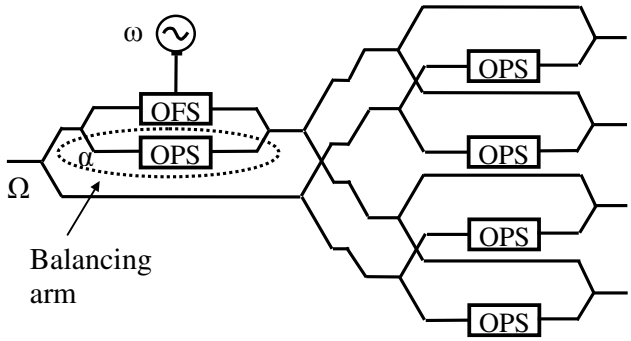


**Figure 2.16** *A 4 outputs optical MW PS with balancing arm*

***INTEGRATED BFN:*** Different integrated beamformer structures have been proposed. A photonic chip able to drive a 16 element linear phased array has been proposed [*Stulemeijer et al. 1998; Stulemeijer et al. 1999; Stulemeijer et al. 2000*]: this coherent beamformer provide more than 360º phase range, obtained by exploiting the electro-optic effect, and 20dB amplitude range based electro-absorption amplitude modulators.

A silica based beamformer for smart antennas working at 60GHz has been proposed. It provides the phase and amplitude control by exploiting thermo-optic effect. The beamformer exploits the two lasers coherent scheme [*Kuhlow et al.*; *Grosskopf et al.*].

Moreover, a lithium-niobate beamformer, based on surface acoustic wave transducer, has been proposed [*Riza and Psaltis*] and his design procedure has been studied in detail in [*Armenise et al.*]. This structure provides continuous beam steering for antennas with 100 radiating elements working at about 800MHz.

# 3 NON COHERENT APPROACHES

The non coherent phase control techniques are here covered. These are the fiber optic beamforming, in-phase quadrature modulator and optical injection locking of the microwave oscillators.

***FIBER OPTIC BEAMFORMING:*** Fiber optic beamforming techniques have been widely studied since '80s. The growth of the MW monolithic integrated circuits (MMIC) technology, in fact, promoted the developing of active transmit/receive antennas. Accordingly, fibers were introduced to perform signal distribution in large active phased array [*Daryoush et al. 1987*].

Regarding the beamforming signal distribution, it is worth noting that the use of the fiber optic architecture can allows for both PC and TTD [*Sheehan and Forrest*].

The suggested fiber optic PC systems employ both direct and heterodyne detection.

The first intensity modulation-direct detection scheme is referred as dispersive fiber optic prism [*Benjamin et al.; Benjamin and Seeds*]. The fiber optic BFN (Fig.2.17) is obtained by a tree structure where the path length increases, from element to element, by equal increments of $h\lambda$, where h is an integer and $\lambda$ is the wavelength at the centre MW frequency f. In this way, when operating at center frequency f, the phase increment is equal to a multiple of $2\pi$, thus furnishing a broadside pattern. Accordingly, when changing the operative frequency by an amount df, the relative phase shift is given by:

$$\Delta\phi = 2\pi h \, \delta f / f \tag{II.34}$$

Thus, the beam is scanned by changing the frequency. In particular, for a given frequency variation $\delta f$, the related beam pointing angle $\theta$ is given by:

$$\theta = \arcsin\left( h \frac{\lambda}{d} \frac{\delta f}{f} \right) \tag{II.33}$$

where d is the element spacing.

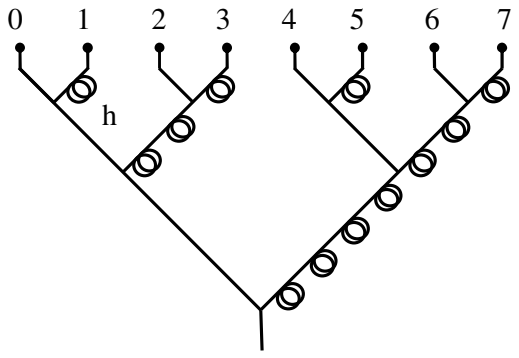


**Figure 2.17** *FO dispersive prism*

Such a BFN does not allow to set the antenna operative frequency, since this is predetermined by the desired scan angle.

To solve this problem a different fiber optic BFN using direct detection has been proposed. It realizes the independent control of the radiated frequency and beam pointing direction. This scheme uses two optical networks, labeled network A and B, as shown in Fig.2.18, followed by the related set of photodetectors. The network A is a fiber optic dispersive prism, while the network B is a non dispersive fiber optic tree, where all the paths have the same length. The network A is driven by a laser, whose intensity is modulated by a MW source at frequency f', that realizes the beam control. The network B is feed by a laser driven by a signal at the frequency f-f', where f is the antenna operating frequency. Then, by varying f', the phase distribution across the output signal of the network A can be changed. On the other hand, the signals detected at the output of the network B are in phase independently from variations in f' or f.

Accordingly, by mixing the outputs of network A and B, and removing the unwanted mixing products, the proper antenna signal distribution at frequency f and with phase driven by the source at frequency f' is achieved.

This technique can be applied to systems working up to 30GHz by using direct or external modulation. A heterodyne version has been also proposed, allowing to work with higher frequencies [*Volker*]. In the coherent scheme only one set of photodetectors is employed, performing, obviously, both the mixing and the detection process.

The approach has been extended to a 2-D PAA by Bélisle et al. [*2000*].

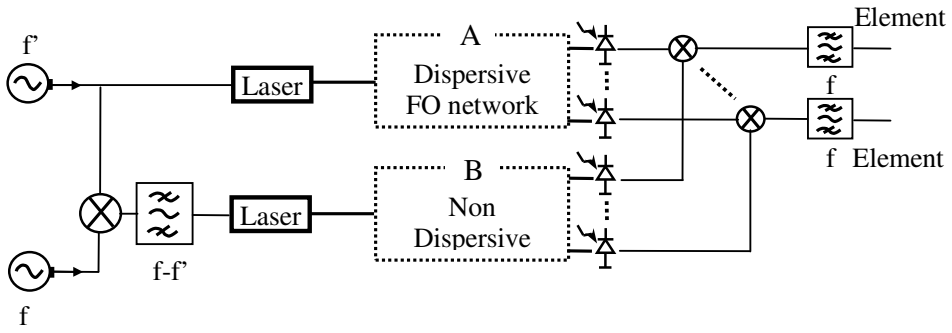


**Figure 2.18** *Frequency independent FO BFN*

***I-Q MODULATOR:*** The second PC approach we describe here is the in-phase quadrature (I-Q) modulator proposed by Coward et. al. [*1993*]. They proposed an optical integrated version of the electronic I-Q phase shifter, whose principle scheme is reported in Fig.2.19.

The input signal is divided to furnish two signals 90º out of phase. Each signal passes through a biphase modulator, that provides a 0º or 180º phase shift, and through an attenuator. The I and Q components are then combined. The biphase modulators define the quadrant where the output signal lies, while the attenuators set the output amplitude.

In [*Coward et al.*], an optical integrated version of the I-Q scheme has been proposed (Fig.2.20). Here a MW signal is divided to furnish two signals 90º out of phase. The latter drives two Mach-Zender modulators (MZM) to modulate the light

from two incoherent lasers having intensity $I_1$ and $I_2$, respectively, as shown in Fig.2.20. The MZM bias voltages are $V_1$ and $V_2$ for the MZM1 and MZM2, respectively. As consequence, at the output of each MZM we have an amplitude modulated light signal, whose amplitude can be varied by changing the MZM bias voltages or the laser beam intensity. The optical beams are then summed and downconverted.

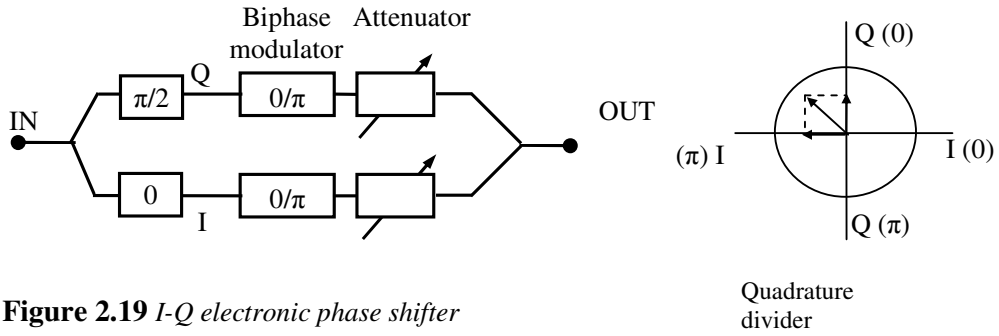


**Figure 2.19** *I-Q electronic phase shifter*

The phase of the obtained MW signal can be changed by controlling $V_1$, $V_2$ and $I_1$ and $I_2$. In fact, if only $I_1$ and $I_2$ are varied, the phase of the MW signal can be varied only from 0º to 90º. On the other hand, when biasing the MZM to the $-V_\pi/2$ or to the $+V_\pi/2$ point, $V_\pi$ being the MZM bias voltage needed to produce a 180º phase shift, the MZM work as a biphase modulator, extending the operation to the other 3 quadrants of the I-Q plane in Fig.2.19.

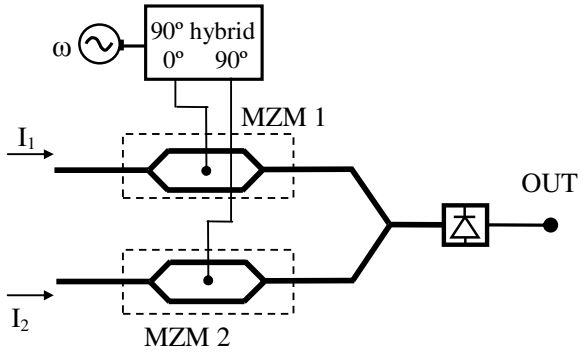


**Figure 2.20** *I-Q photonic phase shifter*

Moreover, a linear I-Q phase modulator, providing a phase shift that changes linearly with the applied voltage, can be obtained. This can be done by using $I_1=I_2$ and $V_2=V_1+V_\pi$, the latter being the MZM bias voltage needed to produce a 180º phase shift. In this way the control wires number can be reduced. However, this condition produces unwanted second harmonics that may limit the dynamic range.

In [*Winnall et al.*] the wideband behaviour of the I-Q photonic phase modulator has been demonstrated from 2GHz to 18GHz. Moreover a photonic MW wideband phase shifter has been reported in [*Henion and Schulz*].

Riza [*1997b*] proposed a BFN based on the I-Q vector modulation principle, where 2-D NLC SLM are used as attenuators. The architecture proposed is suited for large PAA, since it requires less hardware devices than the scheme in [*Coward et al.*].

***OPTICAL INJECTION LOCKING OF MW OSCILLATORS:*** The last technique we mention here is related to the optical control of microwave oscillators. In particular we are interested in optical injection locking of microwave oscillator. This approach allows an accurate phase and frequency control of microwave oscillators [*Blanchflower and Seeds*; *Esman et al. 1989*; *Zhang and Daryoush*].

# CHAPTER 3

# OPTICAL TIME DELAY CONTROL TECHNIQUES

## 1 INTRODUCTION

In the previous chapter we discussed the optical techniques used to implement MW phase shifters. Here, the attention is focused on the use of the optical technology to realize MW time shifters.

The optical TTD techniques received much attention in the specialized literature and several optical TTD architectures have been proposed. These are often referred as optical time steered antennas (OTSA). Following a widespread classification, the most promising approaches can be grouped in two main categories: the switched delay lines (SDL) and the variable propagation velocity lines (VPVL) (Fig.3.1) [*Nirmalathas et al*; *Matthews 1999; Matthews 2000*].

A light signal that propagates within an optical waveguide, having length d, and with a propagation velocity v, experiences a time delay t=d/v. Accordingly, the delay variation $\Delta t$ is given by:

$$\Delta t = \frac{1}{v}\Delta d - \frac{d}{v^2}\Delta v \qquad \text{(III.1)}$$

The only way to change the time delay is to vary the optical path length d, or to change of an amount $\Delta v$ the propagation velocity within the waveguide, as indicated in Fig.3.1

The first optical time shifters were based on the SDL approach [*Ng et al. 1991*]. It represents the optical version of the MW implementation of digital time shifter: different time delays are obtained by driving the light selectively into waveguides having different length, by means of optical or electrical switches. Different SDL solutions have been proposed and are described accurately in the following. They differ mainly about the switch technology adopted and the related optical delay lines. In particular, we will treat bulk optics and IO systems, using free space delay lines, fibers or IO waveguide.

In the second category, the VPVL, the propagation velocity is changed by exploiting the chromatic dispersion of optical devices such as optical high dispersion

fibers (HDF) [*Esman et al. 1993*], Bragg gratings [*Soref 1996*] and arrayed waveguide gratings (AWG) [*Jalali and Yegnanarayanan*].

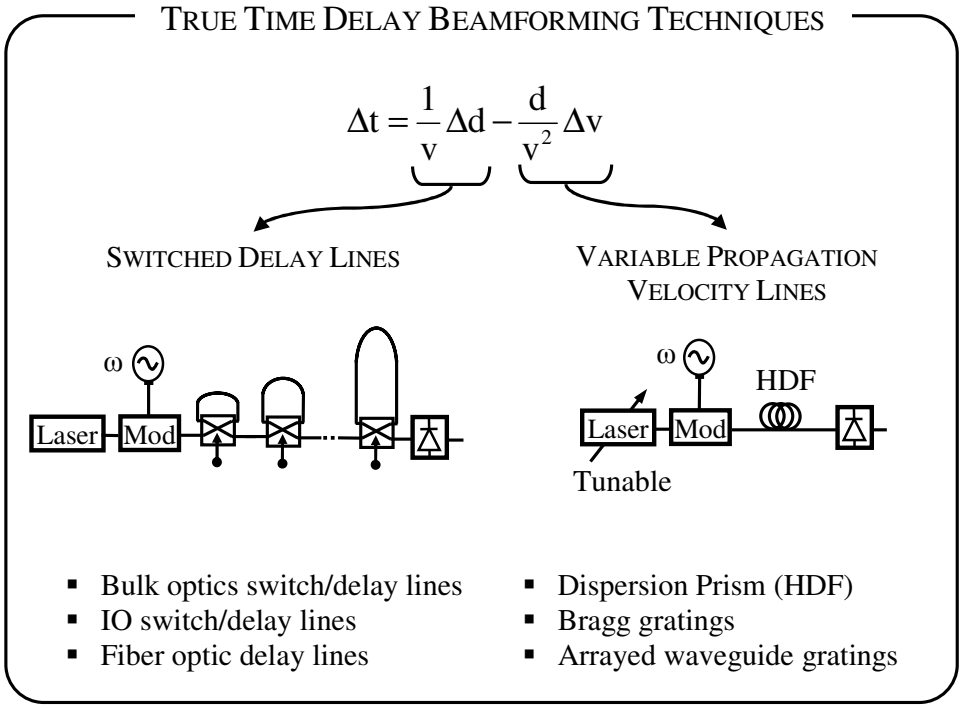


**Figure 3.1** *TTD beamforming techniques scenario*

In Fig.3.1 the layout of the main optical TTD approaches, the SDL and the VPVL, is presented. A representative scheme is depicted for each approach. In particular the exemplificative scheme refers to a direct detection scheme, since it is the most employed detection scheme in such systems. However, also the heterodyne detection has been considered [*Zmuda and Toughlian 1990*]. Moreover, both external and internal modulation schemes have been proposed, although in the exemplificative schemes external modulation has been considered.

Several key aspects have to be considered when realizing an optical time delay control unit for PAA. The main points are:

- Hardware complexity, cost and compactness
- Time delay performances
- Insertion loss

The first issue is related to the system complexity, cost and compactness [*Zmuda and Toughlian 1994*]. These aspects are, obviously, strictly related to the OBFN architecture. Usually, the OBFN is made of as many time shifters as many radiating elements are considered. The TSs can be realized by using SDLs or VPVLs. The complexity and the compactness of the OBFN depend on the TS design and on the number of radiating elements. Accordingly, when dealing with large 1D or 2D PAA, it is necessary to design a TS as compact and low complexity as possible. On the other hand in this case it could be needed to used a different OBFN architecture. In fact,

some OBFNs, as bulk optics ones, are made by one compact time delay unit able to replace several TSs, thus reducing the system bulk and complexity.

The second aspect is related to the achievable time delay distribution. In applications requiring the agile control of the radiated beam, the OBFN has to furnish the time delay distribution needed to obtain the desired pattern properties. The time delay distribution can be varied continuously or discretely. In the latter case the effects of the related quantization error have to be taken into account.

It is worth noting that in multiple beams applications, the OBFN has to be properly designed in order to manage with flexibility the different time delay distributions without increasing excessively the system complexity.

Finally, the IL of the beamforming network represents an important aspect, since if not adequately compensated it could seriously affect the signal to noise ratio. The OBFN design has to be carefully achieved in order to optimize the system losses.

Concerning the OBFN bandwidth, no difficulties arise since the PAA bandwidth is limited only by the characteristics of the MW devices exploited in the antenna systems.

# 2 SWITCHED DELAY LINES

An optical SDL TS is made of several switches to select the proper delay lines, in order to obtain the desired variation of the time delay.

In this section we present the most interesting SDL systems proposed in literature. In particular we considered the SDL architectures allowing to get the best performances regarding the time delay distribution, the IL and the system complexity. Moreover, some of the considered schemes have been employed in the practical implementation of an OTSA.

These SDLs differ regarding the architecture and the implementation.

The architecture refers to the configurations used to arrange the lasers, switches and the delay lines.

The implementation approach refers to the technology adopted to realize the switches and the delay lines. In particular we will refer to the switch implementation technology, since the switches are the key devices of the time delay units. The switches are generally realized by using bulk optics or IO systems. Regarding the delay lines, these are usually implemented by using fibers, free space paths or IO waveguides.

The architecture choice is quite important since it affects the hardware complexity, the IL and the time delay performances. Accordingly, firstly, we will discuss about the more convenient SDL architectures. Later on, we will present the different implementation approaches (bulk optics and IO).

## 3.3 SDL ARCHITECTURES

Essentially the optical delay lines can be arranged in parallel or series connection. The particular choice involves the switches configuration and, as consequence, the hardware complexity, cost and IL [*Zmuda and Toughlian 1994*]. The switches can be implemented by exploiting the electronic as well as the optical technology.

In Fig.3.2 the three main SDL architectures are represented [*Zmuda and Toughlian 1994*]: the parallel optical delay lines structure named PADEL (Fig.3.2a), the square root optical delay line one, also called SRODEL (Fig.3.2b), and the binary optic delay lines, historically called BIFODEL since fiber optic delay lines were used in the earlier proposed schemes (Fig.3.2c).

It is worth noting that each SDL implements one time shifter, thus feeding one radiating element.

The first demonstration of an OTSA has been discussed in the open literature in the early 90's [*Ng et al. 1991]* by using PADEL SDLs (Fig.3.2a). Ng et al. proposed a B bit structure, made of $2^B$ sources connected to fibers having different length (Fig.3.2a) *[Ng et al. 1989; Ng et al. 1990; Ng et al. 1991*]. The obtained delays are changed by selectively driving the laser diode corresponding to the proper length fiber. A fiber combiner is adopted to detect the light signal with one photodetector. A B bit PADEL requires $2^B$ lasers and delay lines. Accordingly, due to the hardware complexity, as described later, is not suited to drive large PAA.

The SRODEL was proposed by Soref [*1984*] in different versions using transmissive or reflective configurations for the delay stages configurations. In Fig.3.2b we refer to the two transmissive stages. This scheme, like the BIFODEL, is a series structure which allows to reduce the hardware complexity by reducing the number of delay lines. For this reason both SRODEL and BIFODEL are referred as delay compressive structures. In the case of a B bit unit, the first transmissive stage uses $E=(2^B)^{0.5}$ fibers with a fiber/waveguide increment equal to $\Delta L_1$, while the second stage uses an increment $\Delta L_2 = E\Delta L_1$. In this way only 2E fibers/waveguides and one laser are adopted.

The BIFODEL (Fig.3.2c) is the most-employed delay compressive architecture: the optical signal is selectively routed through N fiber segments whose lengths increase successively by a power of 2. In this way only B fibers and one laser are required for a B bit shifter. Different BIFODEL schemes are discussed in [*Zmuda and Toughlian 1994; Goutzoulis and Davies*].

In order to evaluate the hardware complexity for each scheme and make a useful comparison among the different approaches, it is worth to introduce a proper figure of merit. Goutzoulis and Davies [*1990*] proposed the figures of merit useful to evaluate the hardware complexity associated to the different architectures. For a linear array with N elements, using a B bit TS for each radiating element, the main hardware complexity parameters are: the number of laser diodes $C_{LD}$, the number of fibers/waveguides $C_F$ and the number of elementary switches $C_s$. Accordingly, in Tab.3.1 the figures of merit related to the architecture proposed in Fig.3.2 are reported, showing that the BIFODEL is the SDL with the minimum hardware.

Different alternatives were proposed to reduce the hardware complexity. The PADEL structure introduced in [*Ng et al. 1991*], was optimized in [*Lee et al. 1995a*; *Loo et al.*]. Here a 5 bit TS was proposed exploiting a proper arrangement of the laser diodes and detectors in order to reduce the overall hardware required. Moreover, different SRODEL structures were proposed [*Soref 1984*] and different BIFODEL too [*Zmuda and Toughlian 1994; Goutzoulis and Davies; Goutzoulis et al. 1989*].

However, the hardware complexity is not the only parameter to identify the most convenient structure. In [*Zmuda and Toughlian 1994; Goutzoulis and Davies*], also the time shifter IL is considered as a figure of merit. The SDL should be designed to guarantee an IL as low as possible and constant for all the realized delay. The latter

aspect is necessary to avoid undesired amplitude variations on the MW signal, discussed in the Section 3.2 of the 1st Chapter. At this end the amplitude uniformity factor has been introduced (AU).

Accordingly, in Tab.3.1 the IL of the discussed schemes is reported indicating with $IL_s$ the losses associated to each switch and taking into account for the coupling losses between the switches and the delay lines corresponding to each delay stage, and assuming that a 1:K divider/combiner has insertion loss in dB equal to $10\log_{10}K$.

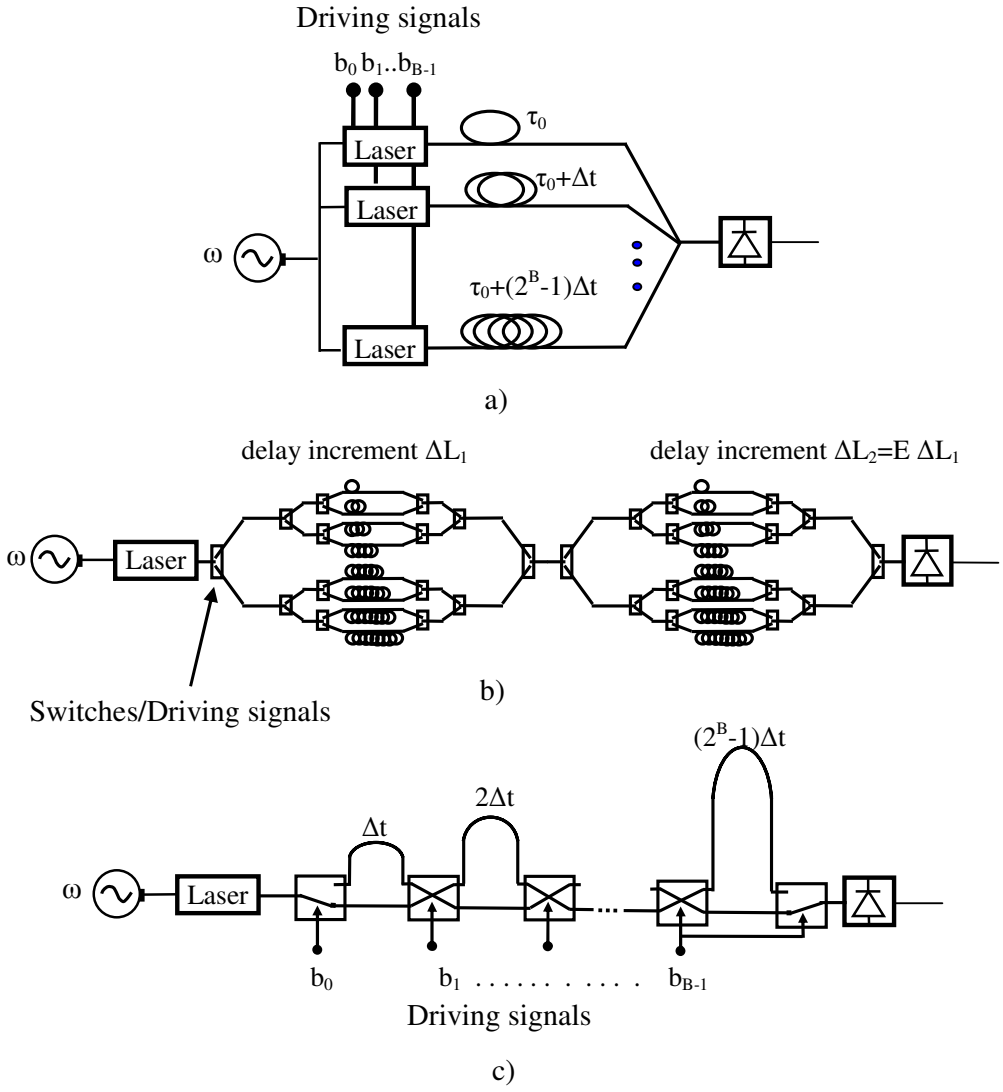


**Figure 3.2** *The main SDL architectures: a)PADEL b)SRODEL c)BIFODEL*

According to Tab.3.1 and referring to the IL, the electronic switch PADEL structure has IL performance essentially limited by output combiner. As consequence the IL grows excessively when a large number of delays is needed.

The ILs of the SRODEL and BIFODEL are comparable and depend upon the losses of the elementary stage $IL_s$. Moreover, all these SDL does not suffer of the mentioned IL instabilities due to different paths within the TS. Accordingly, the related AU is equal to 0dB.

Obviously, also in the BIFODEL shifters with a large number of bits suffer from a total IL which can be excessive. To overcome this problem, Ackerman et al. [*1992*] proposed a BIFODEL structure adopting 4x4 optical switches allowing to use 3 delay lines for each stage, thus reducing the BIFODEL stage number. In particular, they realized an integrated 6 bit time shifters using only 4 stages, thus reducing the IL by 3-4dB.

| | Electronic switch PADEL | SRODEL | BIFODEL |
|---|---|---|---|
| $C_{LD}/C_S$ | $(N-1)2^B$ | $(N-1)(2(2^B)^{0.5}-2)$ | $(N-1)(B+1)$ |
| $C_F$ | $(N-1)2^B$ | $(N-1)(2(2^B)^{0.5})$ | $(N-1)B$ |
| IL | $10\log_{10}2^B$ | $BIL_s$ | $(B+1)IL_s$ |

**Table 3.1** *Comparison of the main SDL architectures*

## 3.4 SDL IMPLEMENTATIONS

Here we present the main proposed SDL implementations for bulk optics and IO systems. For each scheme we report the most important features. These are the maximum achievable delay $\tau_{max}$, or equivalently the maximum achievable steering angle $\theta_{max}$, the time shifter IL, or the single stage losses, and the number B of bits. Moreover, the attainable delay accuracy and the signal stability and the BFN compactness are also reported.

Preliminarily, it is worth to discuss about the peculiar aspect of bulk optics and IO systems.

In bulk optics schemes, the time delay is controlled by using SLM switches that select different paths, usually realized in the free space. Accordingly, when dealing with long delays, bulk BFNs are obtained. The key feature offered by the bulk optic structures is related to their capability of feeding medium/large 2D PAA since compact optical processor, like for PC schemes, can drive a large number of parallel beams, corresponding to the PAA elements. However they suffer from the typical bulk optic drawbacks, such as mechanical and thermal instabilities.

The BFN size reduction, the signal stability and the reduction of realization defects can be achieved by means of IO structures. The refraction index of the IO materials allows to significantly decrease the propagation velocity thus leading to more compact BFN. However, IO BFNs suffer of the problem of the losses within the IO chip. In particular, the choice of the material has to take into account for the trade off among the refractive index, the optical attenuation and the temperature dependence of the refractive index.

Both bulk optics and IO systems can employ fiber optic delay lines to get a better signal stability when realizing long delays. Nevertheless, for large PAA the achieved system is not too compact.

In the following we report the bulk optic and IO schemes. For the bulk optics ones, the switching function has been performed using different SLMs. Accordingly, we describe the main different switching schemes. For IO systems, many solutions

have been proposed. As consequence we separate the reported structures according to the particular optical delay lines employed: fiber or IO waveguides.

### 3.4.1 BULK OPTICS

***Polarization switching:***

One of the first bulk optics beamformer has been proposed by Dolfi et al. [*1989; 1991*]. This is a 2D OBFN, able to perform phase and time delay control, based on a BIFODEL, all optical, structure. In particular NLC SLMs are used to realize polarization switching, thus allowing to cumulate the desired delay obtained by the free space propagation. The maturity of the LC technology allows to implement up to 10000 delay channels contemporaneously within one LC.

The elementary delay module is made of a LC SLM, a polarization beam splitter (PBS) and a mirror or a corner prism (Fig.3.3a). The LC SLM realizes the electronic control of the polarization of all the light beam channels, as shown in Fig.3.3a. The free space light path can be switched by means of the PBS, thus controlling the related delay. The desired path is obtained by using mirrors or total internal reflection corner prisms.

The LC elementary delay unit can then be arranged in a binary fashion to form the BIFODEL structure, as reported in Fig.3.3b.

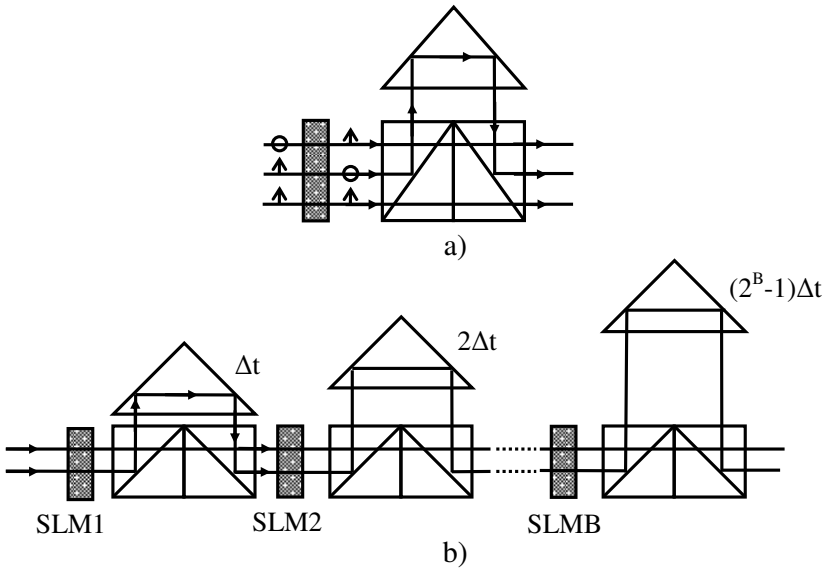


**Figure 3.3** *The bulk optics polarization switching architecture a) operating principle of the delay module b) the BIFODEL structure*

Dolfi et al. [*1989*; *1991*; *1996*] adopted an heterodyne detection scheme in their BFN. The laser light illuminates a bragg-cell that furnishes the undiffracted and the frequency shifted light beams. These beams travel through two separate paths before combining. As consequence, due to this path difference, it is necessary to use a laser having a certain degree of temporal coherence. Moreover, mechanical vibrations or air currents could affect in different manner the two light beams before they are combined: this could generate a phase error on the MW signal.

Successively, Riza [*1991b*] proposed a similar OBFN, using the same NCL SDL architecture, but based on a direct detection scheme. The laser light is, in fact, intensity modulated. This reduces the laser temporal coherence requirements and the phase errors generated by the modulation scheme employed by Dolfi.

It is worth noting that the OBFN proposed by Riza [*1991b*] is properly designed to realize both the transmit and the receive mode. The receive scheme here exploited is similar the one in Fig.1.16 (see Chapter 1, Section 3.1.2): the correct signal reception is obtained by propagating the antenna signals through the OBFN. At the output of the delay lines a spherical lens is used to perform the receive signal set summation, thus avoiding the wideband microwave combiner network required in other control techniques.

Moreover, like for narrow band phase steering BFN, Riza proposed two indipendent optical systems operating in a time-multiplexed fashion to improve the OTSA beam scanning rate [*Riza 1992d*].

An important system issue is related to the BFN compactness. Large arrays with about 1000 elements working under 5GHz do not allow a compact structure.

Dolfi et al. [*1996*] proposed the use of the holographic back plane technology to reduce the BFN size. Riza proposed a solid optics version of the BFN, where materials like glass, for example with a refractive index of 1.5, are employed in place of the free-space sections. This solution allows to reduce the path required for an assigned delay, and make more robust the BFN structure [*Riza 1994*]. Moreover, Riza suggested also an optical SDL using NLC switches, together with fiber optics arranged in a folded structure: polarization maintaining fibers with proper length are wrapped around a single PBS, while a NLC is used to change the polarization of the output of each fiber. In this way, the bulk optics systems can be modified to realize long delays required for very large aperture OTSA. In fact, according to the (I.5), the maximum delay required is proportional to the antenna aperture.

Other practical issues have been addressed by Riza: he proposed the use of imaging lenses to minimize the optical losses from beam spreading and diffraction effects when dealing with long time delays, and the use of polarizer sheets to suppress unwanted polarized light, so realizing good noise removal filters and improving the signal to noise ratio of the OBFN.

The polarization switching OBFN scheme has been experimentally tested by Dolfi et al. [*1996*]. They implemented a 16 element array working in the frequency range 2.7-3.1GHz, driven by 5 bit BIFODEL, allowing a $\tau_{max}$ equal to 1.8ns: the beam steering has been demonstrated from 0º to 20º. Regarding the IL, from the result proposed in [*Dolfi et al. 1996*] an IL per stage of about 1.5dB can be estimated. However, the losses could change according to the path choice, straight or switched path. This is due to misalignments and reflections from optical devices not provided with a suited anti-reflection coating.

Riza and Madamopoulos [*1997*] proposed time delay units based on FLC, able to realize SNR over 96dB with 35μs switching time, well suited for fast scanning PAA.

***Index switching:***

When dealing with mm-wave frequency, over 20GHz, the delay resolution achieved within the optical processor becomes important. In fact, when managing delays of about few femtoseconds, the optical path resolution has to be carefully

controlled. Accordingly, an interesting OBFN, called the index switching TTD device, has been proposed [*Yao and Maleki*].

The single stage of this scheme is made of a birefringent crystal and a LC polarization rotator. According to the desired signal polarization, electronically controlled, the light signal experiences two different refractive indexes, say $n_e$ and $n_0$, thus experiencing different delays $\Delta t$, depending on the lengths l of crystal segments:

$$\Delta t = \frac{(n_e - n_0)l}{c} \qquad \text{(III.2)}$$

By using more stages, with a crystal length increasing of a factor of 2, a very compact BIFODEL structure is achieved (Fig.3.4), able to feed PAA operating up to 40GHz.

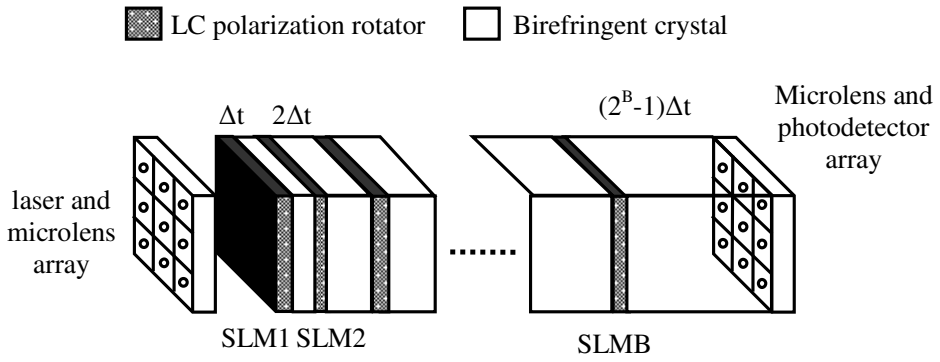


**Figure 3.4** *The bulk optics index switching architecture*

The authors reported the results for a 64x64 PAA working at 40GHz, although the steering of an OTSA prototype has not been demonstrated. In particular, they estimated that a 12 bit BIFODEL allowing a maximum scan angle $\theta_{max}$=60º requires a total length for the crystal equal to 76.4 cm.

***Acousto-Optic Devices:***

A different bulk optics approach uses AOD for implementing TSs. In particular the time delay is controlled by exploiting the interaction between the acoustic wave on the optical beam within the AOD [*Lin and Boughton*], or by using the AOD as a switching beam deflector to illuminate the desired length delay line [*Jemison and Herczfeld 1993*].

*Multichannel AOD:*

In [*Lin and Boughton*] an optical time delay control system based on a multichannel AOD is demonstrated. The delay unit is obtained by illuminating the multichannel AOD, driven by the proper RF signals, by means of a narrow optical beam obtained by using a single-slit rotating mask (Fig.3.5a). The delays variation is achieved by rotating the optical beam as shown in Fig.3.5b.

In fact, when the optical beam is parallel to the transducer plane, the signals associated to each AOD channel have equal delays, related to the distance $l_i$ among the transducer plane and the AOD section illuminated by the optical beam.

Accordingly, by rotating, or translating the optical beam, the distances $l_i$ across the AOD channels change, thus controlling the resulting delays (Fig.3.5).

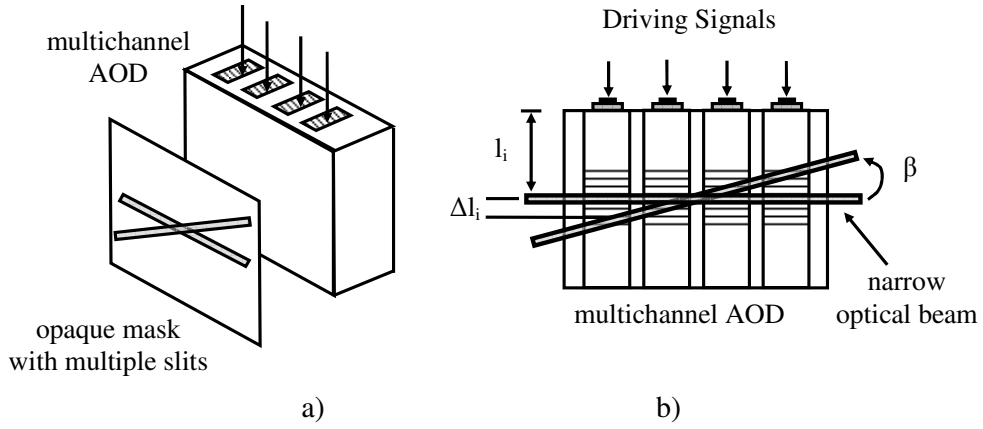


**Figure 3.5** *The multichannel AOD time delay unit. a) view in perspective b) frontal view*

Both heterodyne and direct detection schemes have been taken into account. Regarding the optical beam rotation in [*Lin and Boughton*] a Dove prism has been considered. It provides an almost continuous delay variation depending on the precision of the Dove prism rotating stage adopted. In the experiment a time delay uncertainty of 60ps is referred. The authors show that the system could provide a $\tau_{max}$ of about 156ns.

*AOD Deflector:*

In [*Jemison and Herczfeld 1993; Jemison and Herczfeld 1996*] an AOD is used as deflector to select the desired delay line (Fig.3.6). An intensity modulated light signal illuminates the AOD, driven with a proper MW signal. According to the AOD driving frequency, the deflection angle β, shown in Fig.3.6, can be controlled. In this way the intensity modulated light is coupled with the desired fiber or integrated waveguide placed at the AOD output. The authors estimate an insertion loss of about 6-10dB, if the AOD diffraction efficiency is about 40% and the fiber coupling efficiency is about 60%. The time delay unit can realize a 6/7 bit structure with an isolation between delays better than 25-30dB.

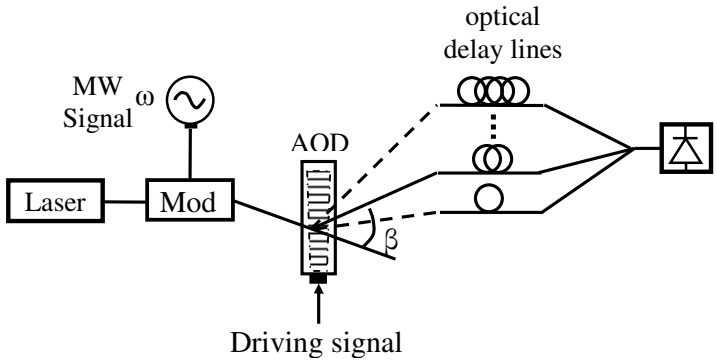


**Figure 3.6** *The AOD deflector switch scheme*

An analogous scheme has been presented by Toughlian and Zmuda [*Toughlian and Zmuda 1993*]. They used a SLM mirror device as optical beam steering unit to select the fibers with the desired length.

***Heterodyne compensated scheme:***

Zmuda and Toughlian [*1990*] also proposed an heterodyne compensated scheme that realizes a TTD control unit for PAA. Typically the heterodyne systems are used to provide MW phase variations, independent from the MW frequency. Here, the authors suggested an heterodyne system using a deformable mirror devices SLM that allows to realize the time delay control. This system is then referred as heterodyne compensated scheme. The scheme, depicted in Fig.3.7, uses a Mach-Zender interferometer structure, where in the lower arm, an AOD or a SSB modulator together with a diffraction grating, is used to modulate and deflect the optical beam according to the signal frequency components. A cylindrical lens images the spatially separated components on a reference plane, where a mirror able of translation and rotation imposes a different path for each frequency components. In particular the path difference $\Delta l$ is a linear function of the MW frequency, and can be changed by translating or rotating the mirror.

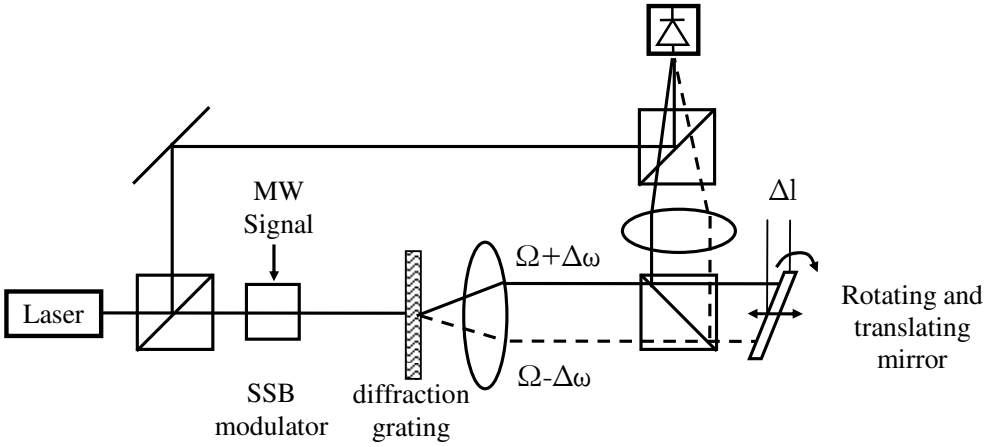


**Figure 3.7** *The frequency compensated heterodyne scheme*

The detected signal presents, therefore, a delay $\Delta t$ proportional to the path difference $\Delta l$ corresponding to the MW frequency $\omega$. In particular, labelled with $\Omega$ the optical carrier, we have:

$$\Delta t = \frac{\beta \Delta l(\omega)}{\omega} = \frac{(\Omega + \omega)\Delta l(\omega)}{\omega c} \approx \frac{\Omega \Delta l(\omega)}{\omega c} \qquad \text{(III.3)}$$

Accordingly, since $\Delta l$ varies linearly with $\omega$, the obtained time delay is independent of the MW frequency, thus realizing a TTD time shifter. They demonstrated the linear behaviour of the phase versus frequency relationship for a 25MHz bandwidth with centre frequency equal to 70MHz. The system should provide a continuous delay tuning although this feature is not documented.

### 3.4.2 INTEGRATED OPTICS

***Fiber delay lines:*** IO technology has found wide application in realizing optical switches for fiber or IO waveguide delay lines.

Among the SDLs using fiber delay lines, the most important time steering demonstrations have been reported in [*Ng et al. 1991; Lee et al. 1995a*] by using the PADEL structure discussed in the section 2.1(Fig.3.2a).

In [*Ng et al. 1991*], a 3 bit PADEL TS has been used to implement a dual band antenna system working at 2GHz and 9 GHz, arranged in 4 subarrays of 2 elements each and 4 subarrays of 8 elements, respectively. The optical BFN allows a maximum scan angle $\theta_{max}$=28º and an angular resolution $\Delta\theta$=4º. The beam squint free behavior has been proved form 1.9GHz to 9GHz. The reported optical IL is about 30dB. Due to path non uniformities the SLL raises up to 8dB, from the 13dB standard level for a uniform array.

In [*Lee et al. 1995a; Lee et al. 1995b*] a 5 bit time shifter is considered to drive a 24x4 PAA, where the steering is realized only across the 24 elements columns. These are arranged in 8 subarrays with 3 elements. The working bandwidth is from 850MHz to 1.4GHz. The $\theta_{max}$ reported is about 60º. The time shifter IL is about 20dB. The system works in both transmit and receive modes.

The SRODEL system proposed by Soref [*1984*], discussed in the section 2.1, has been implemented by using IO switches together with fiber delay lines. Its layout is reported in Fig.3.8.

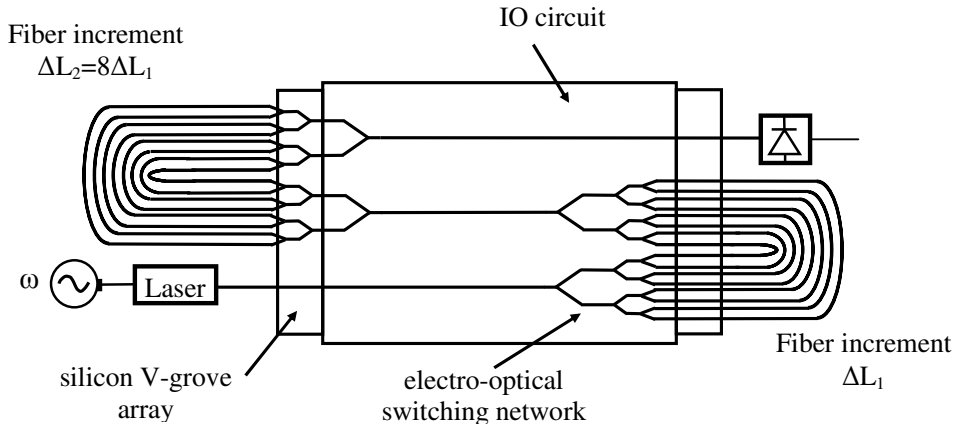


**Figure 3.8** *Programmable 6 bit SRODEL*

Ackerman et al. [*1992*] realized a 6 bit integrated switch unit, using external fiber delay lines, for a 3-6GHz radar PAA. The time shifter allows a $\tau_{max}$ of about 30ns, while the IL is about 14.0dB±0.3dB, although for some delay paths an higher IL of about 15.5dB-16.7dB is reported due to coupling and switching IL asymmetries.

Goutzoulis et al. [*1989*] realized and widely discussed the design of a 7 bit BIFODEL structure, where MESFET based GaAs 1x2 switches were used together with fiber delay lines. The reported $\tau_{max}$ is about equal to 5μs. The working bandwidth is in the range 0.5GHz-1GHz.

In the 1992 Goutzoulis and co-workers [*Goutzoulis et al. 1992*] realized an hybrid TTD unit, based on electronic and optical delay lines. In particular they realized a 6

bit BIFODEL structure. The hybrid control unit has been used to drive a 16 elements OTSA over the 0.35-2.1GHz band and with a ±45° scan coverage [*Goutzoulis et al. 1994*].

***IO waveguide delay lines:***

Ng et al [*1995*] proposed a 4 bit PADEL structure, with a $\tau_{max}$ of about 3.97ns, using silica waveguides chip, instead of optical fibers, ensuring high precision and compactness.

In [*Ng et al. 1994*] the different delays, realized by using GaAs waveguides, are obtained by switching among different detectors, instead of select among different lasers [*Ng et al. 1991*]. This structure has been demonstrated for a 2 bit module allowing a $\tau_{max}$ of about 122ps.

Sullivan et al. [*1992*] realized a photonic integrated circuit (PIC), on GaAs substrate, which implements a 2 bit TSs using integrated switches and waveguides. The circuit allows a $\tau_{max}$ of about 0.5ns and has an IL per stage of about 3dB. The photo of PIC is reported in Fig. 3.9.

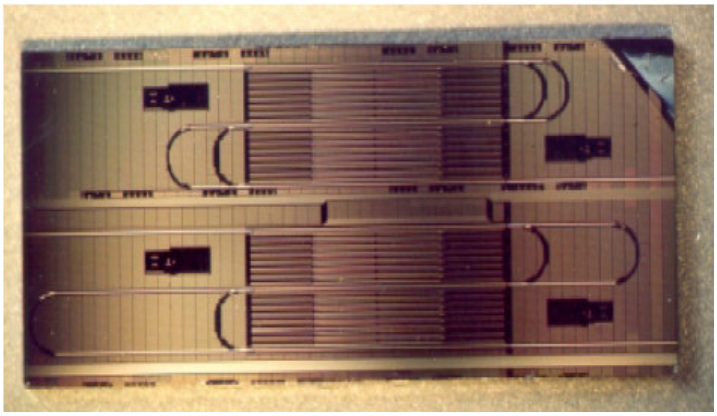

**Figure 3.9** *Photo of the GaAs PIC time shifter proposed in [Sullivan et al.]*

Chen and Li [*Chen and Li 1996; Li and Chen; Li et al.*] proposed a TTD unit based on the system represented in Fig.3.10.

The structure is based on an heterodyne detection scheme. The two frequency shifted light signals, shown in Fig.3.10, are coupled within a substrate, where propagates by means of successive bounces. Holographic grating couplers are used to couple the light into and out of the substrate. Accordingly, different delay lines are achieved. The selection of the desired delay is achieved using switching detectors. The authors proposed a 3 bit time shifter that reports a $\tau_{max}$ of about 336ps and an IL of about 15dB. The system allows an elevated number of bits per chip unit area, thus realizing a very compact TTD shifter. The structure suffers of the intensity attenuation of the delayed signals, due to the series scheme. In fact, differences in the efficiency of the output couplers, and substrate absorption cause this attenuation. Accordingly, by tuning the efficiency of the output coupler the intensity fluctuations have been reduced to ±10% [*Li and Chen*].

A 6 bit TTD unit, having a $\tau_{max}$ equal to 443ps, has been used to realize a 8 element PAA, working in the K band [*Chen and Chen*].

A similar delay unit, based on dispersive waveguide holograms, has been proposed to obtain a continuous delay variation [*Shi et al. 2003*].

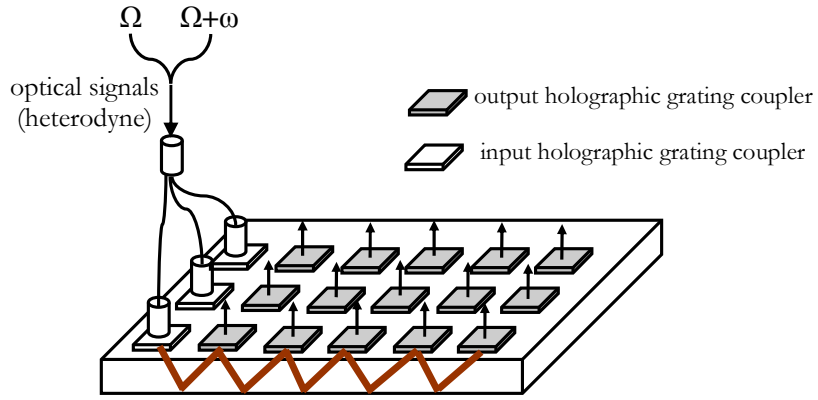


**Figure 3.10** *The TTD based on the substrate mode optical fanout*

Silica waveguides and IO thermo-optic switches have been adopted to realize a 5 bit BIFODEL [*Paquet et al.*].

Wang et al. [*1996*] proposed the use of polymer nonlinear optical materials to implement integrated delay lines. In particular they realized a binary time delay unit using polymeric photonic switches and delay lines.

Magel et al. [*1994*] proposed an optical integrated switch based on metallic membranes. The light propagation in an integrated waveguide is controlled by using metallic membranes that can be electrostatically attracted into contact with the waveguide, thus varying the refractive index of the guide mode.

Riza and Polla [*1992*] introduced the use of micromachined piezo-electric thin-film micro-actuators realizing a switch for fiber delay lines and demonstrated a macro-scale actuator.

A different approach has also been proposed. This is the fiber stretching scheme: a fiber is wrapped around a piezoelectric ring that expands upon the application of an electric field, thus stretching the fiber and realizing a continuous time delay variation [*Herczfeld et al.*]. This method requires high intensity fields to achieve useful time delays.

Accordingly, in Fig.3.11 we report the SDL summary frame wherein the main TTD time shifters schemes are reported. The schemes are divided according to the switching technology.

We use the label I for the PADEL architecture, the label II for the SRODEL, the label III for the BIFODEL and the label C for the schemes providing continuous delay variation. Moreover, another marker, labelled as A, is used to enlighten the time steering demonstration. In this case, all the information about the OTSA system are reported, when available. It is worth noting that in the case of the IO and electronic switching circuits, only few of the practical realizations have been considered, since the main differences concern only the implementation details, while the exploited scheme remains usually the same.

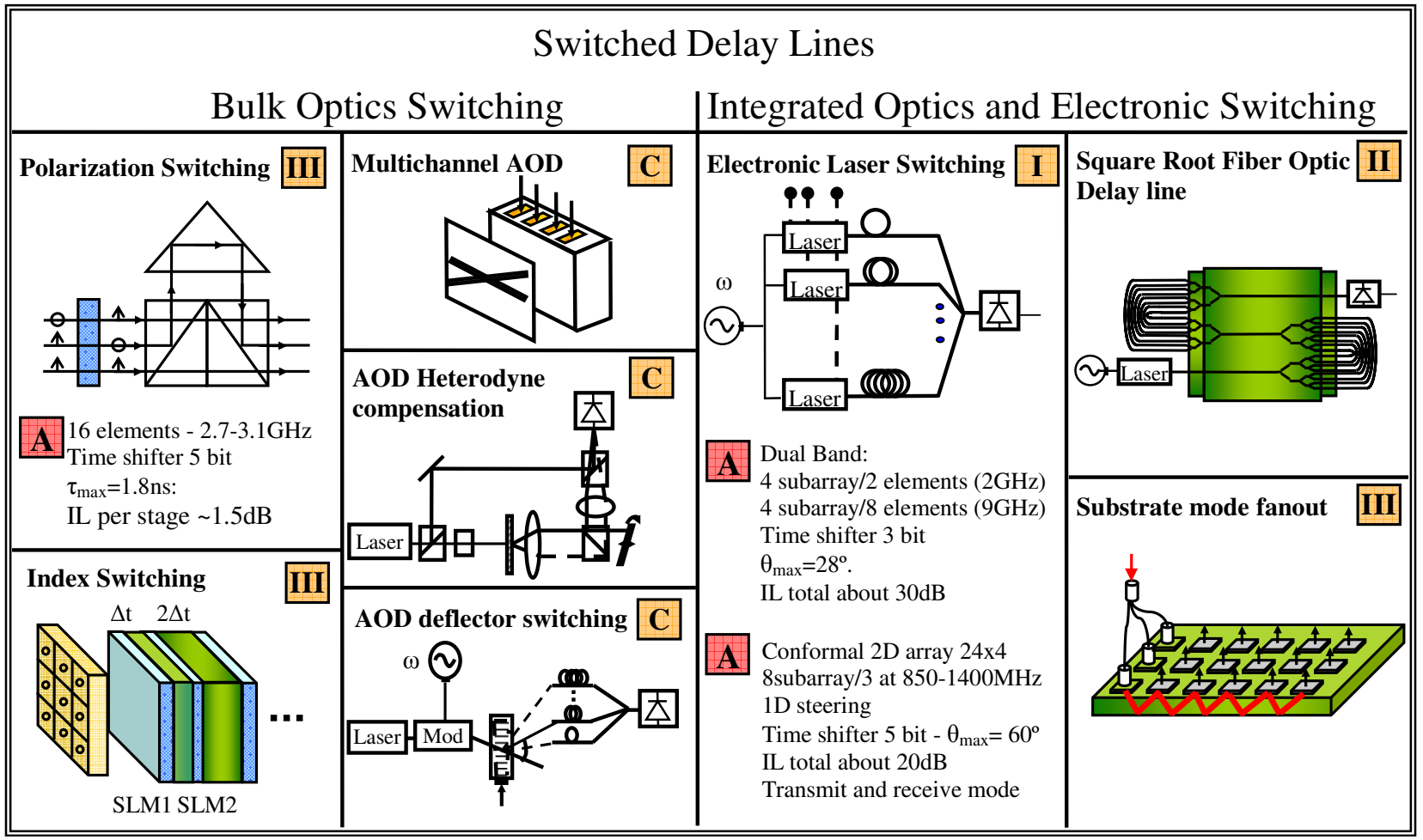


**Figure 3.11** *SDL summary frame*

# 3 VARIABLE PROPAGATION VELOCITY LINES

As told before, the other way to change the time delay of an optical signal is to vary the propagation velocity. In particular, the propagation velocity can be changed by exploiting the chromatic dispersion of some optical devices, such as for example HDF.

In this section we report the main VPVL architectures proposed in literature. Each architecture is based on a specific optical device. In particular, we consider:

- High Dispersion Fibers
- Fiber Bragg gratings
- Arrayed waveguide gratings

Really, it is worth noting that for the last two architectures, unlike the HDFs, the time delay varies without any change in the propagation velocity, but by means of variations in the path length or in the experienced light path, due to changes in the signal wavelength. Therefore, since the time control can be achieved by varying the laser wavelength, thank to the dispersive behaviour of the used device, this type of PAA optical control systems are usually mentioned in the VPVL schemes [*Matthews 2000*], although the delay is controlled as in a SDL.

## 3.1 HIGH DISPERSION FIBERS

The optical dispersion technique was proposed in 1992 [*Soref 1992; Esman et al. 1992*] and demonstrated at the Naval Research Laboratory [*Esman et al. 1993*]. The basic idea is to use HDFs together with tunable lasers, in order to change the propagation velocity by varying the laser wavelength. The light signal is intensity modulated by the MW one and sent into an HDF having a total chromatic dispersion $D_{HDF}(\Lambda)$ assumed constant over the laser wavelength tuning range. It is usually measured in ps/(km·nm). If the fiber has length L, and the tuning range $\Delta\Lambda=\Lambda-\Lambda_0$ is small compared to the centre wavelength $\Lambda_0$, then the reported delay $\tau(\Lambda)$ is given by:

$$\tau(\lambda) = L\left[\frac{1}{v_g} + D_{HDF}\Delta\Lambda\right] \tag{III.4}$$

where the high-order terms have been neglected and $v_g$ is the group velocity. Accordingly, the delay variation due to the laser tuning is:

$$\Delta\tau = LD_{HDF}\Delta\Lambda \tag{III.5}$$

Obviously, if the tuning range amplitude does not allow to neglect the high order terms, the dispersion variation with the wavelength has to be taken into account.

Accordingly, provided the laser tuning system is able to change continuously the wavelength, the time delay can be varied continuously, thus achieving a continuous time steering. The maximum delay $\tau_{max}$ can be varied at will by using fibers with a proper dispersion and length, although excessive long fibers suffer from delay variations due to thermal stabilization problems, as described in the following. Regarding the time resolution, it depends on the laser wavelength stability $\Delta\Lambda_s$. The

latter is defined as the maximum of the laser linewidth, mode spacing and wavelength stability. The time delay resolution is given by $\Delta\Lambda_s/\Delta\Lambda$.

Apart from the conversion losses, the IL of each MW link is essentially due to fiber coupling and attenuation, and then can be easily kept low.

In the BFN suggested by Soref [*1992*] to feed a linear array, a variable delay link is used for each radiating element (Fig.3.12). By referring to a linear array with an inter-element spacing d and assuming that all the dispersive links have equal length, the wavelength tuning needed for the n-th radiating element to steer the beam at the angle $\theta_0$, is given by:

$$\Delta\Lambda(n) = \frac{nd}{cD_{HDF}L}\sin\theta_0 \qquad \text{(III.6)}$$

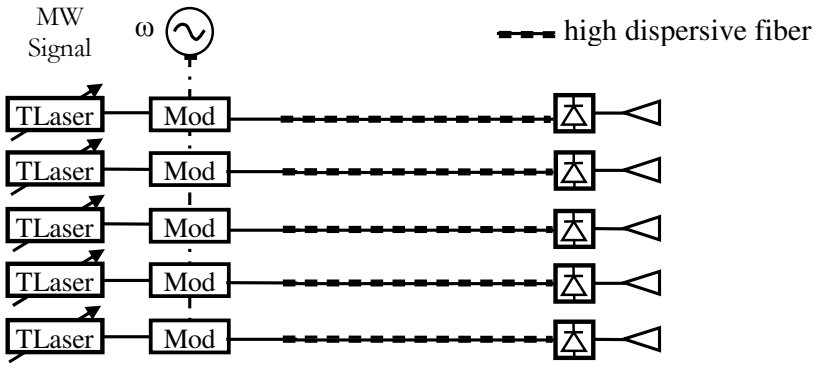


**Figure 3.12** *The HDF variable delay lines architecture*

In particular the laser tuning can be also used to compensate for the $D_{HDF}$ variation across the tuning range. However, when dealing with large antenna this first architecture requires a prohibitive amount of hardware and a complex control unit, since the control signals are different for each laser.

***Fiber Optic Prism:***

Esman et al. [*1993*] proposed an innovative structure called the Fiber Optic Prism (FOP). The suggested scheme, depicted in Fig.3.13, is based on a single tunable laser and on the FOP, a set of optical fiber links with different total dispersion. In particular the net dispersion of each link is proportional to the position of the feed antenna element. Each link is obtained by connecting HDF and non dispersive fibers with different length in order to get the same group delay at the centre wavelength and the proper net dispersion.

Accordingly, at the centre wavelength the time delays for each antenna elements are equal, thus making the antenna beam pointing broadside. At wavelength less or greater than $\Lambda_0$, each dispersive link adds or subtracts a time delay proportional to its dispersion. As consequence, opposite tuning ranges make the radiated beam pointing towards opposite directions, as shown in Fig.3.13. The authors demonstrated the beam squint free behaviour for a two element horn antennas array, from 2GHz to 8GHz. They used a σ-laser [*Esman et al. 1993*], having a $\delta\Lambda$ equal to 0.06nm and a tuning range of about 50nm. The obtained time delay resolution is about 1.2e-3. The FOP

was made of two links. The first was made of an HDF with length equal to 108m, while the second was made of a standard non dispersive fiber with the same length.

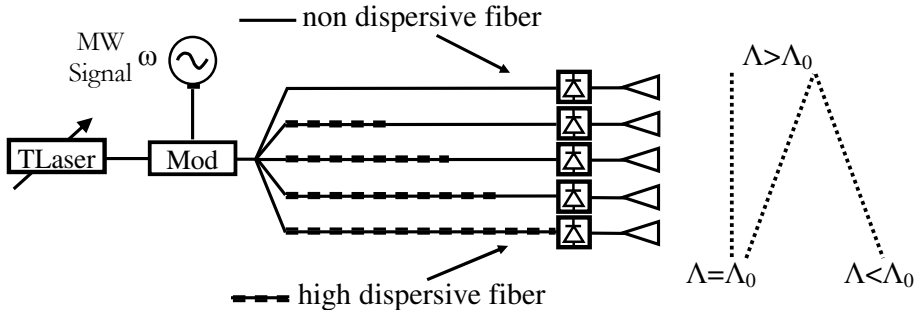


**Figure 3.13** *The FOP scheme*

Let us consider the design of the FOP. For a linear array, with N radiating element and links, the n-th link has total length $l_{link}$, equal for each channel, composed by n sections of HDF, each having length $l_{HDF}$, and a section of non dispersive or dispersion shifted fiber (DSF), with length $l_{link}$-n $l_{HDF}$. Let us denote with $D_{HDF}(\Lambda)$ and $D_{DSF}(\Lambda)$ the dispersion of the HDFs and of the DSFs, respectively. Accordingly, assuming that the dispersion varies linearly with the wavelength [*Frankel and Esman*] as $D_{HDF}(\Lambda)= D_{HDF}+ D'_{HDF}\Delta\Lambda$ and $D_{DSF}(\Lambda)= D_{DSF}+ D'_{DSF}\Delta\Lambda$, the time delay change for the n-th link is given by:

$$\begin{aligned}\Delta\tau_{n-link} &= l_{link}\left(D_{DSF}\Delta\Lambda + D'_{DSF}\,\Delta\Lambda^2\right)+ \\ &+nl_{HDF}\Delta\Lambda\left[\left(D_{HDF}-D_{DSF}\right)+\Delta\Lambda\left(D_{HDF}-D_{DSF}\right)\right]\end{aligned} \qquad \text{(III.7)}$$

Accordingly, the length of the HDF section is obtained by comparing the second term of (III.7), the only one that changes across the array elements, with the time delay required to the n-th element to achieve to assigned steering angle $\theta_0$. We have:

$$l_{HD} = \frac{d}{c\Delta\Lambda\left[\left(D_{HDF}-D_{DSF}\right)+\Delta\Lambda\left(D_{HDF}-D_{DSF}\right)\right]}\sin\theta_0 \qquad \text{(III.8)}$$

By using the system specification adopted in [*Frankel and Esman*], an $l_{HD}$ equal to 46m is required to achieve a maximum steering angle equal to ±60º, for a maximum tuning range $\Delta\Lambda$=±22.5nm, d=2.5cm, and assuming $D_{HDF}(\Lambda)$=-70ps/(km·nm) and $D_{DSF}(\Lambda)$=0ps/(km·nm). Accordingly, the last element (n=30) needs a HDF 1334m long.

In this way, for large array very long fibers are needed. This involves a thermal stability problem, since deleterious variations in the fiber physical length and optical length can be caused by temperature changes [*Frankel and Esman*]. In particular the main effect is the optical length change due to refractive index thermal slope. In [*Frankel and Esman*] a delay link variation of 54ps/ºC is registered. Such temperature instability can generate serious delay variations and, then, beam pointing errors. Moreover, HDF and dispersion shifted fibers present different thermal slopes. To avoid delay asymmetries and drift, the BFN has, therefore, to be placed into an insulated enclosure, provided with a proper thermal stabilization system.

Furthermore, the use of HDFs involves losses at high MW frequency. In particular, the loss $G_{disp}$ is given by [*Matthews et al. 1998*]

$$G_{disp} = 20\log_{10}\left(\cos\left(\frac{\pi D_{HDF} L\Lambda^2 f^2}{c}\right)\right)\ [dB] \qquad \text{(III.9)}$$

This problem is serious only for the edge elements of large arrays, requiring very long HDFs, when the MW working frequency f of the antenna is high. In this case, the frequency range has to be upper bounded in order to reduce the related loss. The amplitude taper produced by the undesired losses has to be properly taken into account to achieve the desired amplitude distribution.

The research group at the Naval Research Laboratory proved the FOP efficiency and flexibility for different applications.

The time steering was demonstrated for a transmitter and receiver arrays [*Frankel and Esman*; *Frankel et al. 1995*; *Frankel et al. 1997*; *Matthews et al. 1998*]. In particular OTSAs able to perform both transmit and receive modes have been realized in [*Frankel and Esman*; *Frankel et al. 1995*], while the receive only mode has been considered in [*Frankel et al. 1997*; *Matthews et al. 1998*].

The adopted receive scheme has already been discussed in the Section 3.1.2 of the 1st Chapter (Fig.1.17): the OBFN provides properly phased local oscillators signals (LO) for downconverting the signals received by the antenna elements (Fig.3.14). The BFN LO signals are mixed together with the antenna received ones, thus generating the intermediate frequency signals. The receiving-mode steering commands are the complementary to the one in the transmit-mode, as discussed in the 1st Chapter. This can easily achieved by inverting the laser tuning range respect to the one adopted in the transmit mode.

Receive arrays, using a binary-tree fiber optic dispersive prism, have been proposed in order to reduce the hardware required and the amount of fibers [*Frankel et al. 1997*; *Matthews et al. 1998*].

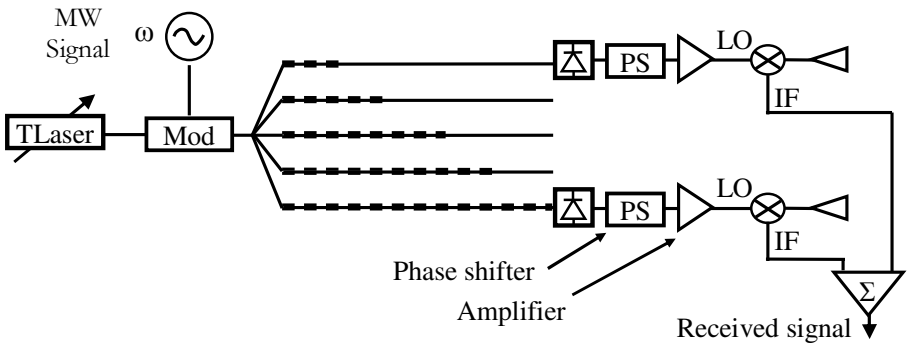


**Figure 3.14** *The FOP receiver scheme*

In [*Frankel and Esman*] the time steering of an 8 elements array in transmit mode and 2 elements in receive mode has been demonstrated respectively from 2GHz to 18GHz, with a $\theta_{max}=\pm 53°$, and from 6GHz to 16GHz, with a $\theta_{max}=\pm 35°$. In their experimental validation, the authors observed amplitude and phase variations of the excitation coefficients, 2-3dB and about 15°, respectively, due to the mismatch among the high output impedance of the photodiodes and the 50Ω impedance of the

following MW devices. These unbalances have to be reduced by properly terminating the photodiodes, or by using broadband insulators, after the detection, to avoid the mismatching changes the photodetectors working point.

The dispersive prism can be easily adapted to generate multiple simultaneous beams at the same or at a different frequency, by adding another wavelength tuned laser [*Frankel and Esman*]. To avoid deleterious intermixing products, in the case of pulsed operation, the two laser wavelengths have to be distant at least $2f_{max}$, the latter being the maximum frequency contained in the modulating MW pulse.

An OBFN able to drive a 2D array, based on the fiber prism, has been also proposed in the 1996 (Fig.3.15) [*Frankel et al. 1996a; Frankel et al. 1996b; Tulchinsky and Matthews 2000*; *Matthews et al. 1996*]. The system is made of $N_{col}$ FOP, one for each array column, called elevation FOPs, whose external modulator is driven by the proper MW signal generated by an azimuth FOP. Accordingly, the azimuth laser, with wavelength $\Lambda_{az}$, drives the delay of the MW signals modulating the different elevation channels. This cascading approach allows a very useful hardware reduction. In the experiment [*Frankel et al. 1996a*] the authors considered a two dimensional array made of 4x4 flared notch elements, working in the 6GHz-18GHz band. The time steering was verified across ±30º in azimuth and range independently. In each link a fiber optic attenuator and a microwave trombone phase shifter are used to compensate for amplitude and time errors. In each azimuth link a MW amplifier with about 39dB gain and 3dB noise figure have been introduced. These amplifiers present an amplitude stability of ±1dB and phase stability of ±10º in the band 6GHz-8GHz. The OBFN has been characterized, showing an RMS variation of ±1dB and ±5º at low and intermediate frequencies, and ±2.5dB and ±10º at the higher frequencies. This behaviour is due to the amplifiers and modulators defects.

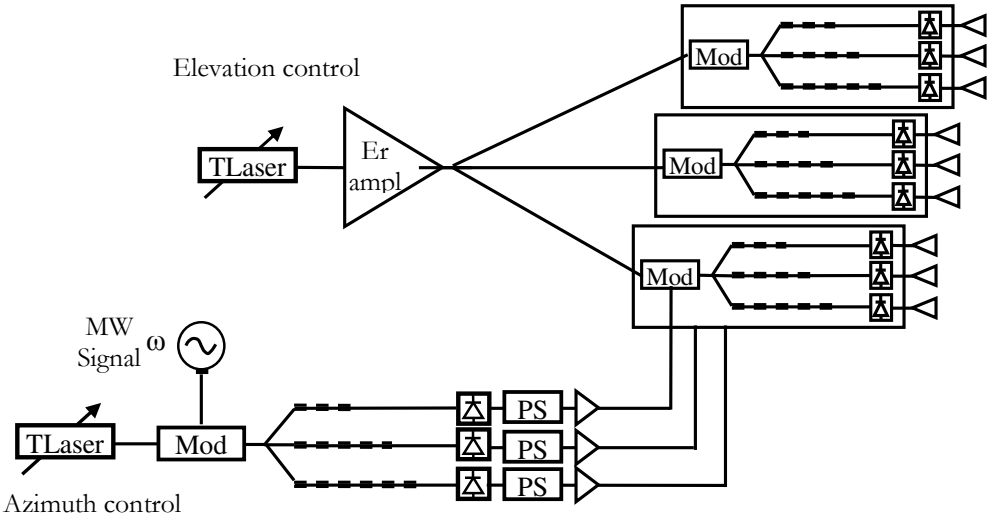


**Figure 3.15** *The FOP 2D feeding scheme*

Finally, it is worth noting that, probably, the first millimetre wave OTSA has been also demonstrated by the Naval Research Laboratory group [*Tulchinsky and Matthews 2001*]. An array prototype of 8 waveguide elements working in the Ka band (26.5GHz-40GHz) has been considered and a squint free range of ±60º has been

proved. Fiber optic stretcher, having resolution better than 0.25ps, are introduced for fine time adjustments. The amplitude and phase-tracking errors have been measured in two different conditions, with or without output MW amplifiers. Good results have been obtained: concerning the amplitude tracking an RMS deviation of ±0.5dB and ±1.8dB, while RMS phase-tracking deviation of ±4.6º and ±8º.

Accordingly, the FOP approach has been demonstrated to be suited also for millimetre wave applications where very stringent time resolution, amplitude and phase tracking requirements are needed.

***Programmable Dispersion Matrix:***

A different architecture, based on the fiber dispersion, has also been proposed [*Tong and Wu 1996a*]. The core of the structure is called the Programmable Dispersion Matrix (PDM) and is shown in Fig.3.16a, while the whole OBFN is shown in Fig.3.16b. The PDM is a dispersive BIFODEL: each stage contains sections of HDFs, having dispersion growing of a factor 2, as shown in Fig.3.16. At the same time, the PDM is designed to be fed by a multi-wavelength laser in order to use only one PDM to drive the whole OTSA. For an N element array, a laser source providing N wavelengths, all intensity modulated by the same MW signal, is used so that the different laser modulated signals realize simultaneously the required delays within the PDM. The different wavelengths are then separated by means of a wavelength division multiplexer (WDM) in order to feed the proper radiating element. In [*Tong and Wu 1996a*] the authors characterized a 2 bit PDM up to 5GHz. A 2D beamformer has been proposed in [*Tong and Wu 1998a*].

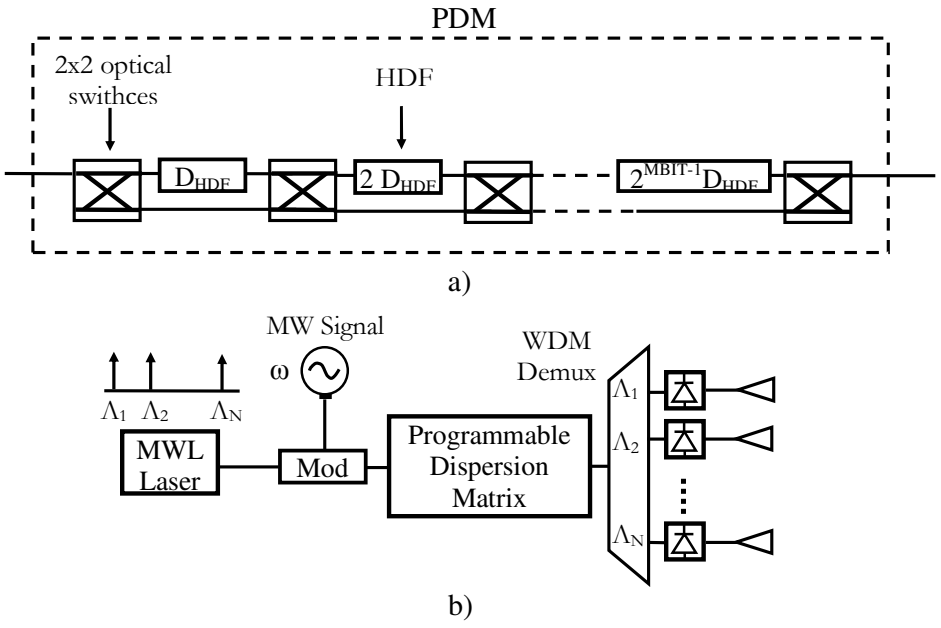


**Figure 3.16** *The PDM architecture: a) PDM b) OTSA based on the PDM*

Unlike the FOP, the PDM does not provide a continuous time delay control but realized a digital TS, avoiding the use of tunable sources. Then, like in the BIFODEL

scheme, the related IL grows with the number of bit. In particular, they estimated that a M bit PDM has an IL of about M+4 dB, provided that the IL of the optomechanical 2x2 switches is 1dB and that the WDM IL is 3dB. Moreover, since each antenna is associated to a specific wavelength, at difference with the FOP, there are no splitting losses related to the signal distribution.

## 3.2 FIBER BRAGG GRATINGS

One of the main problems of the discussed dispersive approaches is, as told before, the thermal stability of the BFN. To overcome this problem, the group at the Naval Research Laboratory suggested chirped FBGs as time delay units in place of the HDFs [*Medberry et al.*; *Roman et al.*]. In fact, as described in the following, by using FBG, fibers with shorter length are employed thus avoiding the thermal stabilisation system. Really, the use of FBG as time delay module for PAA was already proposed, by Ball, Glenn and Morey in the 1994 [*Ball et al.*].

Generally speaking, the FBGs are widely used in the optical control systems for PAA [*Pan and Shi*], to realize tunable laser sources, wavelength division multiplexer and time delay units, we are here mainly interested. Two main approaches have been considered in the FBG delay unit schemes, according to the type of FBG employed: discrete or chirped FBG (CFBG). Discrete FBGs allow to realize discrete time delays, while CFGBs allow for the continuous time control. Initially, time control units based on discrete FBG have been proposed, since chirped FBGs suited for the PAA applications were not available due to realization technique issues. Later, the technology advancements made possible to implement CFGB based time control units.

***Discrete gratings:***

The first scheme, proposed in [*Ball et al.*; *Molony et al.*] uses discrete FBGs distributed along the length of a single fiber at proper distances, individually addressed by varying the laser wavelength (Fig.3.17). In this way different time delays are achieved due to the different position of the selected FBG.

The maximum delay $\tau_{max}$ can be chosen at will by varying the FBG distance. Moreover, since the delay is due to the round-trip, the fiber length required to realize an assigned delay is half the one of a simple fiber delay line.

The maximum number of attainable delay is equal to the maximum number $N_{g\text{-}max}$ of FBGs that can be used in a delay line. The latter depends upon the laser tuning range $\Delta\Lambda$ and on the optical bandwidth of the FBG $\delta\Lambda$ that depends on the achievable FBG length $L_g$.

In particular we have [*Molony et al.*]:

$$N_{g-max} = \frac{\Delta\Lambda}{3\delta\Lambda}$$
$$\delta\Lambda = \frac{\Lambda^2}{2nL_g} \qquad \text{(III.10)}$$

where n is the fiber refraction index.

Delay lines up to 6 bit seem to be feasible [*Molony et al.*].

Regarding the minimum achievable delay $\tau_{min}$, it depends on the grating spacing $G_d$. In fact:

$$\tau_{min} = \frac{2nG_d}{c} \qquad \text{(III.11)}$$

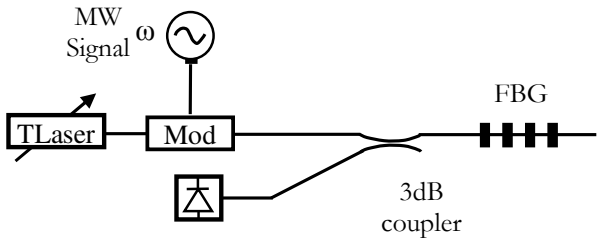


**Figure 3.17** *The FBG delay line*

In particular $G_d$ is set by the FBG length $L_g$. According to Soref [*1996*], the limit is $G_d=0.5L_g$. In this way a $\tau_{min}$ of about 10ps, or some extent lower, can be achieved. This limit affects the maximum frequency of the MW signal to be delayed. In fact, the required minimum delay for two radiators located at a distance equal to half wavelength at the frequency f is:

$$\tau_{min} = \frac{1}{2f}\sin(\theta_{min}) \qquad \text{(III.12)}$$

where $\theta_{min}$ is the minimum steering angle. Accordingly, time steps <10ps can be suited up to 3-4GHz [*Molony et al.*].

The time delay unit losses are essentially due to the coupler/circulator since high reflectivity FBG, over than 90%, can be easily realized. Particular attention has to be taken when realizing the FBGs. In fact, the positioning uncertainty can affect the time delay precision. [*Molony et al.*].

***Fiber Grating Prism:*** An innovative discrete FBG beamformer was proposed by Soref [*Soref 1996*]. He suggested a FBG reflective prism structure, successively realized in [*Zmuda et al.*], where the gratings location is set according to the fixed number of beam configurations to be radiated (Fig.3.18). A tunable laser source is intensity modulated by the MW signal and then divided to feed N fibers, corresponding to the N radiating elements to be fed. Each fiber includes an array of K single frequency FBGs in order to realize the delay distributions for K beams. The separation of the FBG along each fiber depends on the radiating element to be controlled and on the desired beam pointing configuration. According to the used wavelength, the desired gratings are selected to realize the needed time delay distribution. The reflected light signals are driven to the related photodiodes by means of 3dB coupler or circulators located at the output of the FBG prism.

Soref [*1996*] provides the design of the FBG prism considering both discrete and chirped FBG. In particular, he shows how the maximum allowable number of beams decreases with frequency. In fact, by comparing (III.11) and (III.12), we have $G_d=(c/4nf)\sin(\theta_{min})$. Then, by using $L_g=2G_d$ in the expression of the $N_{g\text{-}max}$ we have:

$$N_{g-max} = \frac{c\Delta\Lambda}{3f\Lambda^2}\sin(\theta_{min}) \qquad \text{(III.13)}$$

As consequence, to utilize this BFN from 30GHz to 60GHz, one useful solution is to employ HDFs at the output of the FBG prism. In this way, smaller time steps can be achieved by the subtraction of the two cascaded time-shift profiles, allowing a $\tau_{min}$ of the order of 2ps. An integrated solution has been also proposed [*Soref 1996*].

Regarding the losses, the major contribute is due to the couplers (6dB round-trip). In [*Zmuda et al.*] a FBG prism for three elements and four beams (0º, 30º, 59º and 60º) is demonstrated, by characterizing the FBG achievable delays. The FBG prism requires a tunable laser and as many FBG as the product of the number of required beam configurations and the radiating element number.

A FBG prism using chirped FBG instead of discrete FBG has been also proposed [*Liu et al. 2002a*; *Yang et al.*].

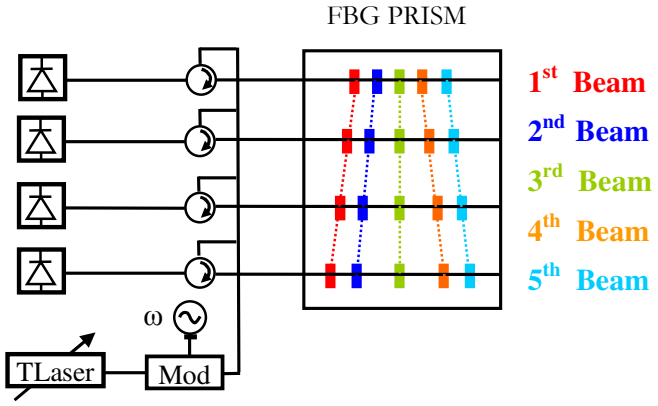


**Figure 3.18** *The FBG prism*

A simpler architecture based on discrete FBGs and a laser operating at a single wavelength has been proposed in [*Ortega et al. 1998*; *Ortega et al. 1999; Ortega et al. 2000a*]. The delay line operates by straining a small part of the grating by means of a magnetic field and a magnetostrictive transducer. The delay is changed by varying the position where the strain is applied. By locating the strain in different position, the grating reflectivity does not vary significantly, while the delay varies linearly with the strain position. Slight oscillations are reported due to the formation of a Fabry-Perot cavity between the uniform sub-gratings existing inside the original grating. The cavity is formed by the ends of the original grating and the section where the strain is applied. By growing the distance of the perturbation, the period of the oscillation decreases while its amplitude increases. For delays up to 350ps, the amplitude variation of the detected MW signal in the range 130MHz-18GHz are below -0.5dB, while the reported time delay fluctuations are under 2ps. Such deterioration can be considered acceptable in the frequency range considered. However, when dealing with more long delays the amplitude of the oscillations could lead to unacceptable errors.

Such a system could, in principle, provide a continuous time delay variation, since the magnet transducer can be placed in arbitrary position along the grating, but as indicated by the authors, in practical systems the actuator can be placed in discrete position with a minimum spacing of about 1mm, leading to a minimum delay of 10ps,

like in previous schemes. The main difference is that in this structure, the number of achievable delays is not limited by the laser tuning range, since single wavelength operation is adopted. Moreover, by using more strain actuators and lasers the system can easily extended to a multiple-beam architecture.

***Chirped Fiber Bragg Gratings:***

When the fabrication technologies allowed the realization of chirped FBG (CFBG) with suited properties, continuously variable TTD OBFNs have been proposed [*Corral et al. 1997a*; *Cruz et al. 1997; Cruz et al. 1998; Roman et al.*].

CFBGs are obtained by changing the period of the refraction index profile. A linear CFBG has, in fact, a refraction index whose period increases along the structure. It could be considered made up of a series of smaller FBG increasing in period. In this way a broadband reflector can be realized: the light signal is reflected by the CFBG section having the proper period. By changing the source wavelength, the reflection point within the FBG can be varied continuously, thus realizing a continuous time delay variation.

The delay properties are estimated once the CFBG main characteristics are known. These are the grating length $L_g$, the grating bandwidth $\Delta\Lambda$ and the group-delay slope $\delta$, usually measured in ps/nm. The achievable $\tau_{max}$ is, in principle, limited to about $2\Delta\Lambda\delta$, while the $\tau_{min}$ depends on the laser tuning resolution.

In Fig.3.19 the scheme of an OBFN based on a CFBG delay unit able to realize continuous time delay control for a PAA is depicted [*Corral et al. 1997a*]. The delay unit is made of a very wide-bandwidth single CFBG that allows driving contemporaneously many antenna elements. In particular each element is controlled by a tunable laser with a narrow tuning bandwidth.

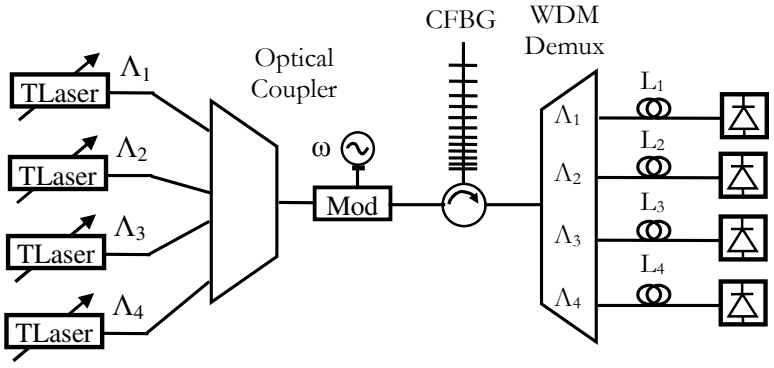


**Figure 3.19** *The CFBG architecture*

For a linear CFBG the delay response is, nominally, assumed linear with the wavelength, as shown in Fig.3.20. The different optical carriers thus experiences different delays that can be independently controlled by imposing a wavelength shift on each carrier. The delayed modulated optical signals are then separated, by means of a wavelength division multiplexer in order to feed the assigned radiating element. Extra fibers, with proper length for each element, have to be used to compensate for the time delay among the different modulated optical carriers, due to the CFBG group-delay response $\delta$. In particular, the length $L_i$ relative to the i-th element is given by [*Corral et al. 1997a*]:

$$L_i = \delta\left(\Lambda_i - \Lambda_1\right)\frac{c}{n} \qquad \text{(III.14)}$$

where c is the velocity speed in the vacuum, $\Lambda_i$ is the wavelength relative to the i-th element and n is the fiber refractive index.

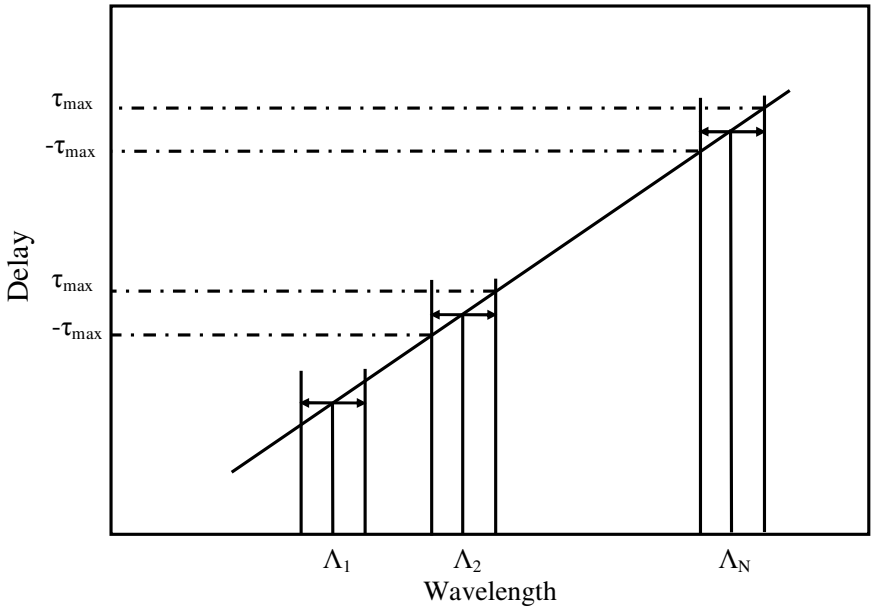


**Figure 3.20** *The CFBG ideal group delay response*

Before we discuss about the system main issues, some observations are in order.

The scheme in Fig.3.19 is the single CFBG architecture. A similar scheme can be realized by using more CFBGs, one for each radiating element, and only one laser. The one CFBG scheme, allows to reduce not only the number of time control units, but also the time delay inaccuracies caused by the position mismatches obtained when using more gratings. However, this choice requires the use of a wavelength demultiplexer or bandpass filter to separate the different channel assigned to each radiating element. Nevertheless, this scheme, unlike the architectures based on discrete FBG or on the FOP, allows any possible antenna element phase distribution, not just a linear phase one. This feature makes the system suitable for advanced beam control techniques that find more applications than the only beam steering.

On the contrary, the architecture using more CFBGs (Fig.3.21), reduces the number of laser sources and avoids the use of a wavelength demiltuplexer, and can be easily extended to the multi-beam mode by using more lasers [*Bratchikov 2000*]. The CFBGs length increases linearly from the first to the last radiating element, thus realizing progressive increasing delays, at the same wavelength, across the antenna elements. By using more lasers, different time delay distributions are obtained contemporarily, thus driving different beams.

In the following we consider the design issues related to the architecture using one CFBG as time control unit, since in this case more design aspects have to be clarified. The issues in the case of the architecture using many CFBGs can be easily derived from the ones discussed in the following.

One of the key parameters of the CFBG architecture is the maximum allowable number of radiating elements $N_{max}$ driven by one CFBG. This parameter depends on CFBG bandwidth $\delta\Lambda_{CFBG}$ and laser tuning range adopted for each wavelength channel. Assuming that the adjacent channel separation is equal to one and half times the laser tuning range $\Delta\Lambda$ used for each element, the maximum number of drivable elements is $N_{max}=\delta\Lambda_{CFBG}/1.5\Delta\Lambda$. On the other hand, the laser range $\Delta\Lambda$ is set in order to realize the maximum delay $\tau_{max}$ required to steer the antenna beam up to the maximum beam pointing angle $\theta_{max}$. In other words we have:

$$\Delta\Lambda = \frac{\tau_{max}}{\delta} = \frac{(N_{max}-1)d\sin(\theta_{max})}{c\delta} \qquad \text{(III.15)}$$

Then, the $N_{max}$ becames:

$$N_{max} \simeq \sqrt{\frac{\delta\Lambda_{CFBG}\, c\delta}{1.5d\sin(\theta_{max})}} \qquad \text{(III.16)}$$

where the group-delay slope $\delta$ has been assumed constant along the whole grating bandwidth. Accordingly, to drive large array with one grating, CFBGs having a wide bandwidth or an high group-delay slope are required.

The $\delta\Lambda_{CFBG}$ grows with the grating length, that is rapidly increasing thanks to the fabrication techniques improvements. In their experiment [*Corral et al. 1997a*], the authors used a 40-cm linear CFBG, with a $\delta\Lambda_{CFBG}$=4nm and a mean group-delay slope $\delta$=835ps/nm. Accordingly, by considering an antenna design frequency of 5GHz, and half wavelength spacing d=3cm, a $\theta_{max}$ of about ±45°, a maximum number of six element can be driven.

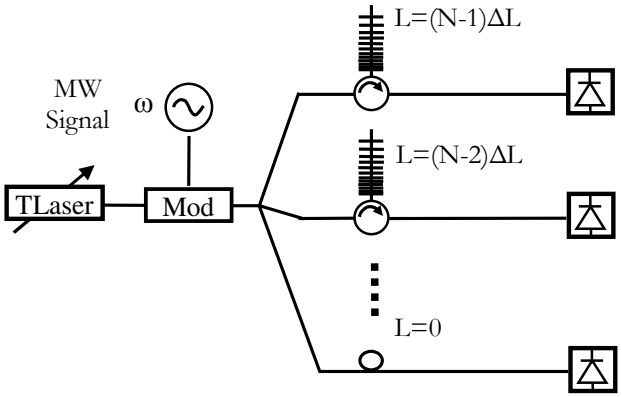


**Figure 3.21** The CFBG architecture using more CFBG units

Regarding the $\delta$, higher slopes while leading to increase the $N_{max}$, require a more strict laser tuning range and, therefore, and higher laser wavelength stability $\Delta\Lambda_s$. In fact, when dealing with a high $\delta$, little variation of the laser carrier produces high time delay errors. Moreover, the group-delay slope can not be assumed exactly constant across the $\delta\Lambda_{CFBG}$, but it is worth to measure the time-delay response in the grating bandwidth. In this way, the group-delay slope $\delta_i$ for the i-th channel/element can be estimated.

This difference among the ideal and the real time delay response allows us to discuss about an important system issue: the time delay errors reported within the CFBG control unit. As mentioned, the main error contributes are the CFBG time delay response deviation $\sigma_{CBFG}(\Lambda_i,f)$ from the linear slope, for each channel and radiating frequency f considered, and the time deviation induced by the laser stability, for each channel, $\sigma_{LASER}(\Lambda_i)= \Delta\Lambda_s\delta_i$. As consequence, time delay precision of the total system can be estimated as:

$$\sigma^2_{TOTAL}(\Lambda_i, f) = \sigma^2_{LASER}(\Lambda_i) + \sigma^2_{CFBG}(\Lambda_i, f) \qquad \text{(III.17)}$$

In [*Corral et al. 1997a*], a laser wavelength stability of 0.01nm and a maximum mean $\sigma_{CBFG}$ of about 9ps are reported. A time delay precision of about 8.94ps has been obtained, corresponding to a 16.1º phase error at 5GHz like a 3.5 bit digital PS. The main error term is due to the laser stability. Accordingly, it could be useful to reduce the $\delta$, although this reduces also the $N_{max.}$ A trade-off among the antenna size and time delay error has to be faced off.

The last design issue regards the adopted modulation scheme. In fact, like in the FOP, for classical modulation scheme where a double side band plus carrier are transmitted (DSB+C), the amplitude of the detected signals varies with frequency. The MW signal power modulating term is [*Corral et al 1997*]:

$$G_{CFBG} = 20\log_{10}\left(\cos\left(\frac{\pi\delta\Lambda_C^2 f^2}{c}\right)\right)\ [dB] \qquad \text{(III.18)}$$

where $\Lambda_C$ is the wavelength at the CFBG bandwidth centre.

Accordingly, the 3dB signal bandwidth is given by [*Corral et al 1997*]:

$$f_{3dB} = \sqrt{\frac{c}{4\Lambda_C^2\delta}} \qquad \text{(III.19)}$$

This problem has been widely discussed by different authors that treated the CFBG BFNs [*Corral et al. 1997*; *Corral et al. 1999a; Corral et al. 1999b; Ortega et al. 1998; Ortega et al. 2000b*]. In fact, for DSB+C modulation each sideband experiences different delay according to the frequency separation and the group-delay slope. When this time delay difference is a radiofrequency period, a destructive interference between the sidebands is obtained thus determining a null in the detected signal.

To show this problem, we assume that the CFBG has response $H(\Omega)= |H(\Omega)|e^{j\eta(\Omega)}$, flat in amplitude and parabolic in phase around the CFBG bandwidth centre $\Omega_C$. In particular we have:

$$\begin{aligned} &\left|H(\Omega)\right| = 1 \\ &\eta(\Omega) = \eta_0 + \eta_1(\Omega - \Omega_C) + \frac{\eta_2}{2}(\Omega - \Omega_C)^2 \end{aligned} \qquad \text{(III.20)}$$

where $\eta_0$ and $\eta_1$ are the insertion phase and group time delay at $\Omega=\Omega_C$, respectively, and $\eta_2$ is the first order dispersion term. The last term represents the slope of the CFBG time response versus the MW signal frequency. In fact, the time delay obtained is given by [*Corral et al. 1999b*]:

$$\tau(\Omega) = \frac{-d\eta(\Omega)}{d\Omega} = -\eta_1 - \eta_2(\Omega - \Omega_C) \qquad \text{(III.21)}$$

Accordingly, the term $\eta_2$ is related to the CFBG group-delay $\delta$ by:

$$\eta_2 = \frac{-\Delta\tau}{\Delta\Omega} = \frac{\Lambda_C^2}{2\pi c}\frac{\Delta\tau}{\Delta\Lambda} = \frac{\Lambda_C^2\delta}{2\pi c} \qquad \text{(III.22)}$$

In particular, let us consider a DSB+C modulation scheme, with an external MZM biased at the quadrature point with a modulation index $m=\pi V/V_\pi$, where V is the amplitude of the modulating MW signal and $V_\pi$ is the voltage required for 100% modulation. The photodetected current is [*Corral et al. 1999b*]:

$$i_{DSB} \propto \sum_{n=0}^{\infty} J_{2n+1}(m) J_{2n}(m) \cos\left((4n+1)\frac{\eta_2}{2}\omega^2\right)\cos\left(\omega(t-\eta_1)\right) \qquad \text{(III.23)}$$

where $\omega$ is the modulation frequency.

For low modulation indexes, the detected current is:

$$i_{DSB} \propto m\cos\left(\frac{\eta_2}{2}\omega^2\right)\cos\left(\omega(t+\eta_1)\right) \qquad \text{(III.24)}$$

To overcome this problem, the single sideband (SSB+C) or the pseudo self-heterodyne (PSH) modulation schemes have been proposed (Fig.3.23). A wide discussion about both schemes can be found in [*Ortega et al. 2000b*]. Here we report the results related to the simple case of the low modulation indexes approximation.

In the case of SSB modulation, the detected current signal for low modulation index is:

$$i_{SSB} \propto \pm\frac{m}{2}\cos\left(\omega(t+\eta_1) \pm \frac{\eta_2}{2}\omega^2\right) \qquad \text{(III.25)}$$

where the sign uncertainty corresponds to the upper or lower single sideband modulation. Then, the amplitude does not vary with the frequency. On the contrary, at an higher modulation index, an amplitude ripple appears.

In the case of PSH, the tunable laser light is intensity modulated by an intermediate frequency $f_{IF}$, with modulation index $m_{IF}$, and then is up-converted by a local oscillator MW signal at frequency $f_{LO}$, biased at its minimum bias point and with modulation index $m_{LO}$. The detected signal is at frequency $f= 2f_{LO}+f_{IF}$. For low modulation indexes, the detected current is:

$$i_{SSB} \propto m_{IF}\cos\left(\frac{\eta_2}{2}\omega_{IF}\omega\right)\cos\left(\omega(t+\eta_1)\right) \qquad \text{(III.26)}$$

Accordingly, under low level signal approximation, the SSB modulation does not suffer of bandwidth limitations. The time unit performances are highly sensitive to the MW level at the MZM input. Moreover, the optical chromatic dispersion of the CFBG is translated to the RF signal, making the time delay grows linearly with the frequency with a slope equal to $\eta_2$. An electrical delay equalizer is, then, required to ensure the correct behaviour.

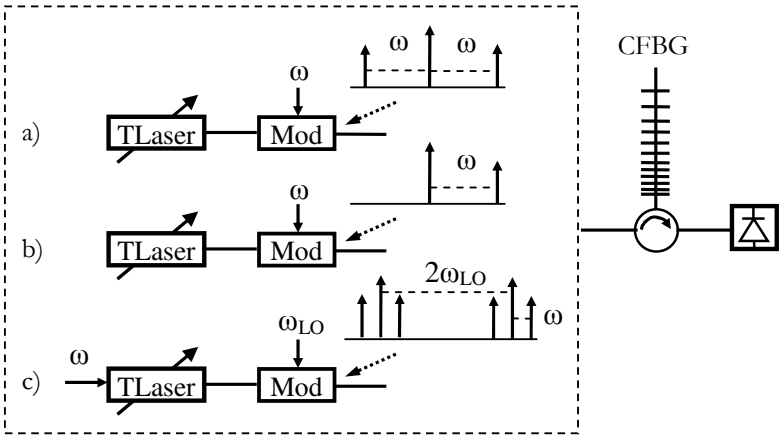


**Figure 3.22** The CFBG architecture with different optical modulation schemes: a)DSB+C b)SSB c)PSH

On the other hand, the PSH scheme is limited to narrow/medium band applications and presents higher losses due to the two stage modulation, but the time delay is not affected by the LO level and does not present dispersion.

Other CFBG architecture have been proposed in [*Medberry et al.; Yao et al. 2002a; Yao et al. 2002b*]

***CFBG Strain Tuning:***

Like for discrete FBGs, also for CFBGs the time delay control can be achieved using a proper strain system, thus avoiding the tunable laser sources. In [*Liu et al. 2002b*] the time delay response of a CFBG is changed by varying the chirp rate by means of the tuning setup showed in Fig.3.23. A multi-wavelength laser is used in place of N tunable lasers. A uniform wavelength spacing $\Delta\Lambda$ is adopted. The grating is surface-mounted on one side of a simply supported beam. The beam is bent under a load P applied at the point O. The time delay difference reported under a beam deflection h, shown in Fig.3.23, is given by:

$$\Delta\tau = \frac{\tau_0 \Delta\Lambda}{kh} \qquad \text{(III.27)}$$

where $\tau_0$ is the whole time delay of the CFBG, k is a constant determined by the beam parameters. A band pass filter is used for each channel, since only one CFBG has been employed. A minimum delay step of about 1ps can be achieved thank to the high precision resolution of the actuators.

Another example of CFBG time delay tuning by means of the control of the strain and temperature distribution across the grating is reported in [*Italia et al. 2005*]

Apart from the two discussed feeding architectures, using one or more CFBGs, different approaches have been proposed. In [*Tong and Wu 1996b*], the PDM approach has been extended by using FBGs in place of the HDFs.

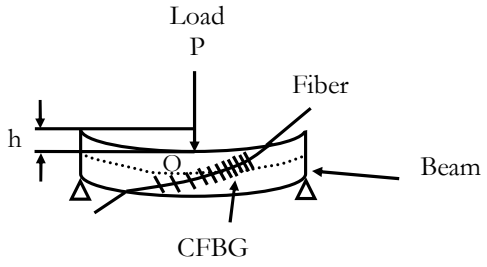


**Figure 3.23** The FBG chirp tuning setup

***Serial Feed Architecture:*** In [*Cohen et al.*; *Chang et al.*; *Tsap et al. 1998*; *Fetterman et al.*] an interesting feed architecture, called the serial-feed scheme, has been proposed. The OBFN implementation scheme is depicted in Fig.3.24. The system, proposed for radar, communication and electronic warfare applications, is made of a timing unit and a tapped optical delay line.

The timing unit is composed of a fast broadband tunable laser, followed by an optical modulator. The modulator is driven by a gated RF signal that modulates the intensity of the light signal with the desired wavelength and is gated at a suited RF pulse width. For N radiating elements, N pulses, each with the desired wavelength, are sequentially generated by the timing unit.

The pulse train is directed to a FBG delay unit: the wavelength of each pulse sets the related time delay. Accordingly, the reflected pulses, properly delayed, enter the tapped delay line. This is a fiber with equally spaced taps, each connected to the detector of the proper radiating element. At the output of each detector there is a microwave switch (Xmit gate) controlled by a gating signal that is used to let the MW detected signals to simultaneously feed the radiating elements.

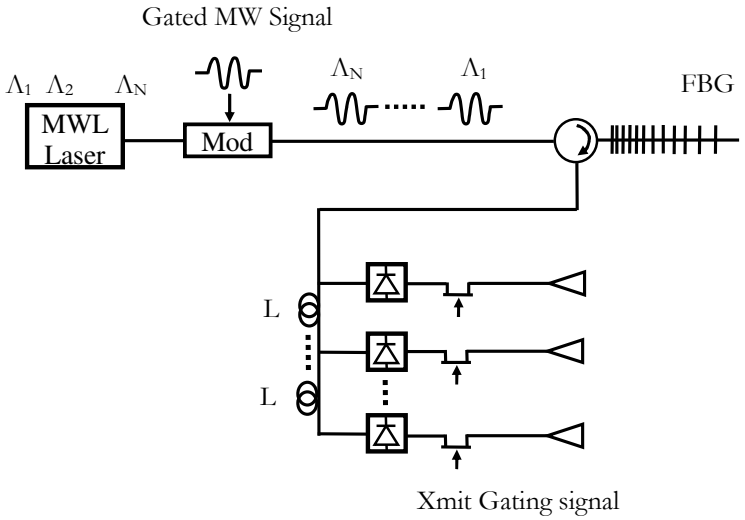


**Figure 3.24** *The serial feed architecture*

The optical delay lines acts as a storing element, since the optical propagation among the taps corresponds to the length of the longest radiated pulse, in order to make all the pulses arrive simultaneously to the related detector: the first pulse is intended for the N-th element, while the N-th pulse is for the first element. Accordingly, when the tapped line is fully loaded, the MW signals at the output of the photodetectors are simultaneously gated on with the MW switches. The signal is radiated and then the switches are turned off and the tapped line is reloaded. The beamsteering properties depend upon the laser available wavelengths and on the FBG specifications.

A demonstration using a two radiating elements OTSA has been done in [*Cohen et al.*; *Chang et al*], considering five beam pointing direction, while the receive mode has also been proved in [*Tsap et al.*], by using the OBFN as local oscillator to achieve the mixing with the received signals, as described in Section 3.1.2 of the 1st Chapter (Fig.1.17).

## 3.3 ARRAYED WAVEGUIDE GRATINGS

The last class of dispersion based delay lines uses AWG as dispersive element to realize the time control. In the 1996 the research group at the University of California proposed a novel wavelength selective TTD unit, realizing and characterizing an 8 channel AWG arranged in a symmetric feedback configuration [*Yegnanarayanan et al. 1996*]. The time control unit scheme is shown in Fig.3.25. The light of a tunable laser source, after being properly modulated by the MW signal, enters the AWG. According to the laser wavelength, the light signal is steered by the waveguide grating to the appropriate AWG output. The signal, then, propagates through a fiber or an integrated waveguide, whose length is chosen according to the desired delay, and is fed back into the AWG symmetric input port. Accordingly, the light signal is steered toward the common output port and is, then, photodetected.

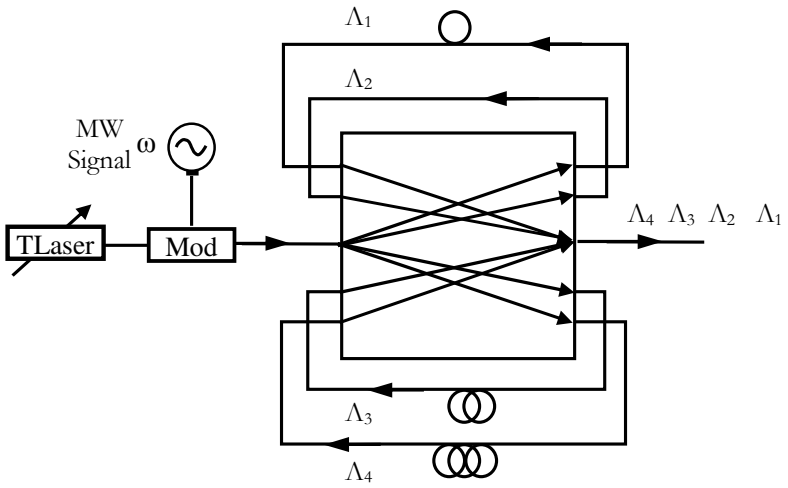


**Figure 3.25** *The AWG wavelength selective time delay unit*

The described structure realizes a digital time control unit of a single radiating element. According to [*Yegnanarayanan et al.1996*] 6-8 bit delay lines can be obtained in compact integrated devices. The reported IL, except for the direct path is given by $IL=2IL_{AWG}+IL_C$, where $IL_{AWG}$ is the AWG loss per channel and $IL_C$ is the loss related to the coupling with the external delay lines. In [*Yegnanarayanan et al.1996*], an 8 channel AWG based on the silica waveguide technology, operating in the 1.5μm wavelength range, with 0.8nm channel spacing and 6.4nm free spectral range has been realized. The reported mean $IL_{AWG}$ is about 6dB, while the crosstalk is about 26dB. An important issue for such scheme is the spectral AWG stability. In fact, temperature variation induces changes in the refractive index of the AWG waveguides, thus varying the spectral response. In the case of silica AWG a thermal shift of 1.03GHz/ºC has been reported, showing a good thermal stability. Nevertheless, in extreme temperature condition, a thermal stabilization system has to be employed.

A 3 bit integrated AWG structure, using silica integrated waveguides in place of fiber delay lines, has been reported [*Yegnanarayanan et al. 1997a; Yegnanarayanan et al. 1997b*].

In [*Yegnanarayanan and Jalali; Jalali and Yegnanarayanan*] a novel 2D architecture based on the described AWG delay unit is presented (Fig.3.26). Like for the 2D HDF scheme (Fig.3.15), there is an azimuth control stage that drives the array columns, provided with an elevation control. The main difference is that the azimuth outputs signals are not downconverted, as in the HDF architecture, but they experience a wavelength conversion and, then, enter directly the array column modules avoiding the optical-electrical-optical conversion. The wavelength conversion is realized by means of a semiconductor optical amplifier [*Yegnanarayanan and Jalali; Jalali and Yegnanarayanan*].

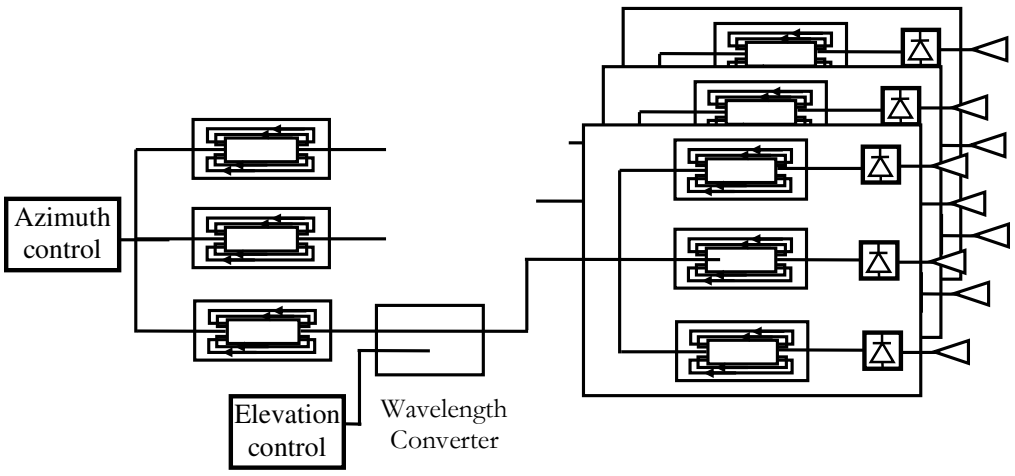


**Figure 3.26** *The AWG 2D architecture using a wavelength conversion*

Finally, Vidal et al. [*2002a; 2002b*] suggested to modify the AWG scheme to feed an entire PAA with one AWG and realize multiple beams. They proposed to use HDF and multiple simultaneous wavelengths to realize multiple simultaneous delays. A wavelength demultiplexer is used to deliver the proper signals to each antenna

element. The antenna beam steering is controlled by tuning each laser wavelength or switching among different wavelength sets. Multiple contemporaneous beams can be radiated by using simultaneously the different wavelength sets.

In Fig.3.27 we report the VPVL schemes we described in this chapter. Here we use the label C for the systems providing continuous time delay, and the label D for system providing discrete time delay control. Moreover, we use the label A when the time steering has been proved, and report the related details.

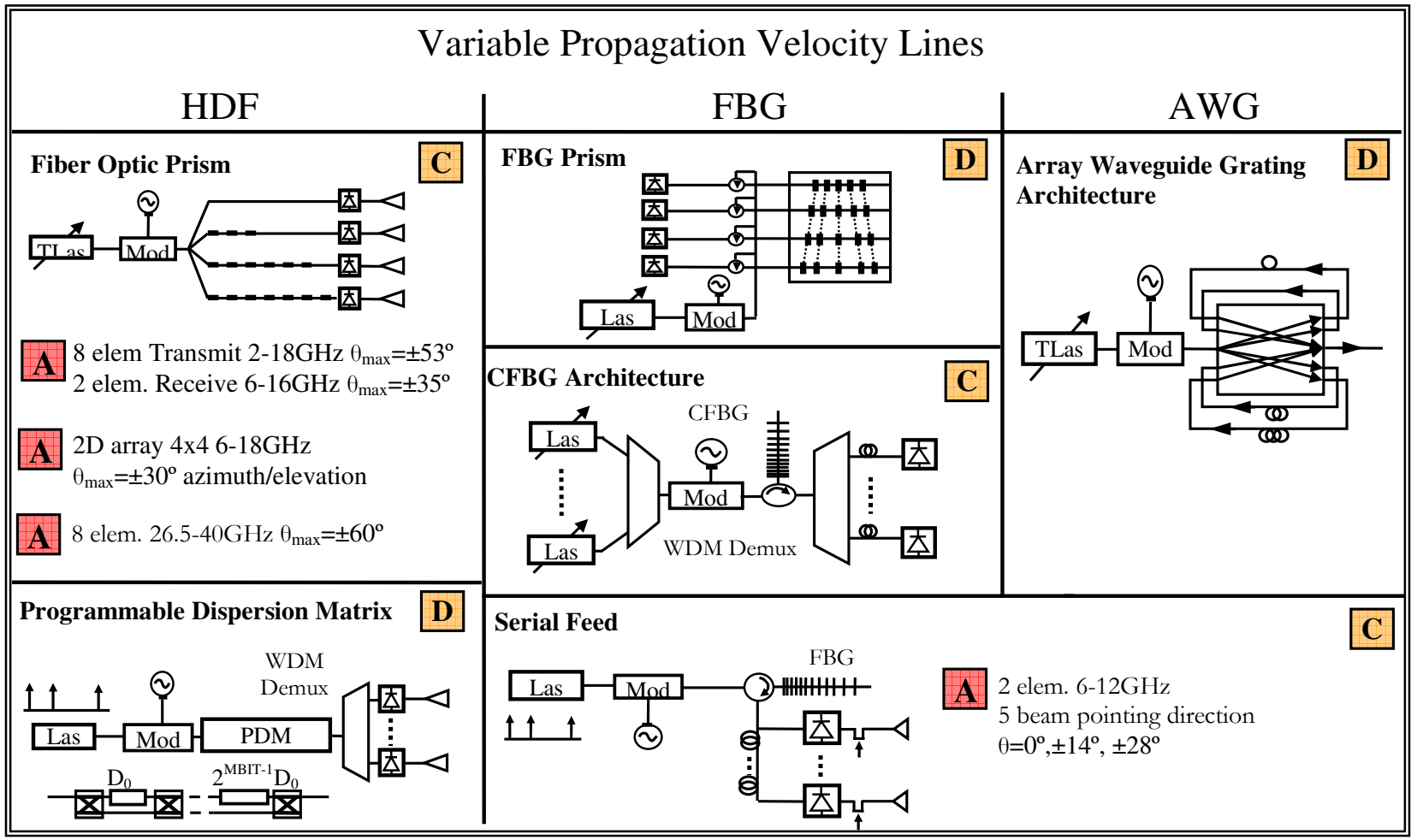


**Figure 3.27** *VPVL summary frame*

# 4 HARDWARE COMPRESSIVE ARCHITECTURES: WDM

The implementation of very large PAA, realizing, eventually, more contemporaneous beams, represents a hard task in term of cost and implementation difficulties, and requires a very bulk and heavy control system. Beside the benefits due to the optical technology, this drawback represents a serious problem for the optical control systems too.

For example, to show how difficult can be the realization of an OBNF for large antennas, we would like to focalize the attention of the reader on a OBFN proposed to realize multiple fixed beams [*Cardone*]. The author suggested a fiber optic Rotman lens for multiple staring beams applications: optical fibers, with proper length, were used to realize the multibeam OBFN. The architecture scheme for a linear array with N radiating elements, working in the receive mode, is depicted in Fig.3.28.

The MW signals received from the antenna elements modulate the laser signals. The modulated light signals are divided among K different fiber delay lines whose length is set according to radiating element position and the desired pointing angle of the m-th beam. Accordingly, the fibers corresponding to one beam pointing angle are combined by means of a 1:N combiner. The OBFN is divided in K subsets of N fixed length fibers.

The hardware complexity of this scheme grows linearly with the number of elements N and the number of beams K. Accordingly, the architecture results impractical for medium or large antenna systems.

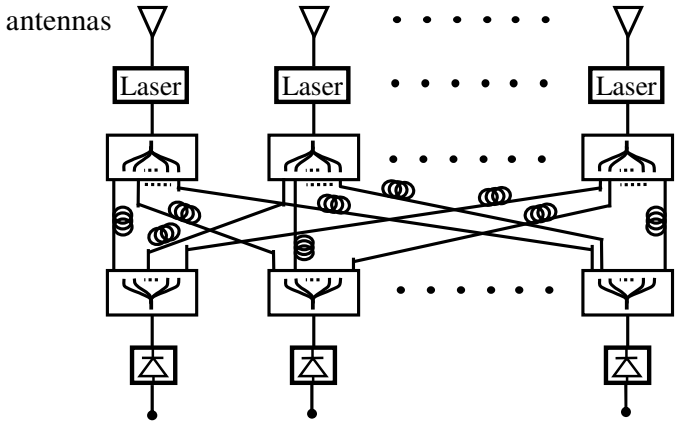


**Figure 3.28** *Fiber optic TTD multi beam BFN*

Obviously, also when using OBFN realizing a single steering beam, the hardware complexity grows linearly with N and with the complexity of the time shifters employed to drive each OTSA element.

Regarding the time shifter, the hardware complexity issue has been already discussed, when presenting the different SDL schemes. To reduce the complexity of the time delay line unit proper delay line compressive architectures have been proposed. It was observed that, a serial architecture, such as the BIFODEL, can

guarantee a good hardware reduction with respect to the PADEL scheme, although in the first architecture the overall IL grows with the number of bits.

However, when dealing with large antennas, it would be preferable not only to employ time shifters having as low complexity as possible, but also to reduce the number of time shifter employed.

In turn, a module compressive strategy is needed.

The most important, and probably the first module compressive strategy, using the WDM, was proposed by Goutzoulis and Davies [*1990*]. Other interesting approaches have been afterwards developed. Here we discuss about:

- WDM compressive techniques
- Coherent detection techniques

Before we present these approaches, it is useful to enlighten, among the architectures previously described, the most interesting schemes regarding the overall hardware reduction. Regarding this aspect, interesting architectures are the FOP, the PDM and the OBFN based on CFBG.

Let us consider an N element array. The FOP exploits one tunable laser and N dispersive fiber links and realizes a continuously variable time delay control. In this way each fiber link replaces the time delay unit, for example a B bit BIFODEL, thus achieving a considerable hardware reduction. Unfortunately, the application of the FOP scheme to large array is limited by the thermal stabilities and amplitude unbalances previously discussed.

The PDM architecture, is based on the unique "wavelength to array element" mapping, like the WDM approach suggested by Goutzoulis et al. In this way, one PDM feeds the entire array, thus reducing the delay elements number. Moreover, since the PDM is arranged in a series fashion, like a BIFODEL, it also reduces the number of delay lines employed. Accordingly, it represents an optical control system well suited for large PAA [*Tong and Wu 1998a*; *Tong and Wu 1998b*].

The same working scheme is used in the CFBG structure adopting multiple tunable laser sources and a WDM demultiplexer. In this architecture one CFBG delay unit drives an entire array.

***WDM Approach:*** The basic idea of the WDM approach is, then, to use one time delay unit to drive more radiating elements corresponding to different wavelength channels. Moreover, to save the hardware employed, the array is partitioned in subarray: the N elements are divided in E sets of M elements, such that N=EM. It could be easily seen that the time delay $T_{ji}$, required by the i-th element of the j-th set is equal to the time delay $\tau_i$ required by the i-th element of the first set, also called the reference set, plus a constant bias delay equal to (j-1) time the delay $\tau_M$ related to the last element of the first set. Accordingly, we have:

$$\tau_{ji} = \tau_i + (j-1)\tau_M \qquad \text{(III.28)}$$

This partitioning of the time delay distribution, described in Fig.3.29, represents the base of the WDM hardware compressive architecture [*Goutzoulis and Davies 1990*]. In fact, the whole time delay distribution for the array can be obtained by using M time delay units to implement the reference set, and E delay units to implement the bias delay needed for each subarray.

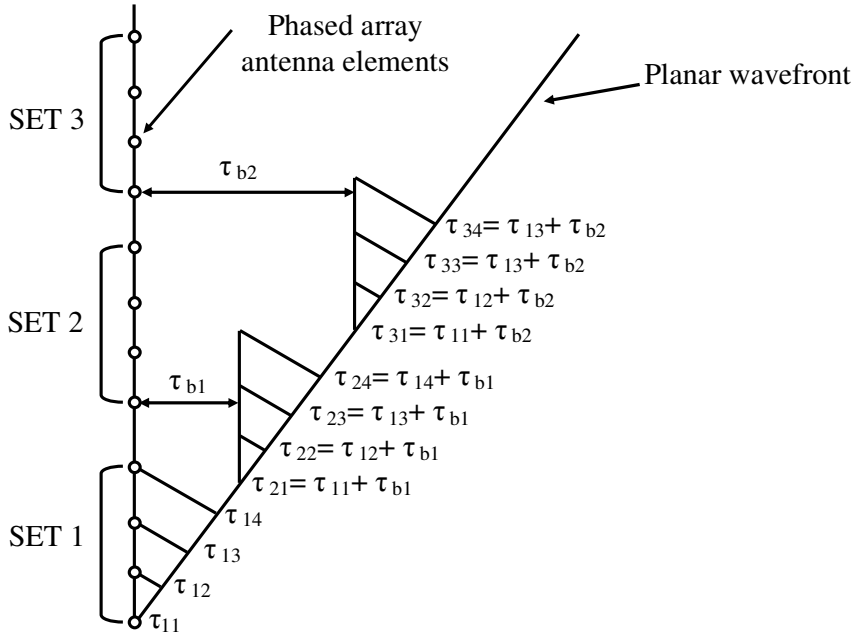


**Figure 3.29** *Partitioning principles for a linear phased array*

The implementation scheme of such architecture is shown in Fig.3.30, where M-1 delay lines, e.g. BIFODEL, operating at M different wavelength $\Lambda_1,\ldots, \Lambda_M$ realize the reference set delays. The delay unit outputs are multiplexed and sent to the E channels corresponding to the antenna subarray. In particular E-1 delay units realize the biasing delay, common to all wavelength channels, for each subarray. The outputs of the biasing delay units feed an optical M-channel demultiplexer needed to assign each wavelength channel to the right antenna element within the subarray.

Since the delays are summed within the beamformer, it could be seem that only positive time slope can be achieved. Instead, the insertion of negative time delay can be realized by properly time-biasing the antenna elements: external delay lines can be used in order that the zero-delay position corresponds to the maximum negative scan angle. In this way the maximum time delay required to steer the antenna beam towards the maximum scan angle $\theta_{max}$ corresponds to the delay required to steer the beam to $2\theta_{max}$. In this way, the broadside beam is achieved when the time delay distribution realizes half of the maximum achievable time delay.

Accordingly, in the case of $M=E=(N)^{0.5}$, the total number of delay units is equal to $2((N)^{0.5}-1)$ instead of N as in the standard non hardware compressive scheme. Moreover, adopting B bit BIFODEL, the overall switch or fiber complexity is given by $2B((N)^{0.5}-1)$. On the other side the insertion loss grows due to the use of two cascaded delay line sections, the introduction of the multiplexer, the 1:E divider and the demultiplexer. The overall IL can be approximately written as:

$$IL = 2(B+1)IL_S + IL_M + IL_C + IL_D \qquad \text{(III.29)}$$

where the first term is due to the cascade of two BIFODEL units, $IL_M$ and $IL_D$ are, respectively the multiplexer and demultiplexer insertion loss, and are about 3.5dB each, while $IL_C$ represents the divider loss about equal to 10log(E). Accordingly, the

hardware compressive architecture introduces additive losses that should be properly compensated to avoid a low SNR.

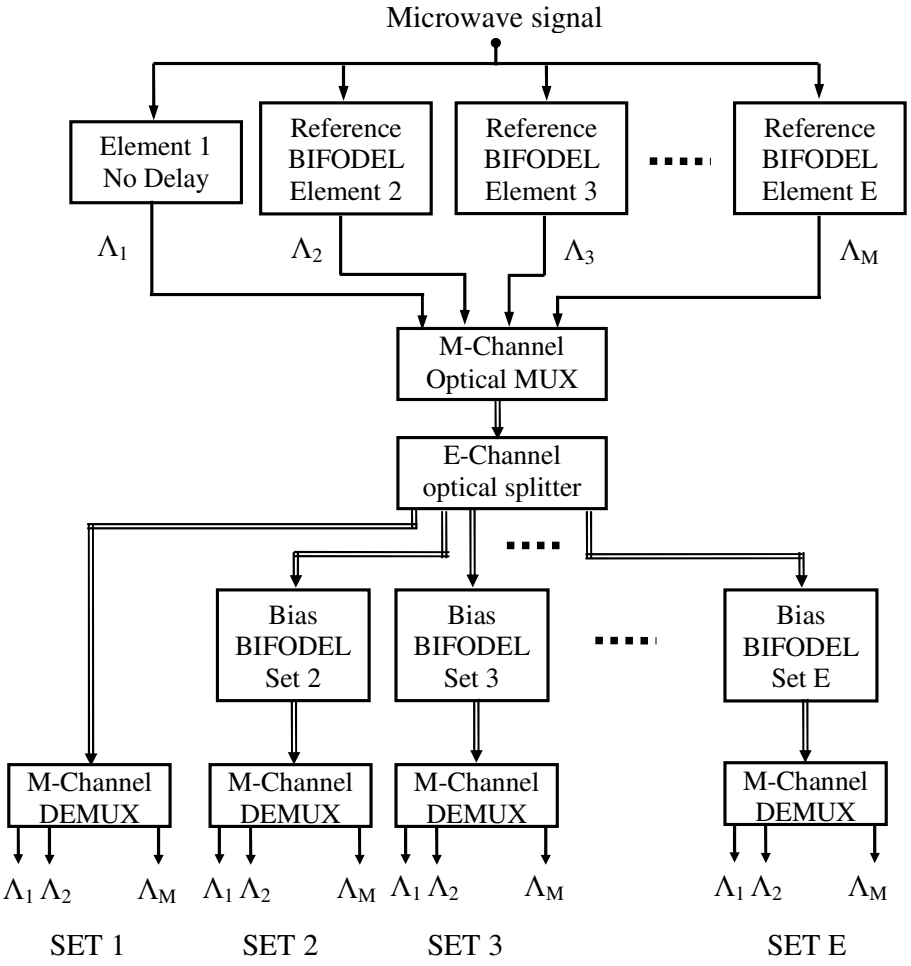


**Figure 3.30** *WDM architecture*

The main drawback of the WDM scheme is represented by the upper limit imposed on the maximum number of channel that can be used to implement the reference set. In fact, this limit is determined by the beat notes between the different wavelengths: the spacing between the wavelengths has to be large enough so that the difference beat note, produced at the detector output, does not fall within the signal bandwidth. About 150 channels operating over a MW bandwidth of 18 GHz are surely possible. A reduction of the system bandwidth could lead to the improvement of the channels number.

Goutzoulis et al. also proposed a hybrid electronic fiber optic wavelength multiplexed TTD architecture, where electronic binary delay lines are used together with fiber optic delay lines. Electronics delay lines, suited up to 3.5-4GHz, offers a low cost and the possibility to realize the reference set in IC form. Accordingly, the electronic delay units, each followed by a laser diode, are used for the reference set, while the BIFODEL are used for the bias delay units. In this way, the WDM

compressive approach is preserved, and the IL reduced, since the cascaded BIFODELs are not used.

In the WDM approach, M BIFODELs, each driven by a laser signal with a different wavelength, are used to realize the reference set delays. Accordingly, the complexity of the reference set delay unit grows with the number of the exploited channels M. To tell the truth, the hardware required to realize the reference set delay unit could be reduced by using one wavelength dependent delay unit, such for example the FOP, the PDM of the CFBG.

***WDM Approach for simultaneous beams:*** The WDM approach has been, successively, extended to the case of multiple beam operation. In fact, the high performance multifunction PAAs require hundred independent and simultaneous beams [*Minasian et al.*; *Minasian and Alameh]*.

A proper strategy is required to deal with the multibeam mode. In fact, to easily extend the WDM architecture, the BFN is replicated for each beam. Obviously, a single delay line is used in place of each programmable BIFODEL. Accordingly, the BFN used for each beam requires about $2(N)^{0.5}$ delay lines, having assumed $M=E=(N)^{0.5}$. The BFN needed to realize K contemporaneous beams requires $2K(N)^{0.5}$ delay lines. Then, for large scale array such a structure requires a prohibitive amount of hardware.

An interesting solution has been proposed to reduce the hardware required when dealing with simultaneous beams. In this approach [*Minasian et al.*], a suited reference set delay unit is proposed, while keeping the WDM architecture unchanged. The scheme of the reference set delay unit is depicted in Fig.3.31. A demultiplexer is used as wavelength path controller to route the different wavelength channels along proper fixed delay paths, in order to generate simultaneously the delays required for the reference set elements. In particular, each of the $M=2^r$ optical signal, with different wavelengths, experiences the proper delay by using only $2\log_2 M=2r$ delay lines.

Accordingly, as shown in Fig.3.31, a 16 wavelength delay unit exploits only 8 delay lines, instead of the 16 delay lines required in the original reference set delay unit.

In this way, the whole BFN needed to realize K beams requires Q delay lines, where Q is given by:

$$Q = K(E+2r) = K\left(\frac{N}{M}+2r\right) = K\left(\frac{N}{2^r}+2r\right) \qquad \text{(III.30)}$$

The minimum value of the integer r that minimizes the total number of delay lines required Q is:

$$r_{opt} = \log_2\left(\frac{N\ln(2)}{2}\right) \qquad \text{(III.31)}$$

The minimum Q is:

$$Q_{\min} = 2K\log_2 N \qquad \text{(III.32)}$$

The corresponding reduction of the optical delay lines, with respect to the standard WDM multibeam approach, is given by:

$$R = 1 - \frac{\log_2 N}{\sqrt{N}} \qquad \text{(III.33)}$$

For example, for N=M=512, a hardware reduction of about 60% is obtained respect to the WDM architecture.

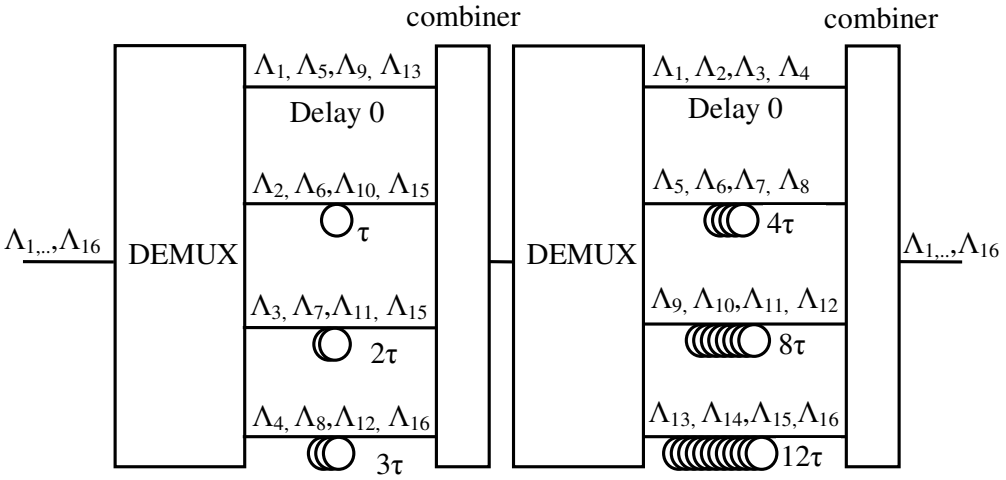


**Figure 3.31** *Wavelength division multiplexed delay unit*

***Coherent Detection Approach:*** The second important approach is the one proposed by Freitag and Forrest [*1993*; *Xu et al. 1995*; *Xu et al. 1996*]. In this architecture there is a unique "wavelength to delay" mapping. All the channels, each with an assigned delay, are simultaneously sent to the whole antenna. The delay selection is obtained by coherent mixing matched wavelengths.

The coherent optically controlled antenna scheme is reported in Fig.3.32. A parallel delay line unit is used to realize all the desired delays. The difference with the conventional PADEL scheme is that there is a different wavelength channel for each delay line. The j-th laser, corresponding to the j-th delay, has optical frequency equal to $\Omega_j$. All the laser sources are intensity modulated by the MW signal. Accordingly for a B bit delay unit, $J=2^B$ transmitter and delay lines are needed. The J signals are combined over a single fiber and sent to the antenna array. Each signal feeds each of the N proper designed coherent receivers [*Freitag and Forrest*], together with a local oscillator laser signal. In particular there are N local oscillator lasers that can be tuned in order to furnish to the considered radiating element an optical signal with frequency $\Omega_j$ corresponding to the desired delay. In this way the desired time delay distribution is selected, thus steering the beam in the proper direction. The system, obviously, needs of a proper frequency stabilization system.

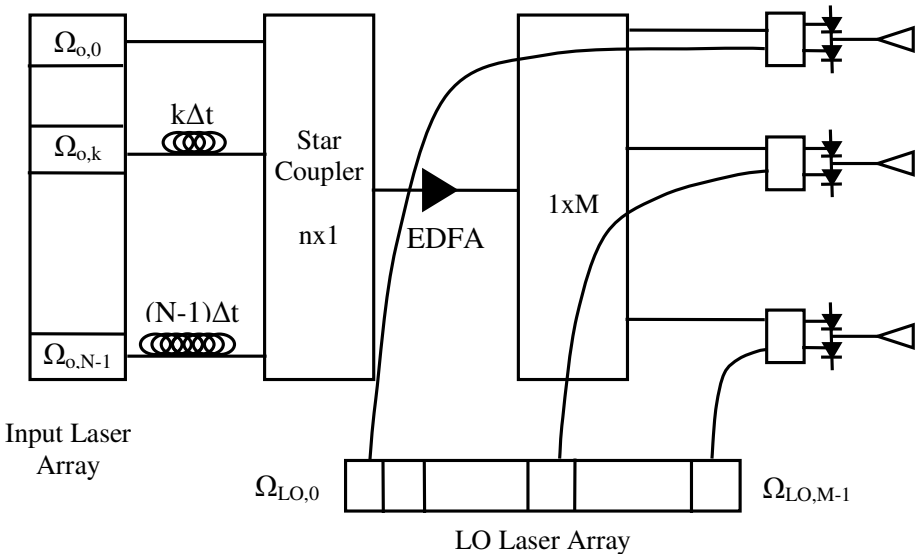


**Figure 3.32** *The coherent optically controlled architecture*

# CHAPTER 4

# THE NEW PHOTONIC TRUE TIME DELAY UNIT

## 2 INTRODUCTION

In this chapter we present the new photonic integrated TTD unit, TTDU in the following, for beam squint free PAA. Then, we show how the TTDU can be efficiently used as a time delay control unit for PAA [*Bucci et al. 2004b; Bucci et al. 2005*]. In particular, different TTDU working configurations have been studied and will be presented. It will be shown that a single TTDU is able to drive PAAs having different characteristics, such as the number of elements or the array design frequency, and allows a flexible tuning of the radiated beam features, such as for example the maximum scanning range and the angular resolution.

Moreover, the working configurations presented in the following have been also optimized to satisfy the main OBFN design issues, such as compactness, hardware complexity and insertion loss.

## 3 THE NEW TIME DELAY UNIT

The TTDU is based on the innovative cross-connect switch presented in [*Fouquet*; *Fouquet et al.*] and realizes a SDL matrix. Its layout is represented in Fig.4.1.

The chip is made by HxH integrated optical waveguides which intersect each other at cross points (the black dots in Fig.4.1).

Let us denote with the index r and s the generic input and output port, respectively. The light entering the input waveguide r can be switched towards the output waveguide s, by means of a driving circuit activating the corresponding cross point (Fig.4.1).

The switching at each crosspoint is made possible by trenches, etched at the waveguide crosspoints and filled with a fluid whose refractive index is matched to the waveguide (Fig.4.2a). To switch the light beam toward the crossing waveguide, a

small bubble is generated at the appropriate crosspoint, by means of a thermal actuator based on the inkjet technology (Fig.4.2b). Since the bubble displaces the liquid, the light beam is reflected toward the crossing waveguide.

Obviously, the light signal delay is due to the optical path corresponding to the switching configuration and can be easily changed by activating a different crosspoint. On the other hand, if no cross points are activated, the light entering the r-th input waveguide passes trough the TTDU and arrives on th r-th "drop" port (Fig.4.1). The "drop" ports together with the "add" ports allow to realize modular structures. In this way, by arranging more basic units, a bigger matrix can be obtained (Fig.4.3). The basic unit is a 4x4 matrix, that is 5 mm wide and 8 mm long [*Fouquet*] and can be used to realize bigger units up to a 512x512 matrix [*Fouquet*]. In Fig.4.3 an 8x8 unit is obtained by arranging the elemental 4x4 modules.

It is worth noting that thanks to its peculiar architecture, the TTDU allows a bidirectional driving strategy.

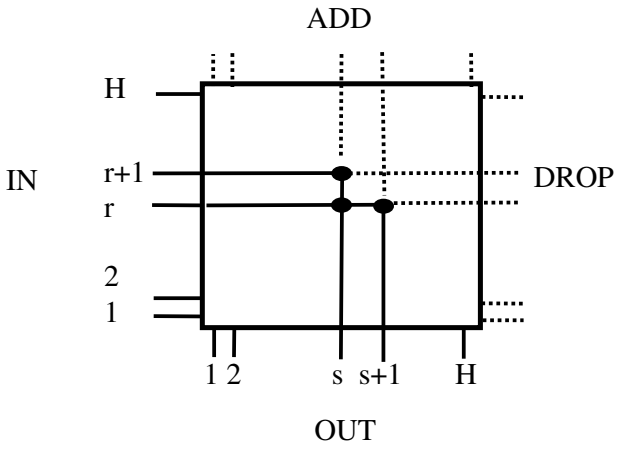


**Figure 4.1** *The TTDU layout*

In order to employ the TTDU to drive a PAA, we need to specify its input-output relationships in terms of delay and insertion loss. In particular, the delay $\tau$ associated to the input-output pair (r,s) is defined by:

$$\tau(r,s) = \tau_{ref} + (r-1)\tau_{\Delta} + (s-1)\tau_{\Delta} \qquad \text{(IV.1)}$$

where $\tau_{ref}$ (equal to zero later on) is the reference delay comprising the connecting fibers delays and the chip entering and output path delay while $\tau_{\Delta}$ (1.5ps) is the elementary delay of the path between two adjacent crosspoints.

The TTDU losses L are obtained from (see Fig.4.1):

$$L(r,s) = 2C + R + (r-1)T + (s-1)T \qquad \text{(IV.2)}$$

where C (0.25dB) is the loss due to the path between the connecting fiber and the first chip crosspoint, T (0.07dB) is the loss due to propagation between two consecutive cross points and R (2.1dB) is the loss related to the reflection at the crosspoint [*Fouquet*].

Moreover, the TTDU allows other interesting features: high reliability, low crosstalk, low switching time (<1ms), and a potential low cost, since it is based on a

low cost technology, the one used for inkjet thermal actuators [*Fouqet et al.*; *Venkatesh et al.*].

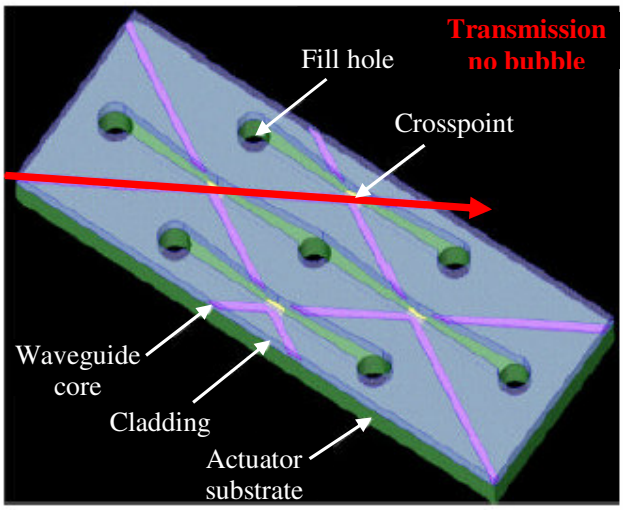


a)

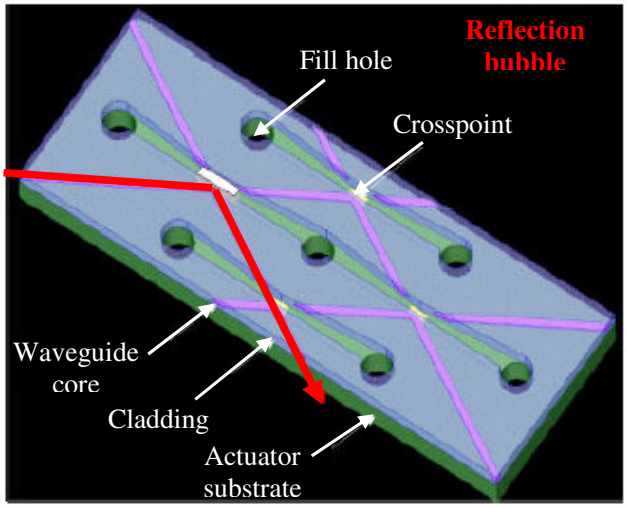


b)

**Figure 4.2** *The TTDU switching mechanism: a) transmission: the light signal passes unaffected trough the crosspoint b) reflection: a bubble is generated at the crosspoint, thus deflecting the light signal towards the crossing waveguide*

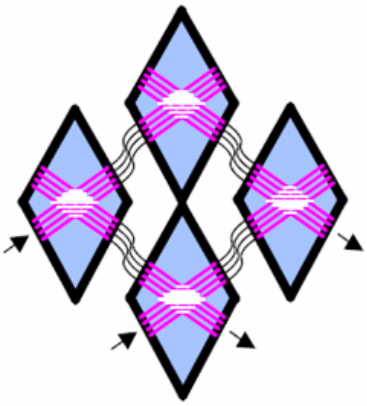

**Figure 4.3** *TTDU modularity: elementary TTDU units can be arranged to realize a bigger module*

# 4 THE TTDU DRIVING STRATEGIES

It will be shown now that the TTDU can be efficiently used as a time delay unit for a PAA.

In particular, the aim of our study has been to introduce a flexible time control system providing an advanced beam control and able to drive antennas with different characteristics, such as the number and the spacing of the radiating elements, and the working frequency.

In fact, in many practical applications it is required the availability of the agile control of the beam pointing angle over a wide scanning range, with an accurate angular resolution while in some cases, only a specified number of beams (also to be radiated at the same time) with fixed beam pointing angles are of interest. A further attractive feature involves the radiation of sum and difference patterns.

Obviously, according to the discussion in the Chapter 1 (Section 1), we are interested in a compact OBFN, with reduced hardware complexity, high reliability, low insertion loss and providing low random errors on the array elements excitations.

The main design requirements are:

- Beam capabilities
  - high spatial scan coverage
  - high angular resolution
  - radiation of fixed beams, also to be radiated at the same time
  - radiation of sum and difference beams
  - ability to drive antennas with different features

- BFN features
  - reduced size and weight
  - compact driving unit
  - low complexity structure – hardware saving
  - low insertion loss IL
  - high reliability

- low random errors

Obviously, to satisfy contemporaneously all these requirements is an hard task. In fact, some requirements are incompatibles. For example, the need for a flexible time delay control requires a more complex and bulky apparatus. Accordingly, a trade-off has to be found.

The OTSA scheme is quite similar to the one reported in the 1st Chapter (Fig.1.14), for an optically controlled antenna. Obviously, a TTD optical network has to be used to realize the time distribution control, according to the results presented in the 3rd Chapter.

In our case the OTSA scheme is based on the TTDU, presented in Section 2, as shown in Fig.4.4. The first three stages represent the Time Phaser (TPH). The TTDU represents the core of the OTSA. Accordingly, its main task is to realize the set of time delay distributions needed to realize the desired beam control. The required time delay distributions set depends on the beam control features and on the PAA properties. On the other hand, the TTDU structure affects the TPH configuration, i.e. the configurations of both the generation and modulation section a) (Fig. 4.4), and of the conversion stage c).

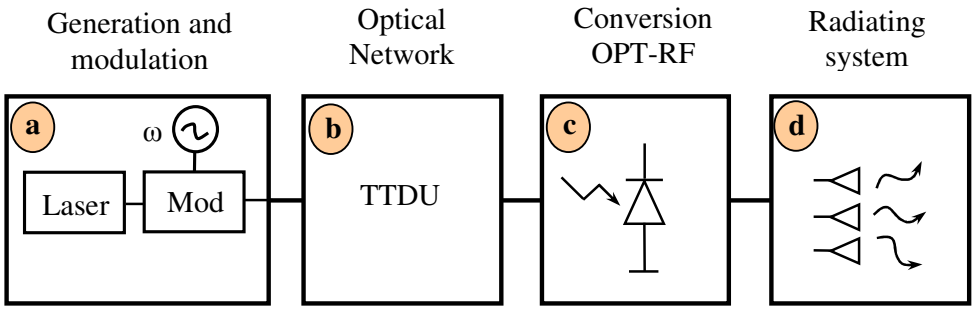


**Figure 4.4** *Layout of the OTSA based on the TTDU*

In principle, the optical network can be made of several TTDU, in number equal to the radiating elements. This solution could improve the beam control performances but increase the system complexity and cost.

Therefore, since the hardware complexity and cost represent important design issues, in the following we will refer to an OTSA driven by a single TTDU, able to drive many radiating element at the same time.

Accordingly, we have to identify the TPH configurations and the TTDU working configurations that optimize the mentioned criteria. In the following we refer to an OTSA prototype driven by a 32x32 TTDU, although bigger modules can be easily obtained, as previously described, when larger PAA with improved performances must be driven.

## 3.1 TIME PHASER CONFIGURATIONS

The TPH layout has to be designed in order to save optical power and reduce size and cost. In particular the stages a) and c) (Fig.4.4) have to be properly designed according to the TTDU working configuration.

In particular, let us first consider the case of a TTDU implementing N TSs, related to N radiating elements. Then, for each TS, the TTDU allows a set of delays, associated to different input-output pairs (r,s), the exploited TTDU inputs and outputs, denoted in the following as active inputs and active outputs.

Accordingly, the first section of Fig. 4.4 must feed all the TTDU active inputs, while the stage c) must drive the delayed signals available at the TTDU active outputs, to the corresponding radiating element.

***SECTION a):*** The section a) includes the laser sources and the modulators needed to drive the TTDU.

In principle, many laser sources and modulators could be employed (see Fig.4.5). For example, the number of the lasers and modulators could be equal to the number of the TTDU input active ports (which depends on the TTDU working mode). A second feeding strategy adopts a number of lasers and modulators equal to the number of radiating elements.

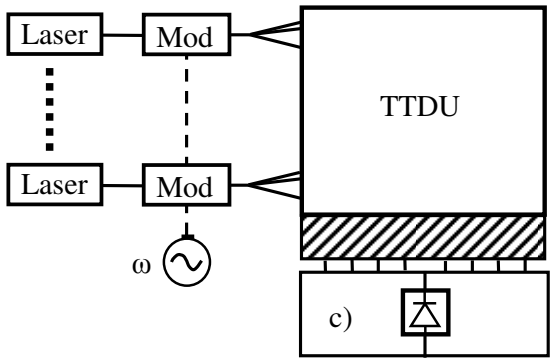


**Figure 4.5** *The stage a) configuration using more lasers and modulators*

In this case, the modulators must be connected to the active input ports of the TTDU by means of a star coupler. If the TTDU working configurations are such that different active inputs are associated to different TSs, integrated star coupler can be employed and the section a) could be integrated with the TTDU, with an increased compactness and reliability.

On the contrary, when the working configuration of the TTDU is such that non contiguous active inputs are used for each TS, fiber couplers must be used.

Both these configurations allow to control the output signal power level, i.e., the amplitude distribution of the excitation coefficients of the array.

However the use of many lasers and modulators increases the system cost that can become prohibitive in the case of large PAA.

A less expensive solution using only one laser, one high speed modulator and an integrated star coupler (ISC) feeding all the TTDU input ports of interest is shown under Fig. 4.6. In this case, a compact input stage is obtained, by using only one star coupler, which can be made by means of integrated optics technology.

However, this configuration does not allow to control the amplitude distribution of the excitation of the array and suffer from a significant drawback: the signal losses are larger than those of other configurations based on the use of a greater number of

lasers. Obviously, the losses can be compensated by suitably introducing amplifying stages along the optical circuit.

On the basis of these considerations, we preferred a solution using a number of laser and modulator as small as possible. In the following the structure reported in Fig.4.6, exploiting a single laser and modulator in the feeding section a), will be discussed.

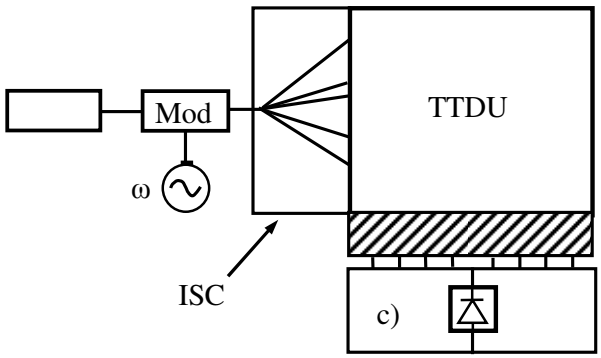


**Figure 4.6** *The stage a) configuration using one laser and one modulator*

***SECTION c):*** Section c) has to drive all the TTDU active outputs, corresponding to each TS, to the corresponding photodetector, whose downconverted signals will feed the associated radiating element.

In principle, it could be possible to use a photodetector for each active output. The detected signals associated to the same radiating element can be transferred to the element by means of a MW coupler or a switch. However, such a solution increases the system complexity and cost and, despite the advantage of the possible integration with the TTDU, is not of practical interest.

On the other side, if the TTDU working configuration exploits contiguous output ports for each TS, ISCs can be used to feed each photodetector, as shown in Fig.4.7a.

On the contrary, when the output port corresponding to each TS are non contiguous (Fig.4.7b), fiber couplers must be used. However, as shown in the following, better performances can be obtained with this configuration.

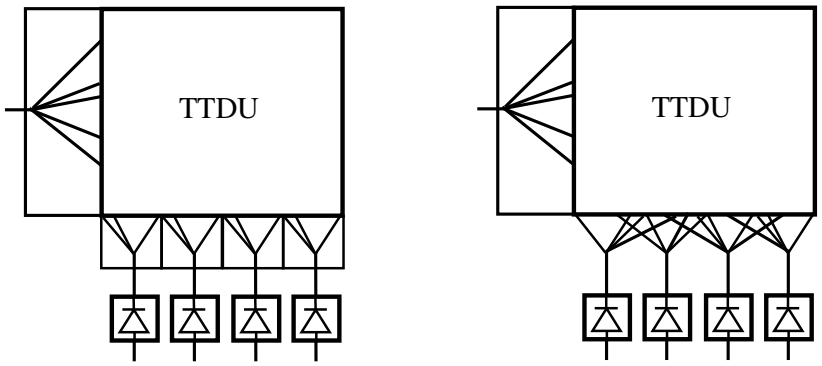


**Figure 4.7** *Output grouping criteria: a) Contiguous outputs b) non contiguous outputs*

As a final remark it must be noted that only the TTDU IN and OUT ports have been considered in the previous schemes reported in Fig. 4.5-4.7 although also the ADD and DROP port sets can be used to achieve a bidirectional management of the TTDU. Obviously, the stages a) and c) should be adapted to realize the correct driving configuration, according to the criteria discussed above.

## 3.2 TTDU WORKING CONFIGURATIONS

In this section we present the TTDU configurations introduced to get good performances according to above mentioned requirements.

In principle the TTDU could be used only as a switch to select among different external delay lines (Fig.4.8). In this case the TTDU works like a PADEL and can drive a number of delay lines equal to the number of the columns of the TTDU. Accordingly, a 32x32 TTDU realizes a 5 bit TS and has an IL at least equal to $10\log 2^5 \approx 15$dB. Such a solution is not convenient not only from the IL point of view, but also from the BFN compactness and the system cost one, since a large amount of external delay lines must be used, and a TTDU is required for each radiating element.

On the contrary, the aim of our study has been to devise the TTDU configurations driving a number of elements as large as possible within the same considered chip. In some instances, to improve the performances, external delays lines will be added.

Another point to be considered is related to the time delay distribution to be realized to drive the antenna.

When dealing with time steering applications, the time delay distribution required to achieve the beam pointing direction $\theta_0$, varies linearly with the element position within the array, according to eq. (I.2). When the beam has to be steered towards two opposite beam pointing angles, $\theta_0$ and $-\theta_0$, two opposite time delay slopes have to be realized (Fig.4.9a). However, to reduce the required maximum time delay it is useful to refer to the configuration shown in Fig.4.9b providing the same beam pointing angles with a $\tau_{max}$ reduced to a half. Accordingly, in the following, we will refer to time delay distributions like the one shown in Fig.4.9b.

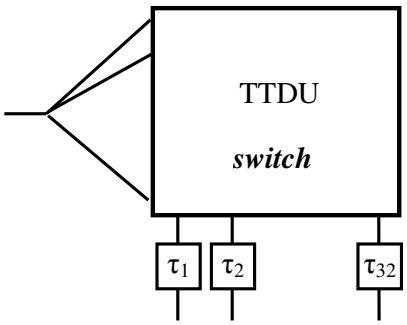


**Figure 4.8** *TTDU as a switch*

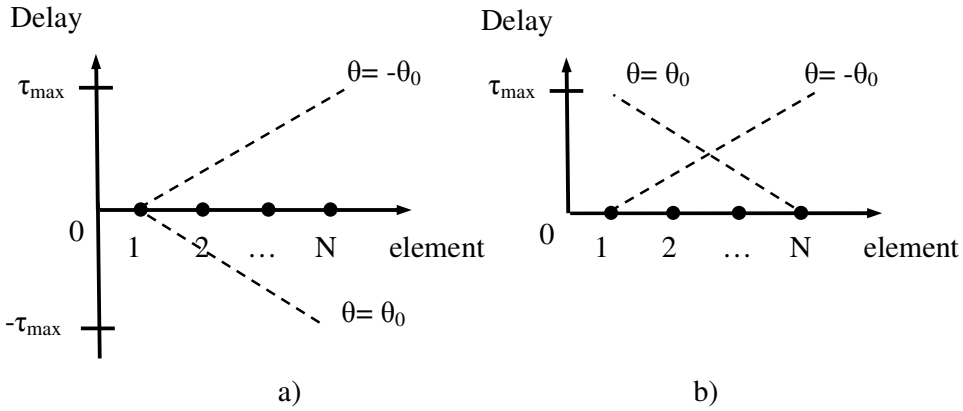


**Figure 4.9** *Time delay distributions*

In the following we will consider two different cases:

- agile beam control (B BIT mode)
- staring beam control (K BEAM mode)

In the first case, the TTDU realizes digital B bit TS units providing the desired time delay distribution (apart from quantization errors). In the staring beam case, the TTDU is required to radiate K fixed beam configurations, that can be selected at will of the designing stage.

As a consequence, to find the TTDU working configurations, we have to find the input-output pairs set which allows the efficient beam control.

In particular, in the B BIT mode, we are interested to identify the TTDU input-output pairs allowing to realize N equal TSs, N being the number of considered radiating elements. Each TS realizes $2^B$ delay, equally spaced from 0 to $\tau_{max}$.

On the contrary, in the K BEAM mode, we are interested to identify K·N input-output pairs that realize the K·N time delays associated to the different beam pointing configurations. In both cases, to drive antennas having different apertures, it would be desirable to vary the maximum time delay $\tau_{max}$, while maintaining constant the quantization level in the B BIT mode.

It must be noted that, designing the TTDU working configurations, we have also to take into account for the losses. In fact, the path losses due to the TTDU can deteriorate the amplitude uniformity factor (AU) of the antenna coefficients and the shape of the radiated beam, as discussed in Chapter 1 (Section 3.2). Accordingly, the TTDU working configurations must be properly designed to reduce the amplitude unbalances due to the TTDU losses.

Some comments on the maximum number of radiating elements which can be efficiently driven by one TTDU, are now in order. In principle, the 32x32 TTDU could drive up to 32 radiating elements by assigning each column to the TS to one radiating element. However, with this solution, according to eq. (IV.1), the maximum time delay $\tau_{max}$ attainable for each TS is equal to

$$\tau_{max} = \tau(32,1) - \tau(1,1) = 31\tau_{\Delta} = 46.5\text{ps} \qquad \text{(IV.3)}$$

and, following eq. (I.2), it results to be too small to efficiently drive a 32 elements array working in the MW frequency range. Moreover, each TS realizes a different time delay range. In fact, the input-output pairs (r,s) corresponding to a given time delay $\tau_n$, must satisfy the relationship:

$$r+s = c_n \qquad \text{(IV.4)}$$

where $c_n$ is a constant value corresponding to the delay to be realized. Equal delays correspond to input-output pairs allocated on a diagonal-like line as the one shown in Fig.4.10. Accordingly, the TS corresponding to the s-th column realizes a time delay range $[\tau_{s,inf}, \tau_{s,sup}]$ translated by an amount equal to $\tau_{\Delta}$ with respect to the preceding TS:

$$\begin{cases} \tau_{s,inf} = \tau_{s-1,inf} + \tau_{\Delta} \\ \tau_{s,sup} = \tau_{s-1,sup} + \tau_{\Delta} \end{cases} \qquad \text{(IV.5)}$$

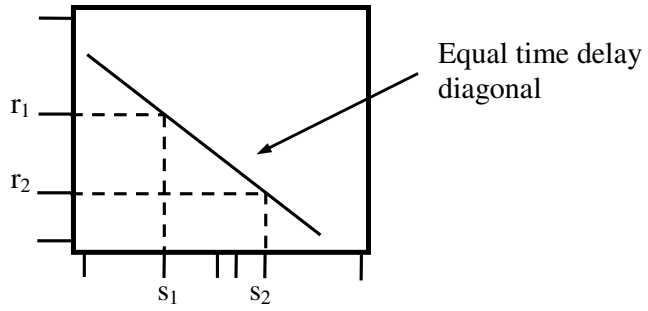


**Figure 4.10** *TTDU input-output pairs configuration realizing the same delay*

Accordingly, to design TSs with an equal delay range it is necessary to consider a reduced number of radiating element with respect to the number of input ports. In the following, we will consider the case of 4 to 8 radiating elements both in the K BEAM and B BIT mode. When dealing with the B BIT mode, a comparison with the SDL analyzed in the 3rd Chapter (Section 2) will be presented.

The working configurations based on the use of the ADD and DROP ports, referred as ADD&DROP mode, will be also discussed in a separated section.

In the next chapter the achievable beam properties for each working configuration will be determined.

### 3.2.1 THE K BEAM MODE

Here we discuss the TTDU working configurations which realize the K BEAM mode. Such configurations can be employed to realize WB or fractional WB PAA (see Chapter 1, Section 2.1).

In fact, the K BEAM mode can be used to realize K fixed squint free beams useful in WB applications. On the other hand this configuration can be employed to implement a fractional WB architecture like the one proposed in the 1st Chapter (Fig.1.5), where the TTDU provides the time delay distributions for a fixed number K of beams, while PS are employed to realize the beam steering over a reduced angular range.

Three different configurations are here considered:

K1) 3 BEAMS - 4 elements
K2) 5 BEAMS - 4 elements
K3) 3 BEAMS - 6 elements

All these configurations work in the contiguous output mode, thus allowing to obtain a fully integrated OBFN. To obtain better performances, the use of some external delays, which can be integrated with the TTDU, has been considered.

The configuration K2, which refers to a 4 elements OTSA, represents an improved version of the configuration K1. The latter is reported only to easily describe the design procedure. On the other hand, the configuration K3 allows to feed up to 6 radiating elements.

For each configuration we report the achievable time delay distribution, the related IL of the system and we discuss about the AU of the antenna coefficients.

In order to make an easy comparison among the various configurations, the performances attainable will be summarized in a table reporting the number of radiating elements N, the number K of beams, the maximum achievable delay $\tau_{max}$, the minimum employed time delay $\Delta t= \tau_{max}/(N-1)$, the OBFN insertion loss IL, and the amplitude uniformity AU.

***K1) 3BEAM – 4 ELEMENTS:***

In this configuration the TTDU has to realize the time delay distributions needed to steer a four elements antenna towards 3 different directions [*Bucci et al. 2004b*]. Let us assume that the considered directions are $\theta_1=0^o$, $\theta_2= \theta$, $\theta_3=-\theta$. Then the TTDU has to realize 4 TSs providing the time delays reported in Tab.4.1.

The time delay $\Delta t$ is chosen according to $\theta$. In particular the maximum $\Delta t$ is equal to $\Delta t = \tau_{max}/3$, where $\tau_{max}$ is the maximum achievable time delay within the TTDU. Our aim is to define the TTDU input-output pairs that realize the time delay required in Tab.4.1, maximize the achievable $\tau_{max}$ while using the smaller number of TTDU inputs and outputs in order to reduce the losses due to the TTDU feeding network.

| | Time shifter | | | |
|---|---|---|---|---|
| **Beam** | **1** | **2** | **3** | **4** |
| $\theta_1 = 0°$ | 0 | 0 | 0 | 0 |
| $\theta_2 = \theta$ | 0 | $\Delta t$ | $2\Delta t$ | $3\Delta t$ |
| $\theta_3 = -\theta$ | $3\Delta t$ | $2\Delta t$ | $\Delta t$ | 0 |

**Table 4.1** *Time delays for the 4 elements array working in the 3 BEAM mode*

The first step is to identify the input-output pairs related to the zero and the maximum delay, $\tau_0$ and $\tau_{max}$, respectively.

As shown in Tab.4.1, the 1st and the 4th TS must realize only these two delays while the 1st and the 4th TS must realize a maximum delay equal to $2\tau_{max}/3$. As consequence, the TTDU is fully exploited when the input-output pairs related to $\tau_0$ and $\tau_{max}$ are located as far as possible (Fig.4.11). Accordingly, we assign to the 1st shifter the outputs from 1 to 15, to the 4th the outputs from 18 to 32, to the 2nd the output 16 and the 3rd the output 17.

Furthermore, to efficiently exploit the TTDU area of each shifter, we use the following strategy. The maximum delay in the 4th TS is obtained when the input-output pairs (18,1) and the (32,32) provide to the $\tau_0$ and the $\tau_{max}$ delays, respectively (the full and the empty dots in Fig.4.11, respectively). In this way we have $\tau_{max}=45\tau_\Delta$ =67.5ps and $\Delta t=15\tau_\Delta$=22.5ps. Obviously, the TTDU can also realize smaller values of $\tau_{max}$ and the $\Delta t$, according to the needed time delay distribution. In particular, the minimum value for $\tau_{max}$ is $3\tau_\Delta$=4.5ps.

On the other hand, the definition of the input-output pairs for the 4th TS defines also the input-output pairs (r,s) corresponding to the $\tau_0$ and the $\tau_{max}$ time delays for the other three shifters.

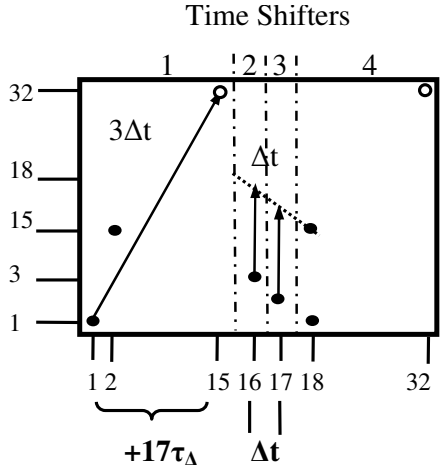


**Figure 4.11** *3 BEAM – 4 elements mode*.

In particular, for the $\tau_0$, the pairs must satisfy the equation r+s=19. The $\tau_0$ pair related to the 1st TS should be (18,1). In this way the 1st TS would be not able to realize the $\tau_{max}$. To circumvent this problem, external biasing delay lines can be used (Fig.4.11). In particular, by exploiting an external delay of $17\tau_\Delta$, the (1,1) input-output pair can be used for the zero delay of the 1st shifter.

Let us note that the broadside beam can be obtained by realizing, for all the shifters, the same delay $\Delta t$. In this way the 1st and the 4th TS do never realize the $\tau_0$ delay at the same time. As consequence, the related input-output pairs can be allocated on the same input without any conflict. Then, to realize the time delay $\Delta t$, the input-output pairs (15,2) and (16,18) are used for the 1st and the 4th TS, respectively. Moreover, this choice reduces the delay range of the 2nd and the 3rd shifters, since they are not required to realize the $\tau_0$. Accordingly, if we use an external delay equal to $\Delta t$ for both TS, to obtain the delay $\Delta t$ the input-output pairs (2,17) and (3,16) have to be used for the 2nd and the 3rd shifters, respectively. As consequence, these two TS have only to realize one delay, equal to $\Delta t$, that is obtained by using the input-output pairs (18,16) and (17,17) for the 2nd and the 3rd TS, respectively (Fig. 4.11)

The resulting input-output pairs for each beam configuration are reported In Tab.4.2.

This configuration exploits 8 TTDU inputs. Accordingly, an 1:8 ISC has to be used in the stage a), thus introducing about 9dB of IL.

Regarding the outputs, the 1st TS uses 3 outputs, the 2nd and the 3rd one output, while the 4th TS uses 2 outputs. Accordingly, integrated combiners can be used to connect the TS outputs to the corresponding photodetectors. Regarding the 2nd and the 3rd TSs no combiners are needed, while the 1st and the 4th TS need asymmetric combiners. The 4th TS, in fact, has to use a 2:1 combiner, while the 1st TS would to use a 3:1 combiner. Since a combiner, made by the series of two 2:1 combiners, causes an IL asymmetry, it is to be preferred the use a 4:1 combiner for the 1st TS. The IL associated to the output combiners is at least equal to 6dB for the 1st TS and 3dB for the 4th TS, while no combiner losses are associated to the 2nd and the 3rd TSs. Obviously, this IL unbalance has to be properly compensated.

| | **Time shifter** | | | |
|---|---|---|---|---|
| **Beam** | **1** | **2** | **3** | **4** |
| $\theta_1 = 0^o$ | (15,2) | (3,16) | (2,17) | (16,18) |
| $\theta_2 = \theta$ | (1,1) | (3,16) | (17,17) | (32,32) |
| $\theta_3 = -\theta$ | (32,32) | (18,16) | (2,17) | (1,18) |

**Table 4.2** *Input output pairs for the 4 elements array working in the 3 BEAM mode*

Accordingly the worst IL, apart form the conversion losses and star coupler excess losses, is related to the 1st TS and is given by three contributes: the IL of the input combiner, the IL due to the TTDU and the IL due to the output combiner. If we consider the minimum IL, associated to the input-output pairs (1,1), according to the (IV.2), we have:

$$\begin{aligned} IL(dB) &= IL_{inputcombiner} + IL(1,1) + IL_{outcombiner} = \\ &= 10\log 8 + (2C + R) + 10\log 4 \approx 18dB \end{aligned} \qquad \text{(IV.6)}$$

Moreover, the IL varies according to the considered input-output pairs. In particular the maximum IL variation due to the TTDU losses, we also refer as the AU factor, is obtained in the steered beam configuration, related for example to the beam pointing angle $\theta_2$, and is given by:

$$AU = IL(32,32) - IL(1,1) = 62T \approx 4dB \qquad \text{(IV.7)}$$

It is worth noting that this IL takes into account also for the power division losses needed to feed the 4 radiating elements. Accordingly, the time control unit insertion loss, $IL_T$, is about 6dB better than the one reported in eq. (IV.6).

The parameters of interest attainable with this configuration, when the maximum possible $\tau_{max}$ is obtained, are reported in Tab.4.3.

| N | K | $\tau_{max}$ | $\Delta t$ | IL | AU |
|---|---|---|---|---|---|
| 4 | 3 | 67.5ps | 22.5ps | 18dB | 4dB |

**Table 4.3** *Performance parameters attainable in the 3 BEAM- 4 elements mode*

***K2) 5BEAM – 4 ELEMENTS:***

By increasing the number of the exploited TTDU inputs it is possible to obtain the delay distributions needed to radiate 5 beams: $\theta_1=0°$, $\theta_2=\theta_A$, $\theta_3=-\theta_A$, $\theta_4=\theta_B$, $\theta_5=-\theta_B$.

To define the TTDU working configuration the same methodology of the previous case can be used. The time delays to be realized are reported in Tab.4.4.

| | Time shifter | | | |
|---|---|---|---|---|
| **Beam** | **1** | **2** | **3** | **4** |
| $\theta_1 = 0°$ | 0 | 0 | 0 | 0 |
| $\theta_2 = \theta_A$ | 0 | $\Delta t_A$ | $2\Delta t_A$ | $3\Delta t_A$ |
| $\theta_3 = -\theta_A$ | $3\Delta t_A$ | $2\Delta t_A$ | $\Delta t_A$ | 0 |
| $\theta_4 = \theta_B$ | 0 | $\Delta t_B$ | $2\Delta t_B$ | $3\Delta t_B$ |
| $\theta_5 = -\theta_B$ | $3\Delta t_B$ | $2\Delta t_B$ | $\Delta t_B$ | 0 |

**Table 4.4** *Time delays for the 4 elements array working in the 5BEAM mode*

Let us assume that the beam pointing direction $\theta_B$ is related to the $\tau_{max}$. Then we have $\Delta t_B = \tau_{max}/3$, and $\Delta t_A<\Delta t_B$.

To avoid the use of asymmetric combiners at the output of the 1st and the 4th TS, we can adopt the following strategy. We choose the input-output pairs in order to realize the time delay related to $\Delta t_B$, on the first TTDU output, rather than the second TTDU output, as in the previous case. Moreover, we avoid use of the same input port to realize the delay $\Delta t_B$ at the 1st and the 4th TS. Accordingly, we slightly reduce the $\tau_{max}$, by moving the $\tau_0$ input-output pair for the 1st TS. In particular, the input-output pairs (4,1) and (1,18) for the 1st and the 4th TS, respectively, are used for $\tau_0$. An external delay equal to $14\tau_\Delta$ is used for the 1st TS. The $\tau_{max}$ pairs are the (32,15) and the (32,29) for the 1st and the 4th TS, respectively. In this way $\tau_{max}=42\tau_\Delta$ =63ps.

The 2nd and the 3rd TS are "time biased" with ax external time delay equal to $\Delta t_B$.

In Tab.4.5 the input output pairs related to the 5 BEAM mode, using $\Delta t_B=7\tau_\Delta=10.5$ps and $\Delta t_A=14\tau_\Delta=21$ps are reported.

This configuration exploits 11 TTDU inputs and, then, requires a proper feeding system that compensates the losses unbalances due to the couplers.

If we assume that a 1:16 coupler is used at the input stage, we obtain IL≈18dB, AU≈4dB. Then, $IL_T$=12dB.

| | Time shifter | | | |
|---|---|---|---|---|
| **Beam** | **1** | **2** | **3** | **4** |
| $\theta_1 = 0^o$ | (11,1) | (3,16) | (2,17) | (8,18) |
| $\theta_2 = \theta_A$ | (4,1) | (3,16) | (9,17) | (11,29) |
| $\theta_3 = -\theta_A$ | (11,15) | (10,16) | (2,17) | (1,18) |
| $\theta_4 = \theta_b$ | (4,1) | (10,16) | (23,17) | (32,29) |
| $\theta_5 = -\theta_B$ | (32,15) | (24,16) | (9,17) | (1,18) |

**Table 4.5** *Input output pairs for the 4 elements array working in the 5 BEAM mode*

The performances attainable with the 5 BEAM – 4 elements mode with the previously reported values of $\Delta t_A$ and $\Delta t_B$, are shown in Tab. 4.6.

| N | K | $\tau_{max}$ | Δt | IL | AU |
|---|---|---|---|---|---|
| 4 | 5 | 63ps | 10.5ps - 21ps | 18dB | 4dB |

**Table 4.6** *Performance parameters s attainable in the 5 BEAM- 4 elements mode*

***K3) 3BEAM – 6 ELEMENTS:***

The K BEAM mode can be also designed in order to feed PAA with a larger number of elements.

Here we report the case of a 6 elements antenna. The configuration is determined following the approach adopted in the previous cases. Obviously, it is necessary to add two TS. As consequence, the area assigned to the 1st and the 4th TS, is smaller than the one employed in the previous case.

In Fig.4.12 the corresponding scheme is depicted, while the time delays and the related input-output pairs, corresponding to a $\tau_{max}=40\tau_\Delta=60$ps and $\Delta t=\tau_{max}/5=5\tau_\Delta=12$ps, are reported in Tab.4.7.

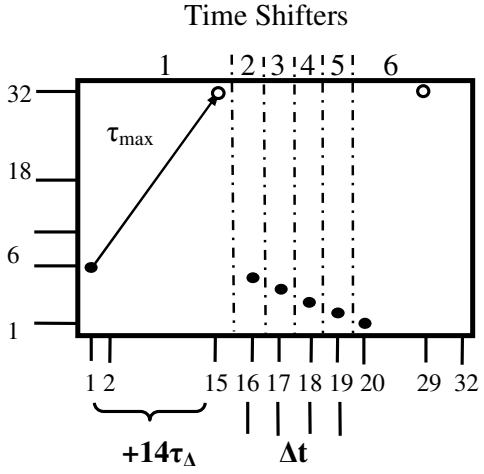


**Figure 4.12** *3 BEAM – 6 elements mode.*

This configuration exploits 15 inputs. Then if we assume to use a 16:1 coupler in the stage a), we have IL≈18dB ($IL_T$≈10dB) and AU≈4B.

In Tab.4.8 the performances attainable with the 3 BEAM – 6 elements mode are shown.

From the tables Tab.4.3, Tab.4.6 and Tab.4.8, it can be seen that the three considered configurations allow almost the same $\tau_{max}$, IL and AU so that the TTDU can be designed to drive antennas with the same aperture and with 4 or 6 elements and 5 or 3 beams, respectively.

It must be noted that the achievable time delay distribution can be selected to feed antennas with different apertures or beam pointing angles, as discussed in the next chapter.

| | **Time shifters** | | | | | |
|---|---|---|---|---|---|---|
| **Beam** | **1** | **2** | **3** | **4** | **5** | **6** |
| $\theta_1 = 0^o$ | $\Delta t$ | $\Delta t$ | $\Delta t$ | $\Delta t$ | $\Delta t$ | $\Delta t$ |
| | (14,1) | (5,16) | (4,17) | (3,18) | (2,19) | (9,20) |
| $\theta_2 = \theta_A$ | 0 | $\Delta t$ | $2\Delta t$ | $3\Delta t$ | $4\Delta t$ | $5\Delta t$ |
| | (6,1) | (5,16) | (12,17) | (19,18) | (26,19) | (32,29) |
| $\theta_3 = -\theta_A$ | $5\Delta t$ | $4\Delta t$ | $3\Delta t$ | $2\Delta t$ | $\Delta t$ | 0 |
| | (32,15) | (29,16) | (20,17) | (11,18) | (2,19) | (1,20) |

**Table 4.7** *Time delay and related input output pairs for the 3BEAM – 6 elements mode*

| **N** | **K** | $\tau_{max}$ | $\Delta t$ | **IL** | **AU** |
|---|---|---|---|---|---|
| 6 | 3 | 60ps | 12ps | 18dB | 4dB |

**Table 4.8** *Performance parameters attainable in the 3 BEAM- 6 elements mode*

### 3.2.2 THE B BIT MODE

Here we discuss the TTDU working configurations allowing to realize the B BIT mode.

These configurations can drive WB or fractional WB PAA, either at array or subarray level (see Chapter 1, Section 2.1). In fact, they allows to implement an OTSA driven by B bit TSs. The TSs can be used to drive the radiating elements or the subarrays, according to the WB control architectures discussed in the 1st Chapter (Fig.1.3a and Fig.1.3b). On the other hand, this TTDU working configuration can be employed in a fractional WB architecture, like the one discussed in the 1st Chapter (Fig.1.14), where the TSs drive the subarray, while PSs are used before each element.

The configurations here presented refer to both the contiguous and non contiguous outputs grouping criteria. The latter modality, as shown in the following, allows us a more flexible use of the TTDU.

In particular we considered the following cases:

B1) 3 BIT – 4 element – contiguous outputs
B2) 3 BIT – 4 element – non contiguous outputs
B3) 4 BIT – 4 element – non contiguous outputs
B4) 4 BIT – 8 element – non contiguous outputs
B5) 5 BIT – 4 element – non contiguous outputs

For each configuration we report the achievable time delay distribution, the related IL of the system and we discuss about the AU of the antenna coefficients. To improve the time delay performances external time delays have been adopted, as in the K BEAM mode.

In order to make an easy comparison among the various configurations, the performances attainable will be summarized in a table reporting the values of N, B, $\tau_{max}$, $\Delta t = \tau_{max}/(2^B-1)$, the time shifter insertion loss $IL_T$, and the AU. Unlike the K BEAM mode, in this case we report the $IL_T$, instead than the IL, since we are interested in comparing the TS performance achievable with each configuration. Moreover, for the working configurations allowing to vary the achievable time shift distribution, the minimum and the maximum achievable time delay range are also reported.

Finally, at the end of the section, a comparison with the SDL schemes analyzed in the 3rd Chapter (Section 2) is reported.

***B1) 3 BIT – 4 ELEMENTS – CONTIGUOUS OUTPUTS:***

In this configuration the TTDU has to realize 4 equal TS. Each TS provides 8 delays $\tau_n = n\Delta t$, with $\Delta t = \tau_{max}/7$ and n=0,…,7 [*Bucci et al. 2004b; Bucci et al. 2005*]. Accordingly, we assign an equal TTDU area to each TS. In particular the outputs from 1 to 8 are assigned to the 1st TS, the ones from 9 to 16 to the 2nd and so on, in order to obtain 8 outputs for TS (Fig.4.13).

Let us set the $\tau_0$ and the $\tau_{max}$ input-output pairs for each TS. Regarding the $\tau_0$ pairs, if we use in the 4th TS the pair (1,25), the other $\tau_0$ pairs (r,s) have to be set in order to obtain r+s=26, along the diagonal-like line shown in Fig.4.13. In particular, the $\tau_0$ pair for the 1st TS is (25,1). As consequence, the maximum time delay $\tau_{max}$ achievable within the area assigned to the 1st TS is obtained by using the input-output pair (32,8). Accordingly we have $\tau_{max}=14\tau_\Delta=21$ps, although the other TSs can obtain a longer delay.

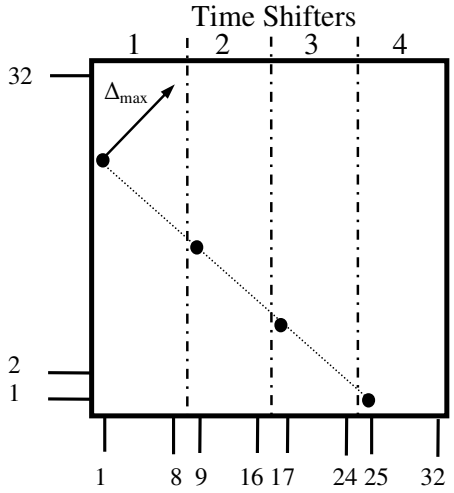


**Figure 4.13** *3 BIT – 4 elements – contiguous outputs mode*

To improve the time delay range, we can use external delay lines in order to attain equal time delay ranges for each TS. In particular we can adopt external delay lines of

$21\tau_\Delta$, $14\tau_\Delta$ and $7\tau_\Delta$ for the 1st, 2nd and 3rd TS, respectively. This allows to obtain $\tau_{max}=35\tau_\Delta=52.5$ps.

The input-output pairs $(r_\alpha,s_\alpha)$ related to the α-th TS to realize the n-th delay are given by:

$$\begin{cases} r_\alpha = 4+4n-(\alpha-1) \\ s_\alpha = 1+n+8(\alpha-1) \end{cases} \qquad \text{(IV.8)}$$

with n=0,..,7 and α=1,..,4.

This configuration exploits all the 32 TTDU inputs and 8 outputs per TS. A 1:32 coupler can be used in the stage a), and a 8:1 combiner can be used in the stage c) to group the outputs of each TS.

Regarding the losses we have: IL≈27dB ($IL_T$≈21dB) and AU=4dB.

The performance parameters attainable in this driving modality are summarized in Tab.4.9.

| N | B | $\tau_{max}$ | Δt | $IL_T$ | AU |
|---|---|---|---|---|---|
| 4 | 3 | 52.5ps | 7.5ps | 21dB | 4dB |

**Table 4.9** *Performance parameters attainable in the 3 BIT - 4 elements – contiguous outputs mode*

***B2) 3 BIT – 4 ELEMENTS – NON CONTIGUOUS OUTPUTS:***

In this case, unlike the previous modality, each TS can be allocated over the whole TTDU. This allows to get a wider time delay range for each TS.

Accordingly, the first step is to select the proper locations of the $\tau_0$ and the $\tau_{max}$ input-output pairs. Then, since all the TSs have to realize the same delays, for each delay a set of four input-ouput pairs (r,s) with r+s=constant, has to be found. So, 8 sets of equal delay pairs have to be determined according to (IV.4).

Let us consider the $\tau_0$ and the $\tau_{max}$ input-output pairs. These pairs should be allocated as far as possible one from each other. Moreover, their location has to be chosen in order to realize four equal delays for both $\tau_0$ and $\tau_{max}$. Accordingly, regarding the $\tau_0$ delay, we set $c_0=5$ in (IV.4), thus selecting the input-output pairs (4,1), (3,2), (2,3), (1,4) for the 1st,2nd, the 3rd and the 4th TS, respectively (the full dots in Fig.4.14). For $\tau_{max}=\tau_7$, we set $c_7=61$ and select the input-output pairs (32,29), (31,30), (30,31) and (29,32) for the 4 TSs (Fig.4.14).

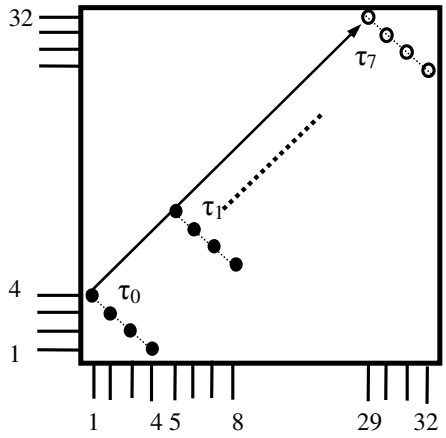


**Figure 4.14** *3 BIT– 4 elements – non contiguous outputs mode.*

All other pairs can be found analogously. In fact, the pairs $(r_\alpha,s_\alpha)$ associated to the n-th delay of the α-th radiating element are obtained from:

$$\begin{cases} r_\alpha = 4 + 4n - (\alpha - 1) \\ s_\alpha = 1 + 4n + (\alpha\text{-}1) \end{cases} \qquad \text{(IV.9)}$$

with n=0,..,7 and α=1,..,4.

The maximum achievable delay is $\tau_{max} = 56\tau_\Delta = 84$ps. Then $\Delta t = 8\tau_\Delta = 12$ps.

This configuration requires a 1:32 ISC to feed the TTDU inputs, and an 8:1 coupler to combine the outputs corresponding to each TS. The IL is, at least, equal to 27dB.

To improve the IL, a different driving strategy has been considered. In fact, for the n-th time delay, four input output pairs have to be found, satisfying the relationship r+s=5+8n. Accordingly, these pairs can be moved along the corresponding diagonal in order to require a minor number of inputs. Moreover, by adopting an external delay, the gate number could be additionally reduced. In particular the α-th TS can realize the proper n-th delay by using the input-output pairs defined by:

$$\begin{cases} r_\alpha = 4 - (\alpha - 1) \\ s_\alpha = 1 + 8n + (\alpha\text{-}1) \end{cases} \qquad \text{(IV.10)}$$

with n=0,..,3 and α=1,..,4, and by

$$\begin{cases} r_\alpha = 32 - (\alpha - 1) \\ s_\alpha = 1 + 8(n\text{-}4) + (\alpha\text{-}1) \end{cases} \qquad \text{(IV.11)}$$

with n=4,..,7 and α=1,..,4 (see Fig. 4.15)

To achieve the proper delay, an external delay of $4\tau_\Delta$ can be added to feed the inputs gates 29, 30, 31, 32 (Fig. 4.15). Only 8 input and four output gates are required for each TS. It is worth noting that with this configuration there are delays corresponding to the same input or output gates. However, since they belong to the same TS, no problem will occur.

In this way, a 1:8 ISC can be used in the stage a), while output combiners 4:1 can be adopted in the stage c). The corresponding IL is about IL=18dB ($IL_T$=12dB), while AU≈3.5dB.

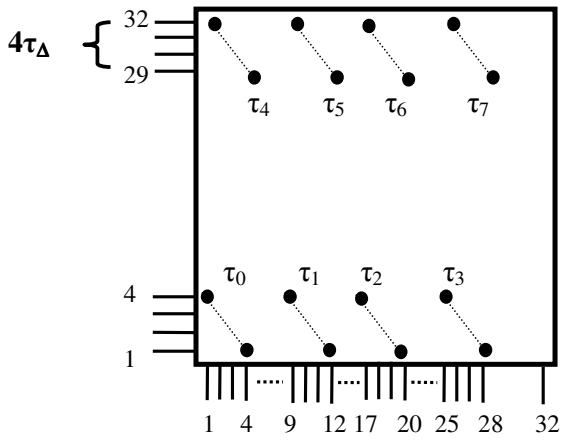


**Figure 4.15** *3 BIT– 4 elements – non contiguous outputs mode: improved configuration*

This configuration offers an interesting feature: it is possible to vary the Δt and the $\tau_{max}$. In particular the Δt can be varied from $\Delta t_{min}=4\tau_\Delta$=6ps to $\Delta t_{min}=9\tau_\Delta$=13.5ps with a step of 1.5ps, then $\tau_{max}$ can be varied from 42ps to 94.5ps with a step of 10.5ps.

In particular, for the minimum delay configuration, the input-output pair ($r_\alpha$,$s_\alpha$) needed to realize the n-th delay for the α-th TS, can be given by $r_\alpha$ =4-(α-1) and $s_\alpha$=1+4n+(α-1). In this way 4 TTDU inputs and 8 outputs are exploited, thus allowing to attain IL=18dB ($IL_T$=12dB) and AU≈2dB.

The other time delay configurations can be easily designed.

Table.4.10 summarizes the performance achievable with this working configuration and, as told before, since it is possible to vary the delay range, the maximum and minimum delay ranges are reported.

| | **N** | **B** | **$\tau_{max}$** | **Δt** | **$IL_T$** | **AU** |
|---|---|---|---|---|---|---|
| MAX range | 4 | 3 | 94.5ps | 13.5ps | 12dB | 3.5dB |
| MIN range | 4 | 3 | 42ps | 6ps | 12dB | 2dB |

**Table 4.10** *Performance parameters attainable in the 3 BIT - 4 elements – non contiguous outputs mode: the parameters refers to the maximum delay range (MAX range), and to the minimum delay range (MIN range)*

***B3) 4 BIT – 4 ELEMENTS – NON CONTIGUOUS OUTPUTS:***

In the previous configuration at the most 8 TTDU inputs are employed (Fig.4.15). The most part of the TTDU area is left unused. Accordingly, by using a larger number of ports, more time delays can be realized and a better quantization level can be attained. Moreover, more external delays are needed and a time delay range wider than the previous one is obtained.

Here we describe the 4 BIT configuration: each 4 BIT TS has to realize 16 delays $\tau_n=n\Delta t$, with $\Delta t = \tau_{max}/15$ and n=0,…,15. Also in this case it is possible to vary $\tau_{max,}$ in particular, from $60\tau_\Delta$=90ps to $135\tau_\Delta$=202.5ps.

We can follow the previous approach. Here we have 16 input-output pairs sets, instead of 8, that must be located in order to save the input ports number and attain the desired time delays. As the in previous configuration, the first set is located in the left down corner of the TTDU. The other 15 sets have to be properly located according to the desired time delay distribution.

Let us consider the function $\lfloor x \rfloor$ that rounds x to the nearest integer towards zero. To attain the $\tau_{max}$=202.5ps, the input-output pair needed to realize the n-th delay for the α-th TS, are $r_\alpha = 4-(\alpha-1)+8\lfloor n/4 \rfloor$, $s_\alpha=1+9(n-4\lfloor n/4 \rfloor)+(\alpha-1)$ (see Fig.4.16). The correct delay is obtained by using three external delays: the r-th exploited input port is fed by means of an external delay $\tau_{ext} = 28\lfloor r/5 \rfloor \tau_\Delta$ (Fig.4.16) i.e., the inputs from 9 to 12 are fed by means of the same $28\tau_\Delta$ external delay, the inputs from 17 to 20 are fed by the $56\tau_\Delta$ external delay, and the inputs from 25 to 28 are fed by the $84\tau_\Delta$ external delay.

This configuration requires a 1:16 ISC in the stage a), and four 4:1 output combiners. The corresponding IL is about 21dB ($IL_T$=15dB), and the reported AU is about 3.5dB.

Regarding the configuration related to the minimum $\tau_{max}$, equal to 90ps, the input-output pair needed to realize the n-th delay for the α-th TS, is $r_\alpha = 4-(\alpha-1)+24\lfloor n/8 \rfloor$, $s_\alpha=1+4(n-8\lfloor n/8 \rfloor)+(\alpha-1)$ and the inputs from 25 to 28 must be fed with an external delay equal to $\tau_\Delta$. Now 8 TTDU inputs and 8 outputs are exploited and we have: IL=21dB ($IL_T$=15dB) and AU=3.5dB.

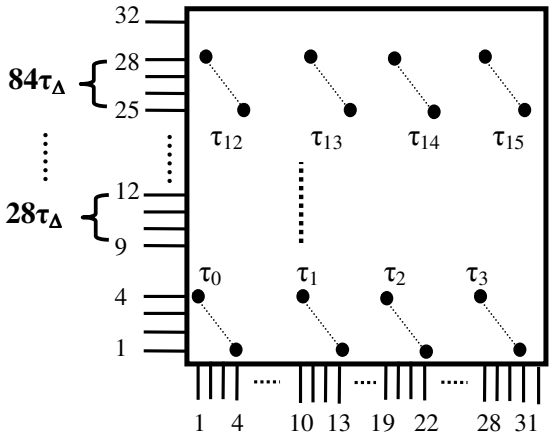


**Figure 4.16** *4 BIT– 4 elements – non contiguous outputs mode*.

The performance parameters related to this working configuration are reported in Tab.4.11.

| | N | B | $\tau_{max}$ | $\Delta t$ | $IL_T$ | AU |
|---|---|---|---|---|---|---|
| MAX range | 4 | 4 | 202.5ps | 13.5ps | 15dB | 3.5dB |
| MIN range | 4 | 4 | 90ps | 6ps | 15dB | 3.5dB |

**Table 4.11** *Performance parameters attainable in the 4 BIT - 4 elements – non contiguous outputs mode: the parameters refers to the maximum delay range (MAX range), and to the minimum delay range (MIN range)*

***B4) 4 BIT – 8 ELEMENTS – NON CONTIGUOUS OUTPUTS:***

The previous TTDU working configuration can be further improved to drive up to 8 radiating elements with a fixed value of $\tau_{max}$. In fact, in this new configuration all the TTDU inputs and outputs will be exploited.

Unlike the 4 BIT – 4 elements mode, now 16 sets of 8 input-output pairs, with the same delay, must be located within the TTDU. As before, we locate the first set in the left down corner: the input-output pairs on the diagonal-like line r+s=9, from the (8,1) to the (1,8) are assigned to the eight TSs. As shown in Fig.4.17, the input-output pairs are defined according to:

$$\begin{cases} r_\alpha = 8 + 8\lfloor n/4 \rfloor - (\alpha - 1) \\ s_\alpha = 1 + 8\left(n - 4\lfloor n/4 \rfloor\right) + (\alpha - 1) \end{cases} \qquad \text{(IV.12)}$$

and three external time delays must be used: the r-th input port is fed with an external delay $\tau_{ext} = 24\lfloor r/9 \rfloor \tau_\Delta$ for r=0,..,32 (Fig.4.17).

We have $\Delta t = 8\tau_\Delta$ and $\tau_{max} = 120\tau_\Delta = 180$ps.

This configuration requires a 1:32 ISC in the stage a), and eight 4:1 output combiners. The corresponding IL is about 24dB ($IL_T$=15dB), and the reported AU is about 3.5dB.

The values of the key parameters attainable with this driving modality are reported in Tab. 4.12. In this case, since the delay range is not variable, only one set of parameter is shown.

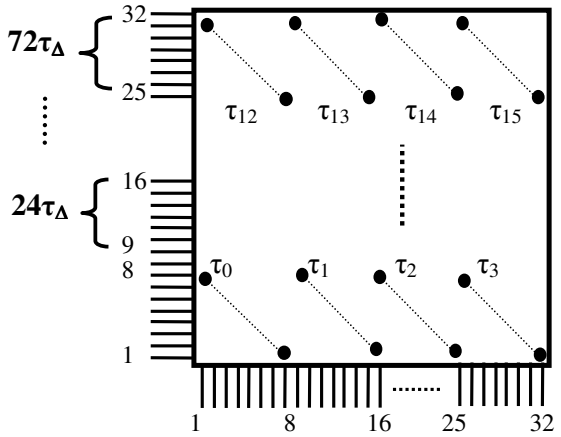


**Figure 4.17** *4 BIT– 8 elements – non contiguous outputs mode.*

| N | B | $\tau_{max}$ | $\Delta t$ | $IL_T$ | AU |
|---|---|---|---|---|---|
| 8 | 4 | 180ps | 12ps | 15dB | 3.5dB |

**Table 4.12** *Performance parameters attainable in the 4 BIT - 8 elements – non contiguous outputs mode*

***B5) 5BIT – 4 ELEMENTS – NON CONTIGUOUS OUTPUTS:***

The time delay quantization attainable with the TTDU can be further improved by using more TTDU ports. A wider time delay range is also obtained.

In this case the TPH must realize four 5BIT TS, i.e. four TS with 32 delays $\tau_n=n\Delta t$, being $\Delta t = \tau_{max}/31$ and n=0,…,31. Also in this case $\tau_{max}$ can be varied by using appropriate external delays; in particular, $\tau_{max} \in$ (186ps, 418.5ps) with a step equal to 46.5ps.

Here we refer to the case $\tau_{max}$=418.5ps. The α-th TS can realize the proper n-th delay by using the input-output pair defined by $r_\alpha=4-(\alpha-1)+4\lfloor n/4 \rfloor$, $s_\alpha=1+9(n-4\lfloor n/4 \rfloor)+(\alpha-1)$ (see Fig.4.18).

Moreover, to ensure to correct delay, each input gate r has to be fed by mean of an external delay $\tau_{ext}$ according to $\tau_{ext}=32\lfloor r/5 \rfloor \tau_\Delta$ (Fig. 4.18). In this way only seven external delay are used, each feeding a 4 input gates group: the input from 5 to 8 are fed by means of a $32\tau_\Delta$ external delay, the input from 9 to 12 are fed by a $64\tau_\Delta$ external delay, and so on, while no delay is used for the first four inputs.

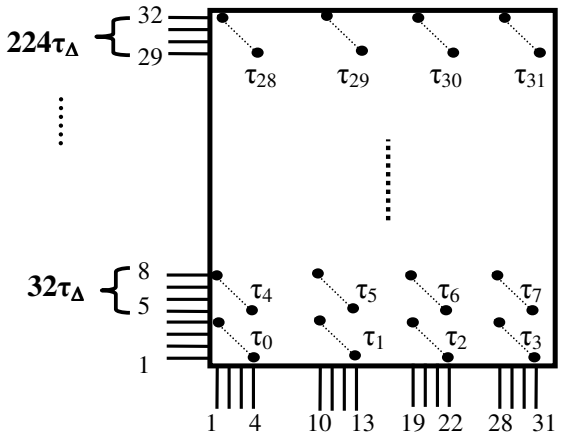


**Figure 4.18** *5 BIT– 4 elements – non contiguous outputs mode.*

This configuration requires a 1:32 ISC in the stage a), and four 4:1 output combiners. The corresponding IL is about 24dB ($IL_T$=18dB), while AU is about 3.5dB.

In Tab.4.13 the performance parameters are summarized.

| | N | B | $\tau_{max}$ | $\Delta t$ | $IL_T$ | AU |
|---|---|---|---|---|---|---|
| MAX range | 4 | 5 | 418.5ps | 13.5ps | 18dB | 3.5dB |
| MIN range | 4 | 5 | 186ps | 6ps | 18dB | 3.5dB |

**Table 4.13** *Performance parameters attainable in the 5 BIT - 4 elements – non contiguous outputs mode: the parameters refers to the maximum delay range (MAX range), and to the minimum delay range (MIN range)*

Let us analyze the results attained in the B BIT modality and make the concluding remarks.

The same time delay quantization level is obtained with the configurations B1 and B2. In particular, the configuration B1 allows a full integrated OBFN, reliable and stable, while the allowed maximum time delay range is almost reduced to a half with respect to the one allowed by the configuration B2. Moreover, the latter configuration also allows to vary the time delay range.

Regarding the other configurations, they represent an improvement of the configuration B2. In fact, by using more TTDU ports, it is possible to attain a better time delay quantization or drive more radiating elements. This is obviously paid with an increase on the $IL_T$. Moreover, different time delay ranges are attainable: in fact, the minimum $\tau_{max}$ is equal to 52.5ps (configuration B1), while the maximum $\tau_{max\ is}$ equal to 418.5ps (configuration B5).

As shown, the configurations B2, B3 and B5, allow to vary the time delay range while maintaining fixed the quantization level. This feature is useful since it allows an efficient driving of antennas with different apertures. F.I., as shown in Tab.4.13, when the 5 BIT mode is designed to realize a $\tau_{max}$ equal to 186ps, the TTDU can be employed to drive a 4 elements OTSA, while when a $\tau_{max}$ equal to 418.5ps is considered, the TTDU can be used to drive 4 subarrays, corresponding to an aperture wider than the previous one.

On the other hand, for a fixed antenna aperture this feature allows to vary the angular scanning region, as shown in the next chapter.

Regarding the $IL_T$ and the TS complexity, a comparison can be done with the SDL architectures discussed in the 3rd Chapter (Section 2).

In particular, as far as the IL is concerned, the TTDU behaves like a PADEL. In fact, apart from the losses due to the TTDU, the $IL_T$ factor is equal to $10\log_{10}(2^B)$, like the PADEL's one (see Chapter 3, Tab.3.1). This factor could be reduced by employing more lasers with an increase of the system complexity.

Concerning this point, several observations are in order.

In principle, to make a quantitative comparison with the PADEL, we could evaluate the complexity parameters of the proposed structure.

According to Tab.3.1, the complexity of a B BIT PADEL structure $C_{PADEL}$ is given by:

$$C_{PADEL} = C_{LD} + C_F = 2^{B+1} \qquad \text{(IV.13)}$$

On the contrary the complexity of the time shifter $C_{TS}$ obtained by using the TTDU working in the B BIT mode is given by:

$$C_{TS} = C_{LD} + C_{TTDU} = 1 + C_{TTDU} + C_{EX} \qquad \text{(IV.14)}$$

where the $C_{EX}$ is the number of the external delay lines, and $C_{TTDU}$ is the complexity of the TTDU. The latter parameter could be estimated as follows.

The TTDU implements a certain number of switched and delay lines. Accordingly, we have $C_{TTDU}=C_S+C_F$. In particular, when working in the B BIT mode, the TTDU implements $C_S=2^B$ switches, to obtain the required time delays.

Regarding the $C_F$, it is lower than $2^B$. In fact, if the TTDU working configuration would require $2^B$ active inputs and $2^B$ active outputs, the number of delay lines implemented within the TTDU would be equal to $2^B$. On the contrary, the TTDU working configuration is designed in order to employ the minimum number of inputs and outputs. Accordingly, the complexity parameter $C_F$ can be defined as:

$$C_F = \frac{N_{IN} + N_{OUT}}{2} \qquad \text{(IV.15)}$$

where $N_{IN}$ and $N_{OUT}$ are the number of TTDU active inputs and outputs, respectively. F.I. in the 3 BIT mode, configuration B2, we have $C_F=3$.

Accordingly, in the 3 BIT mode, we have $C_{PADEL}=16$ and $C_{TS}=13$, since $C_{EX}=C_{LD}=1$. Therefore, the hardware complexity coefficient of our structure, here defined, results lower than the PADEL one.

However, on our opinion, to make an useful comparison is an hard task. In fact, to derive the actual TTDU hardware complexity, we should account for the complexity of the whole integrated chip, and compare it with an analogous solution.

### 3.2.3 THE ADD&DROP MODE

Thanks to the "add" and "drop" ports, the TTDU can be driven in bidirectional way allowing to improve the TPH beamsteering performances.

Here we report two cases.

In the first the TTDU implements 8 TSs, thus allowing to radiate two contemporaneous beams at different frequencies (DUAL BEAM).

In the second case we show how the TTDU can be driven in bidirectional manner to realize four 5 bit TSs. In particular, two different time delay ranges are obtained, using the contiguous or non contiguous outputs modality. The delay ranges attained are smaller than the one reported in the configuration B5.

***DUAL MODE:***

An example of OTSA working in the DUAL mode has been described in the 3rd Chapter (Section 3.1), when dealing with the FOP architecture [*Frankel and Esman*].

In this configuration half TTDU, the left side, works as in the 4 bit – 4 elements mode, while the other side works in the same modality but is feed by the DROP ports. Then, the input-output pairs related to the left side are modified in order to not use the input rows related to the TS on the right side (Fig.4.19).

In this way the TTDU realize 8 TSs: the left side shifters are driven by the signal $s_1$, while that on the right side are driven by the signal $s_2$.

***5 BIT – 4 ELEMENTS – CONTIGUOUS OUTPUTS:***

Also in this case the TTDU is half divided: the left side realizes two TSs while the right side realizes the remaining two TSs (Fig.4.20).

Each side is again divided in two sections: the first 8 output are assigned to the 1st TS, while the outputs from 9 to 16 are assigned to the 2nd TS. Accordingly, to achieve a 5 bit TS, the 32 input-output pairs are obtained by using 4 inputs and 8 outputs. In particular we use $\Delta t_{min}=\tau_\Delta$ and $\tau_{max}=31\tau_\Delta=46.5$ps. The input-output pairs related to the 1st and the 2nd TS are given by:

$$\begin{cases} r_\alpha = 2+8\lfloor n/8 \rfloor-(\alpha-1) \\ s_\alpha = n-8\lfloor n/8 \rfloor+8(\alpha\text{-}1) \end{cases} \qquad \text{(IV.13)}$$

for $\alpha$=1,2 and n=0, ..,31.

The input-output pairs related to the 3rd and the 4th TS are given by:

$$\begin{cases} r_\alpha = 31-8\lfloor n/8 \rfloor+(\alpha-3) \\ s_\alpha = 32-n+8\lfloor n/8 \rfloor-8(\alpha\text{-}3) \end{cases} \qquad \text{(IV.14)}$$

for $\alpha$=3,4 and n=0, ..,31.

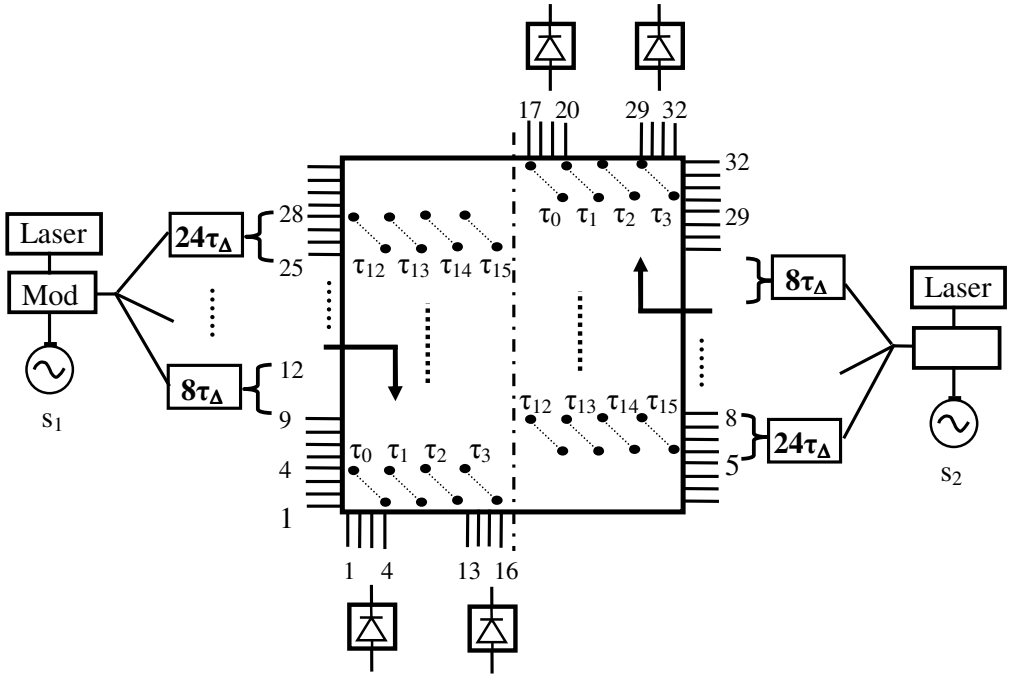


**Figure 4.19** *Dual beam mode.*

External delay lines of $7\tau_\Delta$ have to be used for the outputs of the 1st and the 4th TS.

This configuration requires a 1:16 star coupler made by two 1:8 coupler to feed the left and the right side of the TTDU. Moreover, in the detection stage four 8:1 output combiners are needed. The corresponding IL is about 24dB ($IL_T$=18dB), while AU is about 2.5dB.

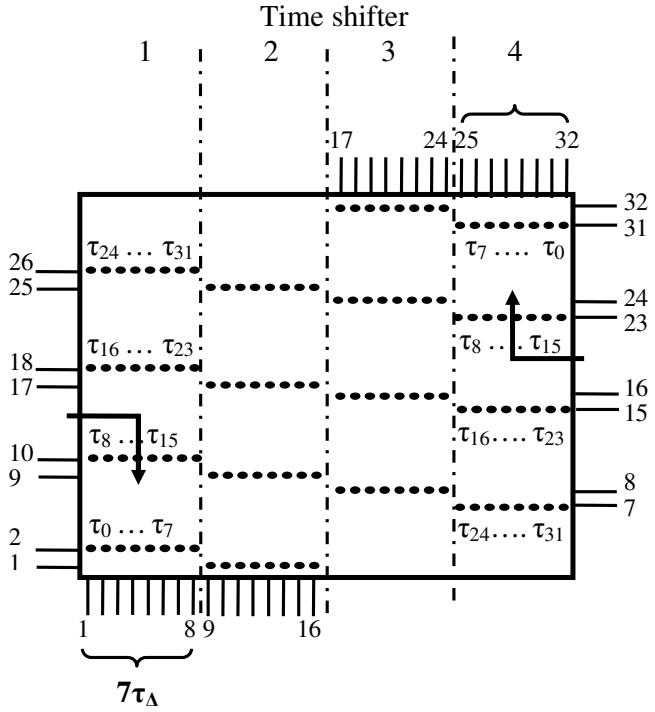


**Figure 4.20** *5 bit – 4 elements – contiguous outputs configuration – ADD-DROP mode*

***5 BIT – 4 ELEMENTS – NON CONTIGUOUS OUTPUTS:***

Following the procedure used in the previous configuration, we can obtain a double time delay range by using a non contiguous outputs arrangement and more external delay unit. In particular we can obtain $\Delta t_{min}=2\tau_\Delta$ and $\tau_{max}=62\tau_\Delta=93$ps. The configuration layout is depicted in Fig. 4.21.

The input-output pairs related to the 1st and the 2nd TS are given by:

$$\begin{cases} r_\alpha = 2+8\lfloor n/8 \rfloor - (\alpha-1) \\ s_\alpha = 1+2(n-8\lfloor n/8 \rfloor)+(\alpha\text{-}1) \end{cases} \qquad \text{(IV.15)}$$

for $\alpha$=1,2 and n=0,..,31.

The input-output pairs related to the 3rd and the 4th TS are given by:

$$\begin{cases} r_\alpha = 31-8\lfloor n/8 \rfloor + (\alpha-3) \\ s_\alpha = 32-2(n-8\lfloor n/8 \rfloor) - (\alpha\text{-}3) \end{cases} \qquad \text{(IV.16)}$$

for $\alpha$=3,4 and n=0,..,31.

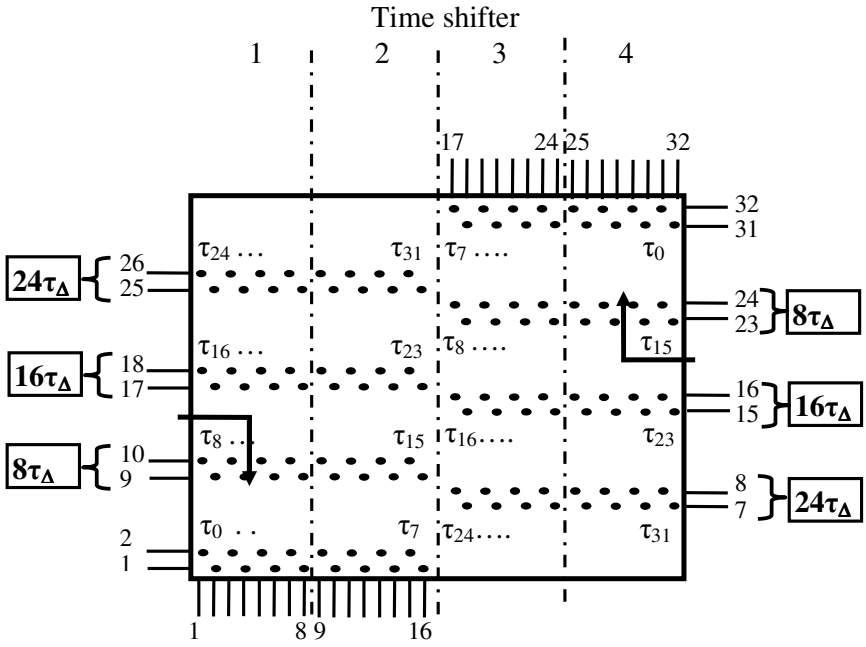


**Figure 4.21** *5 bit – 4 elements – non contiguous outputs configuration – ADD-DROP mode*

Six external delay lines have to be used, three for each side. On the left side, external delay lines of $8\tau_\Delta$, $16\tau_\Delta$, $24\tau_\Delta$ have to be used for the inputs from 9 to 10, 17 to 18, 25 to 26, respectively. On the right side, external delay lines of $8\tau_\Delta$, $16\tau_\Delta$, $24\tau_\Delta$ have to be used for the inputs from 23 to 24, 15 to 16, 7 to 8, respectively.

As before, IL is about 24dB ($IL_T$=18dB), and AU is about 2.5dB.

In Tab.4.14 the performance obtained in the 5 BIT – 4 elements – non contiguous and contiguous outputs configurations are reported.

| | **N** | **B** | **$\tau_{max}$** | **$\Delta t$** | **$IL_T$** | **AU** |
|---|---|---|---|---|---|---|
| Non cont. Outputs | 4 | 5 | 46.5ps | 1.5ps | 18dB | 2.5dB |
| Cont. Outputs | 4 | 5 | 93ps | 3ps | 18dB | 2.5dB |

**Table 4.14** *Performance parameters attainable in the 5 BIT - 4 elements – add&drop mode, reported for the non contiguous and contiguous outputs modality*

These configurations allow to reduce the minimum $\tau_{max}$ achievable with the configuration B5, by a factor 4 or 2, in the non contiguous or contiguous outputs configuration, respectively. Accordingly, the 5 BIT configuration is improved when antennas requiring a smaller time delay range must be driven. F.I. antennas working at a frequency four times higher than the one exploiting the B5 configuration can be considered, as discussed in the next chapter.

# CHAPTER 5

# THE OTSA DESIGN

## 5 INTRODUCTION

The aim of this chapter is to discuss the design of an OTSA based on the new photonic integrated unit presented in the previous chapter.

In particular, we will consider the design of an OTSA using a 32x32 TTDU working in one of the configurations described in the Chapter 4 (Section 3.2). The OTSA layout is depicted in Fig.5.1.

The radiating system is made by a printed array. In fact, printed antennas, allow interesting features such as low weight and size, low fabrication costs and high integration capabilities with the BFN. Moreover, recently design techniques for wide band printed elements have been introduced [*Fourikis*; *Hall*; *Ghorbani and Waterhouse*; *Targonsky et al.*; *Wang and Tripp*]. In particular, we will consider a strip-slot-foam-inverted patch (SSFIP) element [*Zurcher and Gardiol*], whose design is described in the Appendix C where are also reported the results concerning the realization and experimental characterization of printed antenna prototypes.

The SSFIP architecture shows good bandwidth performances and allows reducing the deterioration of the element pattern due to the feed line, since the feed line and the patch are separated by the ground plane. In the following, an array of 4 SSFIP printed elements will be considered and the key points encountered when facing the design of the OTSA prototype will be discussed.

In particular, we will refer to two different designs.

In the first case we consider a classical OTSA structure radiating sum beam squint free patterns, like the most of the OTSA presented in the open literature [*Ng et al. 1991*; *Esman et al. 1993*; *Frankel et al. 1996a*; *Lee et al. 1995a*]. In the second case we refer to an OTSA architecture able to realize both sum and difference beam squint free patterns. To this end we introduce an innovative optical architecture, based on the optical phase and time control techniques described in the 2$^{nd}$ and the 3$^{rd}$ Chapter, respectively.

Since the design procedure is quite similar for both the OTSA structures, only the design of the OTSA realizing sum beam squint free patterns will be widely described

while the innovative optical architecture introduced for the array radiating sum and difference beam squint free patterns will be presented at the end of the chapter.

As a first issue, we consider the definition of the antenna excitation distribution. In fact, since the beam steering is obtained by using the phase/time control, the antenna amplitude distribution corresponding to the desired beam shape requirements must be first available. To this end, an external synthesis procedure accounting for the inter-element mutual coupling is employed.

Once the desired aperture distribution is found, the distribution tolerances will be analysed.

Later, the behaviour of the ideal OTSA will be presented by considering the beam steering capabilities and the radiating system properties corresponding to the nominal amplitude and time delay distribution attainable with the TTDU configurations presented in the previous chapter

Once the ideal antenna has been studied, we will present the accurate system modelling we employed to analyze the whole structure. In other words, we will consider a realistic model for each optical and MW device thus obtaining an accurate model of the whole system, able to take into account all the aspects of a real-world prototype, i.e., able to simulate with a good degree of accuracy both the OBFN and the radiating system.

In particular, the modelling will take into account the following aspects:

- Electromagnetic mutual coupling effects on the circuital properties of the antenna
- Excitation distribution errors
  - Random errors due to realization defects
  - Amplitude errors due to the TTDU losses

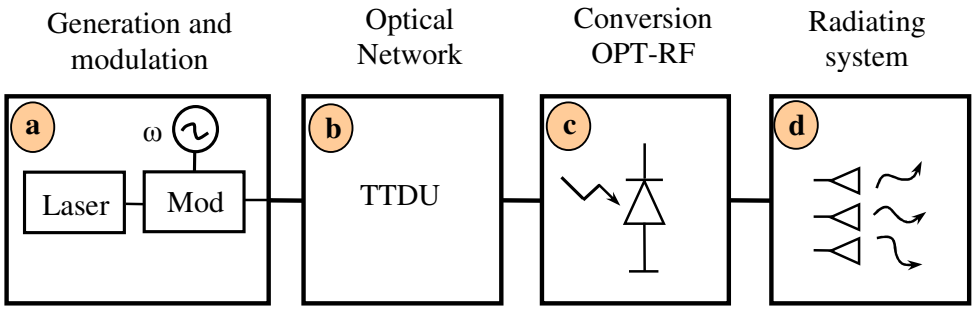


**Figure 5.1** *Layout of the OTSA based on the TTDU*

In fact, the behaviour of the antenna system is affected by the mismatching produced by the electromagnetic mutual coupling among the radiating elements. Moreover, the nominal excitation distribution can be deteriorated by the amplitude and phase/time random errors due to the realization defects, such as asymmetrical power divisions and time delay drifts. At the same time the amplitude distribution is affected by systematic errors due to the TTDU losses, as shown in the previous chapter. Accordingly, we will also present the compensation strategy we developed to reduce the effects of the TTDU losses, discussed in the 4$^{th}$ Chapter, and obtain an amplitude excitations distribution as similar as possible to the desired one.

# 6 ANTENNA EXCITATION DISTRIBUTION

As known, the beam steering can be obtained by using excitation coefficients with a linear phase/time distribution. Concerning the amplitude of the array excitation coefficients, it is convenient to adopt a distribution improving the radiative properties of the antenna such as the Beam Width (BW) and the SLL.

Obviously, improving the SLL increases the BW, so that a good compromise could be a Tchebitchev amplitude distribution giving, in the case of a 4 elements OTSA and a SLL=-15dB, the amplitudes 0.75, 1, 1, 0.75,

The BW of the steered beam grows proportionally to the scan angle deviation from the broadside, while the SLL remains the same.

In the following we will refer to a 4 elements OTSA.

However, the Tchebitchev distribution is obtained by fixing the SLL and requiring the minimum possible BW, without accounting for the mutual coupling effects. Accordingly, in the following we apply a synthesis technique, to verify the relevance of these effects in the case of our interest.

Furthermore, the effects due to unwanted variation of the excitation distribution will be also considered by means of a statistical-numerical analysis giving the acceptable tolerances of the array excitation coefficients.

## 2.1 THE EXTERNAL SYNTHESIS PROCEDURE

To find the antenna excitation coefficients, we applied an advanced conformal array power pattern synthesis able to perform the beam shaping reconfiguration by exploiting only the phase of the excitation coefficients, and taking into account for near field constraints [*Bucci and D'Elia*; *Bucci et al 2004a*].

The synthesis algorithm requires the knowledge of the elements pattern, to calculate the far field diagram, and exploits suitably defined "masks" to enforce the design specifications. Two approaches have been applied. In a first one, the "active" element pattern, accounting for the mutual coupling effects, has been evaluated by using an appropriate electromagnetic simulator and has been used in the synthesis procedure, thus performing the so called "*active synthesis*". In the second one, the ideal element pattern, not accounting for the antenna operating conditions, has been exploited leading to the "*non active synthesis*".

To show the effectiveness of the active synthesis approach we compare the results of the active and non active synthesis procedures.

For the sake of simplicity, a uniform amplitude distribution is considered. The far field amplitude patterns corresponding to the active (dotted line) and non active (dashed line) synthesis are compared to the one obtained by using the electromagnetic simulator Ansoft Ensemble 8 (solid line) and are shown in Fig. 5.2. As seen, the non active approach gives more accurate results.

Therefore, we performed the active synthesis requiring the following specifications:

- Only phase control of three beams ($\theta$=0º,-30º,+30º)

- SLL=-17dB
- BW for all the three beams equal to the one obtained with the Tchebitchev distribution previously considered and corresponding to a SLL=-15dB.

It is noted that these specifications enforce requirements more severe than the one required by the Tchebitchev synthesis demanding the same BW.

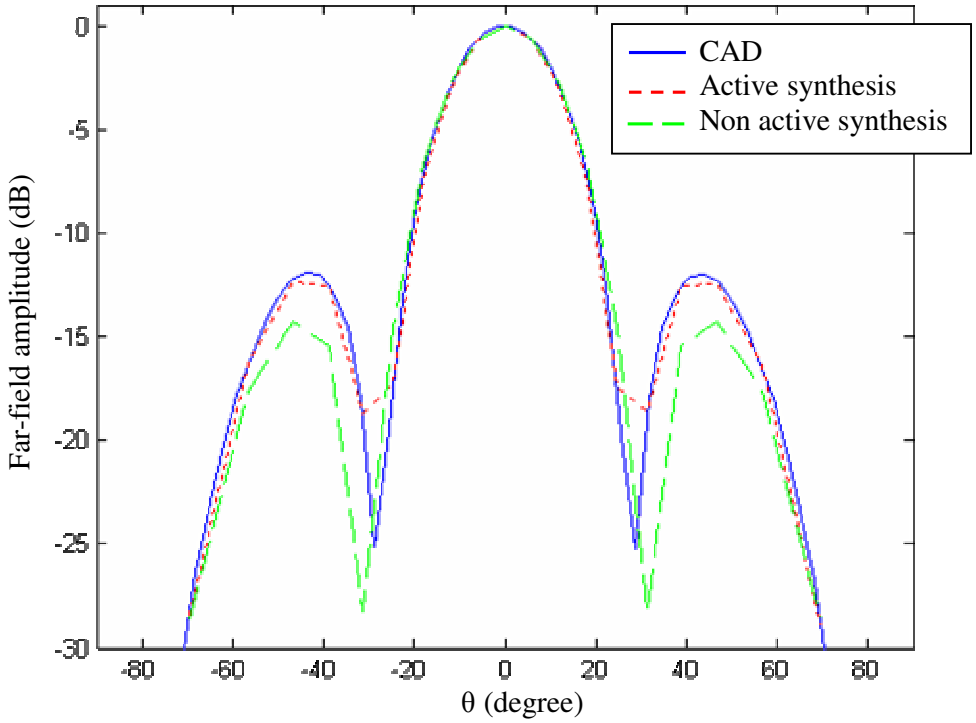


**Figure 5.2** *Comparison between the active and non active synthesis procedures*

The excitation coefficients obtained by applying the synthesis procedure are reported under Tab.5.1. The amplitudes are similar to the Tchebitchev one, while the phase distribution is quite similar to the linear one.

For the sake of comparison, the far field patterns of a broadside array obtained by using the synthesised coefficients and the Tchebitchev ones are shown in Fig. 5.3 as a continuous and dotted line, respectively. In the same Figure are also reported the masks involved in the power pattern synthesis algorithm. They represent the upper and the lower limit required for the power pattern.

The patterns corresponding to a beam pointing angle equal to 30º are reported in Fig.5.4.

These results show that the synthesis technique does not give an appreciable improvement with respect to the Tchebitchev distribution. In fact, a very small BW reduction is obtained at the expense of a 1dB increase on the SLL.

| | | Beam | | |
|---|---|---|---|---|
| | | 0º | 30º | -30º |
| Elements | Amplitude | Phase | | |
| 1 | 0.80 | 0º | -4º | 4º |
| 2 | 1.00 | 0º | 89º | -89º |
| 3 | 1.00 | 0º | 181º | -181º |
| 4 | 0.80 | 0º | 274º | -274º |

**Table 5.1** *Antenna coefficient obtained by means of the active synthesis procedure*

It is believed that, due to the small number of radiating elements, i.e., the number of parameters to be exploited, the synthesis technique cannot significantly improve the radiation pattern. Furthermore, the difference among the amplitude distributions obtained with the synthesis and the Tchebitchev one is small enough to be assumed within the error distribution due to the unavoidable realization defects. Accordingly, in the following, the amplitudes of the excitation coefficients of the antenna prototype will be assumed equal to the Tchebitchev ones.

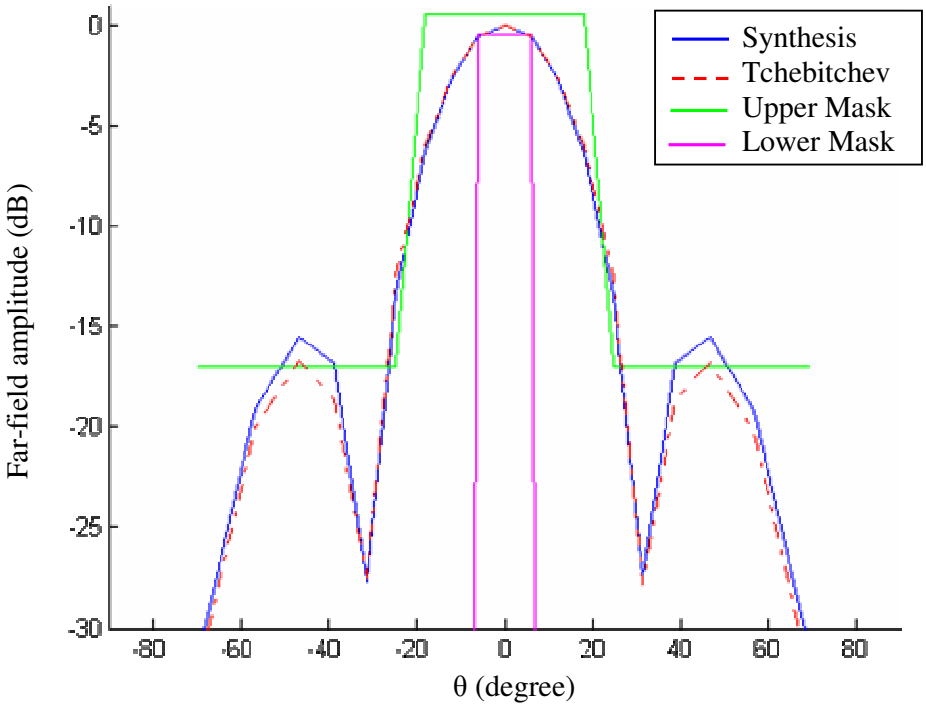


**Figure 5.3** *Comparison between the distribution obtained with the synthesis and the Tchebitchev one: broadside case*

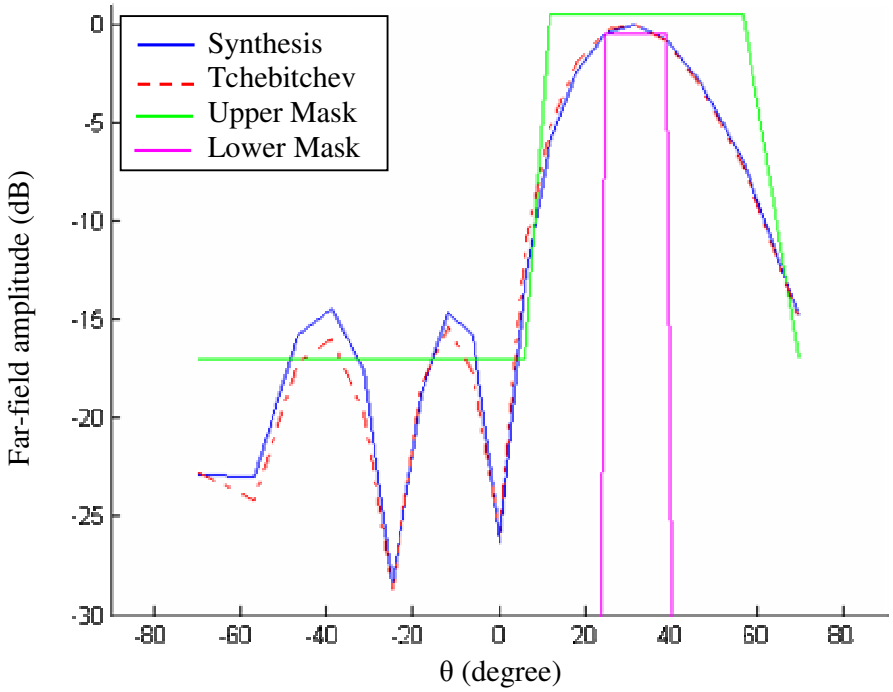


**Figure 5.4** *Comparison between the distribution obtained with the synthesis and the Tchebitchev one: 30º case*

## 2.2 ARRAY TOLERANCES

To realize the desired amplitude distribution, additional hardware components must be used with respect to the one required to control the phase of the excitation coefficients. In principle, we could exploit the modulation of the MW signal upon the optical carrier. In fact, the amplitude of the modulated signal can be controlled by controlling the modulation index. This solution requires a more sophisticated configuration of the stage a) of the OTSA, which could not be made by using a compact, full integrated solution. In fact, it is necessary to use a separate modulator for each radiating element, and to connect each modulator to the corresponding TTDU inputs. Moreover, the unavoidable differences among the transfer functions of the modulators must be carefully taken into account.

An alternative solution is based on the insertion of an amplitude control in the conversion stage c). The control can be realized in the optical or MW domain by using a variable gain amplifier or a variable attenuator, as shown in Fig.5.5. Here we report also an optical amplifier (OA) and a MW amplifier (MWA) needed to compensate for the optical to MW conversion losses.

Obviously, both the MW and the optical section will introduce an error upon the aperture distribution, due to the unavoidable realization defects.

As a consequence, it is necessary to estimate the maximum acceptable error.

The results on the random errors analysis shown in the 1st Chapter (Section 2.2.2.2) can be exploited as guidelines to carry out a numerical analysis.

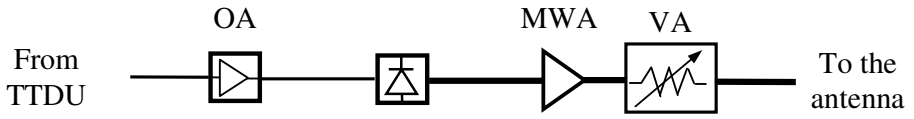


**Figure 5.5** *Conversion stage based on the variable attenuator*

In particular, we considered a 4 elements antenna with a Tchebitchev nominal amplitude distribution and a SLL=-15dB. The maximum accepted SLL variation is 5dB, while the maximum accepted beam pointing angle variation (BPV) is 2º. The maximum acceptable amplitude and phase error amount can be evaluated by using eqs. (I.27) and (I.28). In particular, eq. (I.28) is used to establish the phase RMS error while eq. (I.27), once the phase RMS error is known, is used to find the RMS amplitude error.

As a result, the amplitude and phase root mean square (RMS) errors estimates are equal to 0.82dB and 5º, respectively.

These results have been used to perform a numerical analysis. The antenna pattern has been calculated by introducing a random amplitude and phase Gaussian error with a given RMS. The obtained results confirm that the reported antenna pattern variations are below the expected limits on the SLL and BPV with the assumed confidence levels.

# 7 BEAM FEATURES AND ANTENNA APERTURE SIZE

The radiated beam features are strictly related to the antenna aperture size and the time delay performances achievable with the TTDU.

In the Chapter 4 (Section 3.2), for each TTDU configuration, we found the achievable time delay properties, i.e. the maximum time delay $\tau_{max}$ and the number B of bits, and the number N of achievable TSs.

Now, we have to define the antenna aperture size and the radiated beam features.

Regarding the antenna aperture size, since the number of radiating elements is assigned, we have to find the array design frequency $f_D$ and the element spacing $d_\lambda$, normalized to the wavelength $\lambda_D=c/f_D$.

The radiated beam features are the maximum scanning range $\theta_{max}$, the angular resolution $\Delta\theta$, the peak and the average SLL due to the time delay quantization, $QL_{peak}$ and $\sigma^2_{Tavg}$, respectively. The latter two parameters have been discussed in the 1st Chapter (Section 2.2.2.1). On the other hand, in the K BEAM mode, we are only interested in determining the $\theta_{max}$.

The following design formulas [*Mailloux 2005*; *Ng et al. 1991*] can be used:

$$\tau_{max} = \frac{(N-1)d_\lambda}{f_D}\sin\theta_{max} \qquad (V.1)$$

$$\Delta\theta = \frac{c\tau_{max}}{\left(2^B-1\right)(N-1)\,d\cos\theta_0} = \frac{\sin\theta_{max}}{\left(2^B-1\right)\cos\theta_0} \qquad (V.2)$$

$$QL_{peak}(dB) = 3.92 + 20\log\left(\frac{f\tau_{max}}{2^B - 1}\right) \quad (V.3)$$

$$\sigma^2_{Tavg} = \frac{1}{3D}\frac{\left(\pi f\tau_{max}\right)^2}{\left(2^B - 1\right)^2} \quad (V.4)$$

Eq. (V.1) is used to find the $f_D$, once $\theta_{max}$ and $d_\lambda$ are known. Conversely, if the $f_D$ and $d_\lambda$ are known, eq. (V.1) gives the maximum achievable scanning range. Generally speaking, the maximum scanning range $\theta_{max}$ is chosen according to the intended application: typical scanning ranges are $\theta_{max}=\pm45°$, or $\theta_{max}=\pm60°$ for wide scanning applications. The spacing $d_\lambda$, as described later on, is chosen in order to avoid the grating lobes and reduce the mutual coupling effects.

The (V.2) allows evaluating the angular resolution $\Delta\theta$. This is usually defined at half the scan range, then using $\theta_0= \theta_{max}/2$.

The obtained $QL_{peak}$ and the average SLL $\sigma^2_{Tavg}$ can be easily derived from (V.3) and (V.4) respectively.

To allow a quick and easy determination of the frequency $f_D$ or the scanning range $\theta_{max}$, we introduced in [*Bucci et al. 2004b*] the planning chart depicted in Fig.5.6, in the case of a linear array of 4 radiating elements. It represents $\tau_{max}$ as function of $\theta_{max}$ and the element spacing $d_\lambda$, in the range ($0.5\lambda$, $0.7\lambda$), for a 4 elements array and for three design frequencies $f_D$ (10GHz, 15GHz, 20GHz). According to the $\tau_{max}$ values obtained in the different TTDU working configurations, the planning chart allows to find the values of $f_D$ and $\theta_{max}$, once $d_\lambda$ has been set.

It is necessary to set first the value of $d_\lambda$. As told before, $d_\lambda$ is chosen to avoid the grating lobes and to control the mutual coupling effects. While the mutual coupling will be described during the OTSA prototype modelling, here we discuss the grating lobes phenomenon. The latter imposes an upper bound on the value of $d_\lambda$. For a given $\theta_{max}$, the maximum value of $d_\lambda$ avoiding the grating lobes is:

$$d_{GL} = \frac{1}{\sin\theta_{max} + 1} \quad (V.5)$$

By substituting (V.5) in (V.1), the function $\tau_{max}(\theta_{max})$ can be found, together with the condition on $\tau_{max}$ ensuring the absence of grating lobes. Accordingly, we can introduce in the planning chart a grating lobe free zone, for each design frequency as shown in Fig.5.7 with coloured shadowed regions. Each region represents the area of the planning chart wherein the grating lobes are avoided.

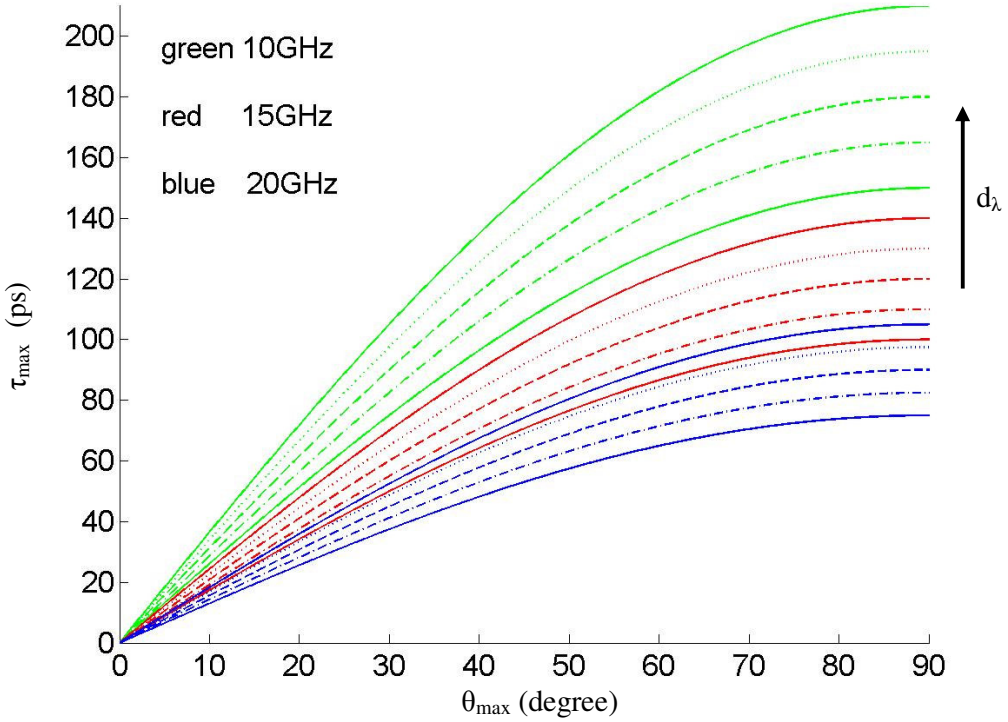


**Figure 5.6** *OTSA planning chart: $d_\lambda$ varies from 0.5λ and 0.7λ, with spacing 0.05λ*

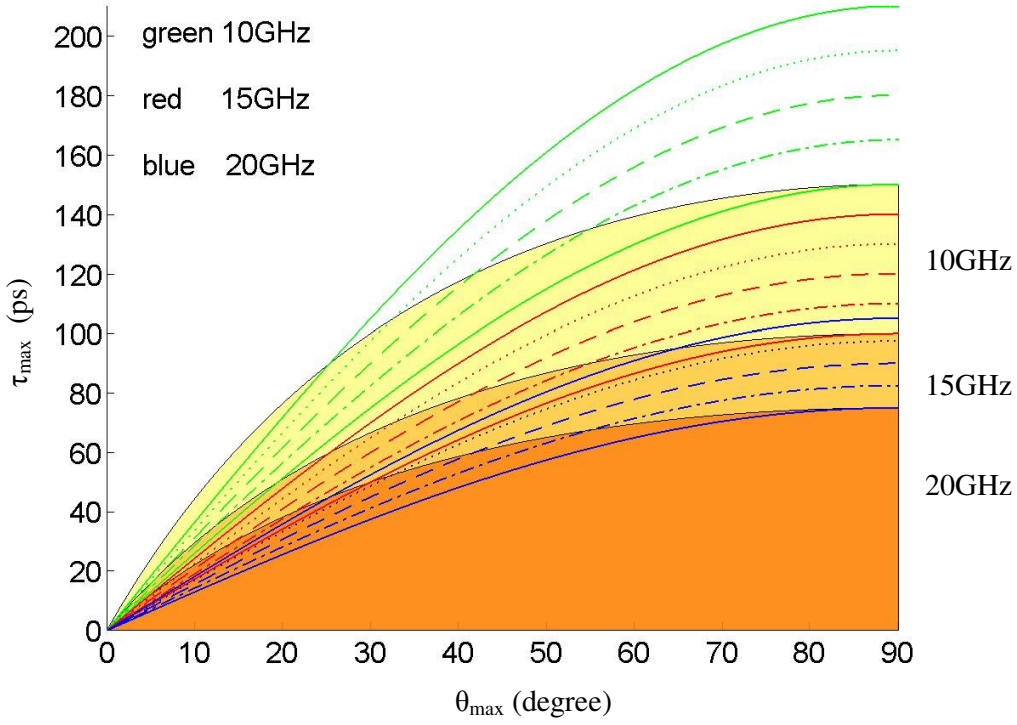


**Figure 5.7** *OTSA planning chart with the grating lobes free zones*

We can now estimate the system capabilities for each TTDU working configurations described in the Chapter 4 (Section 3.2).

***K BEAM MODE:*** In these configurations the TTDU provides the time delay distributions needed to radiate only an assigned number of fixed beams (see Chapter 4, Section 3.2.1). As a consequence, only the design frequency $f_D$ and the $\theta_{max}$ have to be found.

In particular, for the 3 Beams mode, we have considered $\theta_1=0^o$, $\theta_{2,3}=\pm\theta$. Then, using eq. (V.1) we can easily find the $f_D$ values that allows to realize $\theta=45^o$ and $\theta=60^o$.

Regarding the 5 Beams mode, we have considered $\theta_1=0^o$, $\theta_{2,3}=\pm\theta_A$, $\theta_{4,5}=\pm\theta_B$. where $\theta_B$ is related to the maximum delay $\tau_{max}$ while $\theta_A$ to $\tau_{max}/2$. Accordingly, by using eq. (V.1) we can evaluate the values for $f_D$ which allow to have $\theta_B=45^o$ and $\theta_B=60^o$, and to find also the related $\theta_A$ values.

In Tab.5.2 we report, for each K beam configuration, the maximum time delay $\tau_{max}$ and the achievable $f_D$ values for $\pm45^o$ and $\pm60^o$ scanning range, assuming for $d_\lambda$ the value given by eq. (V.5). Moreover, for the 5 Beam mode, we also report the $\theta_A$ value.

| Configuration | $\tau_{max}$ | $f_D$ (45° scanning) | $f_D$ (60° scanning) |
|---|---|---|---|
| 3 Beams – 4 elements | 67.5ps | $f_D$~18GHz | $f_D$~21GHz |
| 5 Beams – 4 elements | 63ps | $f_D$ ~20GHz - $\theta_A$~21° | $f_D$ ~22GHz - $\theta_A$~26° |
| 3 Beams – 6 elements | 60ps | $f_D$~34GHz | $f_D$~39GHz |

**Table 5.2** *Features achievable in the K beams configurations*

***B BIT MODE:*** In these configurations (see Chapter 4, Sections 3.2.2 and 3.2.3) we should evaluate the characteristics of the radiated beam.

In the following we denote with the label A the contiguous output mode, and with the label B the non contiguous outputs mode. Moreover, when dealing with those configurations wherein the time delay distribution can be changed within a certain range, we will refer to both the minimum and the maximum value for $\tau_{max}$.

In Tab. 5.3 we present the most interesting parameters corresponding to the B BIT configuration.

The value of $f_D$ refers to a 60° scanning range. The value of QL_peak and $\sigma^2_{Tavg}$ are referred to the worst case, using $f=f_D$. In particular, the value of $\sigma^2_{Tavg}$ is raised by 2dB to take into account for scan and taper losses [*Mailloux 2005*]. Regarding the 5 Bit – 4 elements mode, we used the label AD to refer to the configuration using the "Add" and "Drop" scheme (Chapter 4, Section 3.2.3). In this case, a label identifying which of the two output configurations, A and B say, is used, has been inserted in the column corresponding to the maximum achievable delay.

In particular it is worth noting that the configuration 5 Bit – 4 elements – non contiguous outputs, can be also used to feed a subarray structure. Then, eq. (V.1) can be easily modified to take into account for the size of the subarray. If we denote with M the number of elements of a subarray, and E the number of subarrays, we have:

$$\tau_{max} = \frac{(E-1)Md_{\lambda}}{f_D} \sin\theta_{max} \qquad (V.6)$$

This equation allows to find the ratio $M/f_D$. For example, the TTDU can drive a 28 elements antenna made of 4 subarrays of 7 elements spaced by a half a wavelength, for $f_D$=22GHz, ensuring a scanning range equal to 60º.

Obviously, also other array configurations are possible. A possible way to define uniquely the value of M and $f_D$, is to take into account for the quantization lobes. In fact, as described in Chapter 1 (Section 2.2.2.1), due to the frequency variation, the subarray architectures are affected by quantization lobes. Assigned the desired quantization lobe level and the frequency variation, by using eq. (I.22), the number M of subarray elements can be found and $f_D$ is easily obtained.

| Configuration | $\tau_{max}$ | $f_D$ | $\Delta\theta$ | QL_peak | $\sigma^2_{Tavg}$ |
|---|---|---|---|---|---|
| 3 Bit 4 elements - A | 52.5ps | ~26GHz | ~8º | ~ - 10dB | ~ - 13dB |
| 3 Bit 4 elements - B | 42ps | ~33GHz | | | |
| | 94.5ps | ~15GHz | | | |
| 4 Bit 4 elements - B | 90ps | ~15GHz | ~4º | ~ - 17dB | ~ - 19dB |
| | 202.5ps | ~7GHz | | | |
| 4 Bit 8 elements - B | 180ps | ~18GHz | ~4º | ~ - 9dB | ~ - 15dB |
| 5 Bit 4 elements - AD | A 46.5ps | ~30GHz | ~2º | ~ - 23dB | ~ - 26dB |
| | B 93ps | ~15GHz | | | |
| 5 Bit 4 elements - B | 186ps | ~7GHz | | | |
| | 418.5ps | ~3GHz | | | |

**Table 5.3** *Features achievable in the B Bit configurations*

# 8 OTSA MODELLING

To verify accurately the working of the whole OTSA we derived an appropriate model for each device employed in the antenna system and we simulated the behaviour of the whole antenna. The usefulness of the simulation, obviously, depends on the accuracy of the considered models. In particular, the latter have been chosen in order to obtain an OTSA model as similar as possible to the real-world case. To this end, several issues have to be taken into account when deriving the model of each OTSA section.

Regarding the radiating system model, we are interested in the circuital behaviour. In fact, the radiative behaviour can be easily evaluated by means of an electromagnetic CAD. Therefore, to estimate the antenna pattern we need only to

know the antenna excitation coefficients, which can be evaluated by performing the circuital analysis.

Accordingly, from the circuital point of view, each radiating element can be modelled as a load equal to its input impedance. Obviously, we have to take into account for the input impedance variations due to the mutual coupling among the antenna elements. The effects of the mutual coupling on the circuital behaviour of our prototype are discussed in Section 4.1.

Regarding the OBFN, we have to model several devices: the laser, the modulator, the star coupler, the combiner, the photodetector and the connections along the devices chain. Moreover we have to employ a proper model for the TTDU.

Regarding the model of the optical devices used in the prototype implementation, we have to take into account for the real characteristics of the commercial devices and for the unavoidable realization defects which can introduce an error on the antenna excitations distribution. The modelling of the considered devices is described in Section 4.2.

Regarding the TTDU model, we refer to the input-output relationship (IV.1) and (IV.2). As discussed in the 4$^{th}$ Chapter, the TTDU losses causes an unbalance of the amplitude of the excitation coefficient which can deteriorate the antenna pattern. A proper compensation strategy has been adopted to reduce the effects of these errors and obtain an amplitude distribution as similar as possible to the desired one. All these issues are discussed in Section 4.3.

Accordingly, once derived a proper model for each OTSA section, the full OTSA model can be found. In this way we can verify the antenna beam squint free behaviour and simulate the whole antenna system. In particular we can evaluate the effects of the realization defects, due to each OTSA device, on the antenna pattern. These aspects are discussed in Section 4.4.

## 4.1 RADIATING SYSTEM MODEL: ELECTROMAGNETIC MUTUAL COUPLING

The electromagnetic coupling effects on the antenna pattern have been already discussed when dealing with the external synthesis procedure. Here we study the effects on the circuital behaviour of the antenna system to derive an efficient model of the radiating system.

To evaluate the circuital deterioration caused by the mutual coupling we have to consider the array impedance matrix $\underline{\underline{Z}} = (Z_{ij})_{i,j=1}^{N}$ [*Mailloux 2005*].

The array can be modelled as an N-port network. Let us denote with $V_1,\ldots,V_N$ and $I_1,\ldots,I_N$ the voltages and currents at each input gate (Fig.5.8). As long as the non linearities of the system can be neglected, we have:

$$\begin{pmatrix} V_1 \\ V_2 \\ \ldots \\ V_N \end{pmatrix} = \begin{pmatrix} Z_{11} & Z_{12} & \ldots & Z_{1N} \\ Z_{21} & Z_{22} & \ldots & Z_{2N} \\ \ldots & \ldots & \ldots & \ldots \\ Z_{N1} & Z_{N2} & \ldots & Z_{NN} \end{pmatrix} \begin{pmatrix} I_1 \\ I_2 \\ \ldots \\ I_N \end{pmatrix} \qquad \text{(V.7)}$$

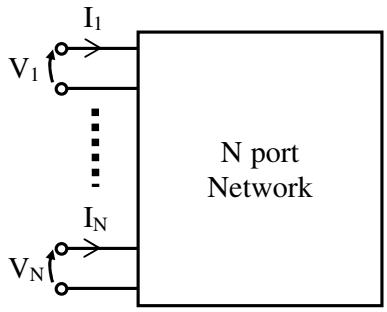


**Figure 5.8** *Circuital model of the array*

The diagonal terms of $\underline{\underline{Z}}$ are referred as autoimpedance terms, while the others are called mutual impedances.

In practice, all the elements are feed. In this case, the impedance at the input of each element, is called active impedance and is given by:

$$Z_{Ai} = Z_{ii} + \sum_{\substack{1 \\ j \neq i}}^{N}{}_{j} Z_{ij} \frac{I_j}{I_i} \qquad \text{(V.8)}$$

The active impedance of the i-th element is given by the autoimpedance term and by a weighted sum of the mutual terms. Accordingly, due to the mutual coupling effects the active impedance can significantly differ from the autoimpedance. Obviously this phenomenon depends on the antenna elements geometry and distance and on the excitation of the array.

The mutual coupling deterioration can cause the bad working of the stage c) of the OTSA (Fig.5.1). In fact, the impedance mismatching can change the detectors working conditions and introduce an unwanted variation of the antenna excitation coefficients.

To estimate the amount of the circuital deterioration caused by the mutual coupling we have carried out a numerical analysis by means of the electromagnetic simulator Ansoft Designer 1.1. In particular, since we are referring to a 4 elements prototype, we considered an array of 4 SSFIP printed elements. Each element has input nominal impedance equal to 100Ω, as described in Appendix C.

The CAD allowed us to evaluate the elements of the impedance matrix as a function of the value of the distance $d_\lambda$ between two contiguous elements, normalized to the wavelength.

The real and the imaginary part of the autoimpedances are reported in Fig.5.9 and Fig.5.10, respectively. As expected, there is symmetry between the 2nd and the 3rd element and between the 1st and the 4th element. We observe that the real parts vary in the interval [98 Ω, 104Ω], while the imaginary parts go to zero when $d_\lambda$ grows. Then, the effects of the mutual coupling on the auto impedances parameters are negligible for $d_\lambda$ above 0.6 ÷0.7.

The magnitude and phase of the mutual impedances, as function of $d_\lambda$, are shown in Fig.5.11 and.5.12, respectively. Thanks to the matrix symmetry we can refer only to 6 elements of the impedance matrix: $Z_{12}$, $Z_{13}$, $Z_{14}$, $Z_{23}$, $Z_{24}$ and $Z_{34}$. It is easy to note

that the mutual coupling effects among close elements can be neglected for values of $d_\lambda$ grater than 0.6÷0.7.

By referring to the broadside beams, the real and the imaginary part of the auto impedance of the 1st and the 2nd element are reported in Fig.5.13 and 5.14, as a blue and a red dashed line, respectively. A significant mismatching is observed.

The same quantities are reported in Fig.5.15 and 5.16, referring to the 30º beam pointing angle case. It must be noted that the real part of the active impedance has a 10% variation when the beam pointing direction is varied from the broadside to a 30° angle.

These analysis confirm that the mutual coupling introduces serious mismatching to be managed with an appropriate approach.

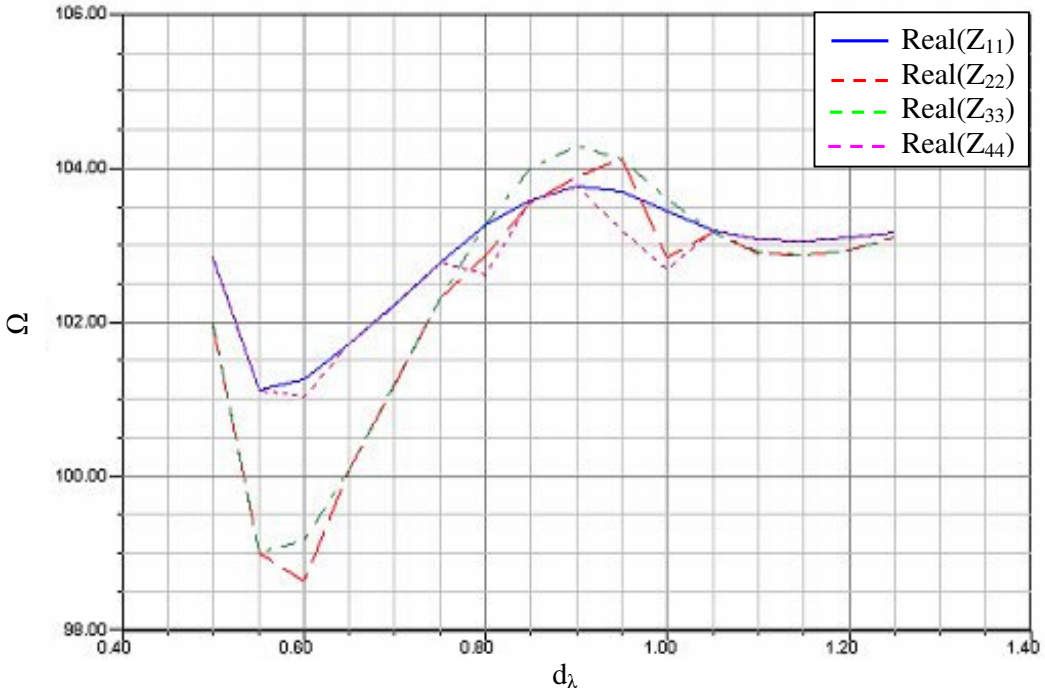


**Figure 5.9** *Real part of the autoimpedances as function of $d_\lambda$*

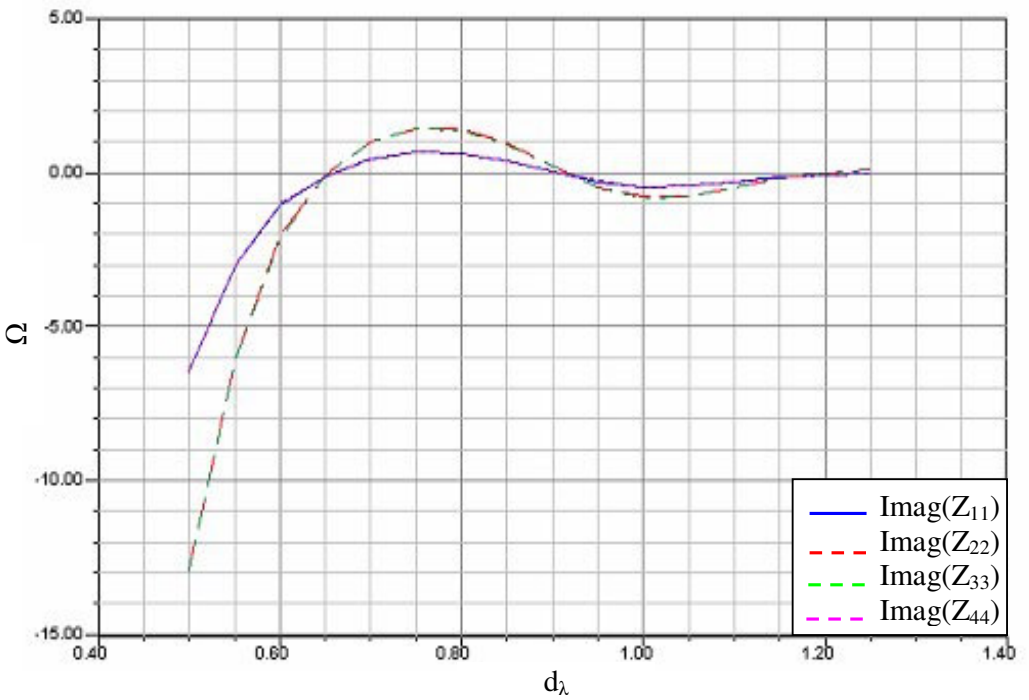


**Figure 5.10** *Imaginary part of the autoimpedances as function of $d_\lambda$*

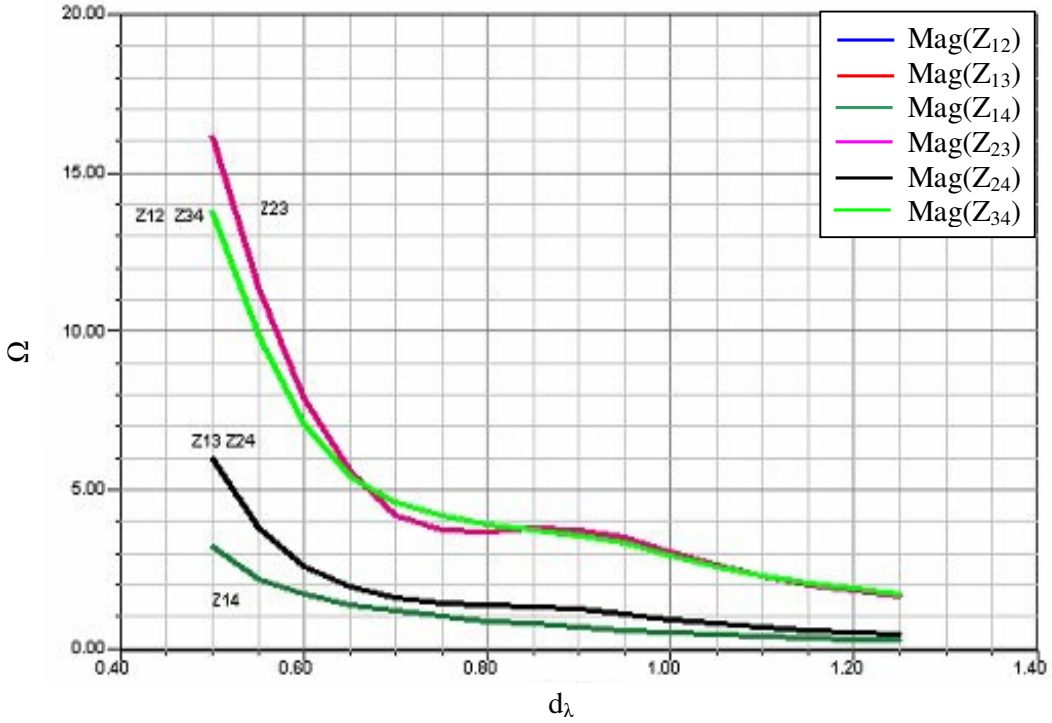


**Figure 5.11** *Magnitude of the mutual impedances as function of $d_\lambda$*

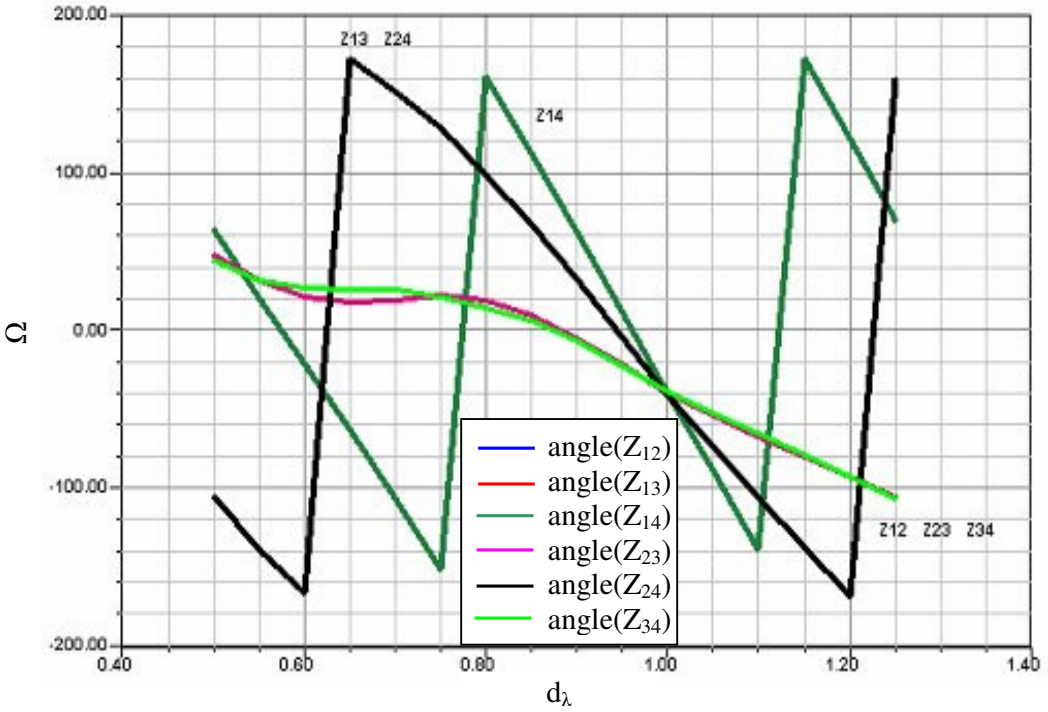


**Figure 5.12** *Phase of the mutual impedances as function of $d_\lambda$*

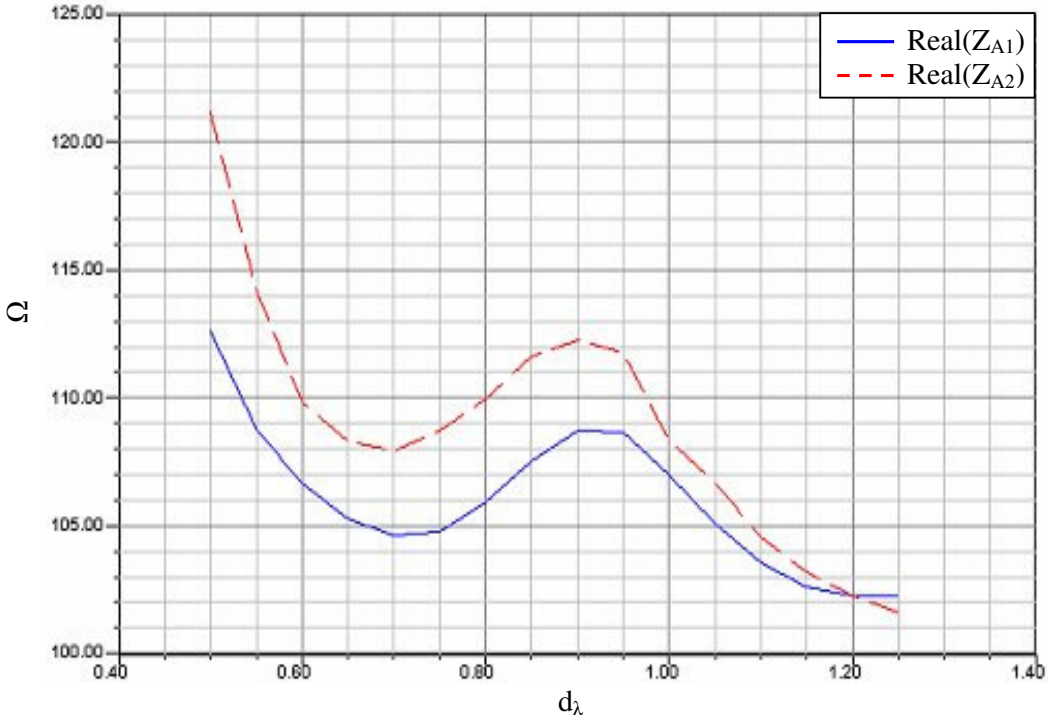


**Figure 5.13** *Real part of the active impedances, related to the 1st and the 2nd element, as function of $d_\lambda$: broadside case*

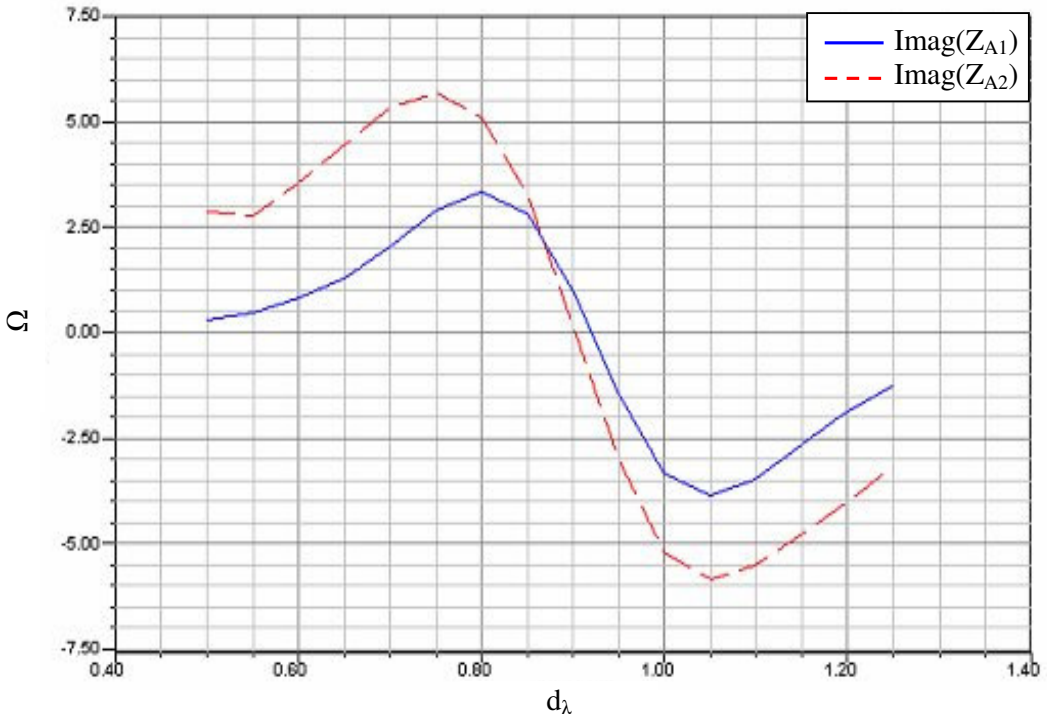


**Figure 5.14** *Imaginary part of the active impedances, related to the 1st and the 2nd element, as function of dλ: broadside case*

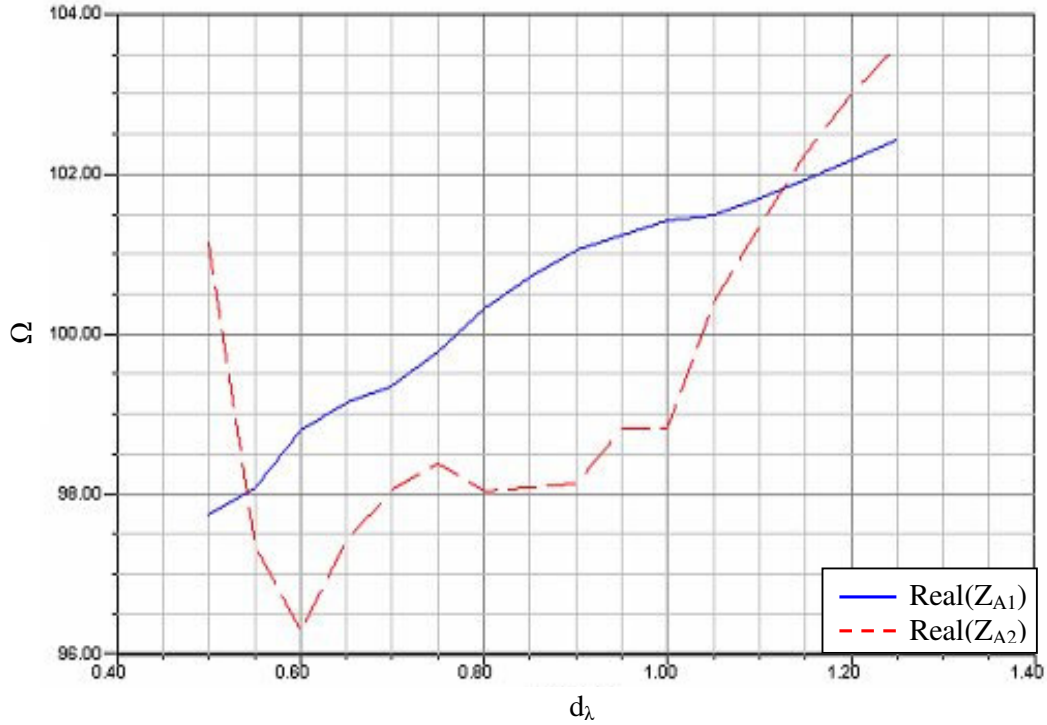


**Figure 5.15** *Real part of the active impedances, related to the 1st and the 2nd element, as function of dλ: 30º case*

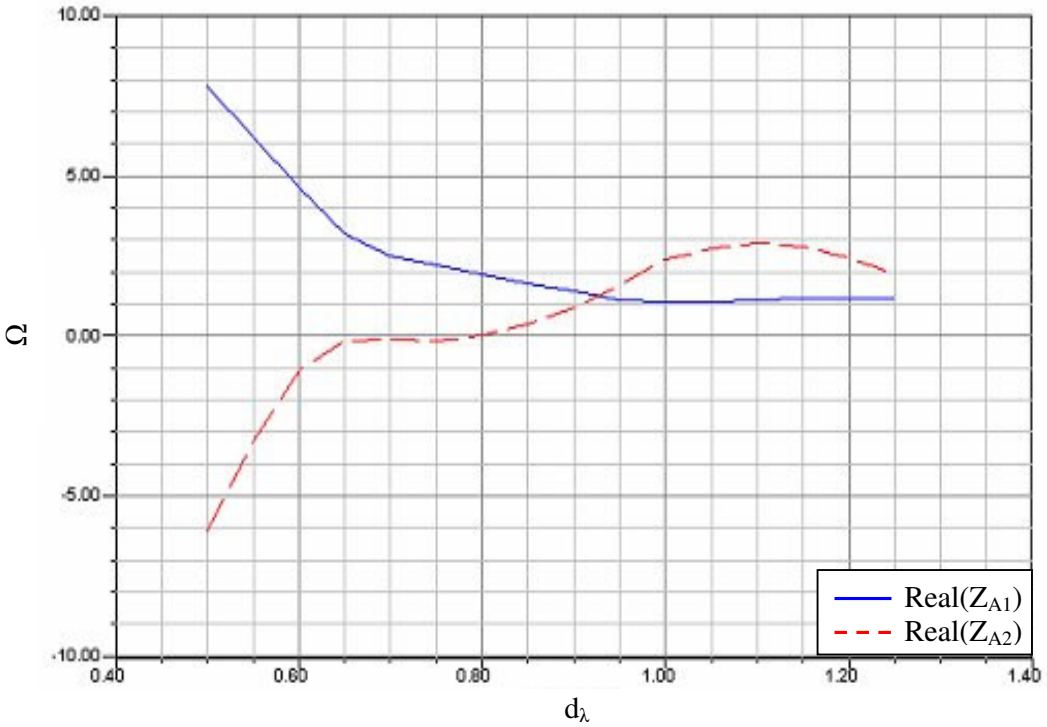


**Figure 5.16** *Imaginary part of the active impedances, related to the 1st and the 2nd element, as function of $d_\lambda$: 30º case*

To control the mismatching effects the conversion stage c) has been modified by introducing an isolation circuit between the photodetector and the radiating element. The isolation can be obtained by using an isolator or an amplifier provided with a good isolation factor between output and input. In Fig.5.17 we report the scheme of the stage c) which includes the isolation section.

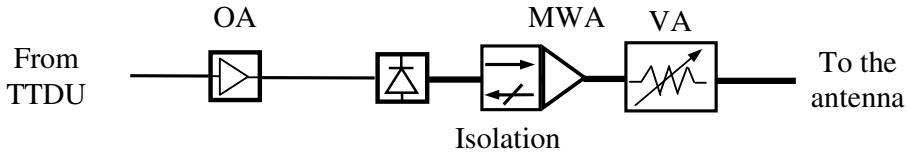


**Figure 5.17** *Conversion stage with the isolation circuit*

Since, according to these considerations, in the real implementation we will employ isolators or matching circuits, the radiating elements can be simply modelled as a load matched to the feeding line.

## 4.2 OPTICAL DEVICES MODELS

As told before, the models of the optical devices needed to implement the OTSA prototype have been designed to take into account for the effective characteristics of the commercial devices and for the unavoidable realization defects.

The main optical devices are the laser, the modulator, the photodetector, the star coupler/combiner and the optical connections.

The laser source has been modelled as a module that furnishes a continuous wave optical signal having frequency $\Omega$ [Hz], linewidth $\Delta\Omega$ [Hz], average power $P_{LAS}$ [W] and having a certain initial phase $\Phi_i$ [degree]. Moreover, to take into account for the noise we can specify the Relative Intensity Noise (RIN) level [dB], measured at a certain power level. Regarding the polarization of the laser light we do not deal about it, since we assume that the optical system allows maintaining the polarization state.

The MZM has been characterized by the following parameters (see Appendix B, Section 1): $V_{\pi DC}$ [V] the DC voltage required to realize a $\pi$ phase difference, $V_{\pi RF}$ [V] the RF voltage required to realize the $\pi$ phase difference, insertion loss [dB] and extinction ratio [dB] that takes into account for the real splitting ratio among the MZM arms.

Regarding to photodetector, it has been modelled as en envelope detector having bandwidth B [Hz] and responsivity $r_{PD}$ [A/W]. Moreover, the model takes into account for thermal, dark and shot noise processes. The thermal noise is defined by the spectral density $N_{TH}$ [$A/Hz^{0.5}$], the dark current is represented by the parameter $i_{PD}$ [A], while the shot noise has a spectral noise density proportional to the photodector output current as discussed in the Appendix B (Section 1).

Regarding the optical star coupler and combiners, the model of these devices is simply characterized by the number $N_{port}$ of inputs or outputs. However, for such devices we have to take into account the unavoidable realization defects like asymmetric power divisions or time delay unbalances. These defects can cause unwanted amplitude or time delay variations that can deteriorate the antenna excitations coefficients. The effects of such errors on the antenna aperture distribution are discussed in Section 4.4.

Here we will describe the model exploited to take into account these unwanted variations. In particular, we will refer to the amplitude variations. The time delay variation can be treated analogously.

The amplitude variations are due to the random variations of the insertion loss of the star coupler/combiner. The characterization of the IL variation of such devices has been studied in the literature where it has been shown that star coupler and power combiner IL variations can be described with a Gaussian distribution [*Harres*; *Herrmann and Murphy*]. Therefore, the star coupler can be modeled as a device imposing a constant power loss, related to the number of outputs, plus a random insertion loss term, different for each channel, having a Gaussian distribution with a proper standard deviation. In the scheme of the corresponding model of a 4 output star coupler is shown (Fig. 5.18). The insertion loss $IL_{SC4}$ is essentially equal to 6dB for each channel. Moreover to account for the random variation of the output power, each outputs is connected to a module imposing a variable random attenuation on the considered signal, having a Gaussian distribution with mean 0 dB and standard deviation $\sigma_i$.

As referred before, time delay unbalances can be taken into account in a similar way.

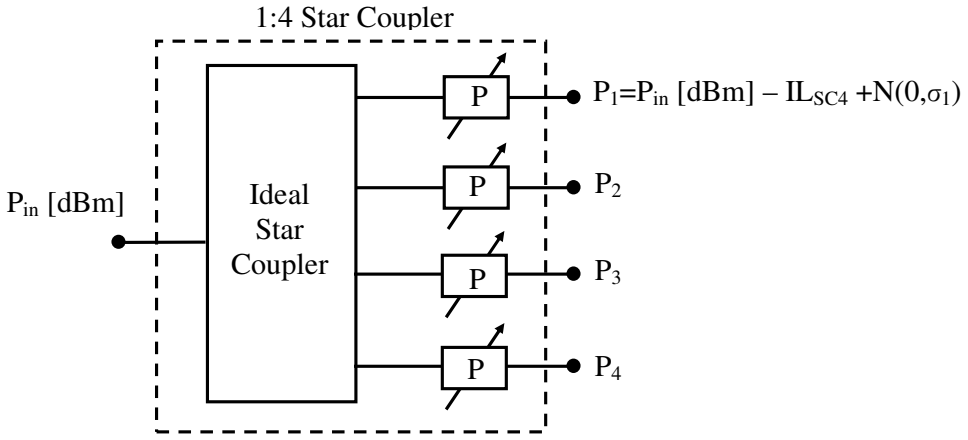


**Figure 5.18** *Model of a 1:4 optical star coupler taking into account for realization defects*

A similar approach can be used to model the optical connections. In fact, the model of the connection is defined by the connection insertion loss (dB) plus a random term taking into account for the practical realization. In particular, a truncated Gaussian [*Herrmann and Murphy*] or a Log-Normal [*Uhing et al.*] distribution can be used.

## 4.3 TTDU MODELLING

According to the TTDU input-output relationship given by eq. (IV.1) and (IV.2), the TTDU determines an attenuation and a programmable time delay on the optical signals.

For the sake of simplicity, let us consider the 3 bit – 4 elements configuration. In particular let us refer to the model of one TS implemented within the TTDU. The model of the other TS can be derived in similar manner.

In this case, each TS realizes 8 delays by exploiting 2 inputs and 4 outputs. As consequence, each input signal generates 4 signals with a certain delay and attenuation, according to the related input-output pair (r,s), as shown in the scheme represented in Fig.5.19.

The realization defects can be taken into account by introducing random attenuation and delay modules with a desired deviation. We can assume a Gaussian distribution for these error sources.

Programmable ideal switches, introducing no signal attenuation or delay, drive the selected signal to related output, according to the TS control unit (Fig.5.19). Obviously, each TS furnishes only one delayed signal. Accordingly, only one TS output is active. The switches related to the non active outputs are wired to a fictitious null signal.

The modules of each TS are used together to realize the model of the whole TTDU. A control logic has been implemented to drive correctly each TS according to the desired beam pointing angle, as shown in Fig.5.20.

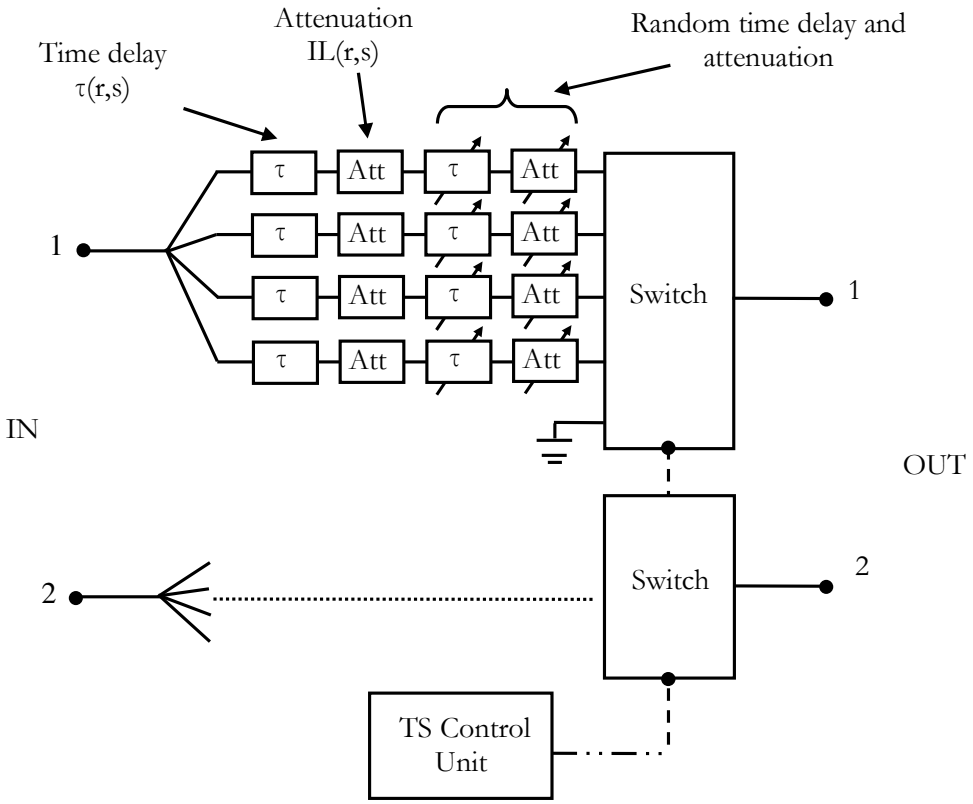


**Figure 5.19** *Model of one TS realized with the TTDU*

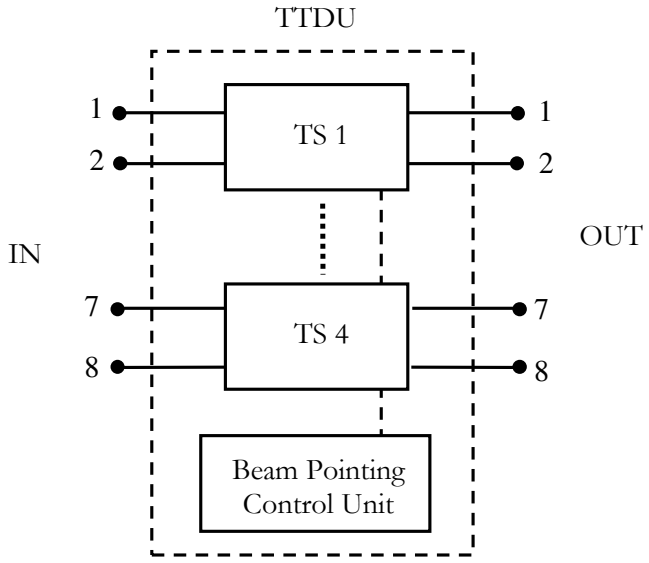


**Figure 5.20** *Model of the TTDU in the 3 bit- 4 element working configuration*

As described in Section 2 of the 4th Chapter, the parameters defining the working of the TTDU are: C, R and T, the desired beampointing angle provided to the beampointing unit, the IL and the time delays standard deviations which take into account for the TTDU realization defects.

### 4.3.1 AMPLITUDE ERRORS DUE TO TTDU LOSSES

As discussed in the Section 3.2 of the 4th Chapter, the TTDU losses cause amplitude errors on the excitations distribution. The losses vary with the input-output pair (r,s) according to eq. (IV.2). As consequence, the effects of these errors change with the beam pointing configuration.

Let us refer to the 4 bit – 4 elements working configuration realizing a $\tau_{max}$=202.5ps. In tab.5.4 we report the input-output pairs and the IL related to the TTDU, for three different beam pointing angle: $\theta=0^o$, $\theta=\theta_{max}$, $\theta=-\theta_{max}$. Accordingly, no amplitude errors are reported for the broadside beam, while the maximum unbalance between the 1st and the 4th element is obtained when considering the maximum scan angle.

| | **IL (dB) – (r,s)** | | | |
|---|---|---|---|---|
| $\theta=0^o$ | 2.81dB– (4,1) | 2.81dB– (3,2) | 2.81dB– (2,3) | 2.81dB– (1,4) |
| $\theta=\theta_{max}$ | 2.81dB– (4,1) | 4dB– (11,11) | 5.19dB– (18,21) | 6.38dB– (25,31) |
| $\Theta=-\theta_{max}$ | 6.38dB– (28,28) | 5.19dB– (19,20) | 4dB– (10,12) | 2.81dB– (1,4) |

**Table 5.4** *TTDU insertion loss and input-output pairs in the 4 bit – 4 elements working configuration*

Accordingly, the related pattern deterioration grows with the beam pointing angle. To give an example of the effects of such errors, let us consider a 4 elements array, with design frequency $f_D$=10GHz and half a wavelength spacing, driven by the TTDU working in the considered configuration and let us refer to the maximum scan angle $\theta_{max}$ achievable with the TTDU. The array factor achieved with a uniform amplitude distribution and the one achieved with the real amplitude distribution realized by the TTDU, according to Tab.5.4, are reported in Fig.5.21. In both cases we refer to the same time distribution furnished by the TTDU to steer the beam towards $\theta_{max}$.

Figure 5.21 shows that the TTDU losses are responsible of a strong deterioration of the beam nulls, an increase the SLL and the broadening of the radiated beam.

Accordingly, it is necessary to cancel these unwanted effects. Losses compensation can be achieved by introducing trimming stages, which amplify or attenuate the light signal, within the OBFN.

The main issue is that the TTDU introduces different unbalances for each beam pointing configuration. Moreover, for each TS, different delays are realized by sharing some common TTDU inputs or outputs. In this way, when compensating the signal, for example by introducing attenuation at one TTDU outputs, an unwanted attenuation is introduced on other time delay configuration related to the same TS. Accordingly, the losses compensation is not a trivial task.

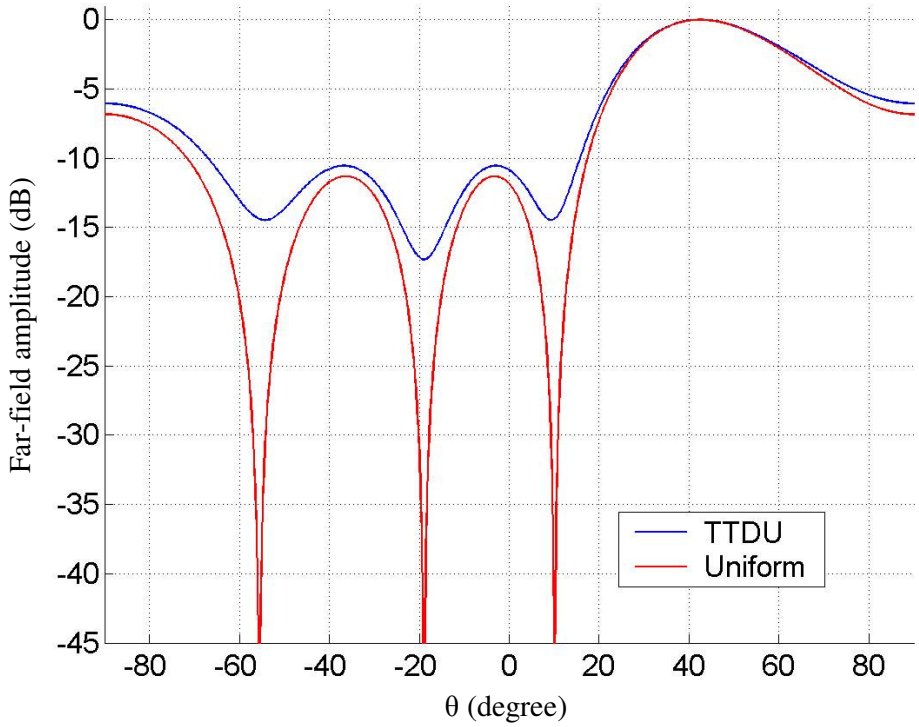


**Figure 5.21** *Comparison between the array factor related to a uniform amplitude distribution and to the one realized by the TTDU corrupted by the losses within the chip*

### 4.3.2 TTDU LOSSES COMPENSATION

In principle, we can introduce a number of trimming devices within the OBFN The trim stages configuration that can be adopted to compensate for the TTDU losses in the considered working configuration is shown in Fig. 5.22. In this case 20 trimming units have been considered.

As seen, to reduce both the pattern deterioration for all the possible beam configurations, to reduce the hardware complexity of the trimming stages network and to efficiently use the available trimming units, it is worth to study an effective trimming strategy. We will consider the mentioned Tchebitchev distribution with normalized amplitude coefficients equal to 0.75, 1, 1, 0.75, previously discussed.

To optimize the effects of the trimming stages and find the number, position and trimming amount (attenuation or amplification) and obtain an amplitude distribution as close as possible to the nominal one, an evolutionary algorithm has been implemented.

To set up the evolutionary algorithm we taken advantage of the know how and the background available at the Electromagnetic research group of the Department of Electronic and Telecommunication Engineering of the University of Naples Federico II [*Capozzoli and D'Elia 2006a*; *Capozzoli and D'Elia 2006b*] and referred to the open literature [*Back et al.*].

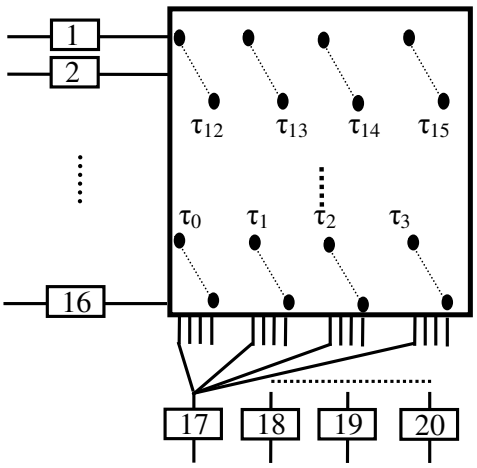


**Figure 5.22** *Trim stages configuration for the TTDU configuration 4 BIT– 4 elements – non contiguous outputs mode*.

For an assigned number of beam configurations and using a small number of trim units, the implemented evolutionary algorithm gives the set of the trimming amount minimizing the TTDU losses effects and ensuring a far field pattern as near as possible to the one achievable with a Tchebtichev amplitude distribution.

An evolving population is considered wherein each individual is made by a set of 20 trimming amounts corresponding to the 20 trim units shown in Fig.5.22. The initial population is made by $N_{pop}$ elements, wherein one element corresponds to a zero trimming amounts for all the 20 trim units, while the other $N_{pop}$-1 elements correspond to trimming amounts randomly distributed over a given interval.

Once the starting population is chosen, the objective functional, say X, is estimated. In our case X is defined as the sum of the distances between the desired amplitude coefficients and the ones realized with the TTDU, for all the K beams, plus the number, say $M_{ON,}$ of trim units, i.e.,:

$$X = \sum_{k=1}^{K}\left(\sum_{n=1}^{4}\left|A_{TTDU}(k,n) - A_{TCH}(n)\right|\right) + \alpha M_{ON} \qquad (V.9)$$

$A_{TTDU}$ being the excitation coefficients provided by the TTDU, (depending on the beam pointing configuration), $A_{TCH}$ the Tchebitchev amplitude coefficients and $\alpha$ a weighting factor. It must be noted that the first term of eq. (V.9) accounts for the trim compensation effect while the second term accounts for the hardware complexity of the trimming stages.

The evolutionary algorithm minimizing the objective functional is based on an iterative process made of three steps: selection, recombination and mutation. In particular we used a tournament selection operator, an extended intermediate recombination process and a Gaussian mutation procedure.

In the tournament selection, $q_T$ individuals are randomly chosen from the population to take part in a tournament. The functional is evaluated for each individual. The winning element is the one corresponding to the minimum functional. In our case the winning elements is inserted into the new population and the procedure is repeated $N_{pop}$ times, until all the individuals of the new population are obtained. In

this procedure the elements that take part in a tournament are not drawn away from the population.

The tournament selection operator gives a new population, made of properly selected individuals of the previous population. A recombination process is then applied to the new population: the extended intermediate operator. Given a pairs of consecutive population individuals, these are used as parents to generate an element of the next population. If we call $a_i$ and $b_i$ the two parents, the related offspring $c_i$ is given by:

$$c_i = a_i + \xi\left(b_i - a_i\right) \tag{V.10}$$

where $\xi$ is a uniform random variable over $[-\delta,1+\delta]$, $\delta$ being a parameter which establishes the exploration interval. Usually $\delta$ is taken greater than zero in order to explore also outside the interval $[a_i,b_i]$. From a geometrical point of view, we can image that the offspring $c_i$ belongs to the hypercube defined by the components of the individuals $a_i$ and $b_i$, incremented to take into account for the exploration parameter $\delta$.

The new population obtained by the recombination procedure undergoes a mutation process. We considered the Gaussian mutation process, where the next population individual $a_i'$ is given by the current population element $a_i$ plus a Gaussian random variable $N(0,\sigma_i)$, with zero mean and standard deviation $\sigma_i$ different for each population individual. In particular we have:

$$a_i' = a_i + N\left(0,\sigma_i\right) \tag{V.11}$$

This procedure is repeated for $N_{pop}$-1 individuals, since the elitist strategy is used. This strategy, improving the algorithm convergence, requires that the best element of the previous population is always maintained in the next population.

The life cycle is repeated until the functional does not reach a certain minimum or until a specified number of iterations $N_{it}$ is obtained.

Here we report the results related to two different configurations corresponding to the 4 bit – 4 elements configuration with a $\tau_{max}$=90ps and a $\tau_{max}$=202.5ps. The latter case involves amplitude unbalances more serious than the first one. For both cases the beam pointing set considered to realize the optimization is given by 5 beam pointing directions: $\theta_1$=0º, $\theta_{2,3}$=±20º, $\theta_{4,5}$=±40º.

In the first case, the TTDU feeds a 4 elements antenna working at 15GHz. The parameters used during the optimization process are $N_{pop}$=100, $N_{it}$=500, $q_T$=10, $\delta$=1, $\sigma_i$=2.5. For the sake of comparison, the nominal Tchebitchev array factor and the ones obtained with and without compensation, for all the five beams are reported in Figs.5.23-5.27. The trimming amounts obtained for all the trim units are reported in Fig.5.28. The evolutionary algorithm allows to obtain a far field pattern quite similar to the desired one by employing only 6 trim units.

In the second case, the TTDU feeds a 4 elements antenna working at 5GHz. Different trim units configurations have been found by varying the weighting parameter $\alpha$. Some configurations allows to obtain a very good agreement for all the 5 beams, by using almost all the possible trim units, while other configurations employ few trim units but do not allow a very good result from the array factor point of view. Here we present an intermediate solution where only 11 trim units have been found. The algorithm parameters are: $N_{pop}$=100, $N_{it}$=1000, $q_T$=2, $\delta$=0.5, $\sigma_i$=0.75. The nominal Tchebitchev array factor and the ones obtained with and without compensation, for all

the five beams are reported in Figs.5.29-5.33. The trim amounts obtained for all the trim units are reported in Fig.5.34.

In conclusion it is necessary to include the trim stages into the OTSA prototype and the algorithm we developed helps the designer to find the correct trim parameters.

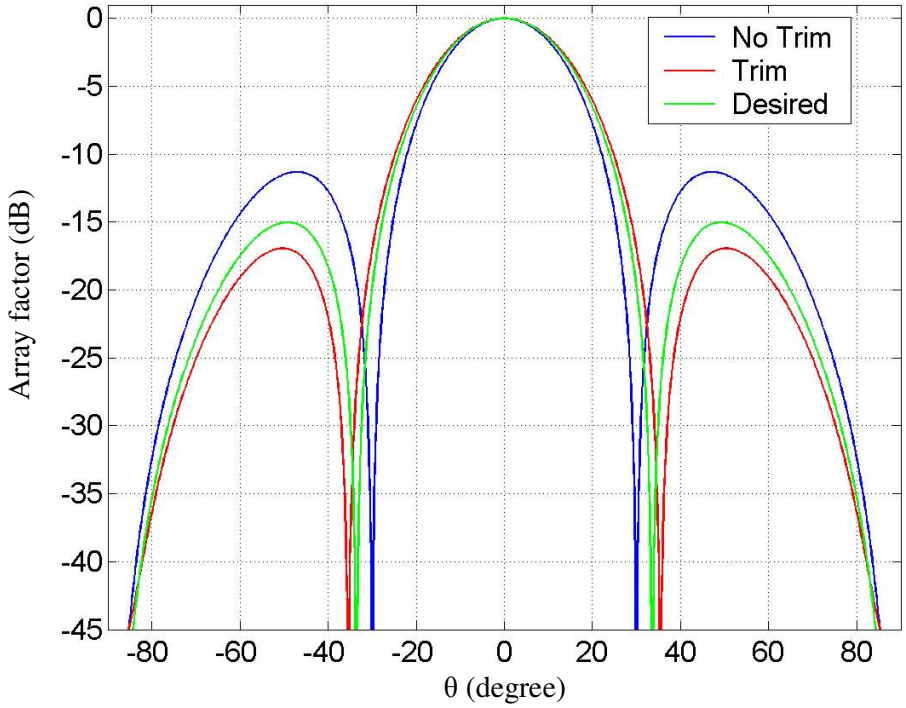


**Figure 5.23** *Comparison among the desired array factor and the one obtained with and without compensation: broadside case ($\tau_{max}$=90ps)*

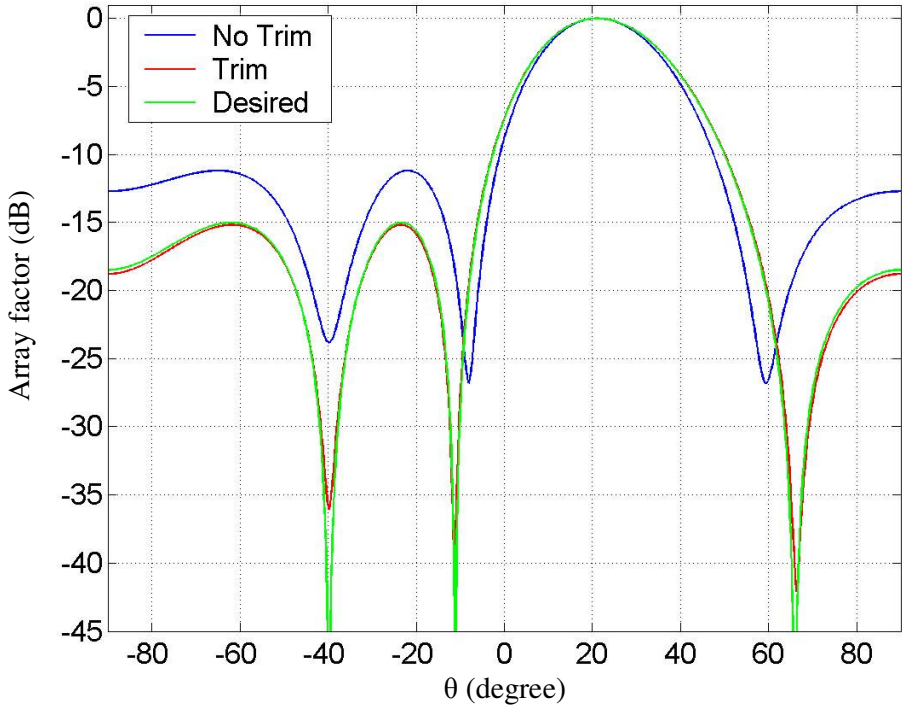


**Figure 5.24** *Comparison among the desired array factor and the one obtained with and without compensation: $\theta$=20º ($\tau_{max}$=90ps)*

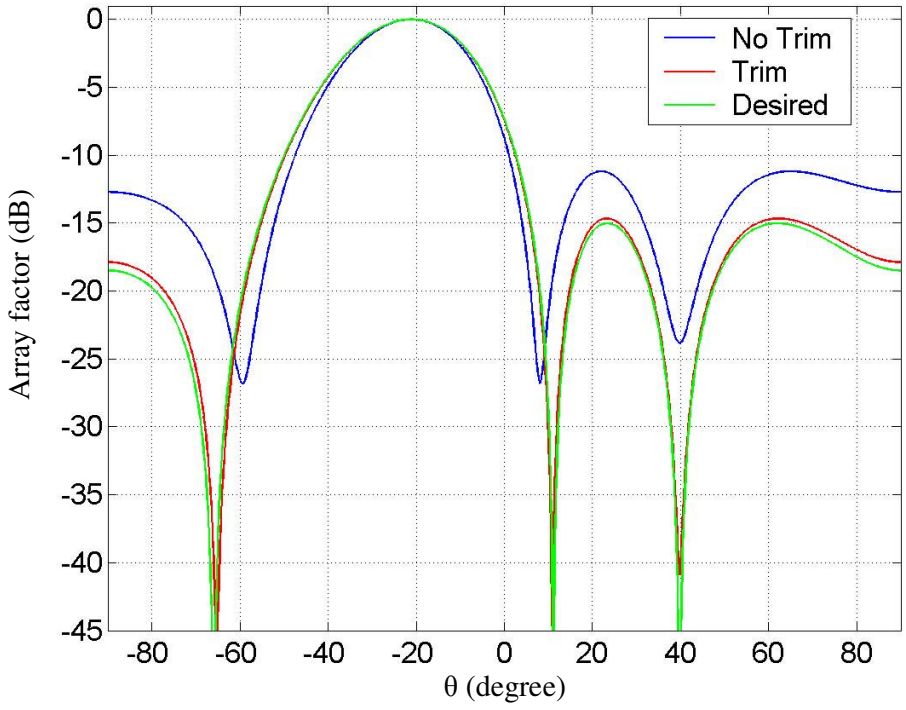


**Figure 5.25** *Comparison among the desired array factor and the one obtained with and without compensation: $\theta$=-20º ($\tau_{max}$=90ps)*

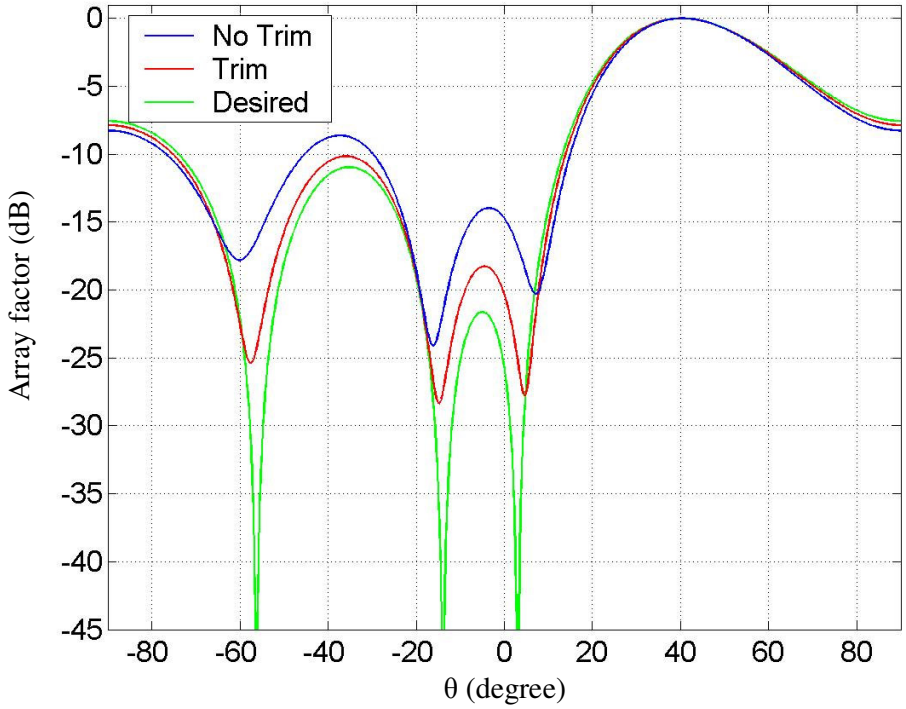


**Figure 5.26** *Comparison among the desired array factor and the one obtained with and without compensation: $\theta$=40º ($\tau_{max}$=90ps)*

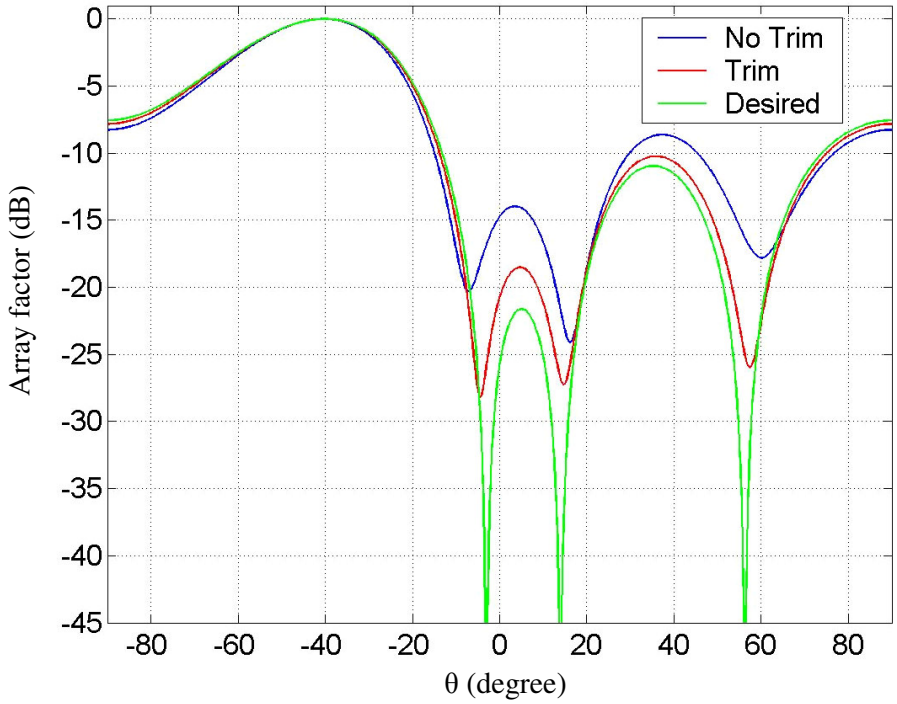


**Figure 5.27** *Comparison among the desired array factor and the one obtained with and without compensation: $\theta$=-40º ($\tau_{max}$=90ps)*

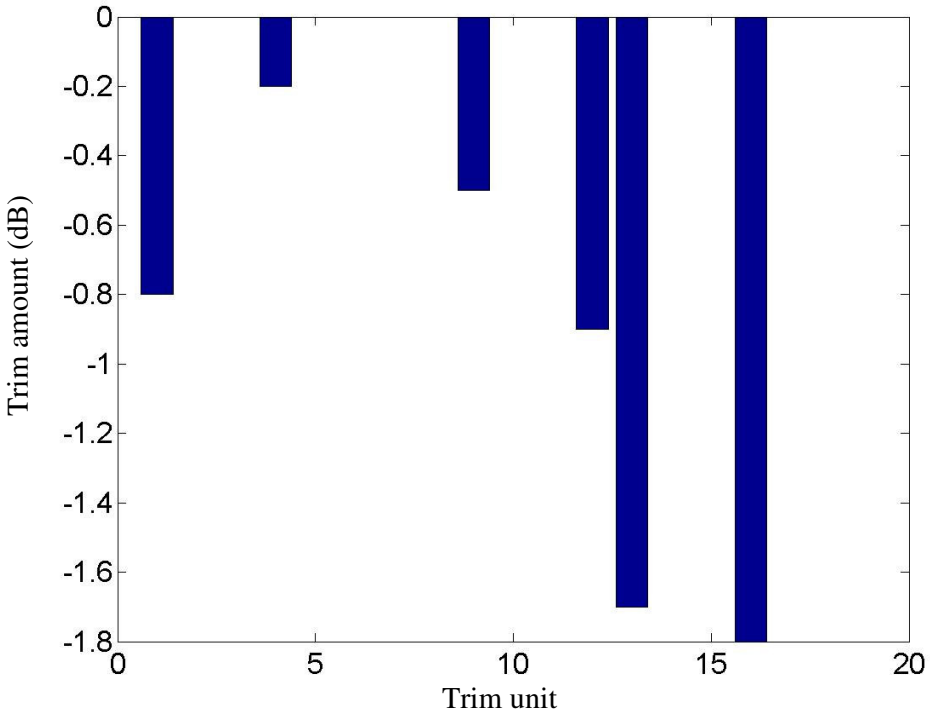


**Figure 5.28** *Trim amounts to be applied for each of the 20 trim devices ($\tau_{max}$=90ps)*

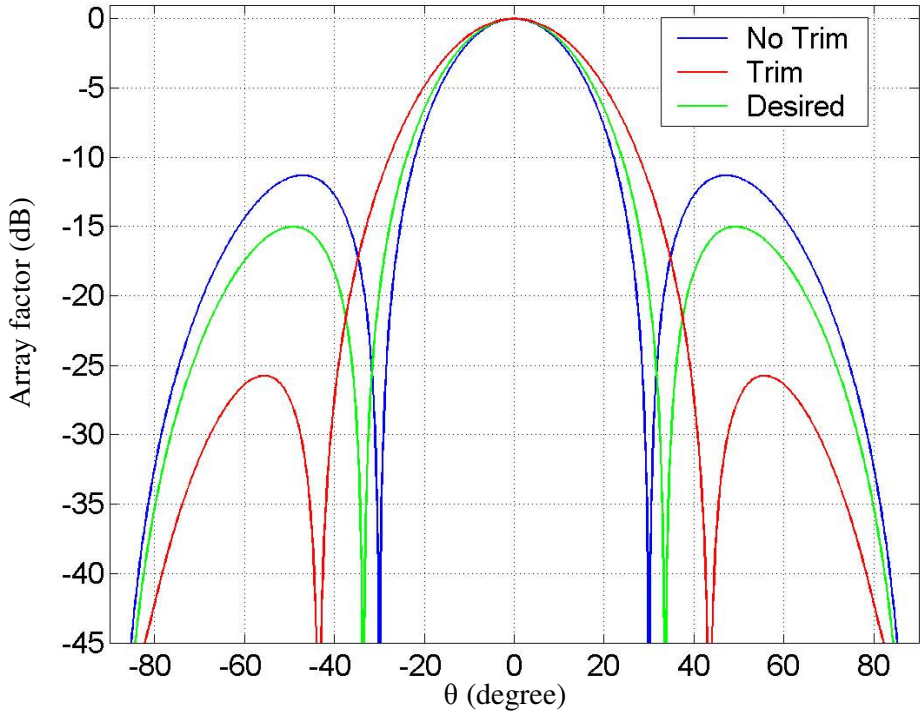


**Figure 5.29** *Comparison among the desired array factor and the one obtained with and without compensation: broadside case ($\tau_{max}$=202.5ps)*

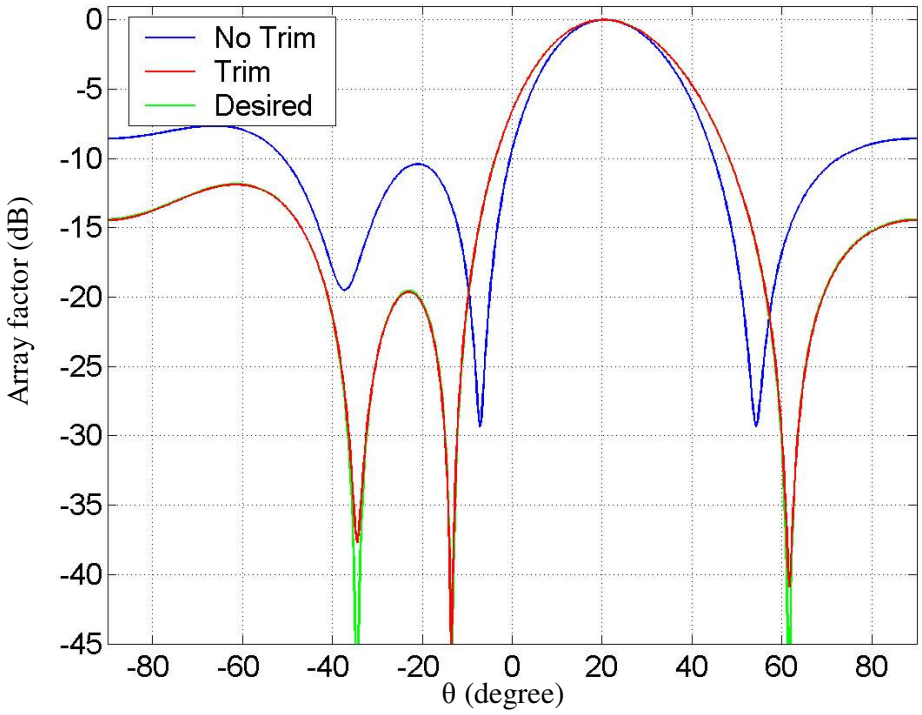


**Figure 5.30** *Comparison among the desired array factor and the one obtained with and without compensation: $\theta$=20º ($\tau_{max}$=202.5ps)*

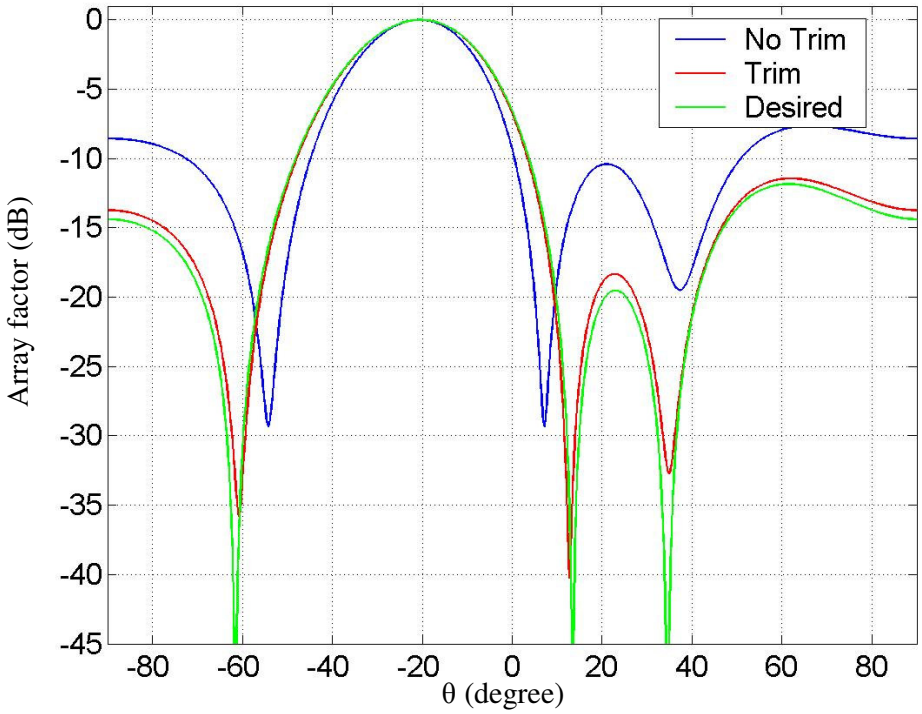


**Figure 5.31** *Comparison among the desired array factor and the one obtained with and without compensation: $\theta$=-20º ($\tau_{max}$=202.5ps)*

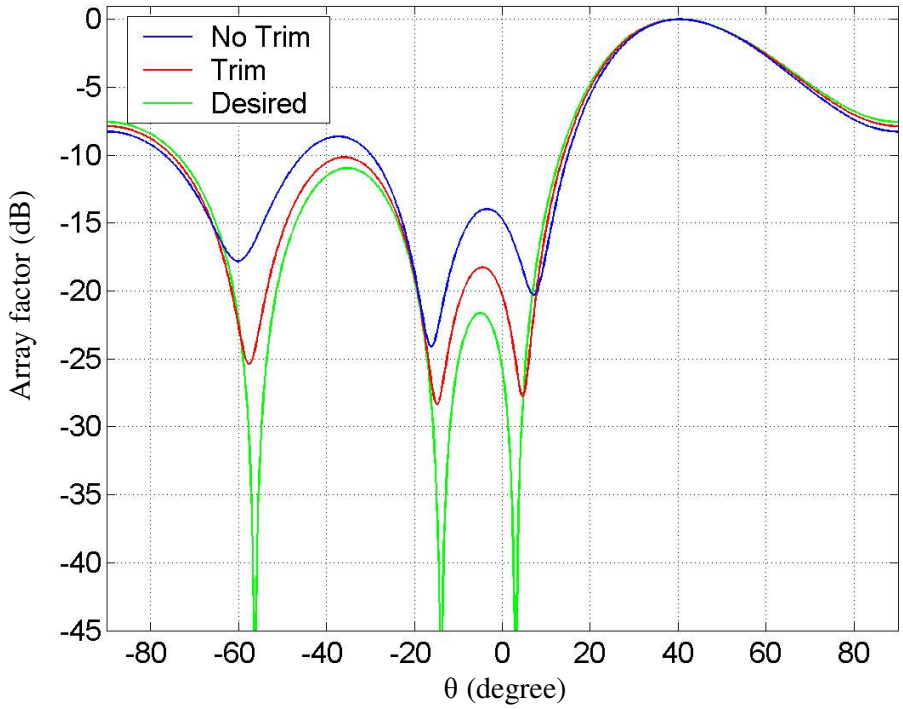


**Figure 5.32** *Comparison among the desired array factor and the one obtained with and without compensation: $\theta$=40º ($\tau_{max}$=202.5ps)*

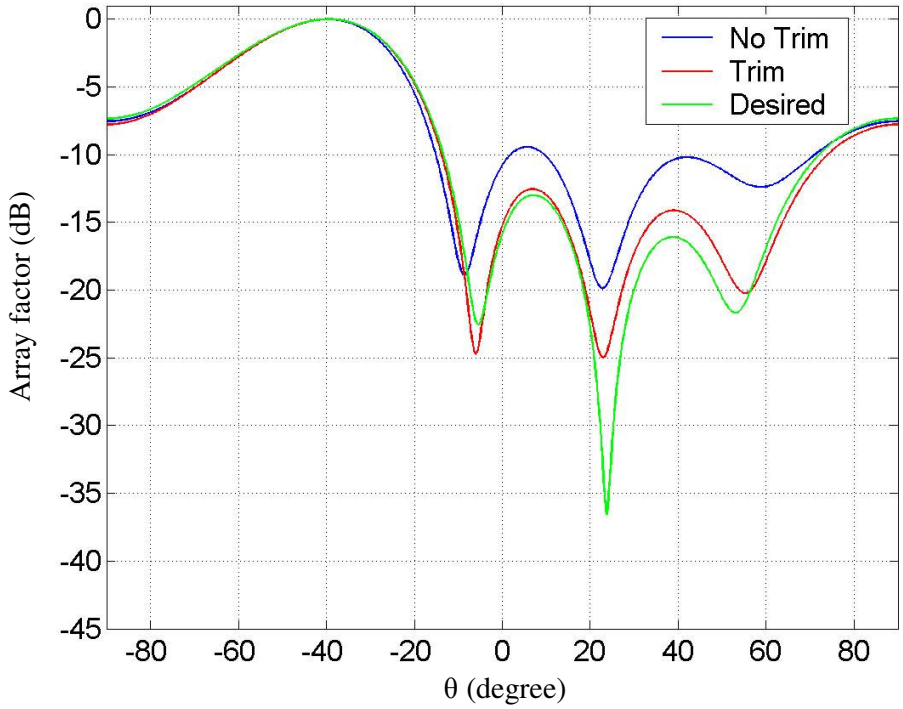


**Figure 5.33** *Comparison among the desired array factor and the one obtained with and without compensation: $\theta$=-40º ($\tau_{max}$=202.5ps)*

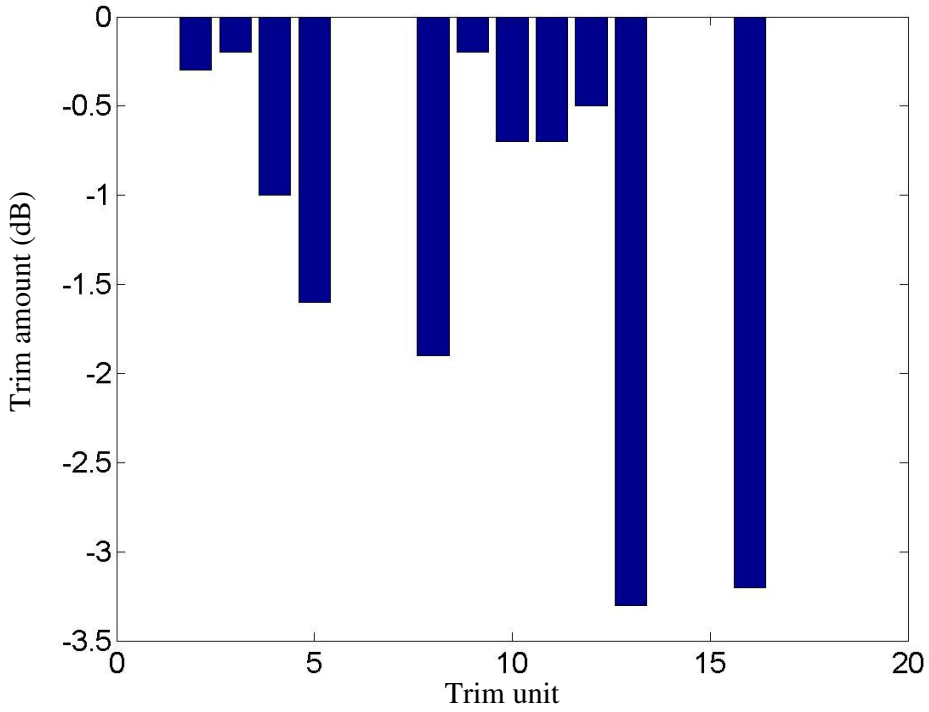


**Figure 5.34** *Trim amounts to be applied for each of the 20 trim devices ($\tau_{max}$=202.5ps)*

## 4.4 OTSA MODEL

Once the model for each OTSA section is derived, we can build the model of the whole OTSA. In particular the scheme of the whole OBFN for the 3 Bit – 4 elements TTDU working configuration is reported in Fig. 5.35.

The laser module generates the optical signal feeding the MZ modulator. Other inputs are also applied to the MZ module: the MW modulating signal and the biasing one. The modulated signal feeds a 1:8 SC, which is wired to the TTDU. The TTDU outputs are driven to the related photodetector by means of four 4:1 combiners. The connections are represented by a little black box. The input section can be realized in the integrated technology. Therefore, when modelling this section, it is reasonable to use random errors smaller than the one related to the output section.

Let us consider a tone modulating the MW signal and assume that the noise sources can be neglected. Under these conditions, the output signals are an attenuated version of the modulating tone, each one properly time shifted, according to the desired beam pointing angle. Therefore, the achievable array factor can be easily derived from the amplitude and the time delay of each output signal. By varying the frequency of the tone, it should be verified the absence of the beam squint. The array factor of an antenna made by 4 half wavelength spaced elements, with a fixed beam pointing angle equal to 20° and a nominal working frequency equal to 15GHz, is reported under Fig. 5.36 as a function of the observation angle and the frequency. As expected, from this Figure, it can be verified the absence of the beam squint

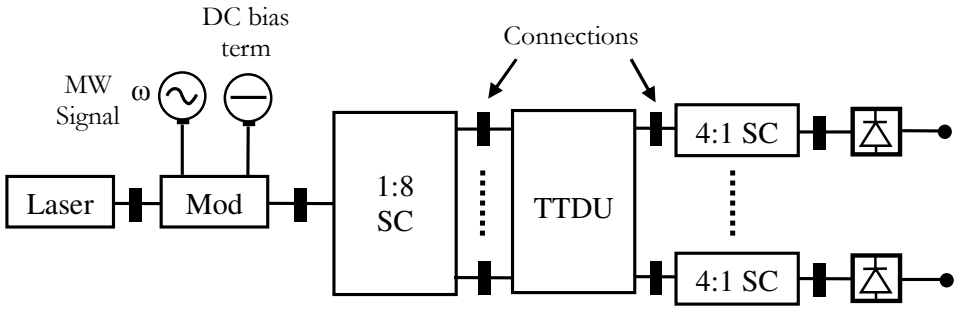


**Figure 5.35** *Model of the OBFN referring to the 3 bit – 4 elements working configuration*

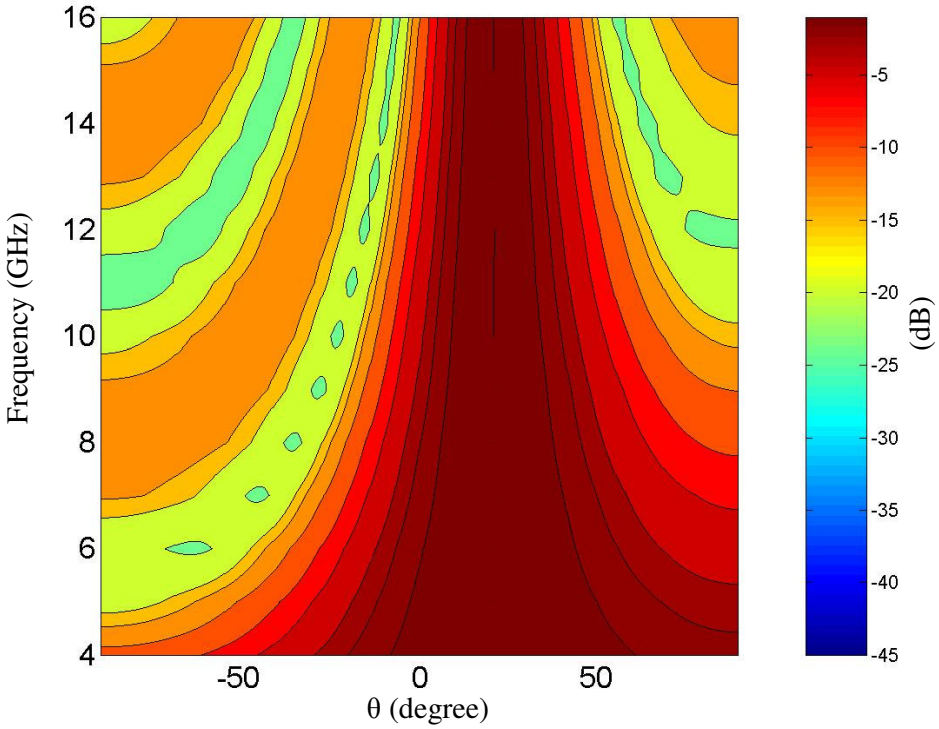


**Figure 5.36** *Array factor intensity plot as function of the angle θ and the frequency of the MW signal achieved using the model of the OBFN based on the TTDU working in the 3 bit – 4 elements configuration.*

The antenna pattern presented in Fig.5.36 has been evaluated without considering the OTSA realization defects and the related antenna excitation deterioration.

Let us now estimate the amplitude and phase errors of the excitation coefficients, due to the realization defects.

In particular, let us refer to the 3 bit – 4 elements working configuration whose scheme, discussed in the 4th Chapter (Section 3.2.2), is reported in Fig. 5.37. The devices related to each TS, responsible of possible realization defects, are: the TTDU, two SCs in the stage a) and c) respectively, the external delay line and all the connection of each device.

Let us analyze the effects of the realization defects on the amplitude of the excitation coefficients. A similar approach can be adopted for the phase.

According to the procedure exploited for the fiber-optic links, two different analyses can be used: the worst case analysis and the statistical one [*Harres*; *Herrmann and Murphy*]. In the worst case procedure, the maximum variation of the excitation coefficients is obtained from the knowledge of the maximum and the minimum IL determined for each components.

On the other hand, the statistical analysis is based on the IL statistical models of each exploited device (see Section 4.2).

Accordingly, for a given beam pointing configuration, corresponding to an assigned TTDU working configuration, the mean value of the IL of each TS is given by the sum of the means of the losses due to the optical devices involved, while the variance is given by the sum of the variances. Since, all the losses can be modeled as Gaussian variables, the resulting IL is a Gaussian variable too.

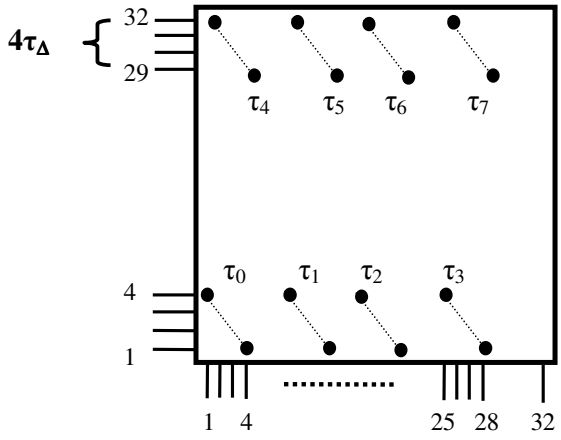


**Figure 5.37** *TTDU working configuration: 3 BIT– 4 elements – non contiguous outputs*

In our case the TTDU is fed by mean of a 1:8 SC, while in the output stage a 4:1 combiner is used. Moreover, there are four connections: the one among the modulator and the input SC, the one between the input SC and the TTDU, the one between the TTDU and the output SC and the one between the SC and the photodetector. The mean loss $IL_{mean}$ is given by:

$$IL_{mean}(r,s) = IL_{TTDU}(r,s) + IL_{SC8} + IL_{CM4} + 4IL_{conn} \qquad (V.12)$$

where the value of the $IL_{TTDU}(r,s)$ is given by the (IV.2), $IL_{SC8}$ is the mean value of the IL related to the 1:8 SC, $IL_{CM4}$ is the mean IL related to the 4:1 combiner, $IL_{conn}$ is the mean value of the losses due to the connections.

On the contrary, the loss variance $\sigma_{IL}^2$ is given by:

$$\sigma_{IL}^2 = \sigma_{IL-TTDU}^2 + \sigma_{IL-SC8}^2 + \sigma_{IL-CM4}^2 + 4\sigma_{IL-Conn}^2 \quad (V.13)$$

where $\sigma_{IL-TTDU}^2$ is the variance related to the TTDU losses, $\sigma_{IL-SC8}^2$ and $\sigma_{IL-CM4}^2$ are the variances related to the losses of the input and output SCs, respectively, and finally $\sigma_{IL-Conn}^2$ is the variance related to the connection losses.

Therefore, the optical devices employed must be designed in order to obtain a total loss deviation $\sigma_{IL}$ below the RMS amplitude error previously reported.

According to the discussion in Section 4.3.2, the OTSA model must also take into account the trim stages. In particular these trimming stages can be introduced in the optical and/or in the MW section (Fig.5.38).

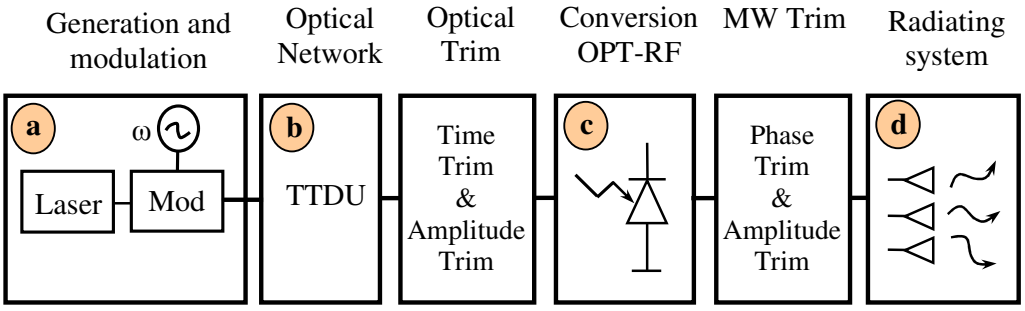


**Figure 5.38** *Layout of the OTSA with the optical and MW trimming stages*

# 9 SUM AND DIFFERENCE ARCHITECTURE

In different applications it is required the availability of an antenna systems able to radiate both sum and difference patterns. The latter are, for example, widely used in navigation systems and tracking radars that are employed in military and civilian applications. Military applications are the weapon control, missile guidance and target tracking, precision landing. In civilian application, tracking radars are used to implement the air traffic control systems and satellite navigation apparatus for ships, aircrafts and automotives [*Skolnik; Chyba*].

Generally, to realize high performance tracking radars, the antenna systems have to guarantee an high angle and range resolution and a good tracking accuracy, and the electronic beam steering control, multiple beams and an efficient control of the radiated pattern shape. Besides, a desirable feature in such systems is to independently control the shape of the sum and difference patterns.

Moreover, in the mentioned applications WB systems are of interest. In particular, ultra-wide band radars promise for improved performance capabilities: better range measurement accuracy and range resolution, capability to perform target recognition, improved radar immunity to passive interference, improved target tracking stability [*Immorev and Taylor*].

Usually, to achieve accurate tracking systems the monopulse technique is employed [*Skolnik*]. The monopulse radar is based on an antenna system able to

radiate three different patterns: a sum pattern and two difference patterns for azimuth and elevation angular tracking.

Here we present an optical architecture which realizes wide band beam squint free sum and difference pattern.

The basic idea is to exploits the results related to the phase and time control techniques. Generally speaking, the optical phase control is achieved by referring to a coherent detection scheme, while the time control exploits a direct detection one.

Wide band sum patterns are realized, as known, by using a proper time delay distribution. In a similar manner, to realize a wide band difference pattern, having the null pointing toward $\theta_0$, the OBFN has to provide an additional phase shift of $\pi$ between the two half of the array.

In order to guarantee the wide band behaviour, the phase opposition term has to be maintained constant across the whole system bandwidth. The optical architecture we propose realizes the control of the phase opposition term by means of an optically controlled phase shifter based on a coherent detection scheme, we refer as an Heterodyne Phaser (HP) [*Soref*].

In fact, the scheme adopted in [*Soref*] can, in principle, realize a differential phase shift constant across a large bandwidth [*Hietala et al.*]. This aspect has not been of interest for pattern control techniques since the phase control method, involving the well know beam squint phenomenon, has been used for narrow band phased arrays.

In particular let us refer to the scheme described in the 2nd Chapter (Section 2.2), [*Soref*], represented in Fig.5.39.

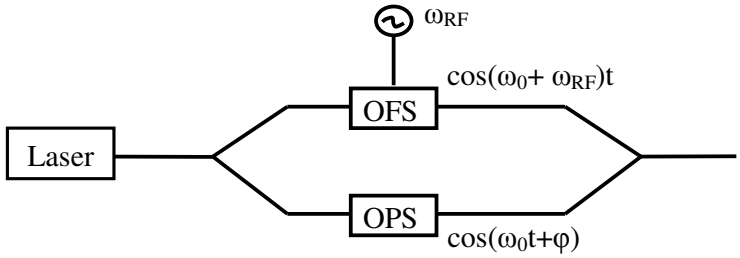


**Figure 5.39** *Scheme of the HP*

The HP bandwidth depends mainly on the spectral properties of the OFS employed. Usually, the single side band OFS is implemented by means of a Mach-Zender modulator (MZM) structure: the interferometer arms are driven by two RF signal 90º out of phase, while a 90º optical shift is added among the two light signals [*Jez et al.*; *Lee at al. 1999*; *Matsumoto et al.*]. These and other structure have been described in the 2nd Chapter (Section 2.2) [*Coward et al.*; *Winnall et al.*; *Henion and Schulz*]. In particular the wide band operation has been demonstrated over a 2 to 18GHz bandwidth in [*Winnall et al.*] and an extension of such a structure up to 40 GHz is under study.

Accordingly, the architecture we propose here, exploit both HP and optical TS to realize sum and difference wide band patterns. The architecture scheme is reported in Fig.5.40. The two half arrays are driven by means of an optical TS in order to allow for a wideband beam squint free beamsteering, while two HPs control the proper phase term needed to achieve a sum or a difference patterns. In Fig.5.40 the phase terms are set in order to get a phase opposition as required in difference patterns.

This architecture allows to compensate for systematic phase errors, introduced by the HP, among the two half array. Moreover, it could be possible to integrate the HPs and the TTD phaser in order to achieve a fully integrated compact BFN.

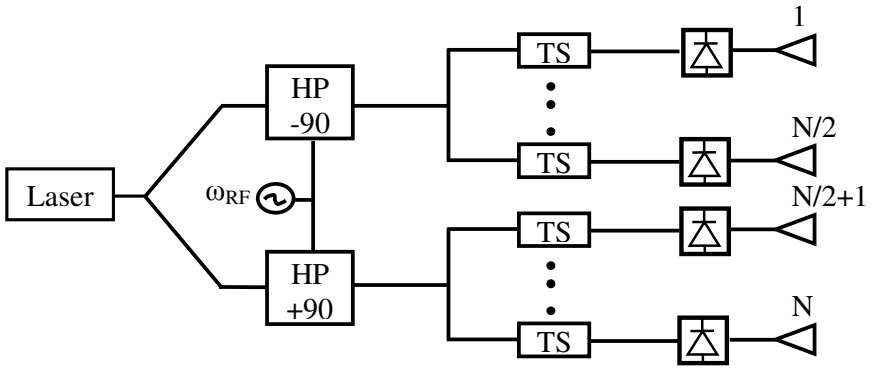


**Figure 5.40** *Scheme of the optical architecture proposed to realize both wide band sum and difference pattern: in the graph the HPs are set in order to get a difference pattern*

The introduced architecture has been tested by simulating the whole structure using the OBFN model previously described. The HP has been modelled by using an ideal OFS and OPS, since we are not interested on the real system bandwidth but only in proving the architecture capabilities. Regarding the time steering unit, we refer to the TTDU working in the 3 bit – 4 elements configuration.

In particular, we considered a 8 elements array, with half wavelength spacing at 20GHz. Each half array is driven by one TTDU. The architecture capabilities have been successfully verified by evaluating the array factor intensity plot as function of the observation angle θ and the frequency (Fig.5.41). In particular, a frequency range from 8 to 20GHz has been considered showing the wide band beam squint free behaviour. In this case we have not considered trim units. Therefore, as consequence of losses inside the TTDU the pattern shape deteriorates as strongly as the beam pointing angle grows. A little degradation is already observable in the graph here reported, referring to a null pointing angle equal to θ=-10º.

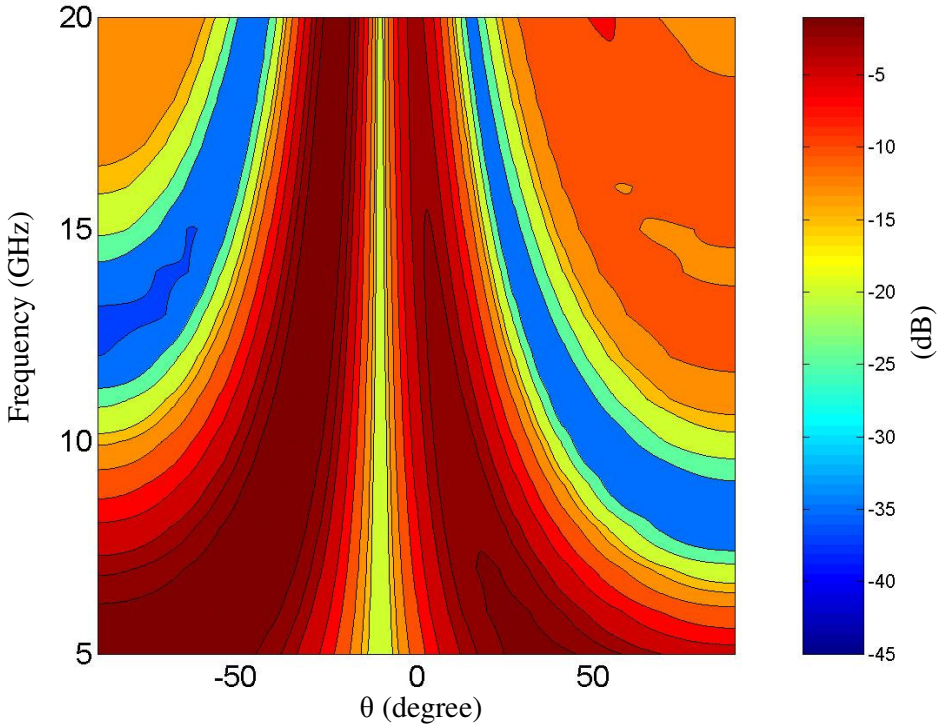


**Figure 5.41** *Array factor intensity plot as function of the angle θ and the frequency of the MW signal: difference beam squint free pattern pointing towards θ=-10º*

# APPENDIX A

# ARRAY THEORY

# FUNDAMENTAL RESULTS

The aim of this appendix is to establish the notation used in the whole thesis and to outline the results of the elementary array theory we will refer in the text. In particular we report only the results needed in thesis, by referring to linear phased array. For a wider discussion, the reader can refer to [*Mailloux 2005*; *Hansen*; *Fourikis*]

## 5. BASIC ARRAY CHARACTERISTICS

Let us consider an array whose radiating elements, located at positions ($x_n$, $y_n$, $z_n$), are excited by a complex weighting $c_n$ and radiate a vector element pattern $\mathbf{f_n}(\theta,\varphi)$. Moreover, an exp(jωt) temporal variation for the fields is assumed, where ω is the angular frequency. Accordingly, at a given frequency f=ω/2π, the array radiation pattern is given by:

$$\mathbf{E}(r) = \frac{\exp(-jkR_0)}{R_0}\sum_n c_n \mathbf{f_n}(\theta,\varphi)\exp\left(+jk\mathbf{r_n}\cdot\hat{\boldsymbol{\rho}}\right) \tag{A.1}$$

where the temporal variation term has been removed, k=2π/λ, λ=c/f being the signal wavelenght, the vectors $\mathbf{r_n}$ define the locations of the array elements. The observation point P is located at a distance $R_0$ from the origin and is defined by the unit vector $\hat{\boldsymbol{\rho}}$ (Fig.A.1). Accordingly we have:

$$\begin{aligned} \hat{\boldsymbol{\rho}} &= \hat{\mathbf{x}}u + \hat{\mathbf{y}}v + \hat{\mathbf{z}}\cos\theta \\ \mathbf{r_n} &= \hat{\mathbf{x}}x_n + \hat{\mathbf{y}}y_n + \hat{\mathbf{z}}z_n \\ R_0 &= \left|\mathbf{r}-\mathbf{r_0}\right| = \sqrt{x^2+y^2+z^2} \end{aligned} \tag{A.2}$$

where u and v are the direction cosines given by:

$$\begin{cases} u = \sin\theta\cos\varphi & \text{(A.3a)} \\ v = \sin\theta\sin\varphi & \text{(A.3b)} \end{cases}$$

with $u^2+v^2\leq 1$.

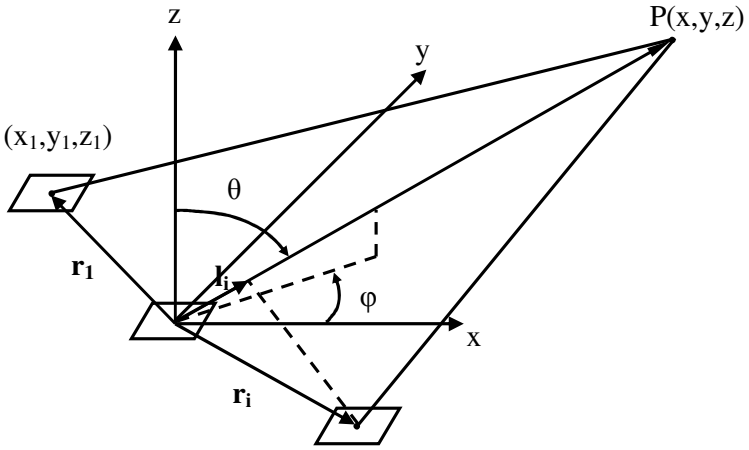


**Figure A.1** *Generalized array configuration*

Accordingly, the term $[\exp(-jkR_0)/R_0]$ is dropped and the same $\mathbf{f_n}$ is assumed for each element, the array radiation pattern can be written as the product of the vector element pattern $\mathbf{f}(\theta,\varphi)$ and the scalar array factor $f_A(\theta,\varphi)$ given by:

$$f_A(\theta,\varphi)=\sum_n c_n \exp\left(+jk\mathbf{r_n}\cdot\hat{\boldsymbol{\rho}}\right) \tag{A.4}$$

When considering a linear array, whose element are uniformly spaced, the eq. (A-4) can be written in a simple form. Let us assume that the array elements are located along the x-axis, with a spacing d. In this case the array factor is constant with φ. Accordingly, by referring to the (x,z) plane, it is given by (see Fig.A.1):

$$f_A\left(\theta\right)=\sum_n c_n \exp\left(+jkndu\right) \tag{A.5}$$

where $u=\sin\theta$.

Generally speaking, the antenna coefficients needed to steer the beam and point in the direction $(\theta_0,\varphi_0)$ are:

$$\begin{aligned} c_n &= |c_n|\exp\left(-jk\mathbf{r_n}\cdot\hat{\boldsymbol{\rho}}_0\right)=a_n\exp\left(-jkl_n\right)\\ \hat{\boldsymbol{\rho}}_0 &= \hat{\mathbf{x}}u_0+\hat{\mathbf{y}}v_0+\hat{\mathbf{z}}\cos\theta_0 \end{aligned} \tag{A.6}$$

where $l_n$ is the projection of the vector defining the position of the n-th element along the observation direction, and $a_n$ is the amplitude of the excitation coefficient $c_n$.

This excitation produces the maximum of the radiation pattern in the direction $(\theta_0,\varphi_0)$: in fact, in this direction the exponential excitation terms into (A.6) cancel those in (A.4), and the array factor maximum, given by the sum of the of the weight amplitudes $a_n$, is obtained.

For a linear array with periodic spacing d the antenna coefficients needed to steer the beam in the direction $\theta_0$ are:

$$c_n=a_n\exp\left(-jknd\sin\theta_0\right) \tag{A.7}$$

The beam properties of main interest are the directivity, the beamwidth, the sidelobe level and the bandwidth of the array system.

Let us denote with $S(\theta,\varphi)$ ($W/m^2$) the power density radiated by the array, Accordingly, the antenna directivity D is defined as the maximum of $S(\theta,\varphi)$ at the beam peak, divided by the total power:

$$D = \frac{4\pi S_{\max}}{\int_0^{2\pi}\int_{-\pi/2}^{\pi/2} S(\theta,\varphi)\sin\theta d\theta d\varphi} \tag{A.8}$$

For a linear array of isotropic elements, with spacing that are an integer number of half-wavelength, D is independent of the scan loss:

$$D = \frac{\left|\sum a_n\right|^2}{\sum a_n{}^2} \tag{A.9}$$

Unfortunately, the constant directivity of (A.9) does not mean that the linear array does not suffer of scan loss. In fact, the mismatch due to element mutual coupling changes with beam scanning and produces scan loss even for omni-directional elements. The (A.9) could be written by introducing the taper efficiency $\varepsilon_T$. In fact, the maximum value of eq. (A.9) is N and occurs when all the antenna coefficients $c_n$ are the same. Accordingly, for half a wavelength spaced isotropic elements the directivity can be written as:

$$\begin{aligned} D &= N\varepsilon_T \\ \varepsilon_T &= \frac{1}{N}\frac{\left|\sum a_n\right|^2}{\sum a_n{}^2} \end{aligned} \tag{A.10}$$

When tapering the array excitation and the power feeding the elements at the centre of the array is higher than that feeding the edge one, the directivity diminishes and the side lobe level is lowered. Moreover, the tapering broadens the array beamwidth.

The half-power beamwidht $\theta_3$ for a linear array is given by:

$$\theta_3 = 0.886\frac{\lambda}{L}B_b \tag{A.11}$$

where L is the array length and $B_b$ is the beam broadening factor, that is unitary for uniformly illuminated array and diminished with the array tapering. When the beam is scanned to the angle $\theta_0$ at the frequency $f_0$, the beam broadens and the directivity changes [*Mailloux 2005*]:

$$\theta_3 = \left[\arcsin\left(u_0 + 0.443B_b\frac{\lambda}{L}\right) - \arcsin\left(u_0 - 0.443B_b\frac{\lambda}{L}\right)\right] \tag{A.12}$$

For large array the (A.12) can be written as:

$$\theta_3 = \theta_3(broadside)/\cos\theta_0 \tag{A.13}$$

The array pattern of a linear array with a peak at $\theta_0$ can also have other peaks, according to the value of d. In fact, other maxima of the array factor can exist at any

cosine direction $u_g$ such that the argument of the exponential in the array factor expression (A.5) is a multiple of $2\pi$. In particular another maximum occurs at $u_g$ given by:

$$u_g = u_0 + (g\lambda / d) \tag{A.14}$$

where g is an integer.

These beam peaks are called the array grating lobes. Since $u=\sin\theta$, the array grating lobes must lie within the region $|u_g| \leq 1$. Then, by enforcing such a condition on the (A.14), the maximum value of d guaranteeing that the beam can be scanned to the angle $\theta_0$ with no grating lobes can be found:

$$\frac{d}{\lambda} \leq \frac{1}{1+\sin\theta_0} \tag{A.15}$$

Regarding the array bandwidth, this is often defined according to the beam squint phenomenon. This happens when the phase of the excitation coefficients does not vary linearly with the frequency. In turn, the eq. (A.7) is satisfied only at one frequency, say $f_0$. In this way the beam peak is located at $\theta_0$ at the frequency $f_0$. Accordingly, at a different frequency f, the beam peak is obtained in the direction $\theta$ such that:

$$\sin\theta = \frac{f_0}{f}\sin\theta_0 \tag{A.16}$$

The beam peak is "squint" as shown in Fig.A.2. The beam pointing angle is reduced for frequencies above the design frequency $f_0$, and increased for frequency below $f_0$.

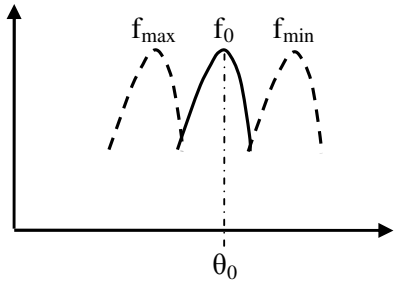


**Figure A.2** *Beam squint*

# APPENDIX B

# FIBER OPTIC LINKS

The aim of this appendix is to identity the characteristics of an analog fiber optic link, discuss the most common devices and the link figures of merit. In particular, we refer to fiber optic systems with intensity modulation and direct detection (IMDD), since these are the most diffused optical link not only for antenna beamforming and remoting but also for other important application fields [*Ackerman and Cox*; *Zmuda and Toughlian 1994*; *Bratchikov 1998*].

## 6. FIBER OPTIC LINK SCHEME

In Fig.B-1 we report the scheme of an IMDD link. The hardware is schematically represented at both stages, the modulation stage and the recovery one. A laser source generates the optical carrier with a proper wavelength. The optical carrier is modulated by means of external (EM) or direct (DM) modulator. The modulated signal is then launched into the optical network and, finally, is downconverted to the MW signal by means of a photodector.

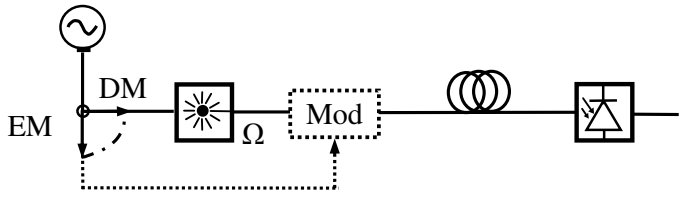


**Figure B-1** *Fiber optic link scheme*

In the DM link, usually semiconductor lasers are used to perform both the signal generation and modulation. By applying the modulation signal over the DC biasing current of the semiconductor laser, a corresponding modulation of the intensity of the emitted radiation is achieved. Two major classes of laser sources for direct modulation

exist: the edge emitters and vertical cavity surface emitters (VCSEL) **Errore. L'origine riferimento non è stata trovata.**. In the first class, the laser light is emitted from the edge of the semiconductor chip. The most employed are the Fabry Perot and the Distributed Feedback (DFB) ones, according to the cavity fabrication technology. In particular, the DFB lasers show high spectral, noise and linearity properties, and so represent the preferred solution for application in the windows 1.3μm and 1.55μm. The VCSEL lasers have a better efficiency than the edge emitters, but can manage a lower output power, due to the smaller cavity volume, thus resulting in a smaller dynamic range.

Key parameters for semiconductor laser are the slope efficiency $s_L$, expressed in W/A, that states the conversion factor between the modulating current and the output optical power, and the modulation bandwidth, set by the laser relaxation–resonance frequency. The maximum bandwidth achievable with a direct modulation link is about 40GHz **Errore. L'origine riferimento non è stata trovata.**, although the most links show a bandwidth below 20GHz [*Bratchikov 1998*].

In Fig.B-2a the laser diode transfer function is reported. It represents the optical power $P_{o,opt}$ versus the laser driving current $i_L$:

$$P_{o,opt} = s_L (i_L - I_T) \tag{B.1}$$

The laser driving current is $i_L=I_B+i_S$, where $I_B$ is the bias current and $i_S$ is the modulating signal current. Accordingly, when operating under small signal conditions ($i_S<<I_B$) and biasing the diode laser with $I_B$ greater than the laser threshold current $I_T$, the laser can be modelled as a current dependent optical power source [*Cox et al.*]. Accordingly, the fiber-coupled modulated optical power $p_o$ is given by [*Cox et al.*]:

$$p_o = s_L i_S \tag{B.2}$$

The external modulator most employed in the EM link are the Mach-Zender interferometric modulators (MZI) and the electro-absorption modulators (EA) **Errore. L'origine riferimento non è stata trovata.**. A MZM modulator is made of an interferometric structure: an optical waveguide is splitted in two arms which are then recombined into one output waveguide. An electric field is applied, by means of a set of electrodes, upon the two arms in order to introduce a phase shift between the light signals propagating through the two arms. The phase shift is induced by the electro-optic effect, whose strength depends obviously on the exploited material. In the EA modulators the laser output intensity is changed by applying an electric field and by varying the optical absorption band edge in a semiconductor. This behaviour is due to either the Franz-Keldysh effect or the quantum-confined Stark effect. Accordingly, a transfer function with a good linearity can be obtained.

An important parameter for an EM is the voltage required to switch between maximum and minimum optical transmission. For a MZM, this parameter is called $V_\pi$, and is the voltage required to get an optical phase shift equal to $\pi$ radians. Another parameter of interest is the modulation bandwidth. The maximum bandwidth achievable with an external modulator is about 70GHz, although improvements up to 94 GHz have been reported [*Ackerman and Cox*].

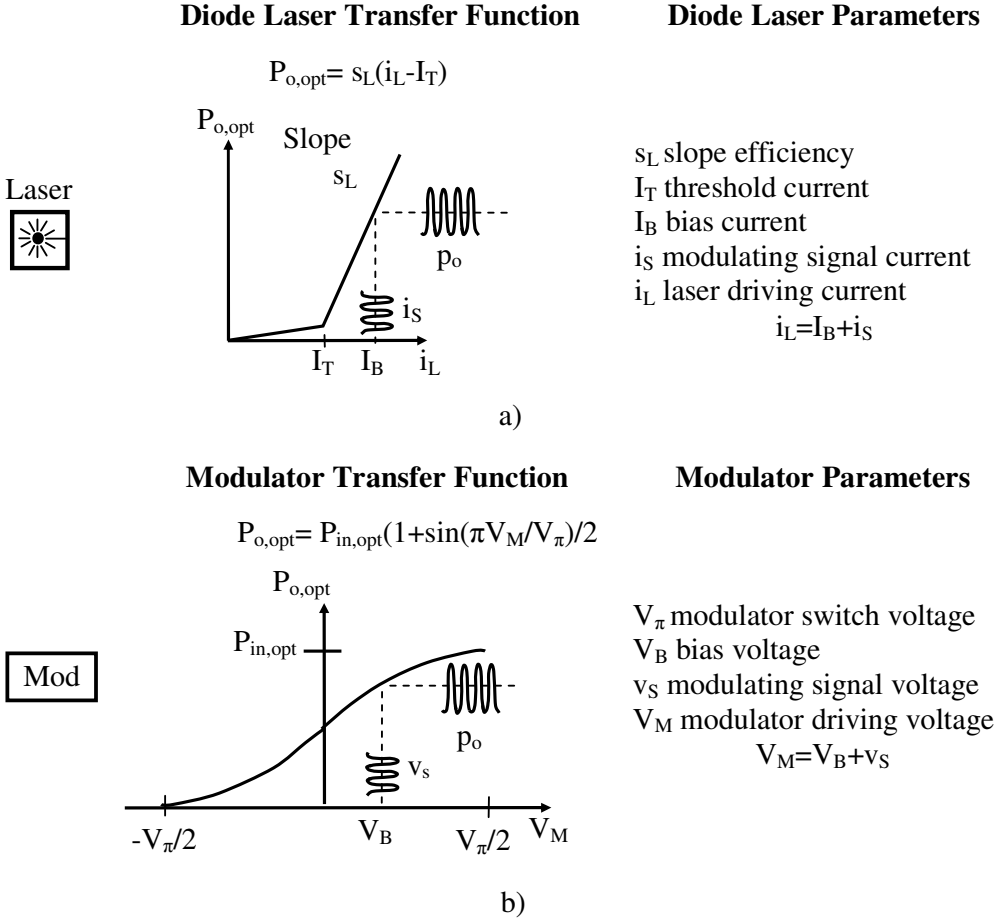


**Figure B-2** *Modulation transfer function: a) DM link b) EM link*

In Fig.B-2b the MZM relationship between the optical output power $P_{o,opt}$ and the modulator driving voltage $V_M$ is reported. This relationship is useful to express the $P_{o,opt}$ in terms of the input optical power $P_{in,opt}$ [*Daryoush et al. 1991*]:

$$P_{o,opt} = P_{in,opt}\cos^2\left(\frac{\pi}{4}-\frac{\pi V_M}{2V_\pi}\right)=\frac{P_{in,opt}}{2}\left(1+\sin\left(\frac{\pi V_M}{V_\pi}\right)\right) \qquad \text{(B.3)}$$

where $V_M=V_B+v_d\sin(\omega t)$, $V_B$ being the bias voltage. Under the small signal approximation, the modulator transfer function can be written as:

$$P_{o,opt} = \frac{P_{in,opt}}{2}\left(\frac{\pi v_d}{V_\pi}\right)\cos\left(\frac{\pi V_B}{V_\pi}\right) \qquad \text{(B.4)}$$

Regarding the photodetection section, the most employed high speed photodetectors for RF fiber links are the metal-semiconductor-metal photodiodes, the avalanche photodiodes and the p-i-n photodiodes [*Ackerman and Cox*]. The latter, in particular, represents the most employed solution. The photodiodes can detect the light illuminating the chip surface (surface-illuminated) or the chip edge (edge-illuminated) [*Ackerman and Cox*]. The main photodetector parameters are the

responsivity $r_{PD}$, the bandwidth and the linearity range. The detector output current $i_{PD}$ is related to the optical power illuminating the detector $P_{opt}$ by:

$$i_{PD} = r_{PD} P_{opt} \tag{B.5}$$

In the surface-illuminated devices, the bandwidth can be improved by reducing the photosensitive volume, thus reducing the responsivity. This leads to a bandwidth-responsivity trade off. Moreover, a bandwidth-linearity trade off also exists for surface-illuminated detectors. In fact, to obtain a good linearity, even under strong optical illumination, large volume detectors have to be used, thus reducing the achievable bandwidth. These problems can be circumvented by using edge-illuminated photodiodes. By properly configuring the electrodes, in fact, both trade-off can be managed.

# 7. FIBER OPTIC LINK FIGURES OF MERIT

The main figures of merit are the link gain, the noise figure and the dynamic range [*Ackerman and Cox*; *Zmuda and Toughlian*; *Bratchikov 1998*; *Cox et al*; *Daryoush et al. 1991*]. These performance parameters are reported on the graph in Fig.B-3. The link gain (G) is simply defined as the ratio between the output and the input power at some signal frequency, say $f_1$:

$$G = \frac{P_{out}}{P_{in}} \tag{B.6}$$

The G is usually expressed in dB.

The noise properties of the link are summarized by the noise figure NF which measures how much the signal-to-noise ratio (SNR) degrades between the input and the output of the link. Accordingly, the NF establish the relationship between the noise power at the input of the link $N_{in}$ and the noise power at the output $N_{out}$:

$$NF = \frac{SNR_{in}}{SNR_{out}} = \frac{N_{out}}{N_{in} G} \tag{B.7}$$

As shown in the Fig.B3 , the NF indicates the noise amount added by the link. Also the NF is usually expressed in dB.

The total output noise $N_{out}$ establishes a threshold level of the useful signal power at the link output. Accordingly, it determines the low end of the link dynamic range (DR).

On the other contrary the upper end of the DR is limited by the link nonlinearities. In particular the link nonlinearities causes two effects observable for large input power: the compression of the output signal amplitude and the generation of unwanted harmonics and intermodulation frequencies.

In particular, for antenna signals consisting of a single MW tone, the DR assumes the form of the compression dynamic range (CDR). When increasing the input signal power, the input-output characteristic of the link begins to saturate, thus deviating from the linear behaviour. The CDR is, then, defined as the output SNR in 1dB compression point, or in other words as the range of input signal power for which the output signal power is above the $N_{out}$ and deviates from the linear behaviour by less

than 1dB, as shown in Fig.B-3. Accordingly, by defining as $P_{in,1CP}$ and $P_{out,1CP}$ the input and output signal power at the 1dB compression point, we have:

$$CDR = \frac{1.259 P_{out,1CP}}{N_{out}} = \frac{P_{in,1CP} G}{N_{out}} = \frac{P_{in,1CP}}{N_{in} NF} \tag{B.8}$$

The CDR is measured in dB·Hz.

When the antenna signal consists of multiple tones, the DR is expressed as the intermodulation free dynamic range (IMFDR). In particular let us consider an antenna signal made of two fundamental frequencies $f_1$ and $f_2$, whose difference is smaller than the resolution bandwidth. In this case, one or both intermodulation third-order (IMD) signals having frequencies equal to $2f_1$-$f_2$ and $2f_2$-$f_1$, respectively, will appear to the receiver. As consequence, the IMFDR is defined as the maximum difference between the noise floor and the fundamental output power, which produces IMD terms with amplitude equal to the noise floor. In other words, the IMFDR is the IMD free range of input power for which the fundamental signal power is above the noise floor. By referring to Fig.B-3 we can define respectively $P_{in,int}$ and $P_{out,int}$ as the input and output power at the third order intercept, where the fundamental signal output power is equal to the third-order IMD signal power. Then, we have:

$$IMFDR = \left( \frac{P_{out,\text{int}}}{N_{out}} \right)^{2/3} = \left( \frac{P_{in,\text{int}}}{N_{in} NF} \right)^{2/3} \tag{B.9}$$

The IMFDR is measured in $dB \cdot Hz^{2/3}$.

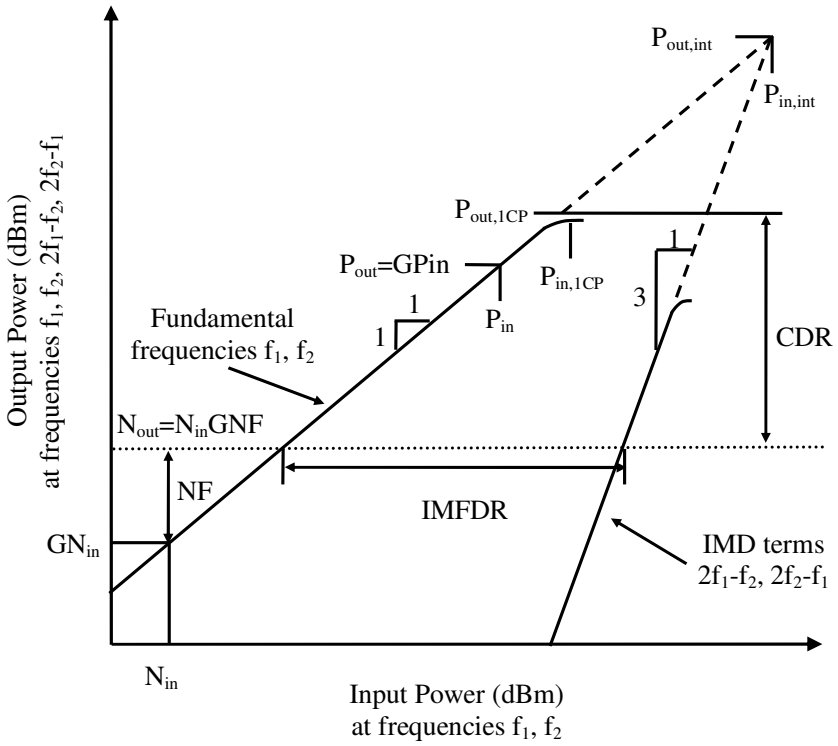


**Figure B-3** *Fiber optic link scheme*

The expression of the main figure of merit can be found by using the proper link models [*Ackerman and Cox*; *Zmuda and Toughlian*; *Bratchikov 1998*; *Cox et al*; *Daryoush et al. 1991*]. The detailed models for the DM and EM links expressing the key parameters as function of the microwave scattering parameters of the full link equivalent circuits are presented in [*Daryoush et al. 1991*]. Here we present a simpler discussion, based essentially on the treatment proposed in [*Ackerman and Cox*; *Zmuda and Toughlian*; *Bratchikov 1998*].

- Gain

By using the gain definition, for a DM link we have:

$$G_{DM} = \frac{P_{out}}{P_{in}} = \frac{i_{PD}^2 R_{LOAD}}{i_L^2 R_{LAS}} \tag{B.10}$$

where $R_{LAS}$ is the laser diode resistance. Using the described transfer functions we can write:

$$\begin{aligned} G_{DM} &= \frac{\left(r_{PD} IL_{LINK} P_{out,LAS}\right)^2 R_{LOAD}}{i_L^2 R_{LAS}} = \\ &= \frac{\left(r_{PD} IL_{LINK} s_L i_L\right)^2 R_{LOAD}}{i_L^2 R_{LAS}} = \left(r_{PD} s_L IL_{LINK}\right)^2 \frac{R_{LOAD}}{R_{LAS}} \end{aligned} \tag{B.11}$$

where $IL_{LINK}$ are the losses due to fiber input-output coupling, fiber attenuation, eventual power splitting among different channels, $P_{out,LAS}$ is the laser output power. The losses due to the matching circuits have been neglected.

On the same way we can derive the gain expression for EM links

$$\begin{aligned} G_{EM} &= \frac{i_{PD}^2 R_{LOAD}}{v_M^2 / R_{MOD}} = \\ &= \frac{\left(r_{PD} P_{out,MOD}\right)^2 R_{MOD} R_{LOAD}}{v_M^2} = \\ &= \frac{\left(r_{PD} \dfrac{\pi T_{MOD} v_M}{2V_\pi} P_{out,LAS} IL_{LINK}\right)^2 R_{MOD} R_{LOAD}}{v_M^2} = \\ &= \left(r_{PD} \frac{\pi T_{MOD}}{2V_\pi} P_{out,LAS} IL_{LINK}\right)^2 R_{MOD} R_{LOAD} \end{aligned} \tag{B.12}$$

where $R_{MOD}$ is the modulator resistance, $P_{out,MOD}$ is the modulator output power, $T_{MOD}$ is the modulator insertion loss coefficient.

In the standard configuration, for the DM link we have $G_{DM}$=-(15÷30)dB, while the EM link shows a gain about 30dB worse than the DM one, $G_{EM}$=-(35÷60)dB. It is worth noting that the in EM links, the gain depends upon the laser optical power. Accordingly, by using high power semiconductor lasers or solid state lasers, the gain improvements can be achieved.

- Noise figure

Before derive the NF expression for DM and EM links, a brief discussion about the noise sources of interest is needed.

The main contributions to the output noise are the relative intensity noise, the shot noise and the thermal noise.

The relative intensity noise is generated by the interference between the optical stimulated laser signal and the spontaneous emission generated within the laser cavity [*Derickson*]. The relative intensity noise usually dominates in the DM links. The output noise power due to the laser relative intensity noise RIN can be written as:

$$N_{RIN} = i_{PD,DC}^2 RIN R_{LOAD} B \tag{B.13}$$

where $i_{PD,DC}$ is the photodetector average DC current and B is the system bandwidth. The RIN is usually expressed in dB/Hz, for example a typical value range is (-120 ÷ -170)dB/Hz.

It is worth noting that, when dealing with EM links, the relative intensity noise power can be neglected by using solid state laser, although this increase the system cost.

The shot noise is due to the discrete nature of both the incident optical radiation and the electric current. The output noise power due to the shot noise is given by;

$$N_{SHOT} = 2qi_{PD,DC} R_{LOAD} B \tag{B.14}$$

where $q=1.6\cdot 10e^{-19}$C is the electron charge.

The thermal noise is due to the random motion and collisions between electron carriers within the ohmic impedances of the MW source, the modulation devices, the photodetector, the interface circuits between the sources and the modulation devices, and between detector and output load. To derive the thermal noise contribution, one should represent the noise sources at the input and at the output of the link by means of an equivalent noise power. Accordingly, the total output noise power can be written as the sum of a noise power term which propagates through the link and the output noise power term. Generally speaking it could be assumed that the total output noise power due to thermal noise is such that:

$$N_{TH,out} \geq kT(G+1)B \tag{B.15}$$

where k is the Boltzmann's constant and T is the absolute Kelvin temperature.

Accordingly, the NF of the link can be written as:

$$NF = \frac{N_{out}}{GN_{in}} = \frac{N_{RIN} + N_{SHOT} + N_{TH,out}}{GN_{TH,in}} \tag{B.16}$$

where $N_{TH,in}=kTB$ is the noise power at the input of the link.

Some observations are in order.

The $i_{PD,DC}$ is proportional to average optical power. As consequence, the $N_{RIN}$ increases quadratically with the optical power, while the $N_{SHOT}$ increases linearly. Consequently, for DM link, the NF, mainly due to relative intensity noise increase quadratically with the optical power. Regarding the EM links, when using solid state lasers, usually, the dominant noise source is the shot one. In this case, the NF decreases linearly with the optical power supplied to the modulator. Conversely, when using semiconductor DFB lasers, often employed to save the link cost, the $N_{RIN}$ can

not be neglected, even when employing lasers with a very low RIN. Accordingly, since the $N_{RIN}$ goes as the square of the optical power, as the gain of the EM link $G_{EM}$, an higher NF will result.

Regarding the thermal noise, when this noise term is the dominant one, for lossy links, with G<<1, a NF at least great as the MW loss will be achieved, since it results NF=1/G. On the other side, when G>>1, the NF exceeds 1, or 0dB when using the logarithmic expression for the NF.

Finally it is worth noting that another parameter often used to specify the noise properties of the link is the SNR, that is defined as [*Bratchikov 1998*]:

$$\mathrm{SNR} = \frac{P_s}{N_{out}} = \frac{\left(m i_{PD,DC}\right)^2 R_{LOAD}}{N_{out}} \tag{B.17}$$

where $P_s$ is the signal power, and m is the modulation depth of the output DC current $i_{PD,DC}$.

The SNR specify the noise conditions at the link output, while the NF gives information about the noise added by the link.

- Dynamic range

Here we consider the derivation of the IMFDR expression [*Kalman et al.*]. Since the IMFDR is the SNR at which the intermodulation power is equal to the noise power, to obtain its expression we have to consider the power related to the intermodulation term.

Accordingly, let us consider a two tones test signal x(t):

$$x(t) = \frac{1}{\sqrt{2}}\left(\cos(\omega_1 t + \varphi_1) + \cos(\omega_2 t + \varphi_2)\right) \tag{B.18}$$

where $\omega_1$ and $\omega_2$ are the frequencies of the two tones, $\varphi_1$ and $\varphi_2$ are arbitrary constant phases. Then, the detector output current will be:

$$i_{PD}(t) = I\left[ m x(t) + b_3 \left( m x(t) \right)^3 \right] + n_{tot}(t) \tag{B.19}$$

where I is the signal amplitude and $b_3$ is a proper constant.

By using (B.19) in (B.18), the power related to the intermodulation terms $i_{IMP}$, at frequencies $2\omega_1$-$\omega_2$ and $2\omega_2$-$\omega_1$ can be found:

$$\left\langle i_{IMP}^2 \right\rangle = \frac{9}{256} I^2 b_3^2 m^6 \tag{B.20}$$

where the $\langle\cdot\rangle$ represents the time averaged mean value.

By setting the intermodulation power equal to the noise power, the maximum intermodulation-free modulation depth m can be found. To this end, let us consider the SNR:

$$\mathrm{SNR} = m^2 \frac{I^2 \left\langle x^2(t) \right\rangle}{\left\langle n_{tot}^2(t) \right\rangle} = m^2 \mathrm{SNR}_0 \tag{B.21}$$

where the $SNR_0$ is the link SNR for a unity modulation index. By expressing the noise power in terms of the $SNR_0$ from (B.21), and then comparing it to the (B.20), the

maximum useful modulation depth ensuring intermodulation-free operation can be found:

$$m^2 = \left( \frac{64}{9} \frac{1}{b_3^2 SNR_0} \right)^{1/3} \tag{B.22}$$

Accordingly, the IMFDR can be found by using the modulation depth expression (B.22) in the SNR formula:

$$IMFDR = \left( \frac{8SNR_0}{3|b_3|} \right)^{2/3} \tag{B.23}$$

# APPENDIX C

# PRINTED ANTENNAS PROTOTYPES

A part of the research activity have been devoted to improve the implementation procedure of printed antenna and circuits set up in the Antenna Lab of the Department of Electronic and Telecommunication Engineering (DIET) of the University Federico II of Naples.

The printed circuits technology allows, in fact, interesting feature. Compact and lightweight radiating systems, conformable to the assigned geometry of the installation site and easily integrable with MW integrated circuits. Furthermore it can be realized with reduced costs. Moreover, advanced design techniques allow to realize radiating elements working over large bandwidths. Thanks to these feature, printed array antennas are a good candidate to realize the radiating system of our OTSA, as discussed. In fact, we have set up the design, the realization and characterization techniques of printed antennas in order to gain the know-how useful to realize the radiating systems of our OTSA prototype.

The aim of this appendix is, then, to describe the main issues related to the design, realization and characterization procedures of printed antennas.

In the following we discuss about the prototypes design and realization, and we report the results related to the characterization of some antennas.

## 10 PROTOTYPES DESIGN AND REALIZATION

To design and realize a printed antenna prototype we have to face different aspects:

- Radiating element design
- External synthesis
- BFN design
- Realization process

The first task is to design the radiating element to be employed in the antenna systems.

An external synthesis procedure has to be employed in a second step to find the antenna coefficients distribution which realizes the desired radiated pattern. Afterwards, the BFN has to be carefully designed in order to realize the distribution of the excitation coefficients provided by the external synthesis step: the BFN design is often referred as internal synthesis.

Finally, the whole antenna system, BFN and radiating system, has to be realized by means of a photolithographic process.

Here we refer to three antenna prototypes having a microstrip BFN. These antennas have been properly designed to validate the different steps of the prototype implementation process. In particular we considered:

- Antenna BS8: Validation of the realization process
- Antenna TCH8: Validation of the design of the BFN, by means of a CAD
- Antenna DUALB11: Use of the external synthesis procedure.

The antenna BS8 has been designed to validate the realization process. In fact, it is a linear array of 8 elements, with half a wavelength spacing, radiating a canonical broadside pattern and using a uniform amplitude distribution. It does not require the external synthesis procedure. Moreover, the design of the BFN, although achieved with an electromagnetic CAD, is quite simple.

The antenna TCH8 has been realized to verify the accuracy of the design, by means of an electromagnetic CAD, of the BFN. In fact it is a linear array of 8 elements, with half a wavelength spacing, radiating a broadside beam and having a Tchebitchev amplitude distribution with a required SLL of about -20dB. The design of this prototype has not required the use of the external synthesis, while the BFN design has been realized using an electromagnetic CAD.

The antenna DUALB11 is a linear array of 11 elements, with half a wavelength spacing, radiating a contoured beam. The external synthesis procedure has been performed by means of the power pattern synthesis algorithm developed within the DIET [*Bucci and D'Elia*; *Bucci et al. 2004a*]. In particular, the synthesis algorithm has been properly modified to take into account for the BFN realization difficulties.

Accordingly, in the following we will firstly discuss about the design of the radiating element, by mean of a CAD. Afterwards we will describe the realization process when the design of the antenna BS8 will be presented. Later, we will present the design, by means of a CAD, of the antenna TCH8 and discuss some of the BFN design issues. Finally we will consider the external synthesis process when dealing with the design of the antenna DUALB11.

## 1.1 DESIGN OF THE RADIATING ELEMENT

The design of a printed radiating element has to be carried out in order to meet different requirements. In particular we are interested to obtain a radiating element having a good operative bandwidth, intended as impedance bandwidth, reduced spurious radiation and cross-polarization and that can be realized without requiring an excessive realization complexity.

Different wideband printed radiating elements can be found in the specialized literature. Some of the most employed printed radiating elements are the Vivaldi antennas [*Fourikis*], the spiral microstrip antennas [*Wang and Tripp*], the aperture stacked patch antennas [*Ghorbani and Waterhouse*].

Among these wideband elements, we focused our attention on patch antennas.

The patch antennas can, in fact, be designed in order to achieve satisfactory bandwidths without a high realization complexity and reduce the spurious radiation produced by the feed structure. In particular we referred to the aperture coupling feeding technique [*Garg et al.*], whose scheme is depicted in Fig.C-1. Here the power is transferred from to feed line to the patch by exploiting the electromagnetic field coupling obtained by means of a slot in the ground plane. This structure allows to efficiently reduce the spurious radiation generated by the feed line, since the latter is placed behind the ground plane. Moreover, since, the coupling slot is usually placed in correspondence of the centre of the radiating patch, low cross polarization level can be obtained. Obviously, such a structure requires the implementation of a multilayer architecture which increases the realization process complexity. However, the stacked configuration offers significant advantages to improve the system performances when compared to a single layer structure.

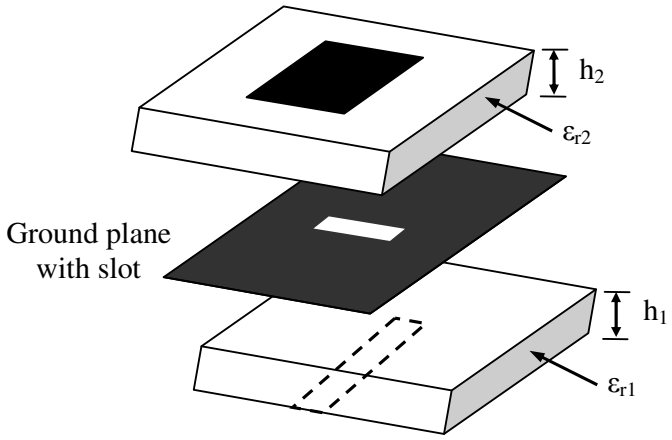


**Figure C-1** *Layout of the aperture coupled patch antenna*

For example, by using a more patches arranged in a stacked configuration, bandwidth (defined for VSWR<2) up to 70% and 120% have been reported respectively in [*Targonsky et al.*] and [*Ghorbani and Waterhouse*].

Since we are interested in structure with a non excessive realization complexity, we referred to a single patch aperture coupled architecture. In particular we considered a Strip-Slot-Foam-Inverted Patch (SSFIP) structure that allows a bandwidth from 12% to 20% [*Zurcher and Gardiol*]. The structure of the SSFIP element, schematically reported in Fig.C-2, is quite similar to the aperture coupled one. A foam layer is used among the ground plane and the patch. The latter is covered with another dielectric layer.

Accordingly, let us discuss the theoretical design guidelines of the SSFIP element. Usually to reduce the radiation generated by the feed line, it is printed on a thin substrate having an high dielectric constant $\varepsilon_r$. Then, for the 1$^{st}$ layer (Fig.C-2) it is useful to adopt a small height $h_1$, compared to the wavelength, and an high

dielectric constant $\varepsilon_{r1}$. Conversely to realize an antenna element having a good bandwidth, thick substrates with a low dielectric constant have to be used [*Garg et al.*]. Moreover, using a low dielectric constant allows to reduce the effects of the surface waves. Foam substrates, having $\varepsilon_r$, very close to the unity, are suited to achieve large bandwidths. Obviously, the bandwidth grows with the foam thickness, while the antenna efficiency decreases. Accordingly, it is necessary to increase the slot dimensions to provide a better coupling and decrease the resonant frequency.

Regarding the top dielectric substrate, it is used since the metal patch can not be printed directly on the foam layer. The dielectric layer with the patch printed on the bottom side, thus called inverted patch, is used. This layer has to be thin in order to introduce no alteration on the antenna pattern.

Generally speaking the non resonant slot over the antenna bandwidth is considered to avoid an high back radiation and the deterioration of the patch radiated pattern. The slot shape, dimensions and position have to be optimized by means of a proper CAD, in order to achieve the proper coupling between the patch and the feed line.

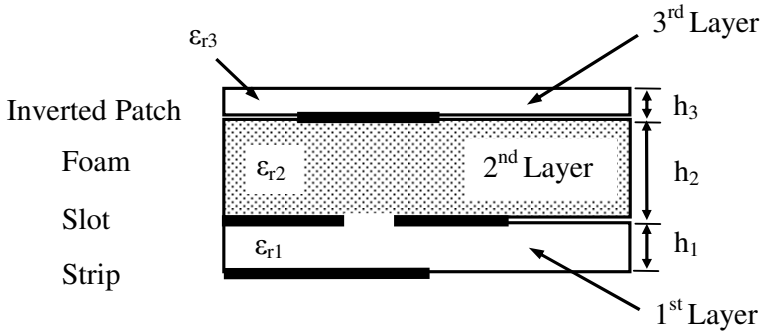


**Figure C-2** *Layout of the SSFIP radiating structure*

In particular we considered a SSFIP radiating element working at 18Hz with a 100Ω input impedance and using a rectangular slot. The geometry of the considered structure is reported in Fig.C-3.

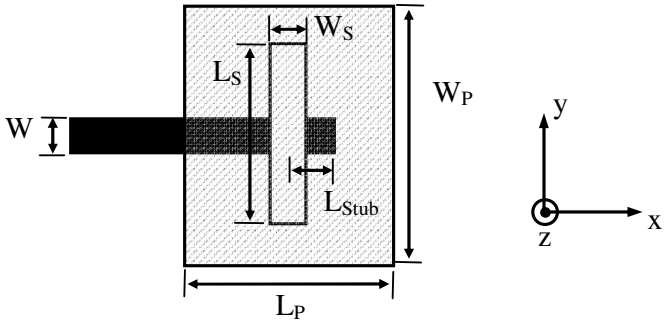


**Figure C-3** *Geometry of the considered SSFIP radiating structure*

The design of the radiating element has been performed by using the electromagnetic CAD Ansoft Designer. A parametrical analysis has been carried out to define the optimal geometrical parameters suited to reduce the effects due to an

unwanted misalignment which could occur in the realization procedure. The analysis has been done for three different input impedances equal to 50Ω, 75Ω and 100Ω. An element having a 100Ω input impedance allowed to achieve the best performances. Here we report only the final results of the mentioned analysis. In particular we refer to the reflection coefficient variation due to the misalignment between the patch and the slot, since this is the most critical step of the assembling procedure of the antenna. Accordingly, in Fig.C-4 and Fig.C-5 we show a Smith Chart reporting the reflection coefficient variations due to misalignments, between the patch and the slot, in the x and in the y direction, respectively. In both cases the misalignments vary in the interval [-2mm, 2mm] with step equal to 1mm.

In tab.C-1 we report the main design parameters, while in Fig.C-6 we present the VSWR diagram as function of the frequency. The achieved bandwidth is about 17%. In Fig.C-7 and Fig.C-8 we report also the copolar and cross-polar field patterns related to the single SSFIP radiating element represented as function of the cosine director u and v. In particular the copolar component is assumed to be the one directed along the x axis while the cross-polar one is directed along the y-axis (see Fig.C-3)

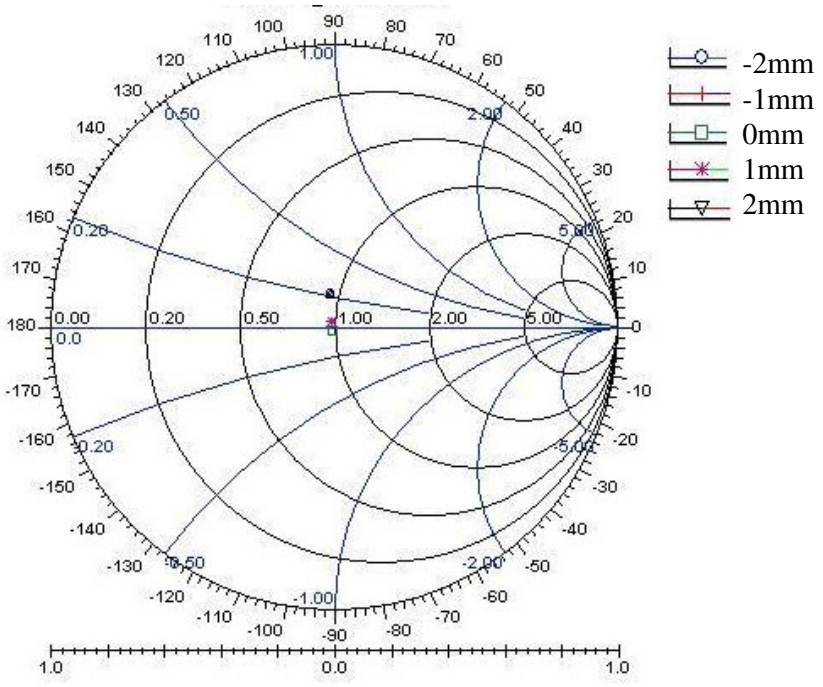


**Figure C-4** *Variations of the reflection coefficient due to misalignment between the patch and the slot in the x direction*

| | |
|---|---|
| Substrates | **Substrate 1:** $\varepsilon_1$=2.33; $h_1$=0.508mm; tanδ=0.0013 |
| | **Substrate 2:** $\varepsilon_2$=1.09; $h_2$=3mm; tanδ=0.0004 |
| | **Substrate 3:** $\varepsilon_1$=2.33; $h_1$=0.508mm; tanδ=0.0013 |
| Patch | $W_P$=7mm; $L_P$=5mm |
| Slot | $W_S$=0.5mm; $L_S$=5.85mm |
| Feedline | W=0.432mm (100Ω); $L_{Stub}$=0.87mm |

**Table C-1** *SSFIP element design parameter*

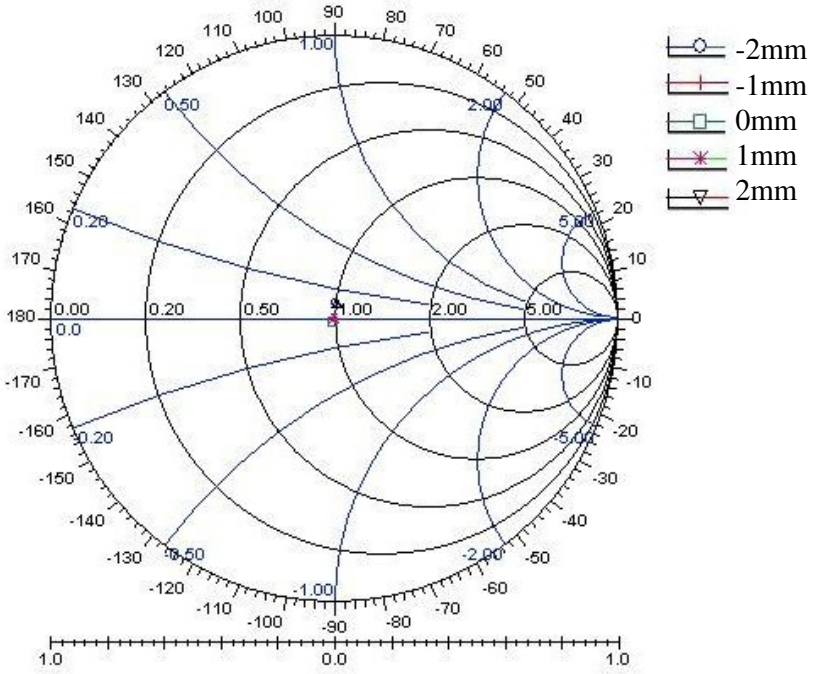


**Figure C-5** *Variations of the reflection coefficient due to misalignment between the patch and the slot in the y direction*

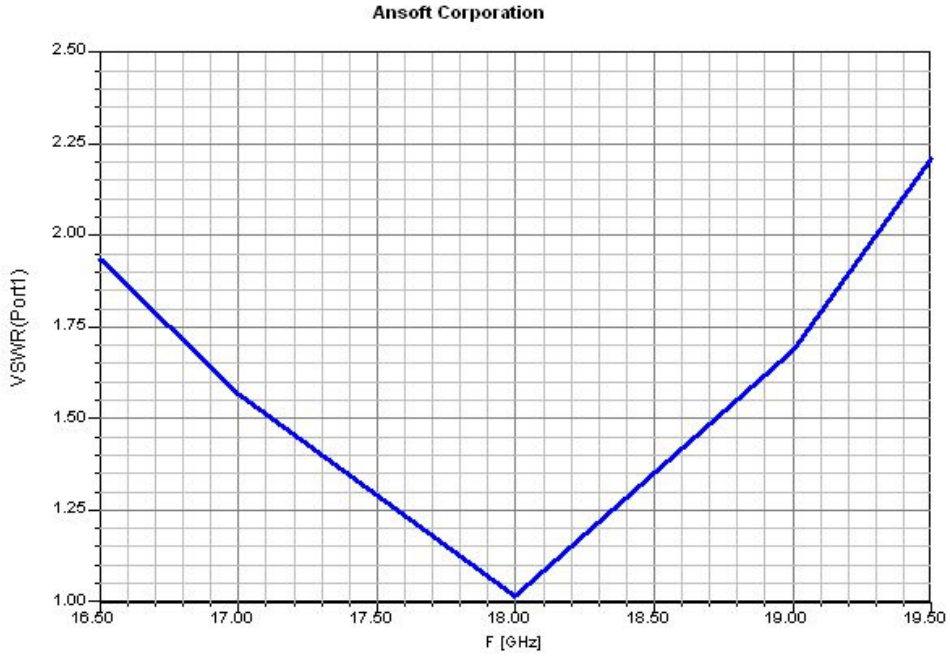


**Figure C-6** *VSWR of the SSFIP element as function of the working frequency*

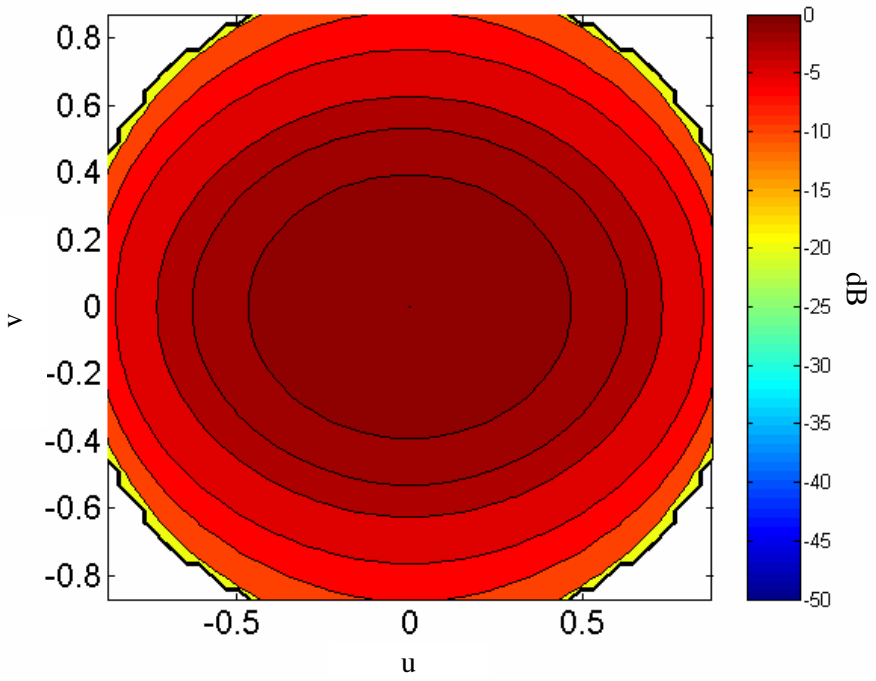


**Figure C-7** *Copolar field pattern of a single SSFIP element at 18GHz.*

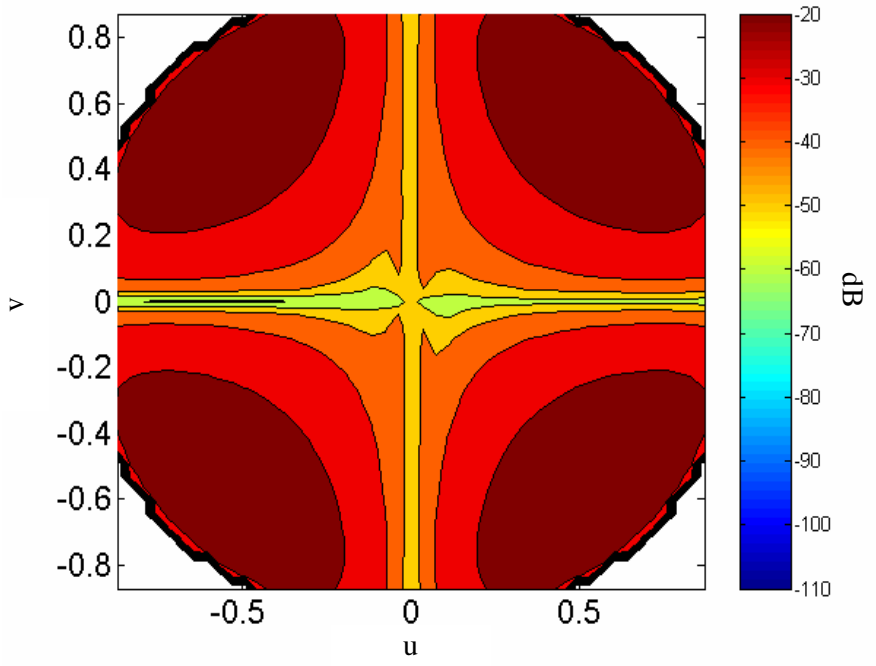


**Figure C-8** *Cross-polar field pattern of a single SSFIP element at 18GHz.*

## 1.2 REALIZATION PROCESS – ANTENNA BS8

Once the design of the radiating element has been carried out, some antenna prototypes have been realized.

In particular a photolithographic realization process has been used. The substrate employed is the Arlon DiClad 870, having $\varepsilon_r$=2.33 and tanδ=0.0013. The foam layer employed is the Cuming C-Stock RH5 having $\varepsilon_r$=1.09 and tanδ=0.0004. To assembly the multilayer structure the adhesive bonding film Arlon CuClad 6250 having $\varepsilon_r$=2.32 and tanδ=0.0013 has been considered.

The laminates have been coated with a liquid positive photoresist, the Futurrex PR1-400D. The coating has been achieved by using the dip-coater Chemat Dipmaster DM201 Automatic. The coated boards have been exposed by using the B2-UV exposition unit furnished by Elmi. The resist development has been obtained by using the Futurrex Resist Developer RD3. The etching process is realized with the foam etching machine EG1/L furnished by Elmi, by using ferric chloride $FeCl_3$. The remaining photoresist is removed by using the Futurrex Resist Remover RR4.

To verify the accuracy of the realization process, we realized the antenna BS8. The BS8 pattern is a canonical broadside one, requiring a uniform amplitude distribution. Such a distribution can be easily realized by using a microstrip corporate BFN. In particular, the BFN can be realized by using all equal power dividers. In this way, in fact, the power at the input of the corporate feed is equally subdivided across all the radiating elements and a uniform amplitude distribution is obtained (Fig.C-9).

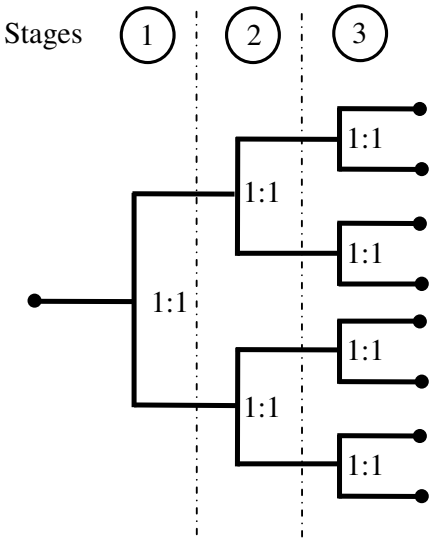


**Figure C-9** *Corporate feed layout showing the power divider splitting ratio needed to achieve a uniform amplitude distribution*

Accordingly, the main task is to design a symmetric power divider. In particular, let us start with the power divider located in the 3rd stage in Fig.C-9.

It has to feed, with the same signal level, the two radiating elements having input impedance equal to100Ω. Then, the power divider can be represented by the transmission line scheme depicted in Fig.C-10. The junction is fed by means of an input transmission line having characteristic impedance $Z_0$, while both output lines

have characteristic impedance equal to the one of the radiating element. This choice allows a 3dB divider between the two arms. Obviously the power divider input is matched if we have to use $Z_0=Z_L/2=50\Omega$.

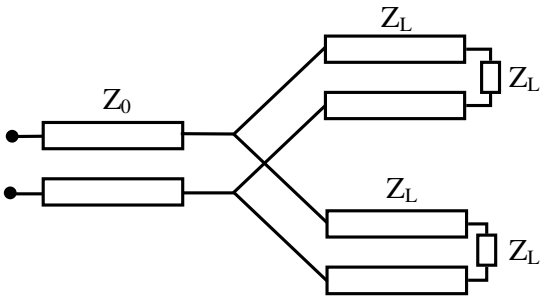


**Figure C-10** *Transmission line scheme of the symmetric power divider*

In Fig.C-11 we report the layout of the T-divider designed with the CAD Ansoft Designer. Here the exploited microwave ports are enlighten (grey elements). Moreover, the widths of the input and output lines are reported: the microstrip 1 has width equal to 1.524mm, corresponding to about 50Ω characteristic impedance, and the microstrip 2 with width 0.4321 corresponds to 100Ω characteristic impedance. In Tab.C-2 we report the scattering parameters evaluated with the software at 18GHz.

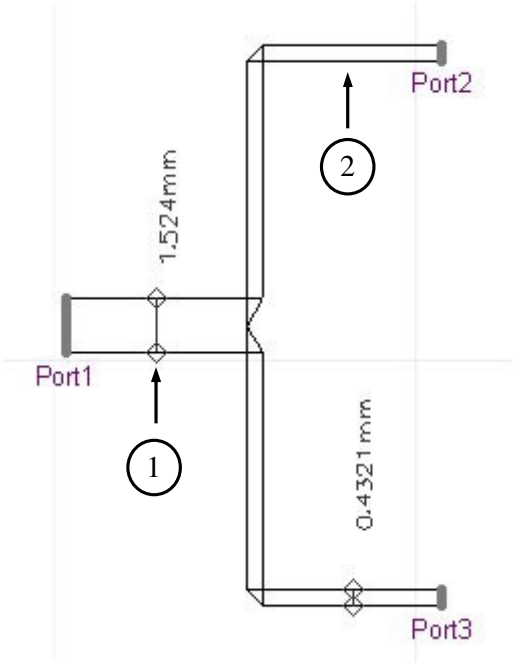


**Figure C-11** *Microstrip layout of the symmetric T-divider designed with the CAD Ansoft Designer. The width of the input and output microstrips are also reported*

| | $S_{11}$ Magnitude; Phase | $S_{12}$ Magnitude; Phase | $S_{13}$ Magnitude; Phase |
|---|---|---|---|
| f=18GHz | 0.082; -93.89º | 0.663; -148.84º | 0.663; -148.84º |

**Table C-2** *Power divider scattering parameters evaluated with the CAD at 18GHz*

Now, we describe the design process of the power dividers related to the 1st and the 2nd stage in Fig.C-9. To this end we can use the above discussed T-junction and introduce λ/4 transformers to get the matching conditions.

In particular the input impedance of power divider to be fed, equal to 50Ω need to be transformed to a 100Ω by means of a λ/4 transformer. The λ/4 transformers are shown in Fig.C-12, where the layout of the whole antenna system designed with the CAD is depicted, together with the adopted Cartesian reference system.

The antenna has been realized by using the equipment of the Antenna Lab of the DIET. The antenna radiative behavior has been characterized by using the planar near field scanning system available in the Microwave Lab of the DIET, located in a semianechoic environment, and using the far field scanning system installed in the Anechoic Chamber of the DIET. A wide campaign of measurements has been carried out to verify the accuracy of the antenna assembly process, before using the adhesive film to gluing together the layer.

The near field measurements have been carried out at 17.8GHz on a plane parallel to the antenna aperture and located at 10λ from the antenna. The measurement plane is about 33λx33λ and is centered on the antenna centre. A sampling distance equal to 8mm has been used for both directions. The probe exploited is an open-ended waveguide WR62 working in the Ku band (12.4GHz – 18GHz). The measurements have been carried out by using the Vector Network Analyzer Anritsu Wiltron 37377C. In Fig.C-13 we report schematically the measurement setup: the array is directed parallel to the y axis shown in Fig.C-13. Two cables Gore PhaseFlex EK, with an high phase stability, each 4m long, have been used to feed the antenna and the probe.

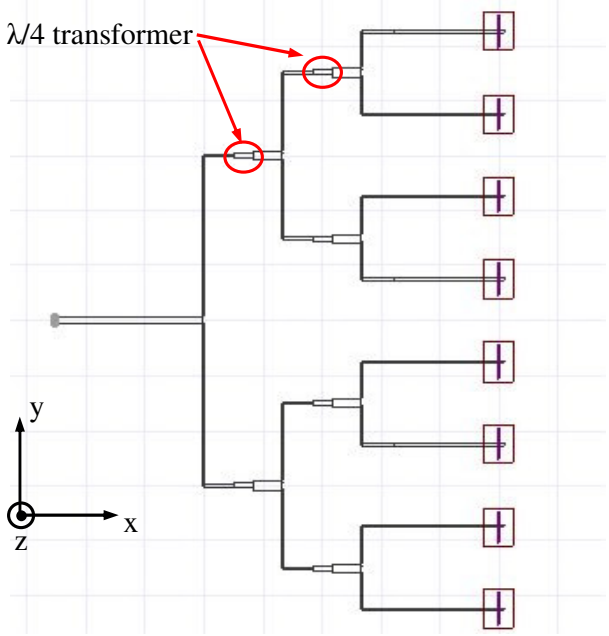


**Figure C-12** *Layout of the antenna BS8 showing the BFN, the slots and the patches.*

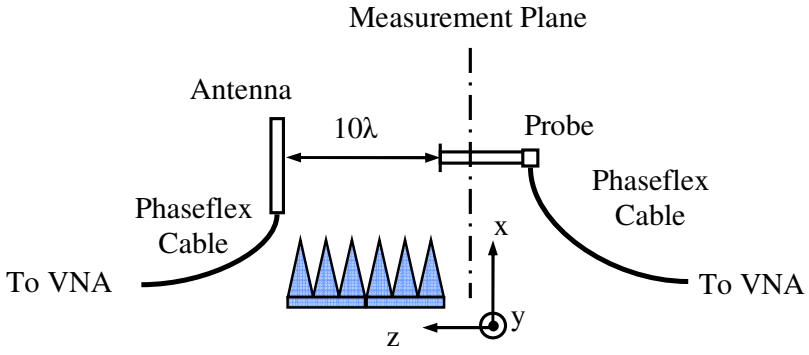


**Figure C-13** *Planar Near Field measurement setup (side view): the array is placed along a direction parallel to the y axis*

Let us denote with $V_x$ the magnitude of the voltage measured across the probe when the short side of the probe aperture is parallel to x axis, and as $V_y$ the magnitude of the voltage across the probe when it is rotated 90º with respect to the previous case.

Accordingly, in Fig.C-14 and Fig.C-15 we report the contour plot of the $V_x$ and $V_y$ observed on the measurement plane, respectively. In particular the $V_y$ component has been normalized to the maximum of the $V_x$ component.

The near field measurements have been properly processed by using a canonical filtering algorithm to reduce the effect of the environmental noise. In particular the near field components have been back propagated to calculate the aperture field. Only the antenna aperture contribution, appearing in the aperture field, has to be considered to achieve the filtered antenna pattern. Afterwards, the aperture field has been windowed according to the known aperture dimension. To tell the truth windowing functions with different extensions have been tested. In Fig.C-16 we report the aperture field, related to the component $V_x$, together with the chosen window function.

The far field components have been computed from the measured near field data by means of a near-field far-field transformation based on the probe compensation approach presented in [*Paris et al.*].

In Fig.C-17 we show the far field φ component, $E_\varphi$, for φ=90º(see the reference system in Fig.C-12). In particular we compare the $E_\varphi$ cut simulated by using the CAD and those measured by using the near-field and far field test range. In Fig.C.18 the contour plot of $E_\varphi$, as function of u and v, obtained from the near field measurement is reported. A photo of the antenna is shown in Fig.C-19.

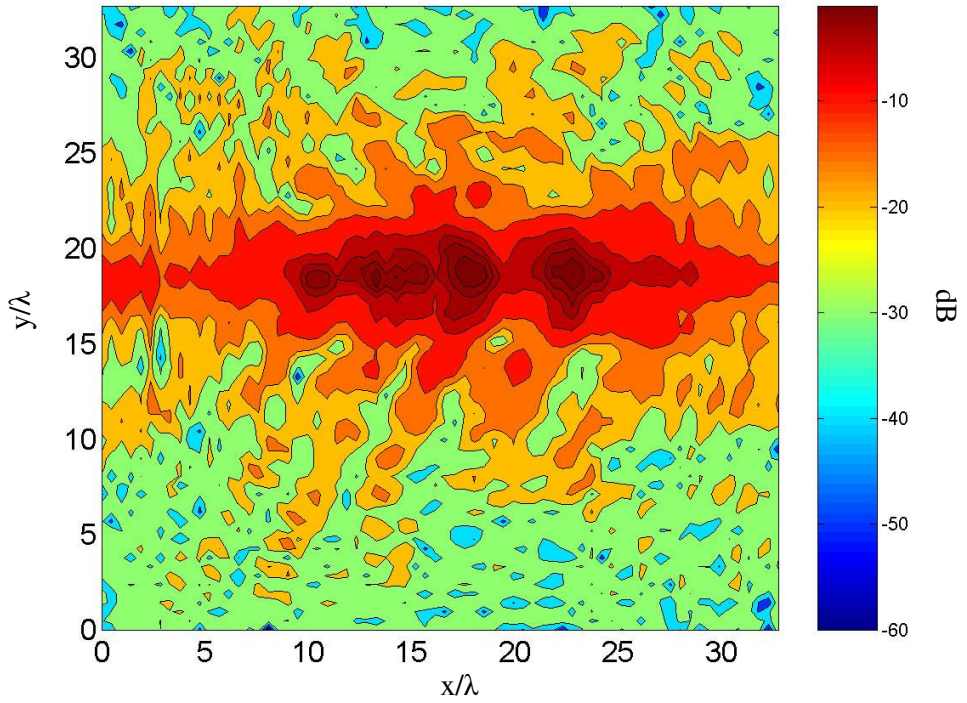


**Figure C-14** *Contour plot of $V_x$*

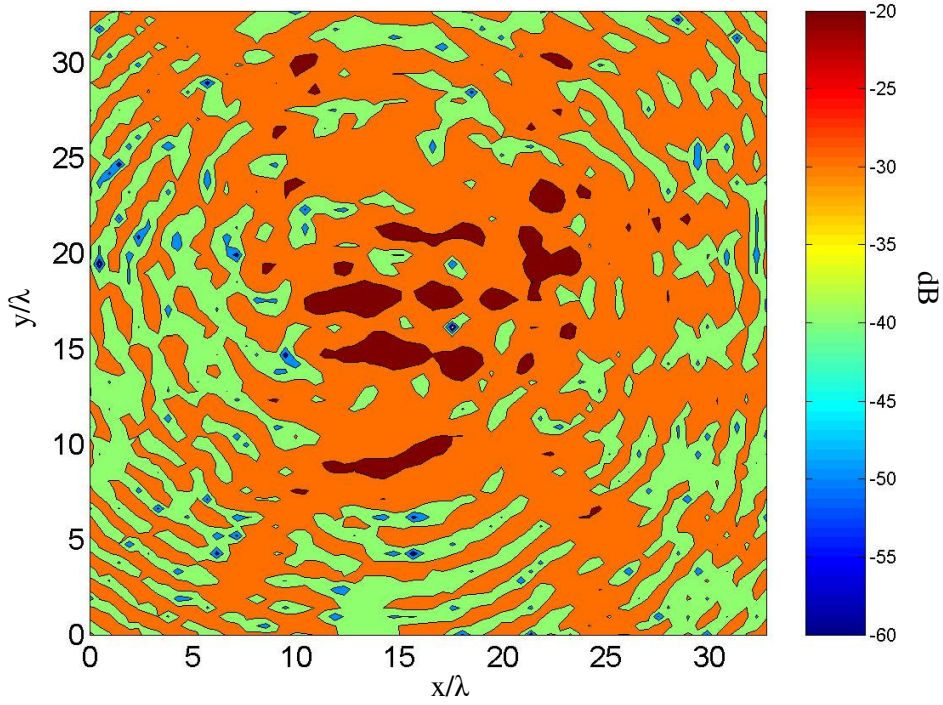


**Figure C-15** *Contour plot of Vy*

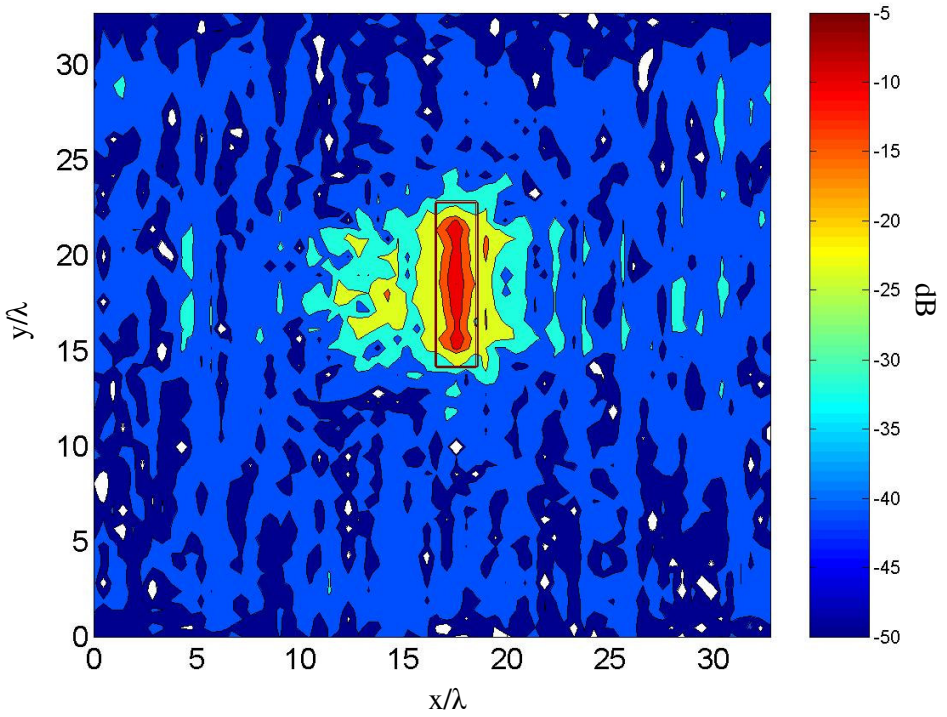


**Figure C-16** *Contour plot of the aperture field amplitude related to the component Vx together with the windowing function used to filter the environmental clutter*

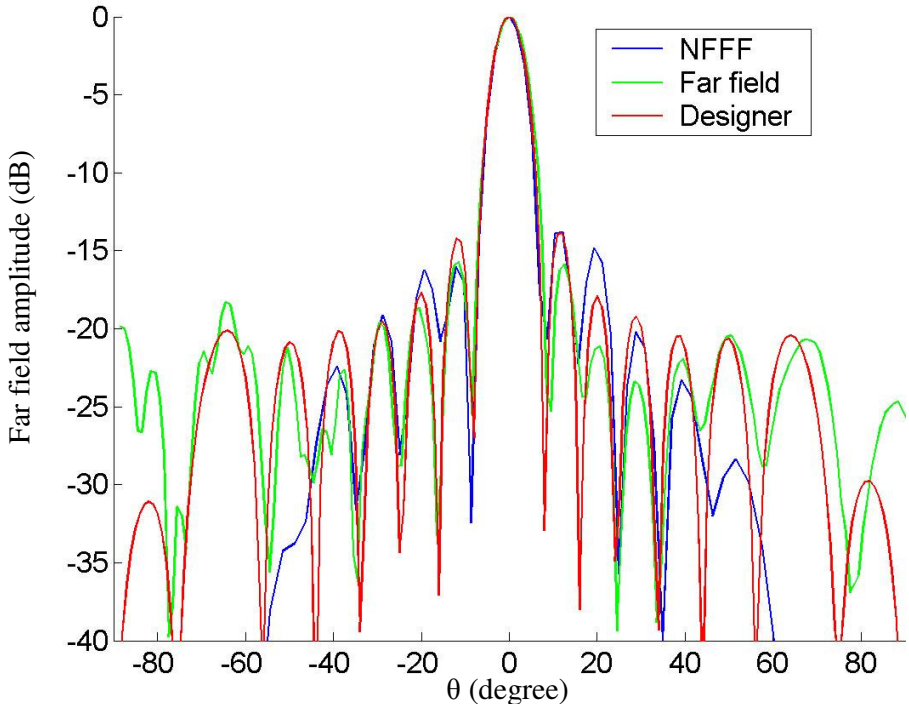


**Figure C-17** *Comparison among the cut of $E_\varphi$, for $\varphi$=90º, evaluated with the CAD, the one measured with the far field systems and the one obtained form the near field measurement*

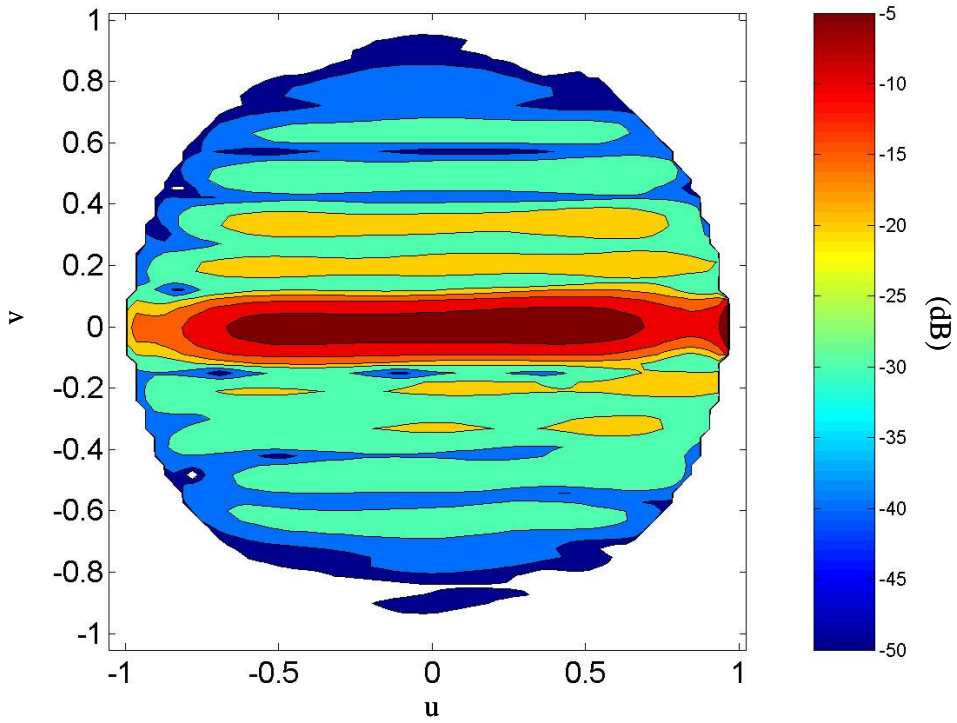


**Figure C-18** *Contour plot of $|E_\varphi|$ obtained from the near field measurements*

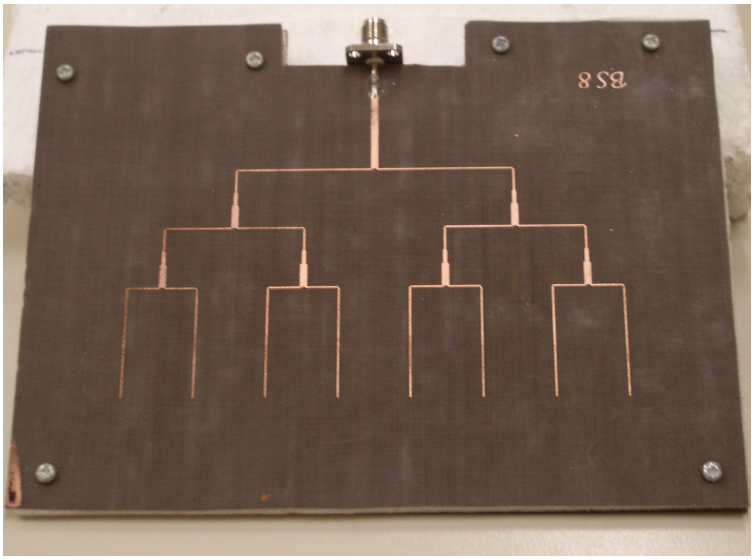


**Figure C-19** *Photo of the antenna BS8 prototype*

## 1.3 DESIGN PROCEDURE WITH THE CAD – ANTENNA TCH8

The design of the antenna BS8, although carried out with the electromagnetic CAD, does not enlighten the real issues related to the design of a microstrip corporate BFN. In fact, the BFN of the antenna BS8 is realized by duplicating the power dividers and by arranging them in a tree shape. In other words, the design of the BFN consists essentially in the design of one power divider. The latter is symmetric and, then, allows a quite simple design.

Accordingly, we considered a more complex antenna, with 8 elements, with half a wavelength spacing at 18GHz, and a Tchebitchev amplitude distribution with a SLL equal to -20dB. Such a distribution requires a more complex design of the BFN. In fact, the BFN requires power dividers with different splitting ratio, even if symmetrical.

The desired normalized distribution of the amplitude coefficients is [0.58 0.66 0.88 1 1 0.88 0.66 0.58]. The BFN dividers have to be designed in order to realize the proper current partitioning. To this end, power dividers with a suited splitting ratio have to be used. To realize such dividers, let us consider the transmission line scheme in Fig.C-20.

In this case, two $\lambda/4$ transformers are used, to match the load to the impedance of the characteristic impedance of the T-junction arm. In particular the characteristic impedance of the two T-junction arms has to be chosen in order to guarantee the proper power partitioning and respect the matching condition to the characteristic impedance $Z_0$ of the input transmission line. Therefore, if we call $K_I$ the ratio of the current $I_2$ flowing in the load $Z_{L2}$ and the current $I_1$ flowing in the load $Z_{L1}$, and $K_P$ the ratio among the power $P_2$ and $P_1$, delivered respectively to $Z_{L2}$ and $Z_{L1}$, we have:

$$K_P = K_I^2 \frac{Z_{L2}}{Z_{L1}} \tag{C.1}$$

The characteristic impedances $Z_1$ and $Z_2$ needed to achieve the proper partitioning are given by:

$$\begin{cases} Z_2 = \dfrac{K_P + 1}{K_P} Z_0 \\ Z_2 = (K_P + 1) Z_0 \end{cases} \tag{C.2}$$

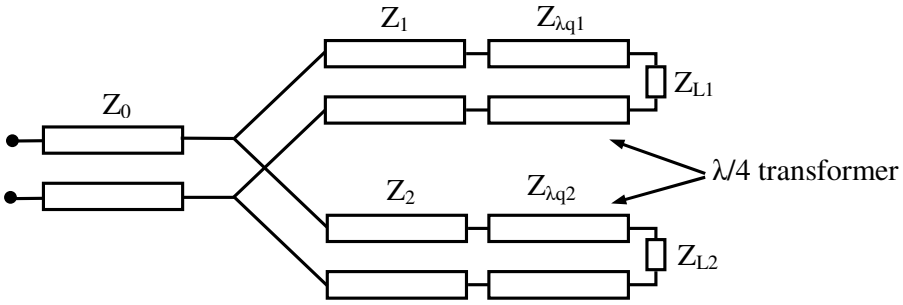


**Figure C-20** *Transmission line scheme of the symmetric power divider*

Accordingly, we have to individuate the splitting ratio of each divider employed in the BFN. In Fig.C-21 the BFN scheme of the antenna TCH8 is reported. Since the amplitude distribution is symmetric, the BFN is symmetric too. In particular, we need to design only 4 dividers, as shown in Fig.C-21. Starting from the desired current distribution, the splitting ratio of each divider can be easily found. These are shown in Fig.C-21. In principle, eq. (C-2) can be used to design each divider junction.

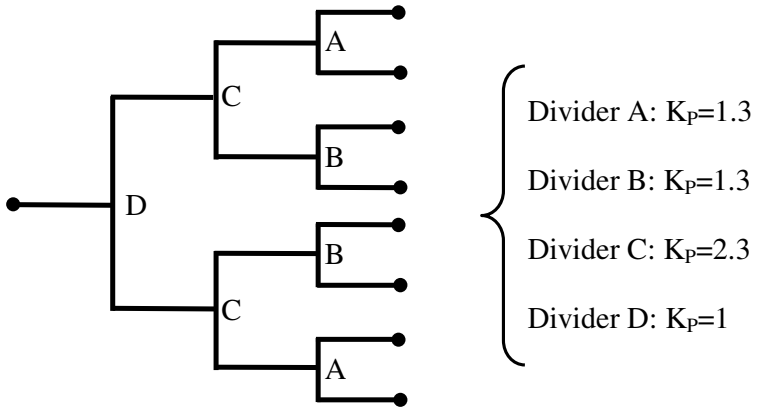


**Figure C-21** *Corporate feed layout of the antenna TCH8. The BFN is symmetrical. Only 4 dividers have to be designed*

Actually, when the required $K_P$ grows, the theoretical design formulas (C-2) are not correct anymore and the design has to be carried out by making a wide use of the CAD. Moreover, a asymmetrical junction generates a phase unbalance among the output arms. These phase unbalances propagate along the whole BFN and, then, need to be compensated by properly lengthening the radiating element feed lines. In Fig. C-22 we report the layout of the BFN realized with the CAD, where the microwave ports are shown with grey dots.

The scattering parameters of the BFN have been evaluated at 18GHz by using the CAD. Accordingly, by referring to the ports configuration in Fig.C-22, we report in Tab.C-3 the phase of the scattering parameters of interest, and their magnitude normalized to the one of the $S_{16}$. In fact, this parameter is related to the radiating element that should have the maximum amplitude coefficient. The ratio of the scattering parameters gives the normalized amplitude distribution we obtained, which is quite similar to the desired one.

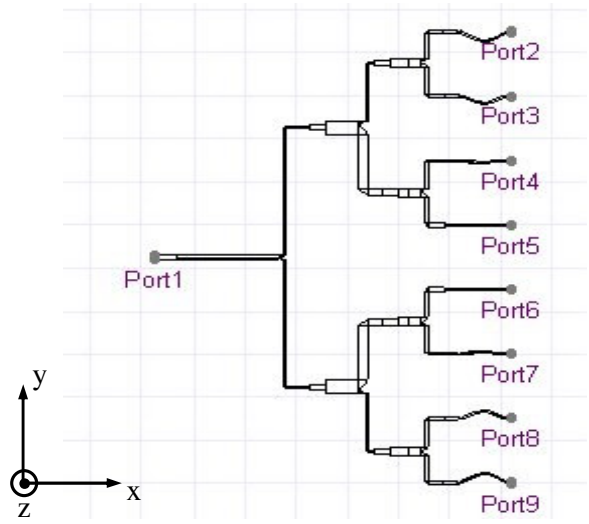


**Figure C-22** *Layout of the BFN of the antenna TCH8 showing the microwave ports configuration*

| | $S_{12}$ | $S_{13}$ | $S_{14}$ | $S_{15}$ | $S_{16}$ | $S_{17}$ | $S_{18}$ | $S_{19}$ |
|---|---|---|---|---|---|---|---|---|
| f=18GHz | Normalized Magnitude | | | | | | | |
| | 0.60 | 0.67 | 0.87 | 1 | 1 | 0.86 | 0.67 | 0.60 |
| | Phase (degree) | | | | | | | |
| | 30.4º | 34.9º | 31.6º | 31.6º | 31.5º | 31.5º | 34.7º | 30.2º |

**Table C-3** *Scattering parameters related to the BFN structure reported in Fig.C-15 evaluated at 18GHz by means of the CAD*

The antenna prototype has been realized and characterized by using the near field planar scanning system and the far field measurement apparatus previously described. In particular the near field measurements have been realized using a setup similar to the one employed to characterize the antenna BS8. The measurements have been carried out at 17.8GHz on a plane 12λ far from the antenna. The measurement plane is about 33λx33λ and is centered on the antenna centre. A sampling distance equal to 8mm has been used for both directions. As usual the probe exploited is an open-ended waveguide WR62.

In Fig.C-23 we report the aperture field related to the component $V_x$. The aperture field shows an unexpected contribution located at the left of the aperture (see Fig.C-23). This contribute is reasonably due to imperfection on the antenna input connection. Accordingly, the filtering is necessary to attain good results.

In Fig.C-24 we compare the $E_\varphi$ cut, for $\varphi$=90º, simulated by using the CAD and those measured by using the near-field and far field test range

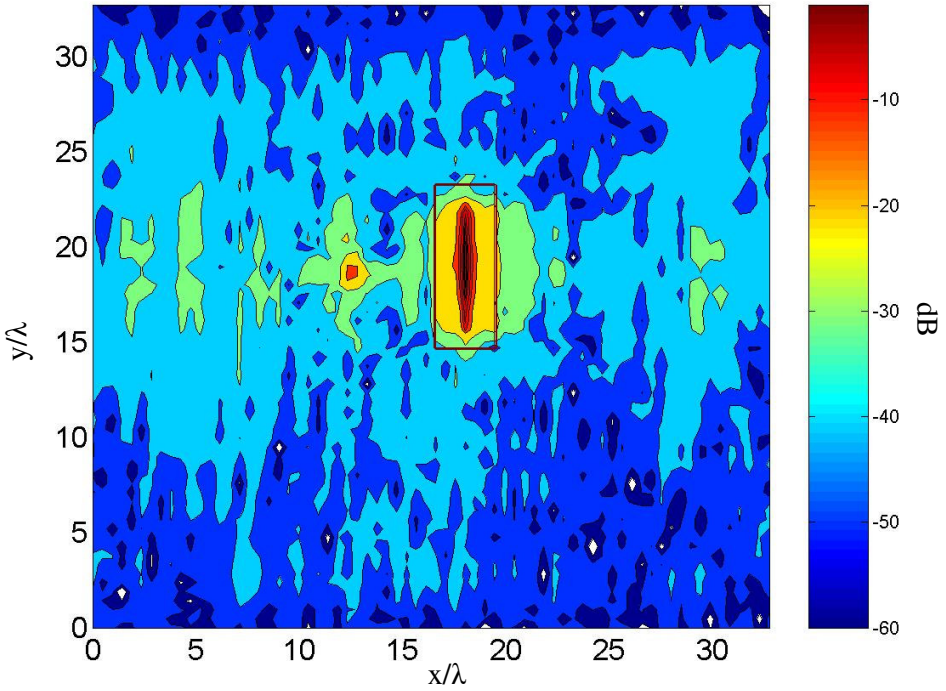


**Figure C-23** *Contour plot of the aperture field amplitude related to the component Vx together with the windowing function used to filter the environmental clutter*

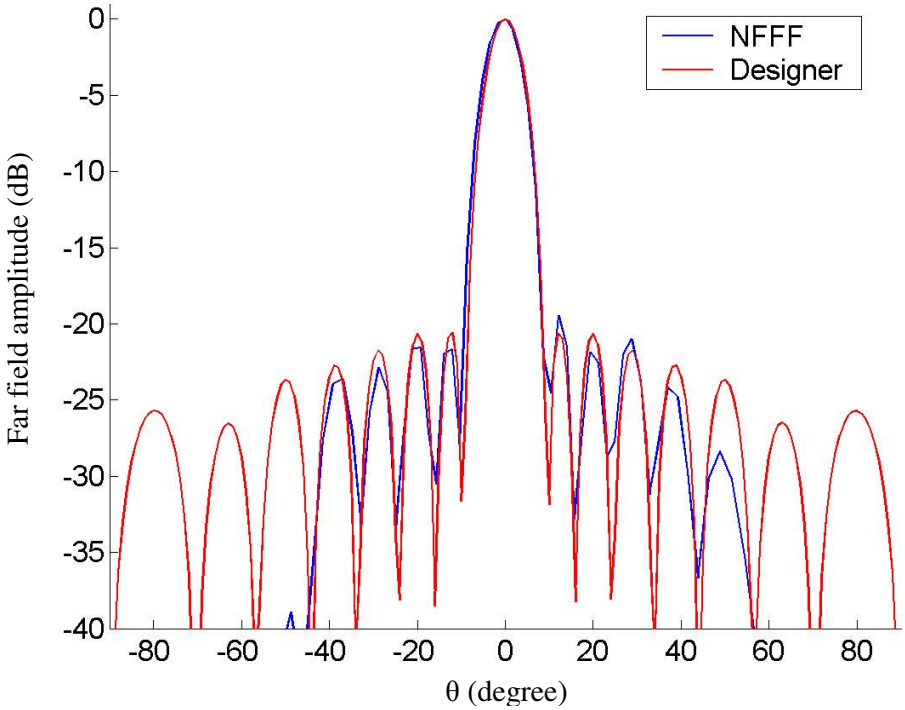


**Figure C-24** *Comparison among the cut of $E_{\varphi}$, for $\varphi$=90º, evaluated with the CAD, the one measured with the far field systems and the one obtained form the near field measurement*

In Fig.C-25 the contour plot of $E_\varphi$, as function of u and v, obtained from the measurement carried out in the near field test range is reported. Finally, the prototype photo is shown in Fig.C-26.

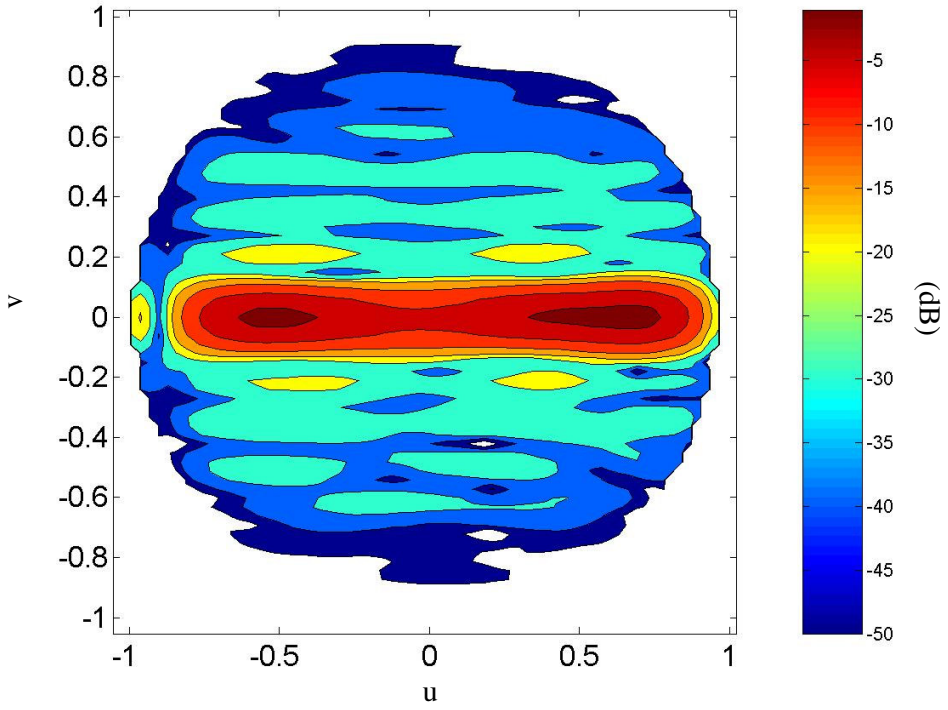


**Figure C-25** *Contour plot of $|E_\varphi|$ obtained from the near field measurements*

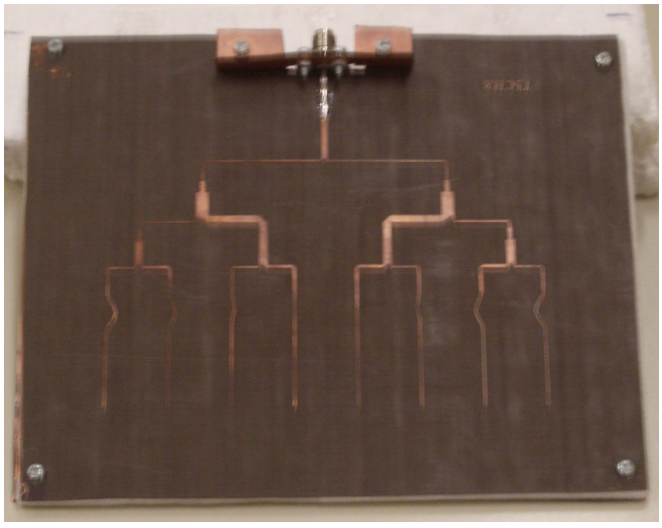

**Figure C-26** *Photo of the antenna TCH8 prototype*

## 1.4 EXTERNAL SYNTHESIS AND BFN DESIGN – ANTENNA DUALB11

The aim of the synthesis algorithm is to provide the excitation coefficients which, from one side match at the best the design specification on the far field patter and on the other side do not require a difficult realization process.

Here we refer to the synthesis technique presented in [*Bucci and D'Elia*; *Bucci et al. 2004a*]. We employed this synthesis algorithm to design a shaped beam antenna. In particular we considered a multiple beam to realize at the same time two links along two different directions. The antenna is made of 11 elements, with half a wavelength spacing, working at 18GHz. To enforce the pattern requirements, suited mask functions have been employed [*Bucci and D'Elia*; *Bucci et al. 2004a*].

Let us assume that the array aperture is located in the plane (x,y) and is directed parallel to the axis y. Accordingly, in Fig.C-27 we report cut for φ=90º of the mask functions used to set the requirements for the copolar component: the synthesis algorithm has to find the excitations ensuring the power pattern lying among the upper and the lower masks.

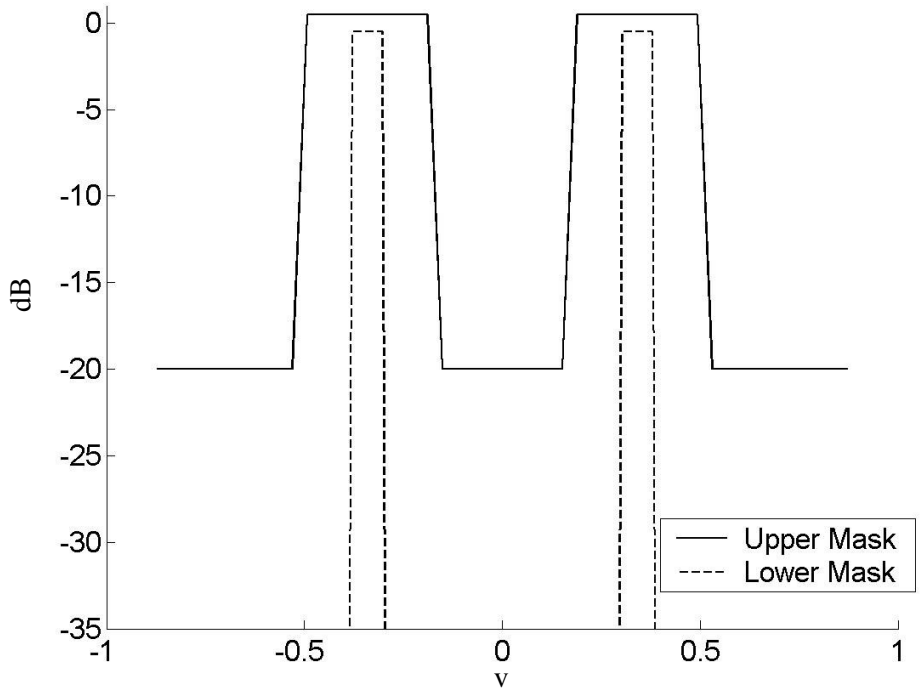


**Figure C-27** *Mask functions used in the synthesis procedure to set the power pattern requirements*

On the other direction the masks function used have the same behaviour of the square amplitude copolar component of the radiating element. Regarding the cross-polar component, a maximum level of -20dB under the copolar has been required.

The synthesis procedure has been carried out, by using the active synthesis approach, allowing to take into account for the mutual coupling effects on the element pattern. The set of excitation coefficients found, in amplitude and phase, is shown in Fig.C-28. In Fig.C-29 we report the cut of the far field copolar component, for φ=90º,

evaluated with the synthesis algorithm, compared to the mask functions and to the same cut of the copolar component cut computed by means of the CAD. It can be seen that, by using the active synthesis approach, there is an excellent agreement between the results provided by the synthesis algorithm and the CAD. In Fig.C-30 the contour plot of the amplitude of the copolar component evaluated by the synthesis algorithm is reported, as function of u and v.

By inspecting Fig.C-28 it appears clearly that the variations of the synthesized amplitude of the excitation coefficients can be too high to be effectively realized by the beamforming network. In other words the internal synthesis of the BFN becomes very difficult, since, as shown before, it is difficult to design unbalanced power dividers. Moreover, some dividers could require thin microstrips, difficult to be realized. On the other hand, a small amplitude dynamic is also useful to reduce the mutual coupling effects.

Accordingly, we introduced in the synthesis algorithm approach some constraints drawn from the internal synthesis problem and avoid the simplified subdivision of the synthesis problem in two separate design steps. We enforced a bound on the total dynamic variation of the amplitudes of the excitation coefficients and a bound on the maximum amplitude variation between two consecutive elements.

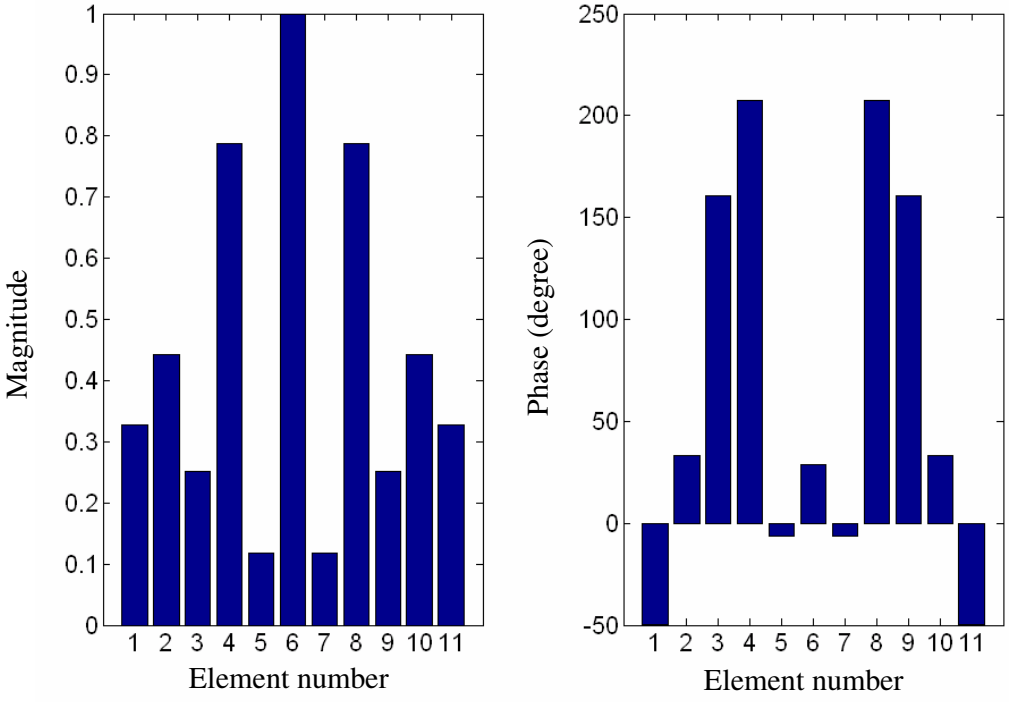


**Figure C-28** *Amplitude and phase of the excitation coefficients obtained with the synthesis procedure*

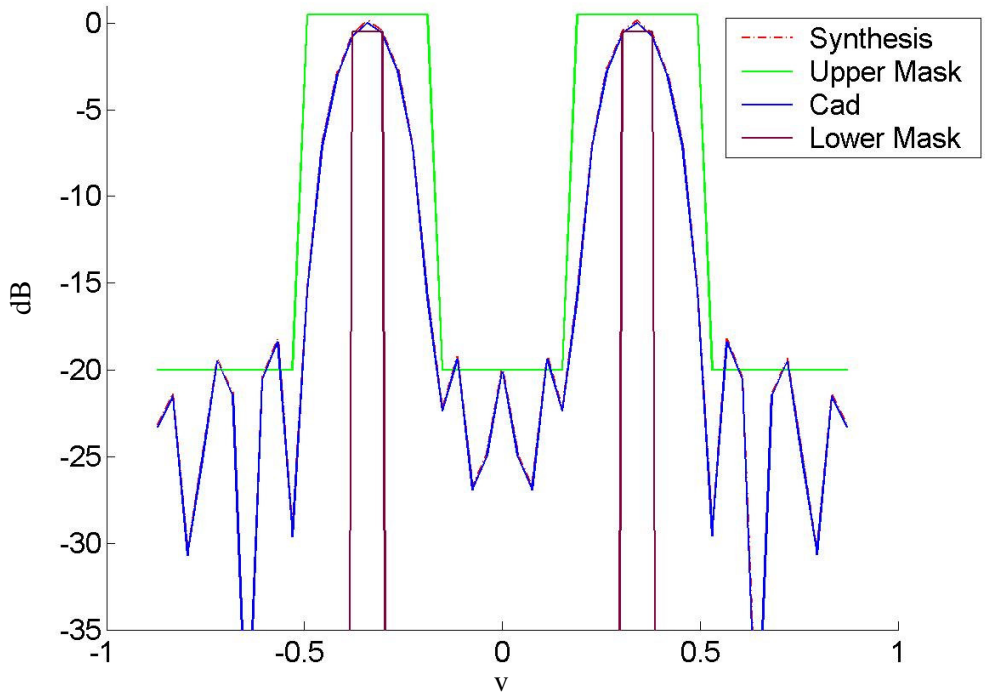


**Figure C-29** *Comparison among the cut of the copolar component, for φ=90º, obtained using the synthesis procedure and the one obtained by using the CAD*

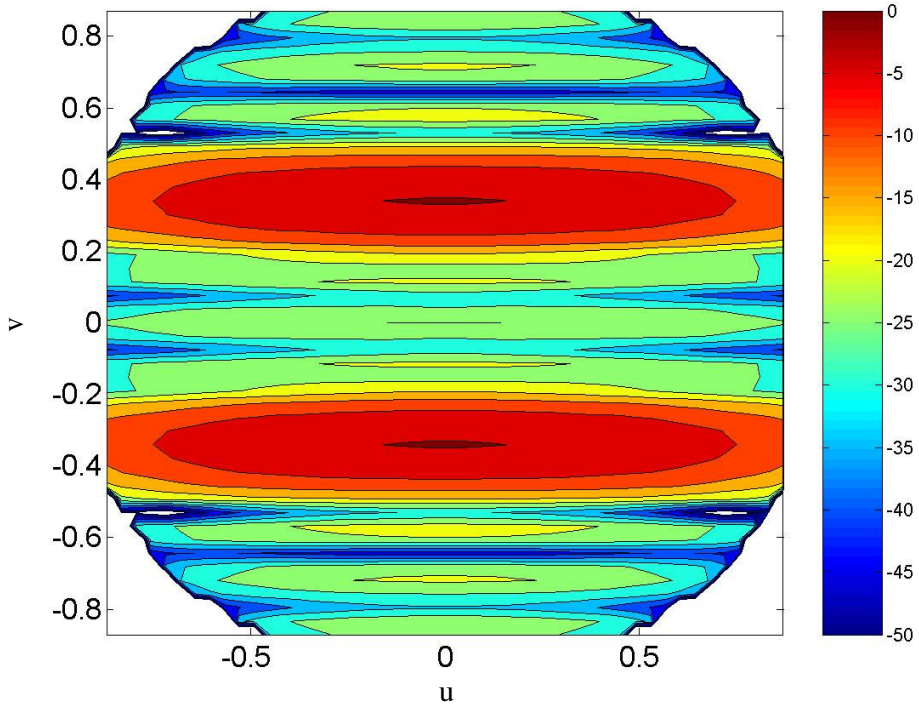


**Figure C-30** *Contour plot of the copolar component, obtained with the synthesis algorithm, as function of the cosine directors*

Let us now discuss the details of the synthesis algorithm we developed. Let us denote with $a_n$ the amplitude coefficient of the n-th element and with $x_n$ the normalized amplitude coefficient defined by:

$$x_n = \frac{a_n}{(a_n)_{\max}} \tag{C.3}$$

To fix the dynamic range for $x_n$ we required that each $x_n$ must lie within the range [1-Bg, 1], where $B_g$ define the dynamic variation. In particular let us denote with $B_{gD}$ the bound on the total dynamic of the normalized amplitude coefficients, with $B_{gN}$ the bound on the variation between two consecutive elements and with N the number of array elements. Accordingly we have:

$$B_g = \min\left\{B_{gD}, c_{n-1} \pm B_{gN}\right\} \quad n = 2,...N \tag{C.4}$$

In Fig.C-31 we compare the copolar power pattern, related to the cut for φ=90º, obtained without using the dynamic constraints and the one obtained by using the constraints with $B_{gD}$=1/3. By enforcing the constraint the antenna pattern slightly degrades, while a significant reduction of the coefficient amplitude variation is obtained, as shown in Fig.C-32, where both the antenna amplitude coefficient sets, found with the synthesis algorithm, are presented. In Fig.C-33 the contour plot of the copolar component obtained by using the synthesis algorithm employing the dynamic constraints is reported, as function of the cosine directors.

Accordingly, once a proper set for the excitation coefficients has been found, the design of the BFN has been achieved by using the CAD, following the discussed design criteria. The BFN layout obtained and simulated by means of the CAD is reported in Fig.C-34. The BFN structure is made of two sections in order to reduce the number of power divider requiring very unbalanced structures. Regarding the phase distribution, it has been obtained by proper lengthening the microstrip lines feeding the radiating elements.

In Fig.C-35 we compare the amplitude and the phase of the excitation coefficients required and the ones realized with the CAD.

The antenna prototype has been realized and characterized by using the near field cylindrical scanning system and the far field measurement apparatus installed in the anechoic chamber of the DIET and the planar scanning systems installed in a semianechoic environment within the Microwave Lab of the DIET.

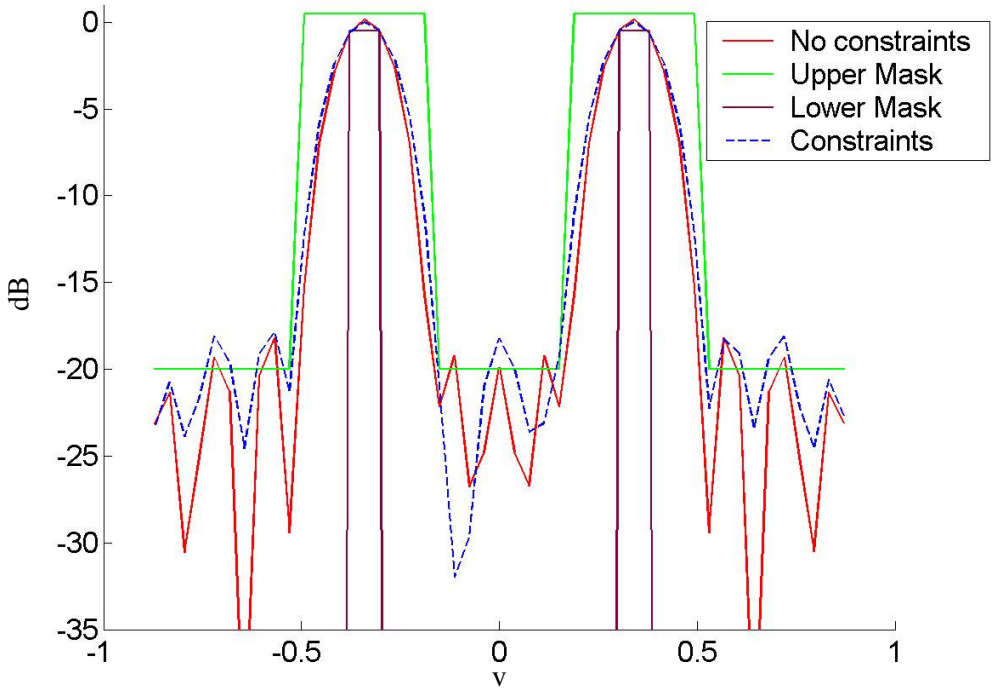


**Figure C-31** *Comparison between the cut of the copolar component, for φ=90º, obtained using the synthesis procedure with and without the constraints on the amplitude dynamic*

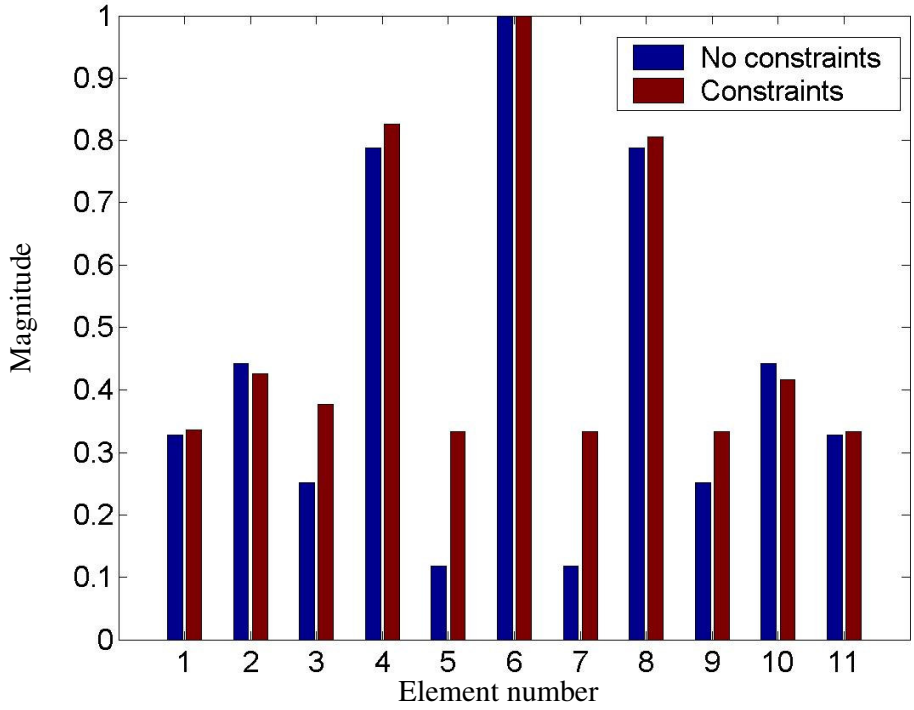


**Figure C-32** *Comparison between amplitude coefficients obtained by using the synthesis procedure with and without the constraints on the amplitude dynamic.*

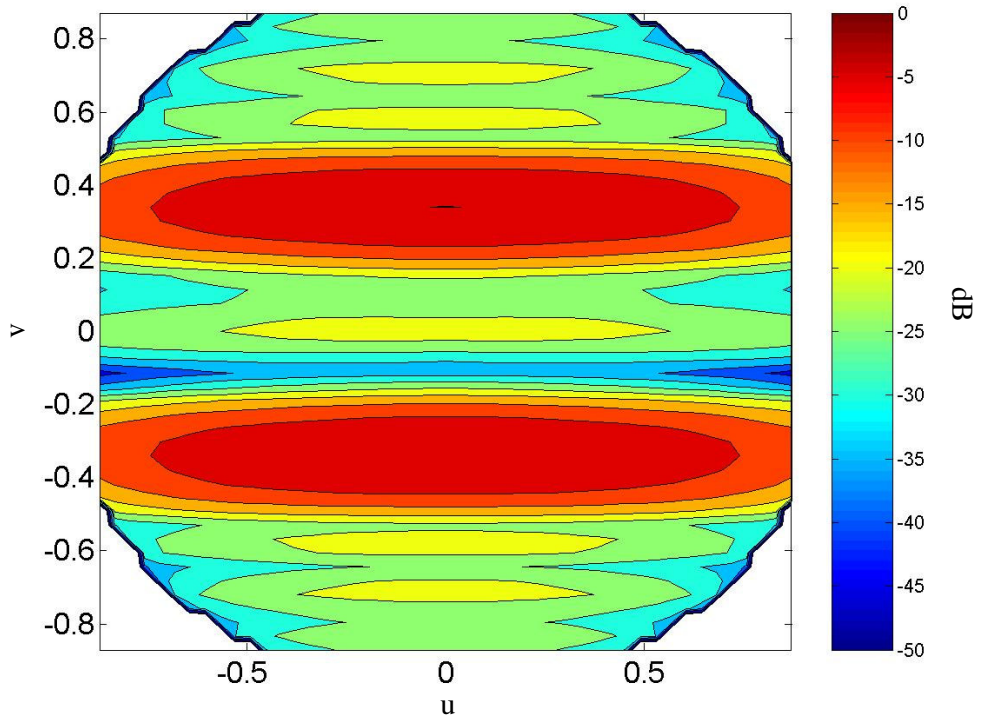


**Figure C-33** *Contour plot of the copolar component, as function of u and v, obtained by the synthesis algorithm when constraints on the amplitudes of the excitation coefficients are enforced*

Regarding the near field scanning system, the measurements have been carried out at 17.8GHz. The measurement setup related to the near-field cylindrical test range is shown. The measurement surface is cylindrical and is centered in the antenna centre. The surface radius is 18λ, its height is 47λ, while its angular extension is symmetric with respect to the antenna, as shown in Fig.C-36, and is 2α=240º. The measurement points are sampled along z with a step of about 8mm, and along φ with a step of about 3º. The probe exploited is an open-ended waveguide WR62. The measured near field components have been processed to calculate the far field components. The near-field far-field transformation is based on the probe compensation approach presented in [*Leach and Paris*; *Curcio*]. In Fig.C-37 we present the contour plot of the copolar component obtained from the cylindrical near field measurements as function of u and v.

Regarding the planar near field measurements these have been realized by using a setup similar to the one used for the antenna BS8 and TCH8. The measurements have been carried out at 17.8GHz on a plane located at 7λ from the antenna. The measurement plane is about 33λx33λ and is centered on the antenna centre. The sampling distance is equal to 8mm in both directions. The probe exploited is an open-ended waveguide WR62. The canonical filtering strategy has been employed to reduce the environmental noise effects. In particular, in Fig.C-38, we show the aperture field related to the component $V_x$ together with the employed window function. Also in this case the noise due to the imperfection on the antenna input connection is clear.

In Fig.C-39 the contour plot of the copolar component, as function of u and v, obtained from the near field measurements is reported. Finally, the prototype photo is shown in Fig.C-40.

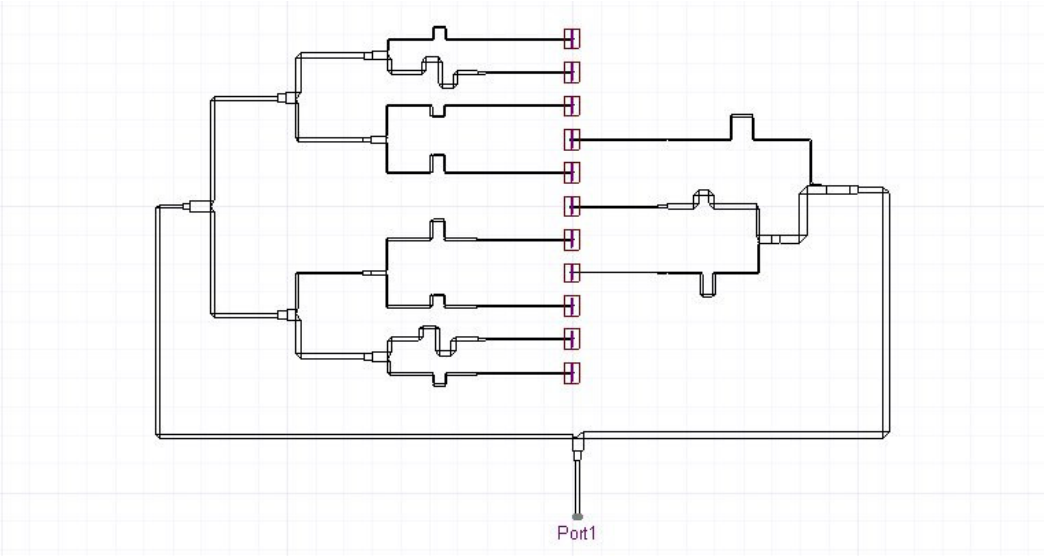


**Figure C-34** *Layout of the BFN of the antenna Dual11*

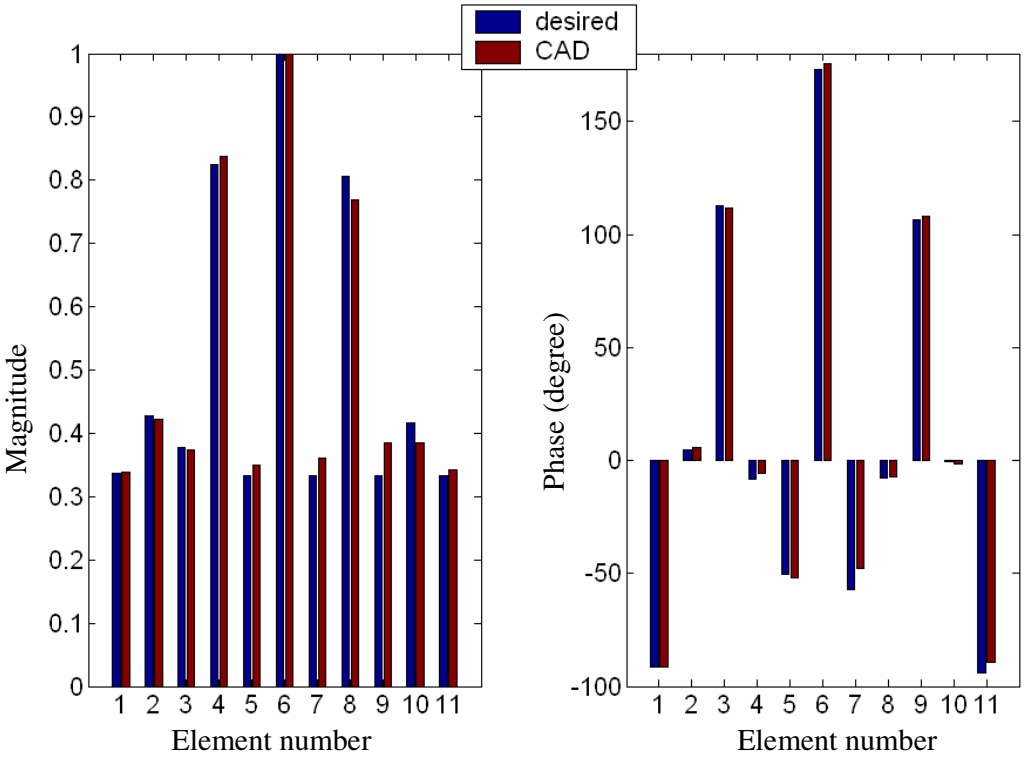


**Figure C-35** *Comparison between the amplitude and phase of the excitation coefficients obtained with the synthesis procedure and the ones obtained with the CAD*

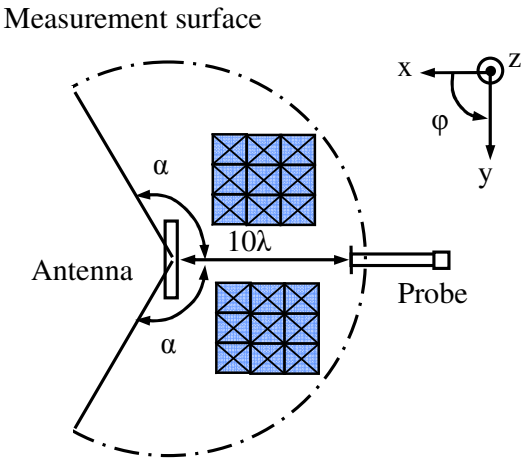


**Figure C-36** *Cylindrical Near Field measurement setup (top view): the array axis is the z axis*

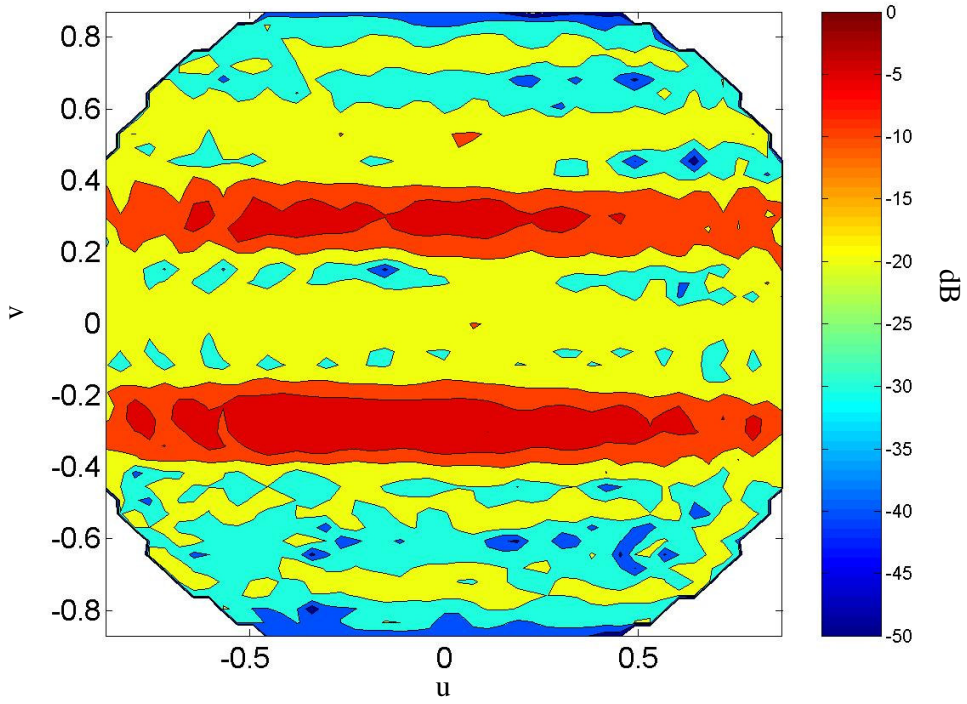


**Figure C-37** *Contour plot of the copolar component, obtained from the near field measurements carried out by using the cylindrical scanning system*

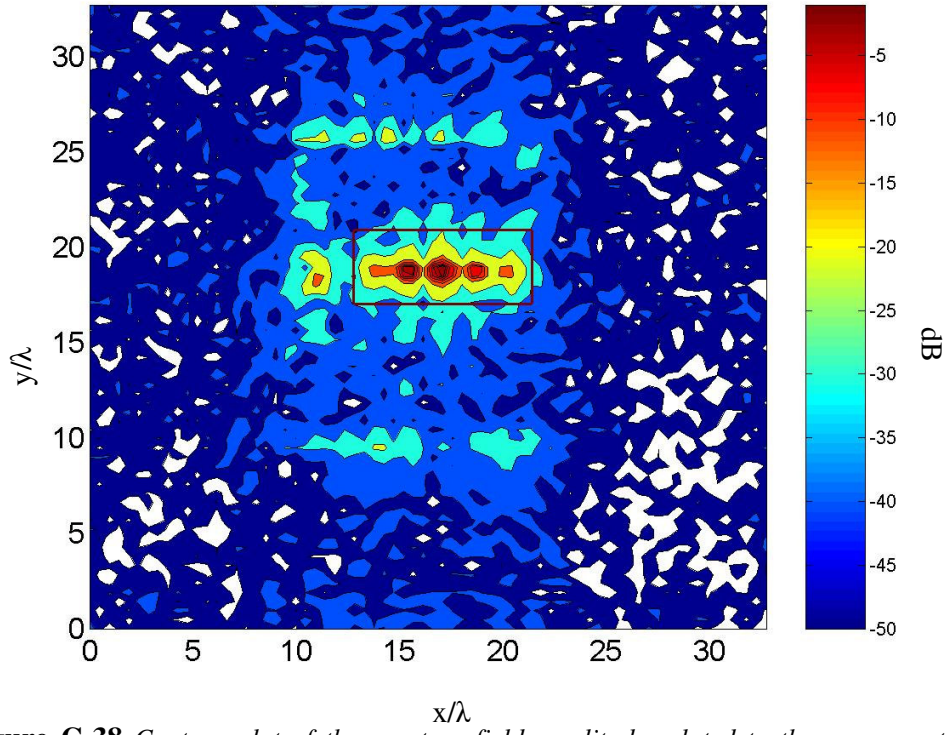


**Figure C-38** *Contour plot of the aperture field amplitude related to the component Vx together with the windowing function used to filter the environmental clutter*

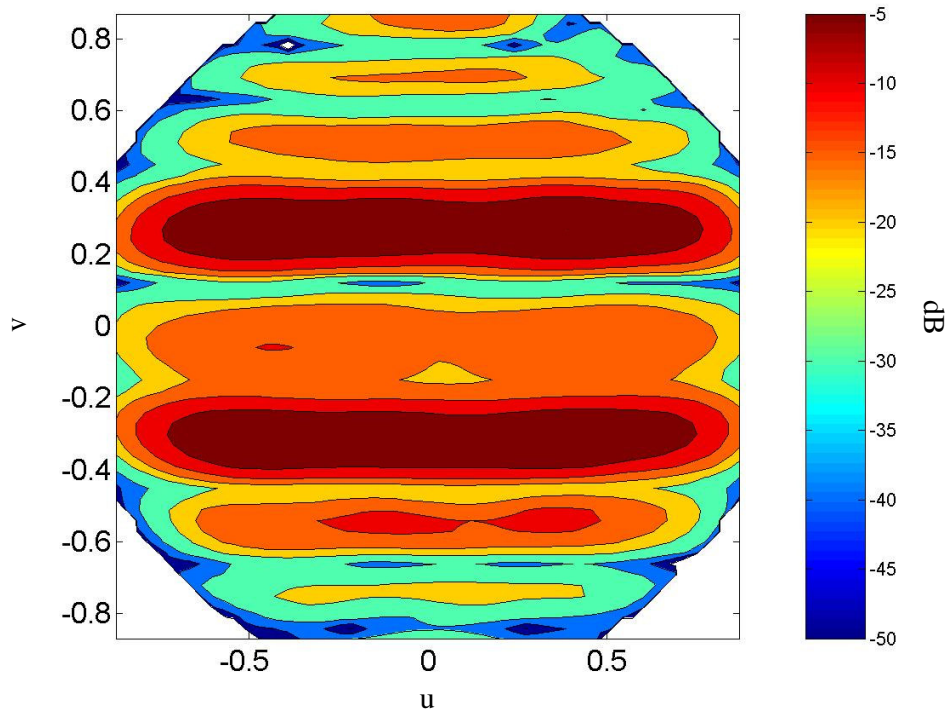


**Figure C-39** *Contour plot of the copolar component, obtained from the near field measurements carried out by using the planar scanning system*

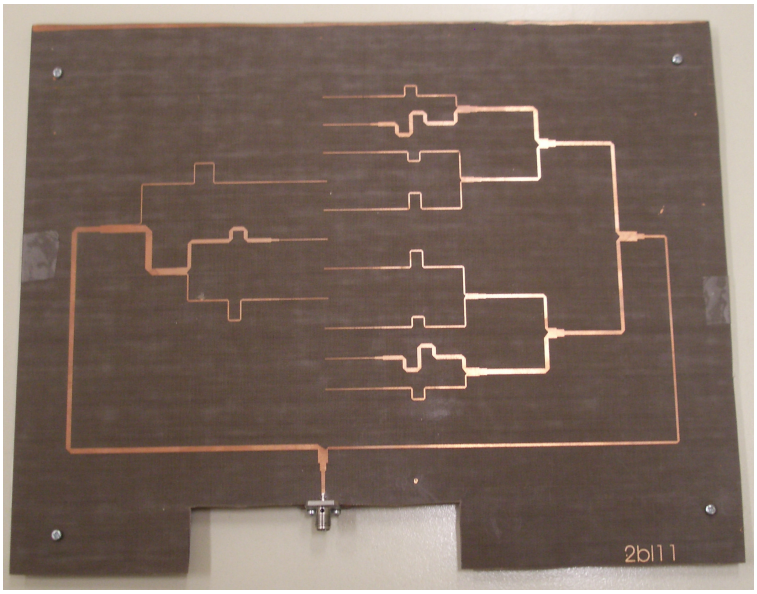


**Figure C-40** *Photo of the antenna Dualb11 prototype*

# REFERENCES


[*Ackerman and Cox*] Ackerman, E.I. and C.H. Cox (2001), RF fiber-optic link performances, *IEEE Microwave Magazine*, 2, 4, 50-58

[*Ackerman et al.*] E. Ackerman et al. (1992), Integrated 6 bit photonic true time delay unit for lightweight 3-6GHz radar beamformer, IEEE International Microwave Symposium, 2, 681-684

[*Agrawal and Holzman*] Agrawal, A.K. and E.L. Holzman (1999), Beamformer architectures for active phased-array radar antennas, *IEEE Trans. Antennas Propagat.,* 47 (3), 432-442

[*Akiyama et al. 1999*] Akiyama, T., K. Inagaki and Y. Mizuguchi (1999), Beam-steering and multibeam formation of Ku-band phased array antenna using optical signal processing beam-forming network, International Topical Meeting on Microwave Photonics, 17-19 Nov. 1999, 1, 173-176

[*Akiyama et al. 2001*] Akiyama, T., K. Inagaki, T. Ohira, and M. Hikita (2001), Two-dimensional optical signal-processing beamformer using multilayer polymeric optical waveguide arrays, *IEEE Trans. Microwave Theory Tech.,* 49 (10), 2055-2061

[*Alameh et al.*] Alameh, K.E., R.A. Minasian and N. Fourikis (1995), High capacity optical interconnects for phased array beamformers, *J. Lightwave Technol.*, 13 (6), 1116-1120

[*Anderson and Boldissar*] Anderson, L.P. and F. Boldissar (1987), Antenna beamforming using optical processor, IEEE International Symposium on Antennas and Propagation, 1, 431-434

[*Armenise et al.*] Armenise, M.N., V.M.N. Passaro and G. Novello (1994), Lithium niobate guided-wave beam former for steering phased-array antennas,*Applied Optics*, 33 (26), 6194-6209

[*Back et al.*] Back, T., D.B. Fogel and Z. Michalewicz (1997), *Handbook of evolutionary computation*, Institute of Physics Publishing and Oxford University Press

[*Ball et al.*] Ball, G.A., W.H. Glen and W.W. Morey (1994), Programmable fiber optic delay line, *IEEE Photon. Technol. Lett.*, 6 (6), 741-743

[*Belisle et al.*] Belisle, C., C. Delisle and J. Oldham (2000), Photonic differential delay beam forming network for phased-array antennas**,** International Topical Meeting on Microwave Photonics, 11-13 Sept., 81-84

[*Benjamin and Seeds*] R. Benjamin and A.J. Seeds (1992), Optical beamforming techniques for phased array antennas, *IEE Proceedings-H*, 139(6), 526-534

[*Benjamin et al.*] Benjamin, R., C.D. Zaglanikis and A.J. Seeds (1990), Optical beam former for phased arrays with independent control of radiated frequency and phase, *Electron. Lett.*, 26 (22), 1853-1855

[*Blanchflower and Seeds*] Blanchflower, I.D. and A.J. Seeds (1989), Optical control of frequency and phase of GaAs MESFET oscillator, *Electron. Lett.*, 25 (5), 359-360

[*Bowers*] Bowers, J. (1996), Devices for microwave photonics, International Topical Meeting on Microwave Photonics, 3-5 Dec., 29-32

[*Bratchikov 1998*] Bratchikov, A.N. (1998), Optical fibers and antennas, Proc. JINA 98, Nice, France, 275-289

[*Bratchikov 2000*] Bratchikov, A.N. (2000), Optical beamfoming technology for active phased array, Antennas and Propation Symposium, Davos, Switzerland, April 9-14, 133-138

[*Bratchikov et al.*] Bratchikov, A.N., D.I. Voskresensky and K. van't Klooster (2003), Radio astronomical phased arrays with fiber - optic design architecture, International Conference on Antenna Theory and Techniques, 9-12 September, Sevastopol, Ukraine, 617-623

[*Brookner*] Brookner, E. (2003), Phased arrays around the world – Progress and future trends, IEEE Int. Symp. on Phased Array Systems and Technology, Boston, MA, Oct.14-17, 1-8

[*Bucci and D'Elia*] Bucci, O.M. and G.D'Elia (1998), Power synthesis of reconfigurable conformal arrays with phase-only control, *IEE Proceeding on Microwaves, Antennas Propagat.*, 145 (1), 131-136

[*Bucci et al. 2004a*] Bucci, O.M., A. Capozzoli and G. D'Elia (2004), Power pattern synthesis of reconfigurable conformal arrays with near-field constraints, *IEEE Trans. Antennas and Propagat.*, 52 (1), 132–141

[*Bucci et al. 2004b*] Bucci, O.M., A. Capozzoli, G. Chiaretti, C. Curcio, G. D'Elia and A. Fincato (2004), An integrated photonic true time delay unit for phased array antennas, Atti della XV RiNEM, Cagliari, 13-16 September, 277-280

[*Bucci et al. 2005*] Bucci, O.M., A. Capozzoli, C. Curcio and G. D'Elia (2005), A digital Time shifter for optical time steered antennas, International Conference on Electromagnetics in Advanced Applications, 12-16 Sept., Turin, 1, 823-826

[*Buckley*] Buckley, R.H. (2000), Some aspects of the use of photonics in large sensor manifolds, IEEE International Conference on Phased Array Systems and Technology, 21-25 May, 341-344

[*Capozzoli and D'Elia 2006a*] Capozzoli, A. and G. D'Elia (2006), Global optimization and antennas synthesis and diagnosis, Part one: concepts, tools, strategies and performances, *Progress in Electromagnetics Research*, 56, 195-232.

[*Capozzoli and D'Elia 2006b*] Capozzoli, A. and G. D'Elia (2006), Globall optimization and antenna synthesis and diagnosis, Part two: applications to advanced reflector antennas synthesis and diagnosis techniques, *Progress in Electromagnetics Research*, 56, 233-261

[*Cardone*] Cardone, L. (1985), Ultra-wideband microwave beamforming technique, *Microwave J.*, 28 (4), 121-131

[*Carlson*] Carlson, A.B. (1986), *Communication systems,* McGraw Hill

[*Carver et al.*] Carver, K., W. Cooper and W. Stutzman (1973), Beam-pointing errors of planar-phased arrays**,** *IEEE Trans. Antennas Propagat.,* 21 (2), 199-202

**[***Chang and Tarng***]** Chang, I.C. and S.S. Tarng (1988), Phased array beamforming using acousto-optic techniques, Advances in optical information processing III, D.R. Pape, editor, *Proc. SPIE*, 936, 163-167

[*Chang*] Chang, K. (2003), *Handbook of optics*, John Wiley & Sons

[*Chang et al.*] Chang, Y. et al. (1997), Optically controlled serially fed phased-array transmitter, *IEEE Microwave and Guided Wave Lett.*, 7 (3), 69-71

[*Chen and Chen*] Chen, Y. and R.T. Chen (2002), A fully packaged true time delay module for a k-band phased array antenna system demonstration, *IEEE Photon. Technol. Lett.*, 14 (8), 1175-1177

[*Chen and Li 1996*] Chen, R.T and R.L.Q. Li (1996), Photonic true-time-delays based on multiplexed substrate-guided wave propagation for phased array antenna applications, Radar Processing, Technology, and Applications, W.J. Miceli, editor, *Proc. SPIE*, 2845, 235-243

[*Chyba*] Chyba, M. (2000), Planar array antenna for secondary radar synthesis, International Conference on Microwaves, Radar and Wireless Communications, 22-24 May, 1, 174 – 177

[*Cohen et al.*] Cohen, D.A., Y. Chang, A.F.J. Levi, H.R. Fetterman and I.L. Newberg (1996), Optically controlled serially fed phased array sensor, *IEEE Photon. Technol. Lett.*, 8 (12), 1683-1685

[*Collin and Zucker*] Collin, R.E and F.J. Zucker, *Antenna Theory*, Part 1 and 2, McGraw-Hill, New York, 1969

[*Corral et al. 1997a*] Corral, J.L., J. Martì, S. Regidor, J. M. Fuster, R. Laming, and M.J. Cole (1997), Continuously variable true time-delay optical feeder for phased-array antenna employing chirped fiber gratings, *IEEE Trans. Microwave Theory Tech.*, 45 (8), 1531-1536

[*Corral et al. 1997b*] Corral, J.L., J. Martì, S. Regidor, J. M. Fuster and R. Laming (1997), True time delay scheme for feeding optically controlled phased array antennas using chirped fiber bragg gratings, *IEEE Photon. Technol. Lett.*, 9 (11), 1529-1531

[*Corral et al. 1999a*] Corral, J.L., J. Martì and J. M. Fuster (1999), Optical up-conversion on continuously variable true-time-delay lines based on chirped fiber gratings for millimeter-wave optical beamforming networks, *IEEE Trans. Microwave Theory Tech.*, 47 (7), 1315-1320

[*Corral et al. 1999b*] Corral, J.L., J. Martì and J.M. Fuster (1999), Effects of optical modulation on continuously variable millimeter-wave delay lines based on optical fiber gratings, IEEE Microwave Symposium, 13-19 June, 3, 1117-1120

[*Coward et al.*] Coward, J.F., T.K. Yee, C.H. Chalfant and P.H. Chang (1993), A photonic integrated-optic RF phase shifter for phased array antenna beam-forming applications, *J. Lightwave Technol.*, 11 (12), 2201-2205

[*Cox*] Cox, C.H. (2000), Step towards photonic antennas, IEEE International Conference on Phased Array Systems and Technology, 21-25 May, 339

[*Cox et al.*] Cox, C.H., G. Betts and L. Johnson (1990), An analytic and experimental comparison of direct and external modulation in analog fiber optic links, *IEEE Trans. Microwave Theory Tech.*, 38 (5),501-509

[*Cruz et al. 1997*] Cruz et al. (1997), Chirped fibre bragg gratings for phased array antennas, *Electron. Lett.*, 33 (7), 545-546

[*Cruz et al. 1998*] Cruz, J.L., B. Ortega, M. V. Andres, B. Gimeno, J. Capmany and L. Dong (1998), Array factor of a phased array antenna steered by a chirped fiber grating beamformer, *IEEE Photon. Technol. Lett.*, 10 (8), 1153-1155

[*Curcio*] Curcio C. (2002), Allestimento e analisi delle prestazioni di un sistema di misura per la caratterizzazione di antenne in ambiente anecoico, M.S. thesis, 209 pp., Univ. of Naples Federico II, Naples, 26 June

[*Curtis and Mailloux*] Curtis, D.D. and R.J. Mailloux (1992), A critical look at photonics for phased array systems, Antennas and Propagation Society Symposium, 18-25 July, 2, 117

[*Daryoush et al. 1987*] Daryoush, A., P. Herczfeld, V. Contarino, A. Rosen, Z. Turski and P. Wahi (1987), Optical beam control of mm-wave phased array antennas for communications, Microwave Journal, 30 (3), 97-98 100 102-104

[*Daryoush et al. 1991*] Daryoush, A.S. et al. (1991), Interfaces for high speed fiber optic links: analysis and experiment, *IEEE Trans. Microwave Theory Tech.*, 39 (12), 2031-2044

[*Derickson*] Derickson, D. (editor) (1998), *Fiber optic test and measurements*, New Jersey, Prentice Hall

[*Dolfi et al. 1989*] Dolfi, D., J.-P. Huignard and M. Baril (1989), Optically controlled true time delays for phased array antenna, Optical Technology for Microwave Applications IV, S.-K. Yao, editor,*Proc.SPIE, 1102, 152-161*

[*Dolfi et al. 1991*] Dolfi, D., F. Michel-Gabriel, S. Bann and J.P. Huignard (1991), Two-dimensional optical architecture for time-delay beam forming in a phased-array antenna, *Optics Lett., 16 (4), 255-257*

[*Dolfi et al. 1996*] Dolfi, D., P. Joffre, J. Antoine, J.-P. Huignard, D. Philippet and P.Granger (1996), Experimental demonstration of a phased-array antenna optically controlled with phase and time delays, *Applied Optics*,35 (26), 5293-5300

[*Dolfi et al. 2000*.] Dolfi, D., D. Mongardien, S.Tonda, M. Schaller and J. Chazelas (2000), Photonics for airborne phased array radars, IEEE Int. Symp. on Phased Array Systems and Technology, 21-25 May, 379-382

[*Dolfi et al.*] Dolphi, D., J-P. Huignard and M. Baril (1989), Optically controlled true time delays for phased array antennas, Optical technology for microwave applications, S.K. Yao editor, *Proc. SPIE*, 1102, 152-161

[*Esman et al. 1989*] Esman, R.D., Lew Goldberg and J.F. Weller (1989), Optical phase control of an optically injection-locked FET microwave oscillator, *IEEE Trans. Microwave Theory Tech.*, 37 (10), 1512-1518

[*Esman et al. 1992*] Esman, R.D., M.J. Monsma, J.L. Dexter and D.G. Cooper (1992), Microwave true time-delay modulator using fibre-optic dispersion, *Electron. Lett.*, 28 (20), 1905-1907

[*Esman et al. 1993*] Esman, R.D. et al. (1993), Fiber-optic prism true time-delay antenna feed, IEEE Photon. Technol. Lett., 5, (11), 1247-1249

[*Fetterman et al.*] 2002 Multiple output Fetterman, H. et al. "Multiple output photonic RF phase shifters for optically controlled radar systems", IEEE International Microwave Symposium Digest 2-7 June 2002, Vol. 3, 1937—1940, 2002

[*Fouquet*] Fouquet, J.E. (2000), Compact optical cross-connect switch based on total internal reflection in a fluid-containing planar lightwave circuit, Optical Fiber Communication Conference, 7-10 March, 1, 204-206

[*Fouquet et al.*] Fouquet, J.E., S. Venkatesh, M. Troll, D. Chen, H.F. Wong, and P.W. Barth (1998), A compact, scalable cross-connect switch using total internal reflection due to thermally-generated bubbles, Annual Meeting of the IEEE Lasers and Electro-Optics Society, 1-4 Dec., 2, 169-170

[*Fourikis*] Fourikis, N. (1997), *Phased array based systems and applications*, Wiley-Interscience

[*Frankel and Esman*] Frankel, M.Y. and R.D. Esman (1995), True time-delay fiber-optic control of an ultrawideband array transmitter receiver with multibeam capability, *IEEE Trans. Microwave Theory Tech.*, 43 (9), 2387-2394

[*Frankel et al. 1995*] Frankel, M.Y., R.D. Esman and M.G. Parent (1995), Array transmitter/receiver controlled by a true time delay fiber optical beamformer, *IEEE Photon. Technol. Lett.*, 7 (19), 1216-1218

[*Frankel et al. 1996a*] Frankel, M.Y., P.J. Matthews and R.D. Esman (1996), Two dimensional fiber optic control of a true time-steered array transmitter, *IEEE Trans. Microwave Theory Tech.*, 44 (12), 2696-2702

[*Frankel et al. 1996b*] Frankel, M.Y., P.J. Matthews and R.D. Esman (1996), Wideband array transmitter with two dimensional fiber optic beam steering, IEEE Intern. Symp. On Phased Array Systems and Technology, 15-18 Oct., 425-428

[*Frankel et al. 1997*] Frankel, M.Y., P.J. Matthews and R.D. Esman (1997), Fiber optic true time steering of an utrawide-band receive array, *IEEE Trans. Microwave Theory Tech.*, 45 (8), 1522-1526

[*Frankel et al. 1998*] Frankel, M.Y., P.J. Matthews, R.D. Esman and L. Goldberg (1998), Practical Optical Beamforming networks, *Optical and Quantum Electronics*, 30, 1033-1050

[*Freitag and Forrest*] Freitag, P.M. and S.R. Forrest (1993), A coherent optically controlled phased array antenna system, *IEEE Microwave and Guided Wave Lett.,* 3 (9), 293-295

[*Friyges and Seeds*] Frigyes, I. and A.J. Seeds (1995), Optically generated true time delay in phased array antennas, *IEEE Trans. Microwave Theory Tech.*, 43 (9), 2378-2386

[*Galwas*] Galwas, B.A (1998), Photonic technology for microwave engineering, Int. Conf. on Microwave and Radar, 20-22 May, 4, 117-134

[*Garg et al.*] Garg, R., P. Bhartia, I. Bahl and A. Ittipiboon (2001), *Microstrip antenna design handbook*, Norwood, MA, Artech House

[*Ghorbani and Waterhouse*] Ghorbani, K. and R.B. Waterhouse (2002), Ultrabroadband Printed (UBP) Antenna, *IEEE Trans. Antennas Propagat.*, 50 (12), 1697-1705

[*Goldberg et al.*] Goldberg, L., R.D. Esman, K.J. Williams (1992), Generation and control of microwave signals by optical techniques**,** *IEE Proceedings J Optoelectronics*, 139 (4), 288-295

[*Goutzoulis and Davies*] Goutzoulis, A.P. and D.K.Davies (1990), Hardware compressive 2D fiber optic delay line architecture for time steering of phased array, *Applied Optics*, 29 (36), 5353-5359

[*Goutzoulis and Gouse*] Goutzoulis, A.P. and R.P. Gouse (1997), Comparison of conventional and fiberoptic manifolds for a dual band (UHF and S) phased-array antenna, *IEEE Trans. Antennas Propagat.*, 45 (2), 246-253

[*Goutzoulis et al. 1989*] Goutzoulis, A.P., D.K. Davies and J.M. Zomp (1989), Prototype binary fiber optic delay line, *Optical Engineering*, 28 (11), 1193-1202

[*Goutzoulis et al. 1992*] Goutzoulis, A.P., D.K. Davies and J.M. Zomp (1992), Hybrid electronic fiber optic wavelength-multiplexed system for true time-delay steering of phased array antennas, *Optical Engineering, 31 (11), 2312-2322*

[*Goutzoulis et al. 1994*] Goutzoulis, A.P., D.K. Davies, J.M. Zomp, P. Hrycak and A. Johnson (1994), Development and field demonstration of a hardware-compressive fiber-optic true-time-delay steering system for phased-array antennas, *Applied Optics, 33 (35), 8173-8185*

[*Grosskopf et al.*] Grosskopf, G. et al. (2001), Silica based beamformer for 60 GHz smart antennas, 27th European Conference on Optical Communication, 30 Sept.-4 Oct., 1, 12-13

[*Gupta and Simonis*] Gupta, N. and G. Simonis (1990), Lithium niobate integrated-optics demonstration of optical control of microwaves, Optoelectronic Signal Processing for Phased-Array Antennas II, B.M. Hendrickson, G.A.Koepf, editors, *Proc. SPIE*, 1217, 92-100

[*Hajimiri et al.*] *Hajimiri, A., A. Komijani, A. Natarajan, R. Chunara, and X. Guan (2004),* Phased Array Systems in Silicon, *IEEE Commun. Magazine*, 42 (8), 122-130

[*Hall*] Hall, P.S. (1986), Multioctave bandwidth log-periodic microstrip antenna array, *Proc. IEE part H*, 133 (2), 127-136

[*Han et al. 2002*] Han, J. (2002), Multiple output photonic RF phase shifter using a novel polymer technology, *IEEE Photon. Technol. Lett.*, 14 (4), 531-533

[*Han et al. 2003*] Han, J., B.J. Seo, S. Kim, H. Zhang and H.R. Fetterman (2003), Single-chip integrated electro-optic polymer photonic rf phase shifter array, *J. Lightwave Technol.*, 21 (12), 3257-3261

[*Hansen*] Hansen, R.C. (1998), *Phased array antennas*, Wiley-Interscience

[*Harres*] Harres, D.N. (2001), Using statistical methods to predict link quality in COTS-based fiber optic networks, 20th Conference Digital Avionics Systems, 14-18 Oct., 1, 4D3/1 - 4D3/8

[*Hecht*] Hecht, E. 2002, *Optics*, Addison Wesley, San Francisco

[*Hemmi et al.*] Hemmi, C., R.T. Dover, F. German and A. Vespa (1999), Multifunction wide-band array design, *IEEE Trans. Antennas Propagat.*, 47 (3), 425-431

**[***Henion and Schulz***]** Henion, S.R. and P.A. Schulz (1998), Electrooptic phased array transmitter, *IEEE Photon. Technol. Lett.*, 10 (3), 424-426

[*Herczfeld*] Herczfled, P. (2004), Optically controlled phased array antenna from X-band to terahertz, International Topical Meeting on Microwave Photonics, 4-6 Oct, 8-11

[*Herczfeld et al.*] Herczfeld, P.R., A.S. Daryoush, M. Kieli, S. Siegel and R.A. Soref (1987), Wide-band true time delay phase shifter devices, Intern. Microwave Symp., 87 (2), 603-606

[*Herrmann and Murphy*] Herrmann, J.J. and K.W. Murphy (1993), Statistical optical analysis of passive optical networks provides "plug and play" installation with fiber in the loop system, 5th Conference on Optical/Hybrid Access Networks, 7-9 Sept., 3.04/01 - 3.04/0

**[***Hietala et al.***]** Hietala, V.M., G.A. Vawter, W.J. Meyer and S.H. Kravitz (1991), Phased-array antenna control by a monolithic photonic integrated circuit, Optical Technology for Microwave Applications V, S.-K. Yao, editor, *Proc. SPIE*, 1476, 170-175

[*Hong and McMichael*] Hong, J.H. and I. McMichael (1991), Novel optical technique for phased array processing, *Optical Engineering*, 30 (12), 1976-1980

[*Horikawa et al.*] Horikawa, K., Yoshinori Nakasuga, Hiroyo Ogawa (1995), Self-heterodyning optical waveguide beam forming and steering network integrated on

lithium niobate substrate, *IEEE Trans. Microwave Theory and Tech.*, 43 (9), 2395-2401

[*Immorev and Taylor*] Immorev, I.J. and J.D. Taylor (2002), Future of radars, IEEE Conference on Ultra Wideband Systems and Technologies, 21-23 May, 197-199

[*Italia et al.*] Italia, V., M. Prisco, S. Campopiano, A. Cusano and A. Cutolo (2005), Chirped fiber bragg gratings for electrically tunable time delay lines, *IEEE J. Quantum Electron.*, 11 (2), 408-416

[*Izutsu et al.*] Izutsu, M., S. Shikama and T. Sueta (1981), Integrated optical SSB modulator/frequency shifter, *IEEE J. Quantum. Electron.*, 17 (11), 2225-2227

[*Izutsu*] Izutsu, M. (1999), Microwave photonics: new direction between microwave and photonic technologies, *Electronics and Communications in Japan, Part 2*, 82 (6), 46-54

[*Jalali and Yegnanarayanan*] Jalali, B. and S. Yegnanarayanan (2000), Optically controlled phased array antenna using wavelength-selective true time delay, Int. Conf. Phased Array Systems and Technology, 21-25 May, 367 - 370

[*James and Hall*] James, J.R. and P.R. Hall (1988), *Handbook of microstrip antennas*, IEE Electromagnetic Wave Series, Peter Peregrinus Ltd.

[*Jemison and Herczfeld 1993*] Jemison, W.D. and P.R. Herczfeld (1993), Acoustooptically controlled true time delays, *IEEE Microwave and Guided Wave Lett.*, 3 (3), 72-74

[*Jemison and Herczfeld 1996*] Jemison, W.D. and P.R. Herczfeld (1996), Acoustooptically controlled true time delays, *IEEE Microwave and Guided Wave Lett.*, 6 (8), 283-285

[*Jespersen and Herczfeld*] Jespersen, N.V. and P.R. Herczfeld (1990), Phased array antennas with phasers and true time delay phase shifters, Antennas and Propagation Society Symposium, 7-11 May, 2, 778-781

[*Jez et al.*] Jez, D.R., K.J. Cearns, P.E. Jessop, “Optical waveguide components for beam forming in phased array antennas”, Microwave and optical technology letters, Vol.15, 1, 46-49, 1997

[*Ji et al.*] Ji, Y., K. Inagaki, O. Shibata, Y. Karasawa (1997), Beam formation by using optical signal processing techniques, Antennas and Propagation Society International Symposium, 13-18 July, 2, 739-742

[*Kalman et al.*] Kalman, R.F., J.C. Fan, and L.G. Kazovsky (2001), Dynamic range of coherent analog fiber optic links, *J. Ligthwave Technol.*, 12 (7), 1263-1267

[*Kane et al.*] Kane, B.C., L.A. Geis, M.A. Wyatt, D.G. Copeland, and J.A. Mogensen (2005), Smart phased array SoCs: a novel application for advanced SiGe HBT BiCMOS technology, *IEEE Proc.*, 93 (9), 1656-1668

[*Kobayashi and Ogawa 1995*] Kobayashi, O. and H. Ogawa (1995), Amplitude and phase control of an RF signal using liquid-crystals by optoelectronic method, *IEICE Trans. Electron.*, E78-C(8), 1082-1089

[*Kobayashi and Ogawa 1995*] Kobayashi, O. and H. Ogawa (1996), A liquid-crystal control, coherent type optoelectronic phased array antenna beam forming network using polarization multiplex optical heterodyning, *IEICE Trans. Electron.*, E79-C(1), 80-86

[*Koepf*] Koepf, G.A. (1984), Optical processor for phased array antenna beam formation, Optical technology for microwave applications, S.K. Yao editor, *Proc. SPIE*, 477, 75-81

[*Konishi et al.*] Konishi, Y., W.Chujo and M. Fujise (1992), Carrier to noise ratio and sidelobe in a two laser model optically controlled array antenna using Fourier optics, *IEEE Trans. Antennas Propagat.*, 40 (12), 1459-1465

[*Kuhlow et al.*] Kuhlow, B. et al. (2002), Silica based optical beamformer in a 60 GHz Radio-over-fiber system, International Zurich seminar on broadband communications, 10-21 Feb., 25-1 25-4

[*Kumar*] Kumar, A. (1996), *Antenna design with fiber optics*, Norwood MA, Artech House

[*Lacomme*] Lacomme,P. (2003), New trends in airborne phased array radars, IEEE International Symposium on Phased Array Systems and Technology, 14-17 Oct., 17-22

**[***Leach and Paris.***]** Leach, W. and D. Paris (1973), Probe compensated near-field measurements on a cylinder, *IEEE Trans. Antennas Propagat.*, 21 (4), 435-445

[*Lee et al. 1995a*] Lee, J.J. et al. (1995), Photonic wideband array antennas, *IEEE Antennas and Propagat.* , 43 (9), 966-982

[*Lee et al. 1995b*] Lee, J.J, R.Y. Loo, S. Livingston, H.W. Yen and G. Tangonan, Conformal array controlled by photonics, *Electron. Lett.*, 31 (19), 1620-1621

[*Li and Chen*] Li, R.L.Q. and R.T. Chen (1997), 3-bit substrate guided mode optical true time delay lines operating at 25GHz, *IEEE Photon. Technol. Lett.*, 9 (1), 100-102

[*Li et al.*] Li, R.L.Q., Z. Fu and R.Chen (1997), High packing density 2.5 Thz true-time-delay lines using spatially multiplexed substrate guided waves in conjunction with volume holograms on a single substrate, *J. Lightwave Technol.*, 15 (12), 2253-2258

[*Lin and Boughton*] Lin, S.C. and R. S. Boughton (1989), Acousto-optic multichannel programmable true time delay lines, Optical Technology for Microwave Applications IV, S.-K. Yao, editor, *Proc. SPIE,* 1102, 162-173

[*Liu et al. 2002a*] Liu, Y., J. Yang and J. Yao (2002), Wideband true-time-delay unit for phased array beamforming using discrete-chirped fiber grating prism, *Optics Communications*, 277, 177-187

[*Liu et al. 2002b*] Liu, Y., J. Yang and J. Yao (2002), Continuous true-time-delay beamforming for phased array antenna using a tunable chirped fiber grating delay line, *IEEE Photon. Technol. Lett.*, 24 (8), 1172-1174

[*Lo and Lee*] Lo, Y.T. and S.W. Lee (1988), *Antenna handbook - Theory, applications and design*, Van Nostrand Reinhold Company, New York

[*Loo et al.*] Loo R.Y. et al. (1995), 5 bit photonic time shifter for wideband array, *Electron. Lett.,* 31 (18), 1532-1533

[*Magel et al.*] Magel, G.A., T.H. Lin, L.Y. Pang and W.R. Wu (1994), Integrated optic switches for phased array applications based on electrostatic actuation of metallic membranes, Optoelectronic Signal Processing for Phased Array Antennas IV, B.M. Hendrickson, editor, *Proc. SPIE*, 2155, 107-113

[*Mailloux 1981*] Mailloux, R.J. (1981), Phased array technology for advanced systems, *IEEE Antennas Propagat. Society Newsletter*, 23 (5), 4-9

[*Mailloux 1984*] Mailloux, R.J. (1984), Array gratin lobes due to period phase, amplitude and time delay quantization, *IEEE Trans. Antennas Propagat.*, 32 (12), 1364-1368

[*Mailloux 2005*] Mailloux, R.J. (2005), *Phased array antenna handbook*, Artech House, Norwood, MA

[*Matsumoto et al.*] Matsumoto, K, M. Izutsu, T. Sueta, "Microwave phase shifter using optical waveguide structure", Journal of Lightwave technology, Vol.9, 11, 1523—1527, 1991

[*Matthews 1999*] Matthews, P.J. (1999), Practical photonic beamforming, International Topical Meeting on Microwave Photonics, 17-19 Nov., 1, 271-274

[*Matthews 2000*] Matthews, P.J. (2000), Photonics for phased array systems, IEEE International Conference on Phased Array Systems and Technology, 21-25 May, 348-352

[*Matthews et al. 1996*] Matthews, P.J., M. Y. Frankel and R. D. Esman (1996), Fiber optic control of a two dimensional, true time-steered array transmitter, Int. Sym. Antennas and Propagation Society, 21-26 July, 2, 1512-1515

[*Matthews et al. 1998*] Matthews, P.J., M. Y. Frankel and R. D. Esman (1998), A wide-band fiber-optic true-time-steered array receiver capable of multiple independent simultaneous beams, *IEEE Photon. Technol. Lett.*, 10 (5), 722-724

[*Medberry et al.*] Medberry, J.B., P.D. Biernacki and P.J. Matthews (2000), Range demonstration of an ultra-wideband, continuous, time steered array using a fiber-optic, cascaded grating prims, IEEE Symposium on Microwave Theory and Techniques, 11-16 June, 1, 597-600

[*Minasian and Alameh*] Minasian, R.A. and K.E. Alameh (1997), Optical fiber grating-based beamforming network for microwave phased arrays, *IEEE Trans. Microwave Theory Tech.*, 45 (8), 1513-1518

[*Minasian et al.*] Minasian, R.A., K.E. Alameh and N. Fourikis (1995), Wavelength-multiplexed photonic beam-former architecture for microwave phased arrays, *Microwave Optical Technol. Lett.*, 10 (2), 84-88

[*Molony et al.*] Molony, A., C. Edge and I. Bennion (1995), Fiber grating time delay element for phased array antennas, *Electron. Lett.*, 31 (17), 1485-1486

[*Neff et al.*] Neff, J.A., R.A. Athale and S.H. Lee (1990), Two-dimensional spatial light modulators: a tutorial, *Proceedings of the IEEE*, 78 (5), 826-855

[*Ng et al. 1989*] Ng, W., A.A. Walston, G.L. Tangonan, I.L. Newberg and J.J. Lee (1990), Wideband fiber-optic delay network for phased array antenna steering, *Electron. Lett.*, 25 (21), 1456-1457

[*Ng et al. 1990*] Ng, W., A.A. Walston, G.L. Tangonan, J.J. Lee and I.L. Newberg (1990), Optical steering of dual band microwave phased array antenna using semiconductor laser switching, *Electron. Lett.*, 26 (12), 791-793

[*Ng et al. 1991*] Ng, W., A.A. Walston, G.L. Tangonan, J.J. Lee, I.L. Newberg and N. Bernstein (1991), The first demonstration of an optically steered microwave phased array antenna using true-time-delay, *J. Lightwave Tech.*, 9 (9), 1124-1131

[*Ng et al. 1994*] Ng, W., D. Yap, A. Narayanan and A. Walston (1984), High-precision detector-switched monolithic GaAs time-delay network for the optical control of phased arrays, *IEEE Photon. Technol. Lett.*, 6 (2), 231-234

[*Ng et al. 1995*] Ng, W., R. Loo, V. Jones, J. Lewis, S. Livingston and J.J. Lee (1995), Silica-waveguide optical time-shift network for steering a 96-element L-band conformal array, Optical Technology for Microwave Applications VII, A.P. Goutzoulis, editor, *Proc. SPIE*, 2560, 140-147

[*Nickerson et al.*] Nickerson, K.A. P.E. Jessop and S.Haykin (1991), Optical processor for array antenna beam shaping and steering, *Optical Engineering*, 30 (10), 1497-1502

[*Nirmalathas et al.*] Nirmalathas, A., D. Novak, R. Waterhouse and C. Lim (2000), Photonics as an enabling technology for future microwave systems, Asia-Pacific Microwave Conference, 3-6 Dec., 912 - 916

[*Ortega et al. 1998*] Ortega, B., J.L. Cruz, M.V. Andrés, A. Diez, D. Pastor and J. Capmany (1998), Microwave phase shifter based on fibre bragg grating, *Electron. Lett.*, 34 (21), 2051-2053

[*Ortega et al. 1999*] Ortega, B., J.L. Cruz, M.V. Andrés, A. Diez, D. Pastor and J. Capmany (1999), Microwave phase shifter based on fibre bragg grating operating at constant wavelength, Optical Fiber Communication Conference and the International Conference on Integrated Optics and Optical Fiber Communication, 21-26 Feb., 4, 162-164

[*Ortega et al. 2000a*] Ortega, B., J.L. Cruz, J. Capmany, M.V. Andrés and D. Pastor (2000), Analysis of a microwave time delay line based on a perturbed uniform fiber bragg grating operating at constant wavelength, *IEEE Photon. Technol. Lett.*, 18 (3), 430-436

[*Ortega et al. 2000b*] Ortega, B., J.L. Cruz, J. Capmany, M.V. Andrés and D. Pastor (2000), Variable delay line for phased-array antenna based on a chirped fiber grating, *IEEE Trans. Microwave Theory Tech.*, 48 (8) 1352-1360

[*Pan*] Pan, J.J. (1993), Microwave optics for space and ground communications, National Conference on Commercial Applications and Dual-Use Technology, 16-17 June, 1-6

[*Pan and Shi*] Pan, J.J. and Y. Shi (1997), Fiber bragg grating for phased array systems, Int. Sym. Antennas and Propagation Society, 13-18 July, 2, 751-754

[*Pan et al.*] Pan, J.J., S.L. Chia, W.Z. Li and C.H. Grove (1992), Cost-effective optical switch matrix for microwave phased array, Optical technology for microwave applications V, S.-K. Yao editor, *Proc. SPIE*, 1476, 133-142

[*Paquet et al.*] Paquet, S., F. Chenard, Z. Jakubczyk, M. Belanger, M. Tetu, C.Belisle (1995), Optical delay lines in high-silica (SiO2/Si) waveguides,Applications of Photonic Technology, G.A. Lampropoulos, J. Chrostowski, and R.M. Measures, editors, *Proc. SPIE*, 515-518

[*Paris et al.*] Paris, D., W. Leach and E. Joy (1978), Basic theory of probe-compensated near-field measurements, *IEEE Trans. Antennas Propagat.*, 26 (3), 373-379

[*Parker and Zimmermann 2002a*] Parker, D. and D.C. Zimmerman (2002), Phased arrays-part I: theory and architectures, *IEEE Trans. Microwave Theory Tech.*, 50 (3), 678-687

[*Parker and Zimmermann 2002b*] Parker, D. and D.C. Zimmerman (2002), Phased arrays- part II: implementations, applications, and future trends, *IEEE Trans. Microwave Theory Tech.*, 50 (3), 688-698

[*Paul et al.*] Paul, D.K., R. Razdan and B.J. Markey (1996), Optical beam forming and steering architectures for satcom phased-array antennas, International Symposium on Antennas and Propagation, 21-26 July, 2, 1508 - 1511

[*Paul*] Paul, D.K. (1993), Optical beam forming and steering for phased-array antenna, National Conference on Commercial Applications and Dual-Use Technology, 16-17 June, 7-12

[*Riza 1991a*] Riza, N.A. (1991), Acousto-optic architectures for multi-dimensional phased array antenna processing, Optical Technology for Microwave Applications V,S.-K. Yao, editor, *Proc. SPIE*, 1476, 144-156

[*Riza 1991b*] Riza, N.A. 1991, Transmit/receive time-delay beam-forming optical architecture for phased-array antennas, *Applied Optics, 30 (32), 4594-4595*

[*Riza 1992d*] Riza, N.A. (1992), Liquid crystal-based optical time delay control system for wideband phased arrays, Analog Photonics, A.R. Pirich, P. Sierak, editors, *Proc. SPIE*, 1790, 171-183

[*Riza 1992a*] Riza, N.A. (1992), An acoustooptic-phased-array antenna beamformer for multiple simultaneous beam generation, *IEEE Photon. Technol. Lett.*, 4 (7), 807-809

[*Riza 1992b*] Riza, N.A. (1992), An acoustooptic phased array antenna beamformer with independent phase and carrier control using single sideband signals, *IEEE Photon. Technol. Lett.*, 4 (2), 177–179

[*Riza 1992c*] Riza, N.A. (1992), Liquid crystal-based optical control of phased array antennas, *J. Lightwave Technol.*, 10 (12), 1974-1984

[*Riza 1993*] Riza, N.A. (1993),Experimental demonstration of an acousto-optic system for two-dimensional phased-array antenna scanning, *Applied Optics, 32 (11), 1936-1942*

[*Riza 1994*] Riza, N.A. (1994), Acousto-optic liquid-crystal analog beam former for phased-array, *Applied Optics*, 33 (17), 3712-3724

[*Riza 1994b*] Riza, N.A. (1994), Liquid crystal-based optical time delay units for phased array antennas, *J. Lightwave Technol.*, 12 (8), 1440-1447

[*Riza 1997a*] Riza, N.A. (1997), *Selected Papers on Photonic Control Systems for Phased Array Antennas*, Spie Milestone Series

[*Riza 1997b*] Riza, N.A. (1997), Analog vector modulation-based widely tunable frequency photonic beamformer for phased-array antennas, *IEEE Trans. Microwave Theory Tech.,* 45 (8), 1508-1512

[*Riza and Khan*] Riza, N.A. and S.A. Khan (2001), Photonic beamformer with flexible interface for phased array antennas, 14th Annual Meeting of the IEEE Lasers and Electro-Optics Society, 12-13 Nov., 2, 816-817

[*Riza and Madamopoulos*] Riza, N.A. and N. Madamopoulos (1997), Characterization of a ferroelectric liquid crystal-based time delay unit for phased array antenna applications, *J. Lightwave Technol.*, 15 (7), 1088–1094

[*Riza and Polla*] Riza, N.A. and D.L. Polla (1992), Micromechanical fiber-optic switches for optical networks, Integrated Optics and Microstructures, M. Tabib-Azar, D.L. Polla, editors, *Proc.SPIE,* 1793, 108-126

[*Riza and Psaltis*] Riza, N.A. and D.Psaltis (1991), Acousto-optic signal processors for transmission and reception of phased-array antenna signals, *Applied Optics, 30 (23), 3294-3303*

[*Riza et al.*] Riza, N.A., S.A. Khan and M.A. Arain (2002), Flexible beamformer and remoting head for optically controlled phased array antennas, IEEE International Microwave Symposium Digest, 2-7 June, 3, 1941-1944

[*Roman et al.*] Roman, J.E., M.Y. Frankel, P.J. Matthews, and R.D. Esman (1997), Time steered array with a chirped grating beamformer, *Electronics Letters*, 33 (8), 652-653

[*Rondinelli*] Rondinelli, L.A. (1959), Effects of random errors on the performance of antenna arrays of many elements, IRE International Convention Record, 7 (1), 174-189

[*Seeds 1997*] Seeds, A.J. (1997), Application of opto-electronic techniques in phased array antenna beamforming, International Topical Meeting on Microwave Photonics, 3-5 Sept., 15-20

[*Seeds 2002*] Seeds, A.J. (2002), Microwave photonics, *IEEE Trans. Microwave Theory Tech.,* 50 (3), 877-887

[*Seeds 2004*] Seeds, A.J. (2004), Microwave photonic links, International Topical Meeting on Microwave Photonics, 4-6 Oct, 123-126

[*Sheehan and Forrest*] Sheehan, P.G. and J.R. Forrest (1984), The use of optical techniques beamforming in phased arrays, Optical Technology for Microwave Applications, S.-K. Yao editor, *Proc. SPIE*, 477, 92-889

[*Shi et al.*] Shi, Z., Y. Jiang, B. Howlet, Y.Chen, F. Zhao and R.T Chen (2003), Continuously delay-time tunable-waveguide hologram module for x-band phased-array antenna, *IEEE Photon. Technol. Lett.*, 15 (7), 972-974

[*Skolnik*] Skolnik, M.I. (1970), *Radar handbook*, McGraw Hill

[*Soref 1984*] Soref, R.A (1984), Programmable time-delay devices, *Applied Optics*, 23 (21), 3736-3737

[*Soref 1985*] Soref, R.A. (1985), Voltage controlled optical/RF phase shifter, J. Lightwave Technol., 3(5), 992-998

[*Soref 1992*] Soref, R.A. (1992), Optical dispersion technique for time-delay beam steering, *Applied Optics*, 31, 7395-7397

[*Soref 1996*] Soref, R.A. (1996), Fiber grating prism for true time delay beamsteering, *Fiber and Integrated Optics,* 15, 325-333

**[***Stulemeijer et al. 1998*] Stulemeijer, J., D.H.P. Maat, I. Moerman, F.E. van Vliet and M.K. Smit (1998), Photonic integrated beamformer for a phased array antenna, 24th European Conference on Optical Communication, 20-24 Sept., 1, 637-638

**[***Stulemeijer et al. 1999*] Stulemeijer, J., F.E. van Vliet, K.W. Benoist, D.H.P. Maat and M.K. Smit (1999), Compact photonic integrated phase and amplitude controller for phased-array antennas, *IEEE Photon. Technol. Lett.,* 11 (1), 122-124

**[***Stulemeijer et al. 2000*] Stulemeijer, J., R. van Dijk, F.E. van Vliet, D.H.P. Maat and M.K. Smit (2000), Photonic chip for steering a four element phased array antenna, International Topical Meeting on Microwave Photonics, 11-13 Sept. 20-22

[*Sullivan et al.*] Sullivan, C.T. et al. (1992), Switched time delay elements based on AlGaAs/GaAs optical waveguide technology at 1.32μm for optically controlled phased array antennas, Optical Technology for Microwave Applications VI and Optoelectronic Signal Processing for Phased-Array Antennas III, S.-K. Yao, B.M. Hendrickson, editors, *Proc. SPIE*, 1703, 264-271

[*Surette et al.*] Surette, M.R., D. R. Hjelme and A. R. Mickelson (1993), An optically driven phased array antenna utilizing heterodyne techniques, *J. Lightwave Technol.*, 11 (9), 1500-15090

[*Tamburrini et al.*] Tamburrini, M., M. Parent, L. Goldberg and D. Stillwell (1987), Optical feed for a phased array microwave antenna, *Electron. Lett.*, 23 (13), 680-681

[*Tang et al.*] Tang, R., A. Popa and J.J. Lee (1990), Application of photonic technology to phased array antennas, Antennas and Propagation Society Symposium, 7-11 May, 2, 758-761

[*Targonski et al.*] Targonski, S.D., R. B. Waterhouse and D. M. Pozar (1998), Design of Wide-Band Aperture-Stacked Patch Microstrip Antennas, *IEEE Trans. Antennas Propagat.*, 43 (9), 1245-1251

[*Tokoro et al.*] Tokoro, S., K. Kuroda, A. Kawakubo, K. Fujita, H. Fucinami (2003), Electronically scanned millimeter-wave radar for pre-crash safety and adaptive cruise control system, IEEE Intelligent Vehicles Symposium, 9-11 June, 304-309

[*Tong and Wu 1996a*] Tong, D.T.K. and M.C. Wu (1996), A novel multiwavelength optically controlled phased array antenna with a programmable dispersion matrix, *IEEE Photon. Technol. Lett.*, 8 (6), 812-814

[*Tong and Wu 1996b*] Tong, D.T.K. and M.C. Wu (1996), Programmable dispersion matrix using Bragg fibre grating for optically controlled phased array antennas, *Electron. Lett.*, 32 (17), 1532-1533

[*Tong and Wu 1998a*] Tong, D.T.K. and M.C. Wu (1998), Multiwavelength optically controlled phased array antennas, *IEEE Trans. Microwave Theory Tech.*, 46 (1), 108-115

[*Tong and Wu 1998b*] Tong, D.T.K. and M.C. Wu (1998), Transmit/receive module of multiwavelenght optically controlled phased array antennas, *IEEE Photon. Technol. Lett.*, 18 (7), 1018-1020

[*Toughlian and Zmuda 1993*] Toughlian, E.N. and H. Zmuda, Variable time-delay system for broadband phased array and other transversal filtering applications, *Optical Engineering,* 32 (3), 613-617

**[***Toughlian et al.***]** Toughlian, E.N., H.Zmuda and P.Kornreich (1990), A deformable mirror –based optical beamforming system for phased array antennas, *IEEE Photon. Technol. Lett.*, 2 (6), 444-446

[*Tsap et al.*] Tsap, B., D.A., Y. Chang, H.R. Fetterman, A.F.J. Levi, and D.A. Cohen (1998), Phased array optically controlled receiver using a serial feed, *IEEE Photon. Technol. Lett.*, 10 (2), 267-269

[*Tulchinsky and Matthews 2000*] Tulchinsky, D.A and P.J. Matthews (2000), Range demonstration of a reconfigurable fiber-optic time-steered 2D transmit beamformer, International Topical Meeting on Microwave Photonics, 11-13 Sept, 13-16

[*Tulchinsky and Matthews 2001*] Tulchinsky, D.A and P.J. Matthews (2001), Ultrawide-band fiber-optic control of a millimetre-wave transmit beamformer, *IEEE Trans. Microwave Theory Tech.*, 49 (7), 1248-1253

[*Uhing et al.*] Uhing, J., S. Thomas and C. Christodoulou (1990), A statistical approach for estimating the loss contribution of concatenated connectors in fiber-optic links, IEEE National Conference on Aerospace and Electronics, 21-25 May, 1,239-245

[*VanBlaricum*] VanBlaricum, M.L. (1994), Photonic systems for antenna applications, *IEEE Antennas Propagat. Magazine*, 36 (5), 30-38

[*Venkatesh et al.*] Venkatesh, S. et al. (2002), Performance improvements in bubble-actuated photonic cross-connect switches, Annual Meeting of the IEEE Lasers and Electro-Optics Society, 10-14 Nov., 1, 39-40

[*Vidal et al. 2002a*] Vidal, B., D. Madrid, J.L. Corral and J. Martì (2002), Novel photonic true-time-delay beamformer based on the free-spectral-range periodicity of arrayed waveguide gratings and fiber dispersion, *IEEE Photon. Technol. Lett.*, 14 (11), 1614-1616

[*Vidal et al. 2002b*] Vidal, B., J.L. Corral and J. Martì (2002),Optical delay line using arrayed waveguide grating in fold back configuration for phased array antennas, International Topical Meeting on Microwave Photonics, 5-8 Nov., 269-272

[*Volker*] Volker, M. (1992), Coherent all-fibre optical beam-steering technique for phased-array antennas, *IEE Proceedings-J*, 139 (4), 305-308

[*Wand and Tripp*] Wang, J.J.H. and V.K. Tripp (1991), Design of multioctave spiral-mode microstrip antennas, *IEEE Trans. Antennas Propagat.*, 39 (3), 332-335

[*Wang et al.*] Wang, W., Yongqiang Shi, Weiping Lin, James H. Bechtel (1996), Waveguide binary photonic true-time-delay lines using polymer integrated switches and waveguide delays, Photonics and Radio Frequency, B.M. Hendrickson, editor, *Proc. SPIE*, 2844, 200-211

[*Winnall et al.*] Winnall, S.T., A.C. Lindsay, G.A. Knight, ”A wide-band microwave photonic phase and frequency shifter”IEEE Transaction on Microwave Theory and Techniques, Vol. 45, 6, 1003—1006, 1997

[*Xu et al. 1995*] Xu, L., R. Taylor and S.R. Forrest (1995), The use of optically coherent detection techniques for true time delay phased array ad systems, *J. Lightwave Technol.*, 13 (8), 1663-1678

[*Xu et al. 1996*] Xu, L., R. Taylor and S.R. Forrest (1996), True time delay phased array antenna feed system based on optical heterodyne techniques, *IEEE Photon. Technol. Lett.*, 8 (1), 160-162

[*Yang et al.*] Yang, J., Y. Liu and J. Yao (2001), Wideband true time delay system using fiber Bragg grating prism incorporated with a wavelength tunable fiber laser source, International Topical Meeting on Microwave Photonics, 7-9 Jan., 125-128

[*Yao and Maleki*] Yao, X. S. and Lute Maleki (1994), A novel 2-D programmable photonic time-delay device for millimeter-wave signal processing applications, *IEEE Photonics Technol. Lett.*, 6 (12), 1463-1465

[*Yao et al. 2002a*] Yao, Y., J. Yang and Y. Liu (2002), Continuous true-time-delay beamforming employing a multiwavelength tunable fiber laser source, *IEEE Photon. Technol. Lett.*, 14 (5), 687-689

[*Yao et al. 2002b*] Yao, Y., J. Yang and Y. Liu (2002), Continuous true-time delay beamforming system employing a multiwavelength tunable laser source with equally increased or decreased wavelength spacing, Optical Fiber Communication Conf., 17-22 March, 476-478

[*Yegnanarayanan and Jalali*] Yegnanarayanan, S. and B. Jalali (2000), Wavelength selective true time delay for optical control of phased array antenna

[*Yegnanarayanan et al.1996*] Yegnanarayanan, S. P.D. Trinh and B. Jalali (1996), Recirculating photonic filter: a wavelength selective time delay for phased array antennas and wavelength code-division multiple access, *Optics Lett.*, 21 (10), 740-742

[*Yegnanarayanan et al. 1997a*] Yegnanarayanan, S., P.D. Trinh, F. Coppinger and B.Jalali (1997), Compact silicon-based integrated optic time delays, *IEEE Photon. Technol. Lett.*, 9 (5), 634-635

[*Yegnanarayanan et al. 1997b*] Yegnanarayanan, S., P.D. Trinh, F. Coppinger and B.Jalali (1997), Compact silicon-based integrated optical time delay network, SPIE, Optical Technology for Microwave Applications VIII, Anastasios P. Goutzoulis, editor, *Proc. SPIE*, 3160, 2-10

[*Zhang and Daryoush*] Zhang,X. and A. S. Daryoush (1993), Full 360 deg phase shifting of injection-locked oscillators, *IEEE Microwave Guided Wave Lett.,* 3 (1), 14-16

[*Zmuda and Toughlian 1990*] Zmuda, H. and E.N. Toughlian (1990), A photonic RF delay line for phased array antennas, *J. Lightwave Technol.*, 8 (12), 1824–1828

[*Zmuda and Toughlian 1994*] Zmuda, H. and E.N. Toughlian (1994), *Photonic aspects of modern radar*, Norwood, MA, Artech House

[*Zmuda et al.*] Zmuda, H., R.A. Soref, P. Payson, S. Johns and E.N. Toughlian (1997), Photonic beamformer for phased array antennas using fiber grating prism, *IEEE Photon. Technol. Lett.*, 9 (2), 241-243

[*Zurcher and Gardiol*] Zurcher, J.F. and F.R. Gardiol (1995), *Broadband patch antennas*, Norwood, MA, Artech House